Technische Universität München

Fakultät für Mathematik
Lehrstuhl M2 – Fachgebiet Numerische Mathematik (Prof. B. Wohlmuth)

Complexity Reduction for Finite Element Methods with Applications to Eigenvalue Problems

Thomas Horger, M.Sc.

Vollständiger Abdruck der von der Fakultät für Mathematik der Technischen Universität München zur Erlangung des akademischen Grades eines

Doktors der Naturwissenschaften (Dr. rer. nat.)

genehmigten Dissertation.

Vorsitzende: Prof. Dr. Christina Kuttler

Prüfer der Dissertation:

1. Prof. Dr. Barbara Wohlmuth

2. Prof. Anthony Patera, Ph.D., Massachusetts Institute of Technology

3. Prof. Karen Veroy–Grepl, Ph.D., RWTH Aachen

Die Dissertation wurde am 05.07.2016 bei der Technischen Universität München eingereicht und durch die Fakultät für Mathematik am 14.10.2016 angenommen.

"Be true to the game, because the game will be true to you. If you try to shortcut the game, then the game will shortcut you. If you put forth the effort, good things will be bestowed upon you. That's truly about the game, and in some ways that's about life too."

- Michael Jordan

Acknowledgement

First and foremost I would like to express my sincere gratitude to my advisor Prof. Dr. Barbara Wohlmuth for her invaluable guidance and mentoring during the past years. Despite her busy schedule she has always found time to share her profound knowledge and her advice on professional and personal topics. I have greatly benefited from the free and open research environment she created. Furthermore I am thankful to her for introducing me to many challenging new topics while also encouraging me to pursue several exciting side-projects, for giving me the opportunity to present my work at conferences and for introducing me to many new people.

I would like to express my deepest gratitude to Prof. Anthony Patera, Ph.D. and Prof. Karen Veroy-Grepl, Ph.D. for spending their valuable time and putting effort into providing the referee reports for this thesis as well as for being part of the examination committee. I have had the chance to spend a week at RWTH Aachen visiting the group of Prof. Karen Veroy-Grepl, Ph.D. and I am very thankful to her for inviting me and taking time to discuss new ideas. Furthermore I would like to thank Prof. Dr. Christina Kuttler for taking the chair of the examination committee. I am also very grateful to her for her guidance and advice since the time when I was a Bachelor student.

Special thanks to my present and former colleagues at the chair of numerical mathematics (M2) at Technische Universität München for the friendly and inspiring working atmosphere during the last years. I have truly enjoyed working with Klemens Schürholz, Sebastian Otten and Haddar Sleiman, who have each collaborated with me as student assistants for several months. At this point I want to express my sincere gratitude to my colleagues Dr. Klaus-Dieter Reinsch and Linus Wunderlich for proofreading parts of this thesis. Furthermore I would like to thank both of them as well as Ettore Vidotto for welcome distractions, joyful moments and culinary excursions.

During the last years I greatly enjoyed collaborating with the project partners in the AiF/DFG project "Vibroakustik im Planungsprozess für Holzbauten". I would especially like to thank them for the friendly atmosphere and our fruitful discussions. The work presented in this thesis was funded by the Deutsche Forschungsgemeinschaft (DFG) under the grant numbers WO-671/13-1 and WO-671/13-2. I would like to express my gratitude for this financial support.

Finally I would like to thank my parents Adrianne and Marius for their continuous support and love. They have always encouraged me to pursue a career in academics, without them I would not be where I am today. Furthermore I would like to thank my friends for their patience during the last years, when I was often not able to spend as much time with them as I would have liked. Especially I want to thank my awesome girlfriend Aenne for all the fun she brings into my life and the adventures we share. I am also very grateful to her for her caring support, her belief in me and the encouragement during all these years.

Publications by the author

The following publications are included in this thesis:

- Horger, T., Wohlmuth, B., Wunderlich, L.,
  Reduced basis isogeometric mortar approximations for eigenvalue problems in vibroacoustics, accepted for publication in MoRePaS 2015, 2016, [81].

- Horger, T., Pustejovska, P., Wohlmuth, B.,
  Higher order energy-corrected finite element methods, submitted, 2016, [79].

- Horger, T., Wohlmuth, B., Dickopf, T.,
  Simultaneous reduced basis approximation of parameterized elliptic eigenvalue problems, ESAIM: Mathematical Modelling and Numerical Analysis, published online, 2016, [80].

- Horger, T., Melenk, J.M., Wohlmuth, B.,
  On optimal L^2 and surface flux convergence in FEM, Computing and Visualization in Science, Volume 16, pp. 231–246, 2015, [77].

- Horger, T., Huber, M., Rüde, U., Waluga, C., Wohlmuth, B.,
  Energy-corrected finite element methods for scalar elliptic problems, Numerical Mathematics and Advanced Applications - ENUMATH 2013 proceedings, Volume 103 of the series Lecture Notes in Computational Science and Engineering, pp. 19–36, 2014, [74].

- Horger, T., Kollmannsberger, S., Frischmann, F., Rank, E., Wohlmuth, B.,
  A new mortar formulation for modeling elastomer bedded structures with modal-analysis in 3D, Advanced Modeling and Simulation in Engineering Sciences, Volume 1, 2014, [75].

The following publication are not included in this thesis:

- Garcia-Betancur, J.-C., Goni-Moreno, A., Horger, T., Schott, M., Sharan, M., Eikmeier, J., Wohlmuth, B., Zernecke, A., Ohlsen, K., Kuttler, C., Lopez, D., *Cell-fate decision defines acute and chronic infection cell lineages in Staphylococcus aureus*, in preparation, 2016, [62].

- Horger, T., Kuttler, C., Wohlmuth, B., Zhigun, A.,
  Analysis of a bacterial model with nutrient-dependent degenerate diffusion, Mathematical Methods in the Applied Sciences, Volume 38, pp. 3851–3865, 2015, [76].

- Horger, T., Oelker, A., Kuttler, C., Pérez-Velázquez, J.,
  Mathematical modeling of tumor-induced angiogenesis using porous medium diffusion, International Journal of Biomathematics and Biostatistics, Volume 2, pp. 145–165, 2013, [78].

- Kaufmann, S., Horger, T., Oelker, A., Beck, S., Schulze, M., Nikolaou, K., Ketelsen, D., Horger, M.,
  Volume perfusion computed tomography (VPCT)-based evaluation of response to TACE using two different sized drug eluting beads in patients with non-resectable hepatocellular carcinoma: Impact on tumor and liver parenchymal vascularisation, European Journal of Radiology, Volume 84, pp. 2548–2554, 2015, [91].

- Kaufmann, S., Schulze, M., Horger, T., Oelker, A., Nikolaou, K., Horger, M.,
  Reproducibility of VPCT parameters in the normal pancreas: comparison of two different kinetic calculation models, Academic Radiology, Volume 22, pp. 1099–1105, 2015, [93].

- Kaufmann, S., Horger, T., Oelker, A., Kloth, C., Nikolaou, K., Schulze, M., Horger, M.,
  Characterization of hepatocellular carcinoma (HCC) lesions using a novel CT-based volume perfusion (VPCT) technique, European Journal of Radiology, Volume 84, pp. 1029–1035, 2015, [92].

- Syha, R., Grünwald, L., Horger, T., Spira, D., Ketelsen, D., Vogel, W., Claussen, C.D., Horger, M.,
  Assessment of the nature of residual masses at end of treatment in lymphoma patients using volume perfusion computed tomography, European Radiology, Volume 24, pp. 770–779, 2014, [156].

Abstract

This thesis presents finite element complexity reduction techniques for eigenvalue problems. For parameter dependent problems, we propose an adaptive reduced basis algorithm for multi-query outputs with applications to vibro-acoustics. Further efficiency is gained by component mode synthesis and mortar techniques. Additionally we generalize the concept of energy-corrected finite elements to higher order and eigenvalue problems to overcome the pollution effect on non-convex polygonal domains.

Zusammenfassung

In dieser Arbeit behandeln wir Methoden zur Komplexitätsreduktion bei finiten Elementen für Eigenwertprobleme. Mit einem adaptiven reduzierte Basen Algorithmus approximieren wir gleichzeitig mehrere Outputs eines parameterabhängigen Problems aus der Vibro-Akustik. Die Effizienz wird durch Component Mode Synthesis und Mortar Techniken weiter verbessert. Außerdem verallgemeinern wir das Konzept der Energiekorrektur für finite Elemente auf höhere Ordnungen und Eigenwertprobleme, um den Pollution-Effekt auf nichtkonvexen polygonalen Gebieten zu überwinden.

Contents

Chapter I.
Introduction and mathematical background

In this chapter we introduce the modeling problem as well as the theoretical and numerical background for the results presented in this thesis.

1. Introduction

Eigenvalue problems, whose solutions consist of the eigenmodes and eigenfrequencies of a system, arise in many physical and technical application areas. Among those are the vibro-acoustic analysis of building structures, which is the motivation of this work, as well as applications in areas such as electrical circuits and chemical engineering.

Mathematical models and numerical simulations play an important role during the planning process of a building [130, 132, 133]. Besides static and energetic considerations, also the vibro-acoustical analysis is a crucial part in developing an elaborate construction plan. After the construction of the building is completed, the impact as well as the airborne noise will be measured and have to fulfill strict requirements [131, 149].

Figure 1.1: Timber building example.[5]

In order to ensure that these standards will be met upon completion of the building, mathematical models are set up and sophisticated numerical methods are employed for the solution of the eigenvalue problems arising during the vibro-acoustical analysis. The geometry of a building like the one depicted in Figure 1.1 is extracted from a building information model (BIM), which gives information on the physical and functional properties of a building in digital form. A standard data model in the building industry are the Industry Foundation Classes (IFC), which are supported by many computer-aided design (CAD) software packages.

In a general setting, the eigenfrequencies and eigenmodes of the structure as well as the stimulation and the damping are required. Determining the eigenfrequencies and eigenmodes of a structure, which are here the solutions of a linear elasticity eigenvalue problem, allows to identify its vibrational spectrum for a given stimulation using modal superposition (spectral analysis) as in [130]. Modal analysis is typically useful when investigating low frequencies combined with a low eigenmode density. This applies to timber-frame constructions as depicted in Figures 1.1 and 1.2, where acoustic deficits can be found, for example at the intersection of thin walls with ceilings, especially for frequencies below 100 Hz. In the context of these buildings, modal analysis is used to calculate the noise level at the separating and flanking components of the structure, see Figure 1.2.

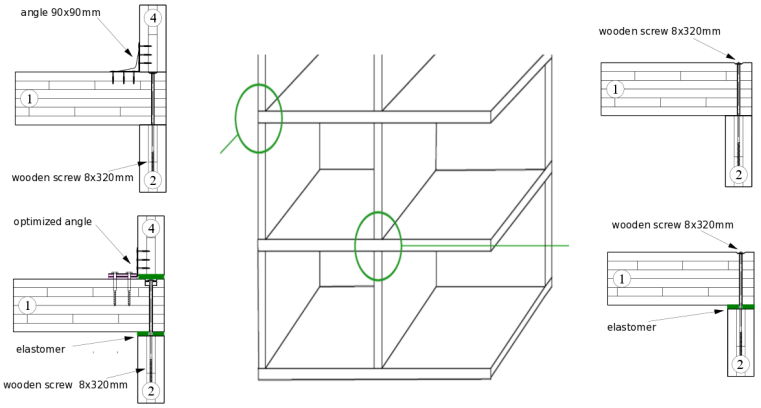

Figure 1.2: Building components.[56]

From this, the sound pressure level in the space under consideration can be calculated using modal coupling [130]. It is important to model the possible couplings of timber elements in a mechanically consistent way regarding vibro-acoustics.

The numerical simulation of the problems allows to gain insight into the behavior

of the system under varying parameters. These predictions give the opportunity to reevaluate the system and make changes to the materials used or to the construction itself while reducing temporal and monetary costs.

The challenge is to obtain results which are accurate and achieved in a sufficiently small time span. It has to be taken into account that simulations may have to be performed several times during the course of a project. In order for the models to be sufficiently accurate, very large and detailed systems are used for the modeling of the physical phenomena. The simulation of these large-scale systems is very expensive in terms of time and hardware. Thus not only the solutions of this detailed eigenvalue problem play a role, but also the need for reduced order models, which are significantly smaller while preserving the important characteristics of the original system.

In this thesis, we focus on the eigenfrequencies and the eigenmodes of a building structure in the context of model order reduction. The numerical methods were developed with the goal of including them into the planning process of a timber building. This allows the optimal design of single components and the investigation of their vibrational coupling as well as the vibro-acoustic properties of the entire building in an early stage of the planning process. The results presented in this thesis do not only apply to the specific physical situations considered, but can be generalized to a wide range of application areas.

The structure of this thesis is as follows: In Section 2 of Chapter I, we introduce the definitions and the theoretical as well as the numerical background constituting the foundation of the work conducted in this thesis. We start by introducing the necessary function spaces, then we give a short introduction to the equation of linear elasticity, which is used to model the building structures. Finally we present the general eigenvalue problem, which is the tool for obtaining the eigenfrequencies and eigenmodes of a structure.

Chapter II consists of Section 3 and Section 4, where complexity reduction in the sense of mortar methods is presented. In Section 3, we start by introducing mortar finite element methods for eigenvalue problems. These are non-conforming domain decomposition methods, in which the global domain is decomposed into overlapping or non-overlapping local subdomains in a geometrically conforming or non-conforming way. The central idea of mortar techniques is to replace the strong continuity condition of the solution across the interface by a weak one. Mortar

finite elements allow to mesh subdomains of the building such as walls and ceilings independently. This is useful since global meshing is very expensive. We demonstrate the suitability of the mortar method for high order finite elements and apply mortar methods to domains ranging from L-shape domains to whole buildings.

In Section 4 we derive a new mortar formulation designed to replace an explicitely discretized elastomer with a new coupling condition. To this end tailored Robin conditions are applied at the interface as coupling conditions instead of the more standard continuity constraints. We derive the dimensional reduced model with the new coupling condition, show the stability of the model by numerical experiments and subsequently test the performance of the new formulation on benchmark examples and demonstrate the engineering relevance for practical applications.

The following Chapter III deals with model order reduction approaches in the sense of reduced basis methods for eigenvalue problems. The chapter is divided into Section 5, Section 6 and Section 7.

In Section 5 we present a model reduction framework for parameterized eigenvalue problems by a reduced basis method, which is of particular interest for applications in vibro-acoustics since many evaluations have to be performed with changing parameters during the planning process. In contrast to the standard single output case, we approximate several outputs simultaneously, namely a certain number of the smallest eigenvalues. For a fast and reliable evaluation of these input-output relations, we analyze *a posteriori* error estimators for eigenvalues. Moreover, we show different greedy strategies and study their performance systematically. We pay special attention to multiple eigenvalues, whose appearance is parameter dependent.

In Section 6 we present the reduced basis method for eigenvalue problems in combination with isogeometric mortar methods. In contrast to finite elements, isogeometric methods allow to approximate a larger spectrum of eigenvalues and also curved geometries more accurately. We demonstrate that also in this context reduced basis eigenvalue methods are useful to reduce computation cost and time, where we are able to eliminate the Lagrange multipliers introduced by the mortar coupling and formulate a reduced eigenvalue problem for a symmetric positive definite matrix.

In Section 7 the component mode synthesis is presented. This method consists of

dividing a large global geometry setting into many smaller subgeometries. Then instead of considering the eigenvalue problem on the global geometry, it is subdivided into several local eigenvalue problems, which are solved on their own and then coupled to recover the global problem. This is especially useful in the vibroacoustic analysis of building structures since it is straight-forward to divide the building structure into smaller substructures such as walls and ceilings. Thus using reduced basis methods for eigenvalues instead of finite element solutions allows a further complexity reduction to save time while achieving a satisfying accuracy.

In Chapter IV, which contains Section 8, Section 9 and Section 10, we then deal with issues related to corner singularities, which arise in polygonal domains with reentrant corners. These can be found in buildings as, e.g., depicted in Figure 1.2, at window frames and doors and where walls meet the ceiling. The impact of the singularities on the numerical calculations is investigated and adequate countermeasures are presented.

We begin Section 8 by demonstrating the impact of the singularities theoretically in a simplified setting, given by the Laplace equation in two dimensions. It is well known that the regularity of the solutions of elliptic partial differential equations on domains with reentrant corners is limited depending on the maximal interior angle. This pollution effect on the solutions results in reduced convergence rates in the L^2- and H^1-norms for finite element approximations on families of quasi-uniform meshes and cannot be compensated by applying weighted norms. Furthermore we shortly describe the graded mesh method, which is a well-known procedure to obtain optimal L^2-convergence in the finite element context.

In Section 9, we introduce the energy correction method for the two-dimensional Laplace equation, which is a method for domains with reentrant corners to regain optimal order of convergence in weighted L^2-norms as well as in the standard L^2-norm. This is achieved by a local modification of the bilinear form in a vicinity of the singularity, which allows to overcome the pollution effect. We present convergence results in weighted Sobolev spaces and illustrate them by numerical tests that demonstrate optimal convergence rates for linear finite elements. Furthermore we show numerically that optimal convergence can be achieved for the three-dimensional Laplace equation as well as for the two-dimensional elasticity equation. We then extend the theoretical as well as the numerical results to include higher order finite elements for the two-dimensional Laplace equation. In

addition we show for the corresponding Laplace eigenvalue problem that an optimal convergence rate for the eigenvalues can be obtained.

In Section 10, we show that it is possible to obtain optimal L^2-convergence by compensating the lack of full elliptic regularity in the dual problem if we have additional regularity of the exact solution. This is achieved using an elliptic shift theorem if the underlying boundary value problem admits a shift by more than $\frac{1}{2}$.

2. Mathematical background

In this section, we set up the foundation for the results presented in this thesis, namely the necessary function spaces and equations and introduce the problem setting. Nevertheless it should be noted that the results presented in the following chapter are a recap of well-known results from standard literature.

2.1. Sobolev spaces

The theoretical as well as the numerical results in the following are based on the notion of weak derivatives and the corresponding Sobolev function spaces. Weak derivatives are a generalization of the concept of classical derivatives suitable for modern function spaces based on Lebesgue function spaces. We now consider the relevant standard results on Sobolev spaces and introduce the definitions needed. For more details we refer to the introductory texts [1, 29, 30, 97].

In the following let $\Omega \subset \mathbb{R}^d$, $d \in \{2, 3\}$ be a bounded polyhedral domain whose boundary is denoted by $\Gamma := \partial\Omega$. We consider now functions $u : \Omega \to \mathbb{R}$ and their partial derivatives $D^\beta u$. In this formulation the multiindex β of order $|\beta| = \beta_1 + \ldots + \beta_d$ denotes a vector of the form $\beta = (\beta_1, \ldots, \beta_d)$, where each component β_i is a non-negative integer. Then the set of the partial derivatives of order k, where k is a non-negative integer, is denoted by

$$D^k u(x) := \{D^\beta u(x) : |\beta| = k\},$$

where

$$D^\beta u(x) := \frac{\partial^{|\beta|} u(x)}{\partial x_1^{\beta_1} \ldots \partial x_d^{\beta_d}} = \partial_{x_1}^{\beta_1} \ldots \partial_{x_d}^{\beta_d} u(x).$$

If functions and their partial derivatives satisfy certain properties, they lie in function spaces. The Lebesque spaces of integrable functions for $1 \leq p < \infty$

are defined as

$$L^p(\Omega) := \{u : \Omega \to \mathbb{R} : \int_\Omega |u(x)|^p \, dx < \infty\}$$

and for $p = \infty$ as

$$L^\infty(\Omega) := \{u : \Omega \to \mathbb{R} : \text{ess sup}\{|u(x)|, x \in \Omega\} < \infty\}.$$

The corresponding norms are defined as

$$\|u\|_{L^p(\Omega)} := \left(\int_\Omega |u(x)|^p \, dx\right)^{1/p}$$

and

$$\|u\|_{L^\infty(\Omega)} := \text{ess sup}\{|u(x)|, x \in \Omega\},$$

respectively. Integrability can also be defined locally and the set of locally integrable functions is given by

$$L^1_{loc} := \{u : u \in L^1(K), K \subset \Omega \text{ compact}\}.$$

If β is a multiindex and $u, v \in L^1_{loc}$, we say that u has the β-th weak derivative v, i.e. $D^\beta u = v$, if

$$\int_\Omega u D^\beta \phi \, dx = (-1)^{|\beta|} \int_\Omega v\phi \, dx$$

for all infinitely differentiable test functions $\phi \in C^\infty_c(\Omega)$ with compact support.

We are now prepared to define Sobolev spaces: For integer orders $k \in \mathbb{N}_0$ and $1 \leq p \leq \infty$ we define the Sobolev spaces as

$$W^{k,p}(\Omega) := \{u \in L^1_{loc} : D^\beta u \in L^p(\Omega), |\beta| \leq k\},$$

the space of all locally integrable functions such that, for each multiindex up to order k, the weak derivative exists and belongs to $L^p(\Omega)$. The corresponding norms are defined as

$$\|u\|_{W^{k,p}(\Omega)} := \begin{cases} \left(\sum_{|\beta|\leq k} \int_\Omega |D^\beta u|^p \, dx\right)^{1/p} & , 1 \leq p < \infty \\ \sum_{|\beta|\leq k} \text{ess sup}_\Omega |D^\beta u| & , p = \infty \end{cases}.$$

All Sobolev spaces $W^{k,p}$ are Banach spaces as well as L^p spaces. The case $p = 2$

constitutes a special case since then a natural inner product on the Sobolev space $W^{k,2}$ is induced by the norm. Thus these spaces are Hilbert spaces and will be denoted by $H^k(\Omega) := W^{k,2}(\Omega)$ in the following. For simplicity of the notation we use the abbreviations $\|u\|_k := \|u\|_{H^k(\Omega)}$ and $\|u\|_0 := \|u\|_{L^2(\Omega)}$.

For some of the following chapters we also require the notion of weighted Sobolev spaces as introduced in [67, 97]. For this let $r = r(x) \geq 0$ denote the distance of the point x to an arbitrary but fixed point x_c, e.g., a singular point. For $\alpha \in \mathbb{R}$ we define the weighted Sobolev spaces

$$H^k_\alpha(\Omega) := \{u : r^{\alpha+|\beta|-k} D^\beta u \in L^2(\Omega), |\beta| \leq k\}$$

equipped with the norm

$$\|u\|_{k,\alpha} := \|u\|_{k,\alpha;\Omega} := \left(\sum_{|\beta|\leq k} \|r^{\alpha+|\beta|-k} D^\beta u\|^2_{L^2(\Omega)} \right)^{1/2},$$

see e.g. [96]. Until now we have only defined Sobolev spaces $H^k(\Omega)$ for integer k. In the following we will define the corresponding interpolation spaces for fractional values of $s = k + \tau$ with $\tau \in (0, 1)$, which include fractional order Sobolev spaces as well as the Besov spaces. In order to do that we will introduce interpolation spaces using the so-called real- or K-method as defined for example in [1, 10, 159]. Let X, Y be two separable Hilbert spaces with $X \subset Y$ dense in Y. Then we can define the interpolation spaces as

$$(X, Y)_{\theta,q} := \{u \in Y : \|u\|_{(X,Y)_{\theta,q}} < \infty\}$$

with the norms

$$\|u\|_{(X,Y)_{\theta,q}} := \begin{cases} \left(\int_0^\infty [t^{-\theta} K(u,t)]^q \, \frac{dt}{t}\right)^{1/q}, & \text{for } 1 \leq q < \infty, \\ \sup\limits_{0<t<\infty} \{t^{-\theta} K(u,t)\}, & \text{for } q = \infty, \end{cases}$$

for $\theta = s - k$ with integer k, where $k < s < k + 1$ and

$$K(u,t) := \inf_{v\in X, w\in Y, v+w=u} \{\|v\|_X + t\|w\|_Y\}.$$

We can now define H^s as

$$H^s(\Omega) := (H^k(\Omega), H^{k+1}(\Omega))_{\theta,2}.$$

Furthermore the space $H_0^1(\Omega)$ is defined as the subspace of $H^1(\Omega)$ in which the traces vanish on $\partial\Omega$ as in [1, 55].

Of special interest for the mortar method is the space $H^{\frac{1}{2}}(\partial\Omega)$, which is the trace space of the $H^1(\Omega)$ and can be defined by interpolation as

$$H^{\frac{1}{2}}(\partial\Omega) := (L^2(\partial\Omega), H^1(\partial\Omega))_{\frac{1}{2},2}.$$

For a detailed review of trace theorems see [1].

For $s > 0$, $s \notin \mathbb{N}$, and $q \in [1, \infty]$ the Besov space $B^s_{2,q}(\Omega)$ is defined by interpolation as

$$B^s_{2,q}(\Omega) := (H^{\lfloor s \rfloor}(\Omega), H^{\lceil s \rceil}(\Omega))_{\theta,q}, \qquad \theta = s - \lfloor s \rfloor.$$

Integer order Besov spaces $B^n_{2,q}(\Omega)$ with $n \in \mathbb{N}$ are also defined by interpolation and can be stated according to [159] as

$$B^n_{2,q}(\Omega) := (H^{n-1}(\Omega), H^{n+1}(\Omega))_{1/2,q}, \qquad n \in \mathbb{N}.$$

In order to give some indication of the relevance of the second parameter q in the definition of the Besov spaces, we recall the (continuous) embeddings [77]

$$H^{s+\varepsilon}(\Omega) \subset B^s_{2,1}(\Omega) \subset H^s(\Omega) \subset B^s_{2,\infty}(\Omega) \subset H^{s-\varepsilon}(\Omega), \qquad \varepsilon > 0.$$

In the following chapters, the notion of the dual space will arise in several of the theorems and proofs. If X denotes a real vector space, we denote its dual space by X'. The space X' contains all continuous, linear mappings from X to $\mathbb{R}$. If the space X is normed, the dual norm on X' is defined as

$$\|f\|_{X'} := \sup_{x \in X} \frac{f(x)}{\|x\|_X}.$$

The dual space of $H^s(\Omega)$ is denoted by $H^{-s}(\Omega)$.

2.2. Variational formulation and the finite element method

The finite element method (FEM) is a widely used numerical technique for approximating solutions of boundary value problems. It relies on the variational formulation of the boundary value problem, which will be introduced below.

Let $\Omega \subset \mathbb{R}^d$ be defined as above and let our simplified model problem be stated as

$$-\nabla \cdot (\mathbf{A}(x)\nabla u) = f \quad \text{in } \Omega, \qquad u = 0 \quad \text{on } \partial\Omega. \tag{1}$$

We assume that $\mathbf{A} \in \mathbb{R}^{d\times d}$ and f are sufficiently smooth. Moreover $\mathbf{A}$ is assumed to be symmetric and uniformly positive definite and $\mathbf{A}(x) \geq \alpha_0 \mathrm{I}$ for some $\alpha_0 > 0$ and all $x \in \Omega$. The boundary value problem (1) can then be restated in the weak form using partial integration, where it reads:
Find $u \in V := H_0^1(\Omega)$ such that

$$a(u, v) = l(v), \qquad v \in V. \tag{2}$$

Here $a(u, v) := \int_\Omega \mathbf{A}\nabla u \cdot \nabla v \, dx$ denotes the bilinear form and $l(v) := \int_\Omega fv \, dx$ is the linear form. The existence and uniqueness of a weak solution to this problem are given by the Lax-Milgram lemma as stated in [29, 30, 37].

Theorem 1 (Lax-Milgram)**.** *Given a Hilbert space H and a continuous, coercive bilinear form $a : H \times H \to \mathbb{R}$, i.e. a mapping such that for $u, v \in H$ and for positive constants c_1, c_2*

$$|a(u, v)| \leq c_1\|u\|_H\|v\|_H \qquad \textit{and} \qquad |a(u, u)| \geq c_2\|u\|_H^2,$$

as well as a continuous linear functional $l \in H'$, there exists a unique $u \in H$ such that

$$a(u, v) = l(v), \qquad v \in H.$$

We approximate the continuous problem given in (2) by its discrete variational formulation. In order to do that we define $(\mathcal{T}_h)_{h>0}$ as a family of triangular meshes obtained by uniform refinement of a conform triangulation of the domain Ω. We then denote the standard finite element space of continuous piecewise polynomials of degree k by

$$V_h^k := \{v \in H_0^1(\Omega) : v|_T \in P_k(T), \quad T \in \mathcal{T}_h\}.$$

In the classical case of second order elliptic equations on a convex domain with an H^1-coercive bilinear form, the finite element method is of optimal convergence

order in the H^1- and L^2-norm, as stated in the following theorem. Its proof uses a duality argument known as the "Nitsche trick", which is an important tool for the convergence analysis in norms such as the L^2-norm. The textbook procedure for optimal order convergence in L^2 is to exploit full elliptic regularity for the dual problem. Versions of this theorem and the corresponding proof can be found e.g. in [29, 37, 155].

Theorem 2. *Let V_h^k be the finite element space and $u \in H^{k+1}(\Omega)$. Then, the finite element approximation u_h differs from the true solution u of (2) in the H^1-norm by*

$$\|u - u_h\|_1 \lesssim h^k \|u\|_{k+1},$$

and under additional assumption of H^2-regularity in the L^2-norm by

$$\|u - u_h\|_0 \lesssim h^{k+1} \|u\|_{k+1}.$$

Proof. The first inequality can be shown using the Céa-lemma as stated in [29, Lemma 4.2] and an interpolation theorem [29, Lemma 6.4]:

$$\|u - u_h\|_1 \leq C \inf_{v_h \in V_h^k} \|u - v_h\|_1 \leq C h^k \|u\|_{k+1}.$$

For the second inequality we use duality arguments, Galerkin orthogonality and continuity of the bilinear form to obtain that for $v \in V_h^k$

$$\begin{aligned} \|u - u_h\|_0 &= \sup_{g \in L^2(\Omega)} \frac{(g, u - u_h)}{\|g\|_0} = \sup_{g \in L^2(\Omega)} \frac{a(u - u_h, \varphi_g)}{\|g\|_0} \\ &= \sup_{g \in L^2(\Omega)} \frac{a(u - u_h, \varphi_g - v)}{\|g\|_0} \\ &\leq C \|u - u_h\|_1 \sup_{g \in L^2(\Omega)} \inf_{v \in V_h^k} \frac{\|\varphi_g - v\|_1}{\|g\|_0}, \end{aligned}$$

where $\varphi_g \in H_0^1(\Omega)$ is the uniquely defined weak solution of $a(w, \varphi_g) = (g, w)$ with $w \in H_0^1(\Omega)$ and $g \in L^2(\Omega)$. Since H^2-regularity holds, we have that $\|\varphi_g\|_2 \leq \|g\|_0$. This approximation is also known as the "Aubin-Nitsche-Lemma" mentioned above. Together with the estimation for the H^1-error, this leads to

$$\|u - u_h\|_0 \leq Ch \|u - u_h\|_1 \leq Ch^{k+1} \|u\|_{k+1}.$$

□

In order to demonstrate the numerical performance, we consider a convex domain

with its respective uniform refinement as shown in Figure 2.1 and investigate the performance for ansatz functions of order one to three. For the demonstration of optimal convergence, we consider the simple Poisson model equation

$$-\Delta u = f \text{ in } \Omega, \qquad u(x,y) = \sin(\pi x)\sin(\pi y) \text{ on } \partial\Omega.$$

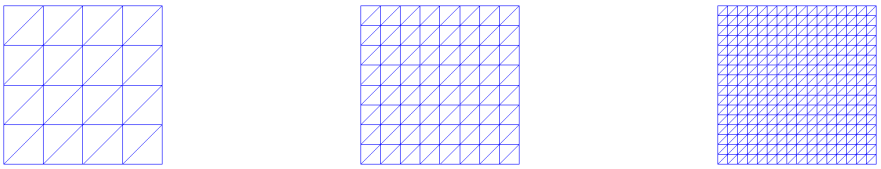

Figure 2.1: Uniform mesh refinement on a unit square.

The corresponding optimal convergence results as stated in the above Theorem 2 are depicted in Table 2.1 for the L^2-norm and in Table 2.2 for the H^1-norm.

	$k=1$		$k=2$		$k=3$	
level	$\|u-u_h\|_0$	rate	$\|u-u_h\|_0$	rate	$\|u-u_h\|_0$	rate
1	1.1534e-01	-	4.7914e-03	-	3.5346e-04	-
2	3.2465e-02	1.83	5.6526e-04	3.08	2.1803e-05	4.02
3	8.3735e-03	1.96	6.9303e-05	3.03	1.3432e-06	4.02
4	2.1100e-03	1.99	8.6184e-06	3.01	8.3249e-08	4.01
5	5.2856e-04	2.00	1.0759e-06	3.00	5.1803e-09	4.01
6	1.3221e-04	2.00	1.3445e-07	3.00	3.2227e-10	4.01

Table 2.1: Optimal L^2-convergence rates on convex domain for ansatz functions of order one, two and three.

	$k=1$		$k=2$		$k=3$	
level	$\|u-u_h\|_1$	rate	$\|u-u_h\|_1$	rate	$\|u-u_h\|_1$	rate
1	8.6008e-01	-	1.3015e-01	-	1.3329e-02	-
2	4.3534e-01	0.98	3.3432e-02	1.96	1.6579e-03	3.01
3	2.1801e-01	1.00	8.4219e-03	1.99	2.0612e-04	3.01
4	1.0904e-01	1.00	2.1097e-03	2.00	2.5685e-05	3.00
5	5.4521e-02	1.00	5.2769e-04	2.00	3.2054e-06	3.00
6	2.7261e-02	1.00	1.3194e-04	2.00	4.0035e-07	3.00

Table 2.2: Optimal H^1-convergence rates on convex domain for ansatz functions of order one, two and three.

2.3. Elasticity equation

In the following, we will briefly introduce the principal concepts of linear solid mechanics required for the mathematical modeling of building structures. We do not intend to give an extensive overview of the topic, but will rather introduce the necessary basics for solid mechanics. For further details on solid and structural mechanics we refer to the literature such as [29, 134, 147, 183].
It is our aim to determine the displacements u of an elastic material, assuming small displacements. In the three-dimensional setting, a displacement corresponds to a mapping $\phi : \Omega \to \mathbb{R}^3$, which is given by

$$\phi = Id + u.$$

Here $\phi(x)$ is the new location of the original point $x \in \Omega$ under the mapping u. The mapping ϕ is called a deformation if its deformation gradient

$$\nabla\phi = \begin{pmatrix} \frac{\partial\phi_1}{\partial x_1} & \frac{\partial\phi_1}{\partial x_2} & \frac{\partial\phi_1}{\partial x_3} \\ \frac{\partial\phi_2}{\partial x_1} & \frac{\partial\phi_2}{\partial x_2} & \frac{\partial\phi_2}{\partial x_3} \\ \frac{\partial\phi_3}{\partial x_1} & \frac{\partial\phi_3}{\partial x_2} & \frac{\partial\phi_3}{\partial x_3} \end{pmatrix}$$

statisfies $\det(\nabla\phi) > 0$.

Then the Green-Lagrange strain tensor is given as $\frac{1}{2}(\nabla\phi^T\nabla\phi - I)$, where $I \in \mathbb{R}^{3\times3}$ denotes the identity matrix. In linear solid mechanics, only the linear parts are considered, yielding the linearized strain tensor defined as

$$\epsilon(u) := \frac{1}{2}(\nabla u + \nabla u^T).$$

The tensor describes local deformations inside the body such as extensions, volume changes and shear strains. To represent the symmetric tensor with reduced order we use the Voigt notation, which allows to write the second order tensor as

$$\epsilon = [\epsilon_x, \epsilon_y, \epsilon_z, \epsilon_{xy}, \epsilon_{yz}, \epsilon_{zx}]^T.$$

The relationship between stress and strain depends on the constitutive law of the specific material. If we assume that Hooke's law holds, this relationship is linear and the linearized stress σ is defined as

$$\sigma(u) := \mathbb{C}\epsilon(u),$$

where $\mathbb{C}$ denotes Hooke's tensor, which we assume to be positive definite. Depending on the matrial law, the matrix $\mathbb{C}$ changes: In the most general case of an anisotropic material, the matrix can have 31 independent entries. We will however restrict our studies to the orthotropic and isotropic cases due to the materials considered in the planning process. According to [130] for orthotropic materials like wood, which contain fibers with different orientations and thus different Young's moduli, the stiffness tensor $\mathbb{C}$ takes the form

$$\mathbb{C} = \begin{pmatrix} A_{11} & A_{12} & A_{13} & 0 & 0 & 0 \\ A_{21} & A_{22} & A_{23} & 0 & 0 & 0 \\ A_{31} & A_{32} & A_{33} & 0 & 0 & 0 \\ 0 & 0 & 0 & G_{xy} & 0 & 0 \\ 0 & 0 & 0 & 0 & G_{yz} & 0 \\ 0 & 0 & 0 & 0 & 0 & G_{zx} \end{pmatrix}$$

with the material parameters

$$\begin{aligned} A_{11} &= \frac{E_x}{D_0}(1-\nu_{yz}^2\frac{E_z}{E_y}), \qquad A_{12} = A_{21} = \frac{E_y}{D_0}(\nu_{xy}+\nu_{yz}\nu_{zx}\frac{E_z}{E_y}), \\ A_{13} &= A_{31} = \frac{E_z}{D_0}(\nu_{xy}\nu_{yz}+\nu_{zx}), \qquad A_{22} = \frac{Ey}{D_0}(1-\nu_{zx}^2\frac{E_z}{E_x}), \\ A_{23} &= A_{32} = \frac{E_z}{D_0}(\nu_{yz}+\nu_{xy}\nu_{zx}\frac{E_y}{E_x}), \qquad A_{33} = \frac{E_z}{D_0}(1-\nu_{xy}^2\frac{E_y}{E_x}), \end{aligned}$$

where

$$D_0 = 1-\nu_{yz}^2\frac{E_z}{E_y}-\nu_{xy}^2\frac{E_y}{E_x}-2\nu_{xy}\nu_{yz}\nu_{zx}\frac{E_z}{E_x}-\nu_{zx}^2\frac{E_z}{E_x}.$$

Since orthotropic materials have different material properties depending on the direction in space, we have to consider a total of nine independent parameters. While E_i, $i \in \{x,y,z\}$ denote Young's moduli, the

$$G_{ij} \text{ with } (i,j) \in \{(x,y),(y,z),(z,x)\}$$

denote the shear moduli and the

$$\nu_{ij} \text{ with } (i,j) \in \{(x,y),(y,z),(z,x)\}$$

denote Poisson's ratios. For orthotropic materials the Poissons's ratios represent three independent material parameters. In this case the only relation between the ratios is $\nu_{ij}E_j = \nu_{ji}E_i$. To ensure that $\mathbb{C}$ is positive definite it has to satisfy the

conditions

$$\frac{E_x}{E_y} > \nu_{xy}^2 \qquad \text{and} \qquad D_0 > 0$$

on the parameters. Isotropic materials constitute the simplest possible case with $\mathbb{C}$ stated as

$$\mathbb{C} = \frac{E}{(1+\nu)(1-2\nu)} \begin{pmatrix} (1-\nu) & \nu & \nu & 0 & 0 & 0 \\ \nu & (1-\nu) & \nu & 0 & 0 & 0 \\ \nu & \nu & (1-\nu) & 0 & 0 & 0 \\ 0 & 0 & 0 & (1-2\nu) & 0 & 0 \\ 0 & 0 & 0 & 0 & (1-2\nu) & 0 \\ 0 & 0 & 0 & 0 & 0 & (1-2\nu) \end{pmatrix}$$

according to [29]. In the isotropic case we have considerably less parameters since the parameters E_i and ν_i do no longer depend on the direction such that all the Poisson's ratios have the same value, and the $G_{i,j}$ can be calculated from them. In the isotropic case, σ can also be written using the Lamé constants $\tilde{\mu}$ and $\tilde{\lambda}$, which depend on E and ν and are defined as

$$\tilde{\mu} := \frac{E}{2(1+\nu)} \qquad \text{and} \qquad \tilde{\lambda} := \frac{\nu E}{(1+\nu)(1-2\nu)}.$$

In this case, the Poisson ratio fulfills $-1 < \nu < \frac{1}{2}$ in order to have a positive definite $\mathbb{C}$. Then σ can be written as

$$\sigma(u) = 2\tilde{\mu}\epsilon(u) + \tilde{\lambda} \text{ trace } (\epsilon(u))I.$$

The forces inside a body have to be in equilibrium with the forces acting on the body. Thus the equilibrium condition of an elastic body according to Cauchy's law is given by the equation

$$-\text{div } \sigma(u) = f \qquad \text{in } \Omega, \tag{3}$$

where f is the volume force acting on the body and the divergence operator is taken row-wise. In the isotropic case this can be simplified to

$$-(2\tilde{\mu} \text{ div } \epsilon(u) + \tilde{\lambda} \text{ grad div } u) = f \qquad \text{in } \Omega.$$

This equation together with the respective boundary conditions, such as Dirichlet (Γ^D) or Neumann (Γ^N) boundary conditions, determines the displacement in the static case. Dirichlet conditions have to be imposed when the body is clamped at the respective boundary and Neumann conditions are imposed wherever there are boundary tractions. In order to obtain the dynamical case, we can use Newton's second law

$$-\text{div } \sigma(u) = f - \rho\frac{\partial^2 u}{\partial t^2}, \qquad \text{in } \Omega \text{ and } t > 0, \tag{4}$$

where ρ denotes the density. In order to complete the dynamical case, suitable initial and boundary conditions have to be set.

2.4. Eigenvalue problems

In this section, we recall how, from the dynamical case (4) achieved in the last section, we can obtain the eigenvalue problem. We furthermore discuss some of the important properties of the eigenvalue problem and its fundamental solution. This topic is dealt with in many excellent literature references, details on this topic can be found in [10, 23] and the references therein. We consider now the linear elasticity case as an example for an elliptic eigenvalue model problem. All the results derived in the following also hold true for more general elliptic systems and are derived analogously.

Let us now follow [10] and take $f = 0$ in the dynamic elasticity equation. For $u(x,t) \neq 0$ we can use separation of variables to write the solution u as

$$u(x,t) = u(x)T(t).$$

Inserting this into the dynamic elasticity equation leads to

$$\begin{aligned} -T(t)\text{div } \sigma(u(x)) &= -\rho u(x)\frac{\partial^2 T(t)}{\partial t^2} \qquad \text{in } \Omega \text{ and } t > 0 \\ \Leftrightarrow -\frac{\text{div } \sigma(u(x))}{\rho u(x)} &= -\frac{\frac{\partial^2 T(t)}{\partial t^2}}{T(t)} \qquad \text{in } \Omega \text{ and } t > 0. \end{aligned}$$

Since the expressions are equal, but depend on only x and only t, they have to be equal to a constant, which will be denoted by $\lambda \in \mathbb{R}$. We thus need to find $\lambda \in \mathbb{R}$ and $u(x)$ such that

$$-\text{div } \sigma(u(x)) = \lambda\rho u(x) \qquad \text{in } \Omega,$$

while fulfilling the respective boundary conditions. The problem as stated above

is called an eigenvalue problem, where λ is the eigenvalue and $u(x)$ is the eigenfunction. The tuple (λ, u) is called the eigenpair of the problem. The eigenvalues of the above problem are numbered as

$$0 < \lambda_1 \leq \lambda_2 \leq \dots$$

and the corresponding normalized eigenfunctions denoted by u_i are orthonormal, fulfilling

$$\int_\Omega u_i(x)u_j(x)\,dx = \delta_{ij},$$

where δ_{ij} denotes the Kronecker symbol. Furthermore the eigenfunctions are complete in L^2, which means that $h(x) = \sum_{i=1}^{\infty} \alpha_i u_i(x)$ for every $h(x) \in L^2$. Then every eigenvalue λ_i has to satisfy the equation

$$-\frac{\partial^2 T(t)}{\partial t^2} = \lambda_i T(t), \qquad t > 0.$$

The solution to this problem is easily determined to be

$$T_i(t) = a_i \sin(\sqrt{\lambda_i}(t + b_i))$$

with the arbitrary constants a_i and b_i, which can be determined using the initial conditions. We can thus find the solutions as $u_i(x)T_i(t)$, which allows us to rewrite $u(x,t)$ as

$$u(x,t) = \sum_{i=1}^{\infty} u_i(x)a_i \sin(\sqrt{\lambda_i}(t + b_i)).$$

The summands in the above equation are called the eigenvibrations of the problem, whose shapes are determined by the functions $u_i(x)$ and whose frequencies by the eigenvalues through $\sqrt{\lambda_i}$.

Our model problem under investigation in the building consists of the linear elasticity eigenvalue problem

$$-\text{div } \sigma(u) = \lambda \rho u \quad \text{in } \Omega$$

with Dirichlet boundary conditions on a closed non-trivial subset Γ^D of the boundary $\partial\Omega$ and homogeneous Neumann conditions on $\partial\Omega \setminus \Gamma^D$.

We now consider the variational formulation of the eigenvalue problem. Then the variational formulation of the elasticity eigenvalue problem (3) reads:
Find the eigenvalues $\lambda \in \mathbb{R}$ and the eigenfunctions

$$u \in V := \left\{ v \in (H^1(\Omega))^d \mid v|_{\Gamma^D} = 0 \right\}$$

such that

$$a(u, v) = \lambda \, m(u, v), \qquad v \in V. \tag{5}$$

The required bilinear forms

$$a(\cdot, \cdot) : (H^1(\Omega))^d \times (H^1(\Omega))^d \to \mathbb{R} \qquad \text{and} \qquad m(\cdot, \cdot) : (L^2(\Omega))^d \times (L^2(\Omega))^d \to \mathbb{R}$$

are given as

$$(u, v) \mapsto a(u, v) := \int_\Omega \mathbb{C}\epsilon(u) : \epsilon(v) \, \mathrm{d}x$$

and

$$(u, v) \mapsto m(u, v) := \rho(u, v)_{L^2(\Omega)} := \rho \int_\Omega u \cdot v \, \mathrm{d}x.$$

In the following chapters, we will use several different discretizations for this variational formulation, which will be described in detail in the respective chapters. Nevertheless certain properties of the continuous problem, such as the ordering and positivity properties of the eigenvalues and the orthonormality of the eigenfunctions, remain valid in the discrete case. Furthermore for conforming discretizations, the discrete eigenvalues λ_h always approach the continous ones from above, i.e. $\lambda \leq \lambda_h$, and the approximation of the eigenvalues is of order $O(h^{2k})$, while the approximation of the eigenfunction is of order $O(h^{k+1})$ if we have sufficient regularity. The corresponding detailed proofs can be found in the book [10].

To demonstrate the described convergence results numerically, we choose for simplicity the Laplace eigenvalue problem $\Delta u = \lambda u$ with Neumann boundary conditions on a unit square as depicted in Figure 2.1. In the following Tables 2.3 and 2.4 we depict the optimal convergence rates of the eigenvalues of $O(h^{2k})$ for ansatz functions of order one and two, respectively.

	1.EV		2.EV		3.EV		4.EV		5.EV	
level	$\lvert\lambda - \lambda_h\rvert$	rate	$\lvert\lambda - \lambda_h\rvert$	rate	$\lvert\lambda - \lambda_h\rvert$	rate	$\lvert\lambda - \lambda_h\rvert$	rate	$\lvert\lambda - \lambda_h\rvert$	rate
1	0.4874	-	0.4882	-	2.9177	-	7.9347	-	7.9885	-
2	0.1250	1.96	0.1250	1.97	0.7474	1.96	2.0087	1.98	2.0322	1.97
3	0.0316	1.99	0.0316	1.99	0.1891	1.98	0.5048	1.99	0.5076	2.00
4	0.0079	2.00	0.0079	2.00	0.0475	1.99	0.1266	2.00	0.1269	2.00
5	0.0020	2.00	0.0020	2.00	0.0119	2.00	0.03170	2.00	0.0317	2.00

Table 2.3: Errors and rates for eigenvalue approximation of order one in the optimal case.

	1.EV		2.EV		3.EV		4.EV		5.EV	
level	$\lvert\lambda - \lambda_h\rvert$	rate	$\lvert\lambda - \lambda_h\rvert$	rate	$\lvert\lambda - \lambda_h\rvert$	rate	$\lvert\lambda - \lambda_h\rvert$	rate	$\lvert\lambda - \lambda_h\rvert$	rate
1	0.0047	-	0.0049	-	0.0615	-	0.2768	-	0.2793	-
2	0.0003	3.90	0.0003	3.94	0.0043	3.84	0.0196	3.82	0.0196	3.83
3	2.0014e-05	3.97	2.0058e-05	3.98	0.0003	3.95	0.0013	3.94	0.0013	3.94
4	1.2573e-06	3.99	1.2549e-06	4.00	1.7584e-05	3.99	8.0432e-05	3.99	8.0426e-05	3.99
5	7.3055e-08	4.11	7.0385e-08	4.16	1.0414e-06	4.08	4.7606e-06	4.08	4.7551e-06	4.08

Table 2.4: Errors and rates for eigenvalue approximation of order two in the optimal case.

It should also be noted that for the error given by $|\lambda - \lambda_h|$, we have to compute a reference solution which was obtained on a level seven refined mesh.

Chapter II.
Model reduction by mortar techniques

The results in this chapter were partly published by the author with S. Kollmannsberger, F. Frischmann, E. Rank and B. Wohlmuth in the paper entitled "A new mortar formulation for modeling elastomer bedded structures with modal-analysis in 3D" in Advanced Modeling and Simulation in Engineering Sciences in the year 2014, [75].

3. Mortar methods for vibro-acoustics

In the context of timber building constructions, a method to divide a large structure into smaller substructures such as walls, floors and ceilings and mesh them separately is helpful in many cases. The construction of analysis-suitable conforming three-dimensional meshes in this complexity is non-trivial and increases the number of elements significantly as a local mesh refinement in only one of the components automatically spreads to the others. In the following, we build on the work of [175], which demonstrates the excellent applicability of the mortar method for problems in structural mechanics for discretizations of high orders.

3.1. Introduction to mortar finite element methods

Mortar methods are domain decomposition methods as depicted in Figure 3.1, which allows a separate independent meshing of the subdomains. This enforces that the approximative solution satisfies an equality in the weak sense on the subdomain boundaries $\Gamma_{s,m}$ inside the domain Ω instead of the more strict C^0 continuity of the ansatz space of the finite element solution on the whole domain. Thus finite element calculations can be performed on non-conforming meshes, as suitable for our building simulations. Using mortar methods allows to mesh and discretize walls and slabs separately although this may result in non-matching meshes at the interfaces. The mortar method thus significantly reduces the complexity of the mesh generation and allows for great flexibility of the numerical setting, making the setting computationally attractive for a variety of numerical problems, for example coupled multi-physics problems. The original mortar method was introduced

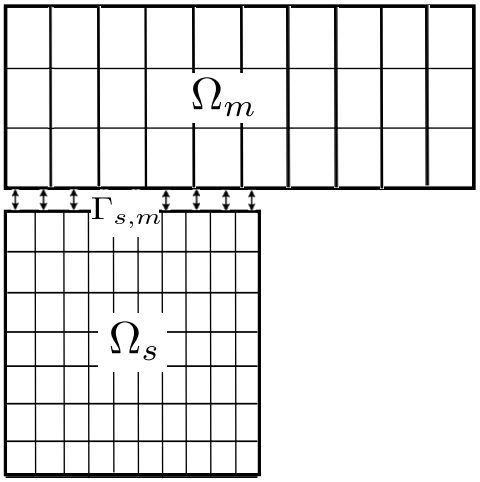

Figure 3.1: Illustration of a non-conforming coupled mortar mesh.

by [19] and can be formulated in several ways. The formulation as proposed by [19] is a method to couple spectral elements with finite elements, where the ansatz space is weakly constrained. We will however in the following focus on the formulation as introduced in [16], which views the mortar method in the more popular context of enforcing the coupling conditions by means of Lagrange multipliers, which relies on an abstract saddle point formulation. The formulation by means of Lagrange multipliers allows to identify the multipliers with the normal stress on the contact between two subdomains. Furthermore the saddle point formulation is beneficial since several well-known convergence results from functional analysis such as the inf-sup (Babuska-Brezzi) condition [29, 30] are applicable. Further theoretical results can be found in [16, 17, 19, 176].

Mortar methods have been applied successfully to many engineering applications, including elastic contact problems [71, 127, 153, 177], dynamic and static structural analysis [35, 58, 72], coupled problems in acoustics [57, 164] and flow problems [95, 125, 126]. Further, the mortar method is used to simulate eigenvalue problems in [33, 98]. Most contributions deal only with first or second order approaches. For a detailed review on mortar methods see e.g. [176] and the references therein. Mortar methods are also used for high order finite elements and the corresponding theory is well understood [18, 152]. Nevertheless the implementation of higher order quadrature formulas on cut elements in three-dimensional simulations is technically challenging.

In the following we will start by giving a short introduction to the mortar setting,

starting from the domain partitioning

$$\bar{\Omega} = \bigcup_{i=1}^{I} \bar{\Omega}_i$$

of the domain Ω into I non-overlapping subdomains Ω_i. We then define the common interface between two components as

$$\Gamma_{s,m} := \partial\Omega_s \cap \partial\Omega_m,$$

where one of the adjacent subdomains is chosen as the master (m) and one as the slave (s) domain. By $\mathbf{\Gamma}$ we denote the union of all these interfaces, i.e.

$$\mathbf{\Gamma} := \bigcup_{(s,m)} \Gamma_{s,m}.$$

In order to obtain the finite element solution, we now define the spaces needed for the mortar formulation. The solution lies in the primal space, which is defined as the product space

$$X := \prod_{i=1}^{I} V(\Omega_i),$$

where

$$V(\Omega_i) := \{u \mid u \in (H^1(\Omega_i))^d, u(\Gamma^D \cap \partial\Omega_i) = 0\}$$

with $i = 1, \ldots, I$ and the dimension $d \in \{1, 2, 3\}$. The space needed for the weak matching on our subdomain interfaces is the Lagrange multiplier space, which is denoted by

$$M := \prod_{(s,m)} (H^{-\frac{1}{2}}(\Gamma_{s,m}))^d,$$

where $H^{-\frac{1}{2}}(\Gamma_{s,m})$ is the dual space of $H^{\frac{1}{2}}(\Gamma_{s,m})$. Also note at this point that our Lagrange multipliers live on the slave side.

Then we can formulate the weak coupling condition on the interface as

$$b(u, \widehat{\tau}) = 0, \qquad \widehat{\tau} \in M$$

with the bilinear form $b(u, \widehat{\tau}) := \int_{\mathbf{\Gamma}} [u] \widehat{\tau}\, dx$ for $\widehat{\tau} \in M$, where the jump over the interface is defined as $[u] := u_s - u_m$. We can now introduce a mortar formulation u_h on the discrete space $X_h^k = \prod_i V_h^k(\Omega_i)$ of finite elements of polynomial degree

k on the separate subdomains with the discrete Lagrange multiplier space M_h. In order to obtain the mortar solution, we will use the saddle point formulation, where the weak continuity condition is enforced on $\mathbf{\Gamma}$ as an additional variational equation resulting in the formulation:
Find $(u_h, \tau_h) \in X_h^k \times M_h$ such that

$$\begin{aligned} a(u_h, v_h) + b(v_h, \tau_h) &= l(v_h), \quad v_h \in X_h^k \\ b(u_h, \widehat{\tau}_h) &= 0, \qquad \widehat{\tau}_h \in M_h. \end{aligned}$$

In this setting $a(\cdot, \cdot)$ denotes a bilinear and $l(\cdot)$ a linear form of a model problem as e.g. (2). Note that in the cases of a mortar interface intersecting a Dirichlet boundary or two mortar interfaces intersecting each other where more than two subdomains meet, a conflict of constraints can arise. This is due to the fact that standard choices of the Lagrange multipliers impose the weak coupling condition, while the Dirichlet boundary already sets a certain value on the specific points. In the case of two mortar interfaces there are overconstraints on the corresponding points. Details on the treatment of such points can be found in [176].

Due to the composition of the timber constructions in our project, which consist of thin, layered and orthotropic material, we aim for a fully three-dimensional resolution of the slabs and walls. For this purpose, we use the high order version of the finite element method, as presented for example in [158]. Moreover, it is well suited for the computation of solid, but thin-walled structures because it is robust in terms of the large aspect ratios of the elements which arise naturally in fully three-dimensional models of plates and shells [135]. It also provides better accuracy and convergence properties than low order finite elements. In addition, the high order version of the FEM has already been shown to lead to excellent results for the analysis of sound transition through timber structures [130].

In the following we will apply high order (up to a polynomial degree of 20) techniques to approximate eigenvalues and eigenmodes in cross-laminated timber structures.

3.2. Mortar for eigenvalue problems

We now consider mortar methods for eigenvalue problems in a general setting. Due to our aim of applying our results to the vibro-acoustic analysis of timber building structures, we recall the linear elasticity eigenvalue problem as presented

in Section 2.4, which is given by

$$-\text{div } \sigma(u) = \lambda \rho u. \tag{6}$$

We will assume that the domain $\Omega \subset \mathbb{R}^3$ is bounded and polyhedral. In addition, we enforce Dirichlet boundary conditions on a non-trivial set Γ^D and homogeneous Neumann boundary conditions on the remaining parts of the boundary. We now need an adequate domain partitioning for the mortar method. For simplicity, in the first investigations we use only two subdomains such that there is just one interface. The domain Ω is decomposed into the two non-overlapping subdomains Ω_m and Ω_s, so that

$$\bar{\Omega} = \bar{\Omega}_m \cup \bar{\Omega}_s, \qquad \Omega_m \cap \Omega_s = \emptyset.$$

In our example, in the context of timber buildings the wall could correspond to the slave domain and the ceiling to the master domain. Following standard procedures we define the common interface $\Gamma_{s,m}$ and the Lagrange multiplier space by $M := (H^{-\frac{1}{2}}(\Gamma_{s,m}))^3$. Furthermore in this setting we assume to have no crosspoints such that $\partial\Gamma_{s,m} \cap \overline{\Gamma}^D = \emptyset$ and thus no modifications on $\partial\Gamma_{s,m}$ have to be taken into account. The primal space X is defined as above in Section 3.1. Now we can define our bilinear forms for the mortar method as a special case of the ones above with only two subdomains as

$$\begin{aligned} a(u,v) &:= a_{\Omega_m}(u,v) + a_{\Omega_s}(u,v), \quad b(u,\widehat{\tau}) :=< u_s - u_m, \widehat{\tau} >^*, \\ m(u,v) &:= m_{\Omega_m}(u,v) + m_{\Omega_s}(u,v), \end{aligned}$$

where $< \cdot, \cdot >^*$ denotes the duality pairing of $(H^{\frac{1}{2}}(\Gamma_{s,m}))^3$ and $(H^{-\frac{1}{2}}(\Gamma_{s,m}))^3$ and $a_{\Omega_i}(\cdot,\cdot)$, $m_{\Omega_i}(\cdot,\cdot)$ are defined by

$$a_{\Omega_i}(u,v) := \int_{\Omega_i} \mathbb{C}\epsilon(u) : \epsilon(v)\, dx, \qquad m_{\Omega_i}(u,v) := \rho \int_{\Omega_i} u \cdot v\, dx.$$

The eigenvalue problem (6) can then be written in the following variational form: Find the eigenvalues $\lambda \in \mathbb{R}$, the eigenfunctions $u \in X$ and the Lagrange multiplier $\tau \in M$ so that

$$\begin{aligned} a(u,v) + b(v,\tau) &= \lambda m(u,v), \quad v \in X \\ b(u,\widehat{\tau}) &= 0, \qquad\quad \widehat{\tau} \in M. \end{aligned} \tag{7}$$

Equation (7) now defines the saddle point problem arising from the mortar method. The Lagrange multiplier τ corresponds to the negative surface traction $-\sigma n$ of

Ω_s on the interface $\Gamma_{s,m}$, where n is the outward unit normal of Ω_s. For the discretization of the primal variable of (7), we employ hexahedral finite elements of high order on each subdomain Ω_m, Ω_s. The dual space is discretized by the trace space of the discrete primal space on Ω_s. This choice guarantees inf-sup stability [17, 176] and the mortar method for solving (7) can be written as

$$A(u, \tau; v, \widehat{\tau}) = \lambda m(u, v)$$

with $A(u, \tau; v, \widehat{\tau}) := a(u, v) + b(v, \tau) + b(u, \widehat{\tau})$. The bilinear form $A(\cdot, \cdot; \cdot, \cdot)$ fulfills the conditions in [10, Remark 13.4], and thus the theory given in [10, Section 8] ensures convergence of the discrete eigenvalues and eigenfunctions.

As a first example, we consider two plates as depicted in Figure 3.2 in order to compare the mortar discretization to the conforming discretization.

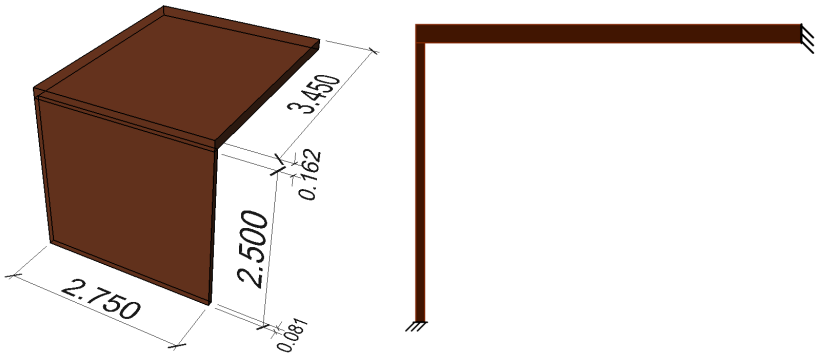

Figure 3.2: L-shaped connection of a slab to a wall in the first example. Measurements in meters.

It resembles a rigidly supported wall connected to a slab on one side and clamped at the other side. The corresponding discretizations are depicted in Figure 3.3. The discretization consists of ten hexahedral elements in the conforming case on the left and eight in the mortar case on the right. At this stage, for simplicity we consider the components to consist of one isotropic material. For our case of simplified timber materials we assume that Young's-modulus has the value $9790 \cdot 10^6 [N/m^2]$ and the Poisson ratio ν is 0.05.

The variational formulation in the conforming case is defined as in Section 2.4, Equation (5) and we again use elements of high order associated with hexahedral meshes. The basis functions are hierarchical shape functions based on integrated Legendre polynomials [157, 158].

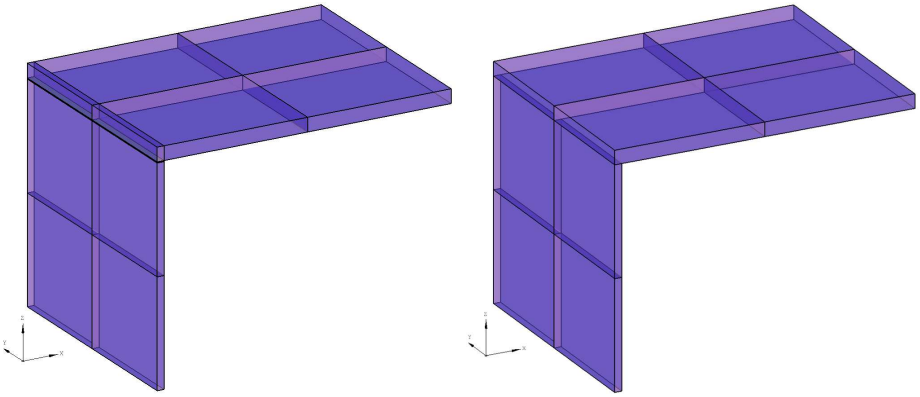

Figure 3.3: Hexahedral discretization: Left conforming, right mortar.

The eigenvalues for a sequence of high order FEM computations with polynomial degree $k \in \{3, 7, 10, 15\}$ are depicted in Table 3.1 along with the relative differences between the conforming and the mortar discretization. The main observation here is that for both methods the approximations of the eigenvalues are very similar to each other. Furthermore we observe that the differences between the two methods decrease with increasing polynomial degree. In Figure 3.4 the respective eigen-

	k=3			k=7		
EV	Conform	Mortar	%	Conform	Mortar	%
1	50.720	50.852	0.261	50.289	50.298	0.019
2	70.755	72.006	1.768	69.172	69.942	1.113
3	76.534	78.317	2.330	74.456	74.833	0.506
4	90.707	91.976	1.399	87.931	88.491	0.637
5	159.423	168.390	5.624	125.276	126.069	0.632
6	174.712	174.869	0.090	159.311	159.393	0.051
7	179.359	185.147	3.227	172.931	172.966	0.020
	k=10			k=15		
EV	Conform	Mortar	%	Conform	Mortar	%
1	50.282	50.288	0.012	50.278	50.281	0.006
2	68.929	69.518	0.854	68.749	69.062	0.455
3	74.304	74.535	0.311	74.220	74.341	0.162
4	87.685	88.101	0.475	87.545	87.768	0.255
5	124.818	125.340	0.418	124.581	124.842	0.210
6	159.264	159.315	0.032	159.237	159.264	0.016
7	172.884	172.911	0.016	172.865	172.882	0.010

Table 3.1: Comparison of eigenfrequencies of the L-shaped wall-slab configuration. No elastomer between the wall and slab. The unit for the eigenfrequencies is $[Hz]$.

functions $1, 3$ and 5 are depicted as an example for both the conforming method in the first row and the mortar method in the second row. The presented eigenfuncti-

ons have the polynomial degree of $k = 15$. Also at this point the main observation is the very good agreement between the eigenmodes.

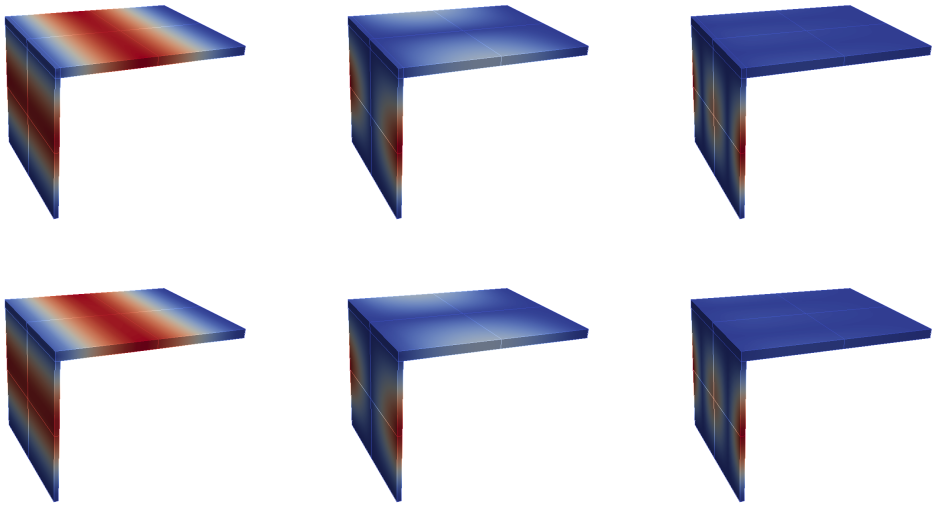

Figure 3.4: Eigenfunction comparison of an L-shape wall-slab configuration of order $k = 15$.

In the next step we investigate multiple interfaces and their impact on the simulation differences between the mortar and conforming approaches. Therefore we proceed with an example which contains three interfaces and four subdomains. Also in this case we will have no crosspoints. This time we have seven elements for the conforming discretization and four elements in the mortar case. In Table 3.2, we show the differences of the first seven eigenvalues between the simulations performed with a conforming method and the ones performed using the mortar method again using ansatz functions of order $k \in \{3, 7, 10, 15\}$. The mesh for the multiple interfaces is coarser than the one in the wall-slab setting. Note that the coarser mesh is the reason for the bigger differences between the mortar and the conforming approach for orders $k = 3$ and $k = 7$ in Table 3.2 and not the larger number of mortar interfaces. Again we observe very good agreement of the eigenvalues, which becomes noticeably better with increasing polynomial degree.

In Figure 3.5, we illustrate the respective eigenfunctions for the eigenvalues $1, 3$ and 5 for order $k = 15$. Also in this test case a very good accordance of the resulting eigenmodes can be observed.

	k=3			k=7		
EV	Conform	Mortar	%	Conform	Mortar	%
1	8.837	9.139	3.417	8.782	8.872	1.025
2	11.191	11.926	6.568	11.092	11.250	1.425
3	14.028	14.504	3.393	13.768	13.894	0.915
4	50.993	56.955	11.691	45.621	45.719	0.215
5	80.825	92.520	14.470	65.627	66.093	0.710
6	83.182	98.240	18.103	75.210	76.556	1.790
7	103.601	118.300	14.188	82.120	83.420	1.583

	k=10			k=15		
EV	Conform	Mortar	%	Conform	Mortar	%
1	8.760	8.826	0.753	8.740	8.780	0.458
2	11.057	11.168	1.004	11.021	11.091	0.635
3	13.707	13.776	0.503	13.671	13.709	0.278
4	45.596	45.666	0.154	45.574	45.618	0.097
5	65.504	65.837	0.508	65.392	65.604	0.324
6	74.964	75.346	0.510	74.811	75.019	0.278
7	81.758	82.692	1.142	81.457	82.030	0.703

Table 3.2: Comparison of eigenfrequencies of the geometry shown in Figure 3.5. The unit for the eigenfrequencies is $[Hz]$.

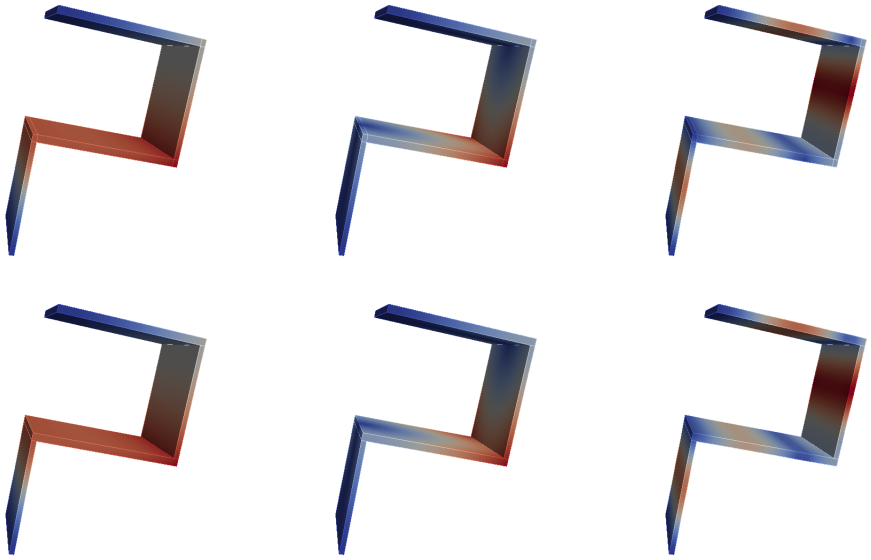

Figure 3.5: Eigenfunction comparison of multiple interface geometry configuration.

3.3. Application to a four level timber building

In the following, we proceed with an engineering example of a detailed four story timber building similar to the one depicted in Figure 3.6. As described in Section 1, building information models (BIM) are used in a building planning process to evaluate different problem settings as for example the modal superpositions for a

Figure 3.6: Four story timber building in Bad Aibling. [5]

vibro-acoustical analysis. From the building information model we can extract the geometries of the building and set up our model as depicted in Figure 3.7 with the respective material parameters.

After extracting the geometries we proceed with the meshing. Due to the use of mortar methods, the meshing process is especially beneficial in large building settings like ours since every geometry part can be treated independently. Nevertheless it is crucial for obtaining good simulation results to ensure that the interfaces on which we impose the weak couplings of the domains have no gaps or intersections. Geometries, and thus also the resulting meshes, from BIM and CAD programs are often inaccurate in that some neighboring domains are not connected, such that gaps occur and interfaces are not identical. Then incorrect solutions, as the ones depicted in the first row of Figure 3.8, are obtained with the incorrect mesh. As ex-

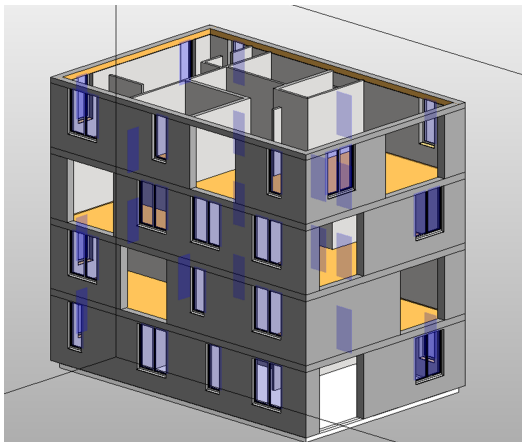

Figure 3.7: Model of a four story timber building without roof.

pected, due to the fact that the domains are not coupled, the displacements are not transferred over the interface. It is advisable to check the mesh in a post-process before the simulations and correct the mesh appropriately. If the modeling, meshing and coupling is executed correctly, simulation results like the ones depicted in the second row of Figure 3.8 are obtained.

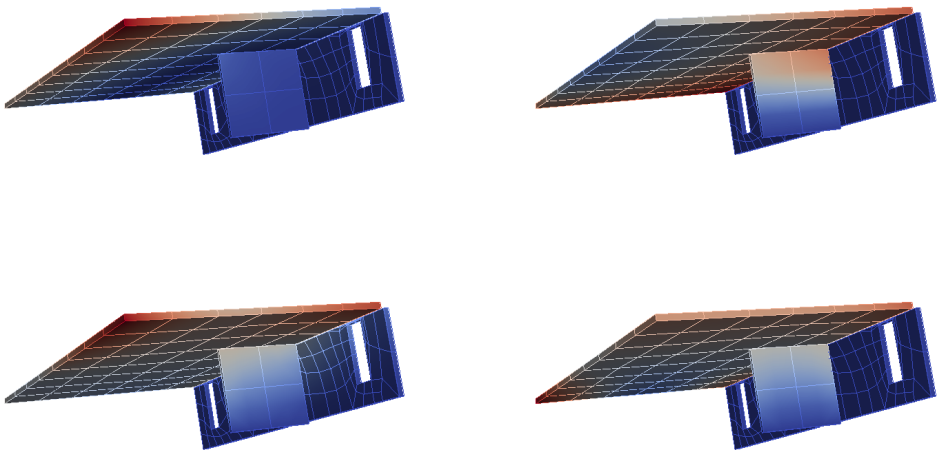

Figure 3.8: Simulation results for coupled (second row) and uncoupled (first row) mortar interfaces for two different eigenvectors on the left and right.

In the context of our timber building project, we have performed a detailed model of a four story timber building as depicted in Figure 3.7. In order to perform these simulations, we have imposed the orthotropic timber material parameters which vary on the different walls of the building. The timber walls and slabs are made from laminated fiber consisting of several layers, which could be considered separately. However we assume that each component has an average blurred material parameter. The mortar calculations have been performed using second order elements, which leads to a system of 146.388 degrees of freedom. The resulting first 14 eigenvalues for a representative parameter set can be found in Table 3.3 and simulations of the eigenfunctions to the first, fifth, tenth and fifteenth eigenvalues can be found in Figure 3.9. As expected the first eigenvalues are global, with displacements of the whole structure with the building moving in x-direction. For higher modes it can be observed that the vibrations are found mostly in areas where there are no bearing walls to stabilize the building and stiffen the geometry.

EV		EV		EV		EV	
1	5.118	8	15.346	15	20.711	22	22.850
2	5.302	9	15.510	16	21.034	23	23.107
3	7.167	10	15.657	17	21.424	24	23.478
4	8.072	11	16.560	18	21.475	25	23.745
5	13.163	12	17.022	19	21.727	26	24.036
6	13.970	13	17.838	20	21.942	27	24.415
7	14.879	14	19.569	21	22.373	28	24.673

Table 3.3: Eigenvalues of the four story timber building.

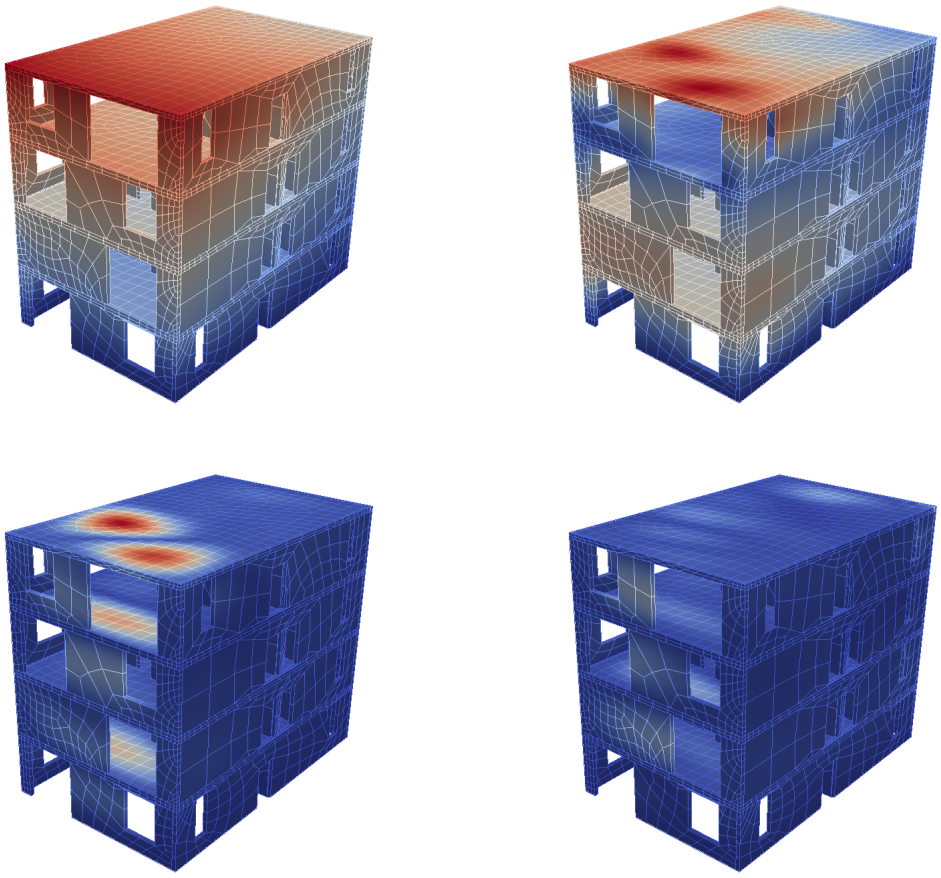

Figure 3.9: Simulated eigenmodes 1, 5, 10 and 15 of the four story timber building.

4. Model reduction of an elastomeric bedded structure

In the following, we consider the same setting as in the previous section with the difference that now the structures are interconnected by thin elastomer layers. To this end, we introduce a new dimensional reduced model which captures eigen-

values and eigenmodes of elastomeric coupled domains in timber structures. Our motivation to derive such a formulation stems from the need to compute the modal analysis which is a main part of vibro-acoustical analysis. In order to control sound transmissions between slabs and walls, these components are often connected by elastomers, which we model by using the linear elasticity equation because of their very thin character.

4.1. Elastomer modeling and influence

The modeling of elastic interface boundary conditions has been the subject for low orders in [70, 143, 174]. Also the modeling of interface elements has been investigated in [118, 179], with a spring boundary condition in [24] and with a Robin-type condition in [13]. Furthermore the elastic foundation model, which is a complexity reduction method in the context of Hertzian contact problems, is presented in [89]. The modeling of an elastomer for vibration isolation has been the subject in [12, 36]. These papers take many mechanical properties like strain and damping directly into account. Alternatively, the modal and spectral analysis can be realized by the modal superposition. In this case, the eigenmodes of the undamped system are required, and the damping is only taken into account in a postprocessing step. Thus we will in the following neglect the damping. Moreover, the elastomer is modeled in terms of the linear elasticity equations because it is comparatively thin in one space direction [130].

In order to obtain an idea of the influence of the elastomer, it is discretely represented by a thin layer of hexahedral elements. The discretization is depicted in Figure 4.1. The green hexahedral elements in Figure 4.1 mark the elastomer and the material properties for typical elastomers are as given in Table 4.1, where hard materials are listed first. We further add the timber material used for the wall and slab, which is for simplicity, as in the previous section 3.2, an isotropic material. The specific type of elastomer chosen in a practical application then depends on the dead load to be expected on the elastomer. In Table 4.1 Poisson's ratio and Young's modulus are denoted by ν and E, respectively.

	Timber	Elast 1	Elast 2	Elast 3	Elast 4	Elast 5
E in $[N/m^2]$	$9790 \cdot 10^6$	$1.8 \cdot 10^7$	$8.0 \cdot 10^6$	$3.7 \cdot 10^6$	$1.7 \cdot 10^6$	$8.0 \cdot 10^5$
ν in $[-]$	0.05	0.4	0.4	0.4	0.4	0.4

Table 4.1: Elastomer properties for the simulations.

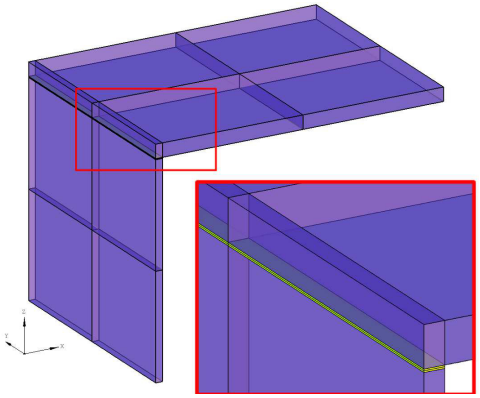

Figure 4.1: Conforming discretizations of the structure whose geometry is described in Figure 3.2. The thin elastomer layer is discretely represented.

The resulting eigenvalues with ansatz functions of order $k = 10$ for the different simulations with the given elastomers are depicted in Table 4.2. Eigenvalues corresponding to a direct connection of wall and slab are depicted as well. It is readily

EV	No Elast.	Elast. 1	Elast. 2	Elast. 3	Elast. 4	Elast. 5
1	50.282	48.584	47.472	45.933	43.157	38.357
2	68.929	52.437	51.461	50.461	48.676	45.275
3	74.304	64.128	61.773	58.287	52.669	45.588
4	87.685	79.851	77.797	74.245	68.109	59.885
5	124.818	110.669	105.449	98.276	90.290	84.003
6	159.264	149.448	141.577	127.098	106.626	89.151
7	172.884	160.956	154.662	140.762	123.733	105.596
8	178.886	162.633	155.910	145.873	127.320	111.518

Table 4.2: Influence of the different elastomers on the eigenfrequencies given in $[Hz]$.

apparent that, depending on the mode and the elastomer under contemplation, the eigenvalues of the system with an elastomer layer are about $5 - 35[\%]$ lower than without the elastomer. This is related to the fact that the coupling of the slab to the wall becomes weaker. Figure 4.2 illustrates the relative decay of each eigenvalue computed from the results depicted in Table 4.2.

Furthermore in Figure 4.3 we depict the eigenfunction for eigenvalue one to show the elastomer influence on the modes. Here it should be noted that the elastomer decouples the wall from the slab and therefore the displacement of one domain is not propagated through the elastomer.

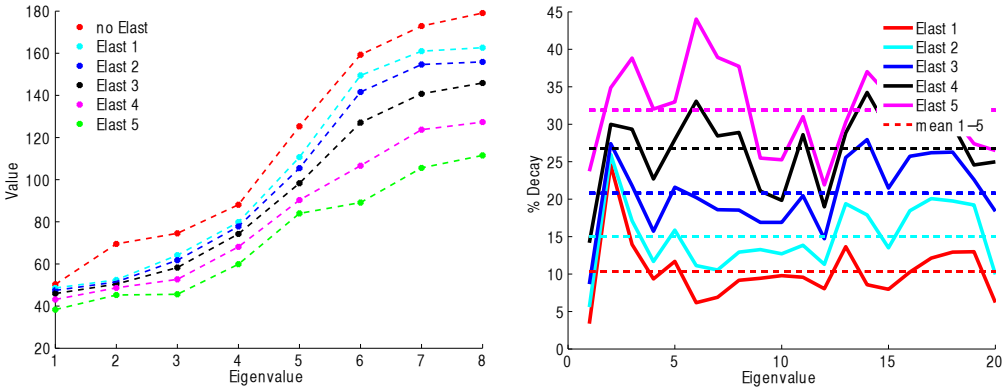

Figure 4.2: Dependence of the first eight eigenvalues of the elastomer (left) and relative decay with respect to no elastomer for the first 20 eigenvalues (right).

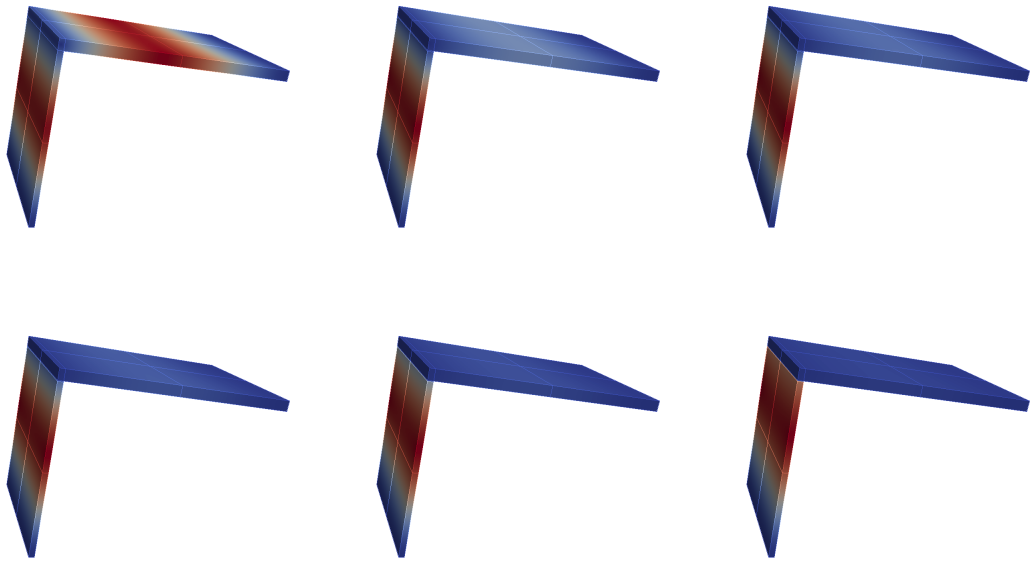

Figure 4.3: Elastomer influence on the first eigenfunction. First row depicts the cases without elastomer layer, with elastomer 1 and with elastomer 2. Second row depicts the elastomers 3 to 5.

4.2. Model reduction of the elastomer

This section will lay out a new modeling approach for the coupling, in order to replace an elastomer. As mentioned above, this new coupling condition results in a dimensional reduced model, which avoids the meshing of the three-dimensional subdomain that corresponds to the elastomer. Dimensionally reduced models are

very attractive from a computational point of view. However, new challenges arise such as the formulation of a suitable coupling condition and its numerical realization. Our new coupling condition still yields a saddle point problem which fits into the implementational framework of mortar methods.

We enforce a non-standard Robin-type condition at the interface by means of Lagrange multipliers instead of the continuity requirements. Robin-type interface conditions have been used to glue non-conforming grids, see, e.g., [61]. We extend this concept to elastomeric coupled domains. The main difference to the current work is that our coupling condition not only aims to glue two non-conforming grids together, but is also able to replace the whole explicit discretization of an elastomer as depicted in Figure 4.4. Therefore, it goes beyond a simple domain decompositon method, it provides also a dimensionally reduced model.

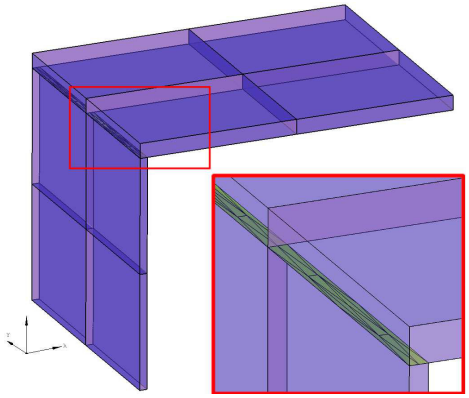

Figure 4.4: Mortar discretization of the structure whose geometry is described in Figure 3.2. The thin elastomer layer is condensed into the mortar interface.

The modeling ideas corresponding to the cases depicted in Figure 4.1 and Figure 4.4 are depicted in Figure 4.5 on the left and right, respectively.

Due to the very thin elastomer layer, in our case 1.2[cm], we simplify the transversal shear in the elastomer and neglect the mass of the elastomer. We assume the elastomer displacement to be linear in z-direction on the solution between the slab and the wall. Without loss of generality, we assume the coordinate system of the mortar interface to be at $z = 0$. Therefore, we define our simplified displacement in the spirit of a Taylor series with $z \in [0, d]$, where d denotes the thickness of the

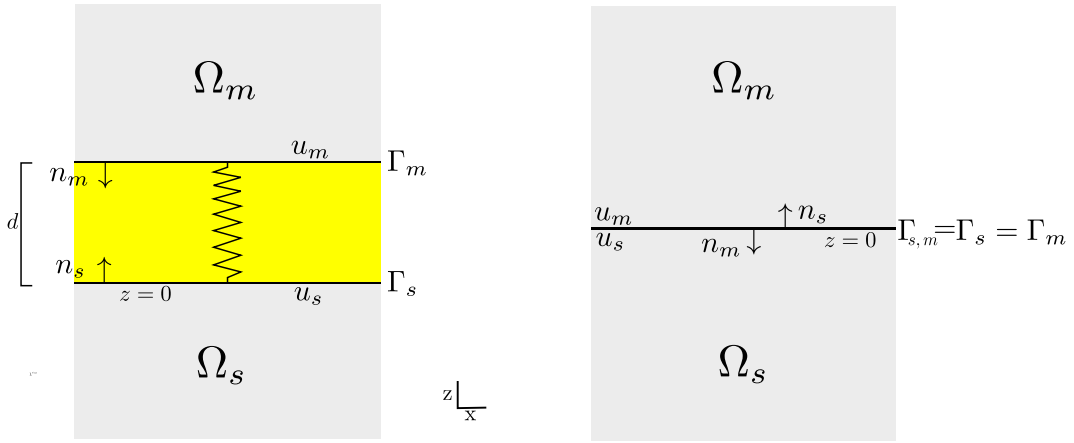

Figure 4.5: Modeling concept: Thin layer (left) and interface formulation (right).

elastomer as

$$u(x,y,z) = u_s(x,y) + \frac{z}{d}(u_m(x,y) - u_s(x,y)).$$

With this definition and with $[u] := (u_m(x,y) - u_s(x,y))$, the gradient of the displacement field at $z = 0$ is given by

$$\nabla u|_{z=0} = \begin{pmatrix} (u_s)_{1,x} & (u_s)_{1,y} & \frac{1}{d}[u]_1 \\ (u_s)_{2,x} & (u_s)_{2,y} & \frac{1}{d}[u]_2 \\ (u_s)_{3,x} & (u_s)_{3,y} & \frac{1}{d}[u]_3 \end{pmatrix}.$$

Now the linearized elastic strain reads

$$\epsilon(u|_{z=0}) = \frac{1}{2}\begin{pmatrix} 2(u_s)_{1,x} & (u_s)_{1,y} + (u_s)_{2,x} & \frac{1}{d}[u]_1 + (u_s)_{3,x} \\ (u_s)_{2,x} + (u_s)_{1,y} & 2(u_s)_{2,y} & \frac{1}{d}[u]_2 + (u_s)_{3,y} \\ (u_s)_{3,x} + \frac{1}{d}[u]_1 & (u_s)_{3,y} + \frac{1}{d}[u]_2 & \frac{2}{d}[u]_3 \end{pmatrix}.$$

Further, we assume the following standard linear isotropic stress-strain relationship with the Lamé parameters $\widetilde{\mu}$ and $\widetilde{\lambda}$ to hold in the elastomer, i.e.,

$$\sigma = 2\widetilde{\mu}\epsilon + \widetilde{\lambda}\,\mathrm{tr}(\epsilon)I,$$

where I denotes the identity matrix. As the interface is assumed to be aligned to z=0, the normal vector on $\Gamma_{s,m}$ directed towards Ω_m is given by $n = [0,0,1]^T$. The

fluxes are then explicitly given by

$$\begin{aligned}\sigma|_{z=0}n &= \begin{pmatrix}\widetilde{\mu}(\frac{1}{d}[u]_1 + (u_s)_{3,x})\\ \widetilde{\mu}(\frac{1}{d}[u]_2 + (u_s)_{3,y})\\ 2\widetilde{\mu}\frac{1}{d}[u]_3\end{pmatrix} + \widetilde{\lambda}\begin{pmatrix}0\\0\\tr(\epsilon)\end{pmatrix}\\ &= \begin{pmatrix}\frac{\widetilde{\mu}}{d}[u]_1 + \widetilde{\mu}(u_s)_{3,x}\\ \frac{\widetilde{\mu}}{d}[u]_2 + \widetilde{\mu}(u_s)_{3,y}\\ (\frac{2\widetilde{\mu}}{d} + \frac{\widetilde{\lambda}}{d})[u]_3 + \widetilde{\lambda}((u_s)_{1,x} + (u_s)_{2,y})\end{pmatrix}\end{aligned} \tag{8}$$

and Equation (8) represents the new coupling condition between displacements and surface traction in the strong form.

Note that in comparison to the standard mortar coupling condition $u_s - u_m = 0$, we additionally obtain dependencies on the derivatives $(u_s)_{3,x}$,$(u_s)_{3,y}$,$(u_s)_{1,x}$,$(u_s)_{2,y}$, and the surface traction $\tau_s = -\sigma|_{z=0}n$ interacts as a spring term with the displacement. The corresponding bilinear forms are now given by

$$\begin{aligned}\widetilde{b}(u,\widehat{\tau}) &= \begin{pmatrix} < [u]_1, \widehat{\tau}_1 >^* + d < (u_s)_{3,x}, \widehat{\tau}_1 > \\ < [u]_2, \widehat{\tau}_2 >^* + d < (u_s)_{3,y}, \widehat{\tau}_2 > \\ < [u]_3, \widehat{\tau}_3 >^* + \beta(< (u_s)_{1,x}, \widehat{\tau}_3 > + < (u_s)_{2,y}, \widehat{\tau}_3 >)\end{pmatrix},\\ c(\tau,\widehat{\tau}) &= < \tau, \widehat{\tau} >,\end{aligned}$$

with $< \cdot, \cdot >$ being the $(H^{-\frac{1}{2}}(\Gamma_{(s,m)}))^3$ scalar product and $\beta = \widetilde{\lambda}d/(2\widetilde{\mu} + \widetilde{\lambda})$. We note that this scalar product on the dual space is realized within the discrete setting as an L^2-surface integral. Both τ and $\widehat{\tau}$ are given by the mesh on the slave side, and thus a standard quadrature formula can be easily applied. For given surface tractions τ_i, the force equilibria of both bodies Ω_i read

$$a_{\Omega_i}(u, v_i) + < v_i, \tau_i > \;\; = \;\; \lambda m_{\Omega_i}(u, v_i).$$

Neglecting the difference between $-\tau_s = \sigma|_{z=0}\, n$ and $\tau_m = \sigma|_{z=d}\, n$, setting $\tau = \tau_s$ and adding both equations we obtain

$$a(u, v) + b(v, \tau) = \lambda m(u, v). \tag{9}$$

The new coupling condition Equation (8) in the weak form and Equation (9) lead

to the dimensionally reduced model given by

$$\begin{array}{lll} a(u,v)+ & b(v,\tau) & = \lambda m(u,v), \quad v \in X \\ \widetilde{b}(u,\widehat{\tau})- & \alpha c(\tau,\widehat{\tau}) & = 0, \qquad\quad \widehat{\tau} \in M \end{array} \tag{10}$$

with the modeling parameter α defined as

$$\alpha := \begin{pmatrix} \frac{d}{\widetilde{\mu}} & 0 & 0 \\ 0 & \frac{d}{\widetilde{\mu}} & 0 \\ 0 & 0 & \frac{d}{2\widetilde{\mu}+\widetilde{\lambda}} \end{pmatrix}.$$

Note that the parameters α and β can be directly computed from the properties of the elastomer. Replacing X by X_h^k and M by M_h gives the discrete version of Equation (10) yielding approximations λ_h of the eigenvalues.

We now test the new mortar model given above by using the discretization depicted in Figure 4.4. The results are compared to the classical, conforming discretization, as depicted in Figure 4.1, where the elastomer was modeled explicitly and calculated in Section 4.1.

Table 4.3 depicts the first eight eigenvalues obtained by the new mortar model along with the relative deviation from the eigenvalues of the explicitly modeled elastic layer whose results were given in Table 4.2.

	Elast 1		Elast 2		Elast 3		Elast 4		Elast 5	
EV	Value	%	Value	%	Value	%	Value	%	Value	%
1	48.664	0.165	47.511	0.082	46.034	0.218	43.206	0.112	38.545	0.490
2	52.678	0.459	51.628	0.325	50.685	0.443	48.997	0.659	45.846	1.262
3	64.315	0.292	61.916	0.231	58.685	0.682	52.891	0.421	46.082	1.083
4	80.059	0.260	78.252	0.585	75.113	1.170	69.159	1.542	61.539	2.763
5	110.912	0.220	105.784	0.317	99.112	0.850	90.606	0.350	84.208	0.243
6	149.371	0.052	141.757	0.127	128.750	1.300	107.303	0.635	89.468	0.355
7	161.365	0.254	155.063	0.259	142.314	1.103	124.127	0.319	109.623	3.814
8	162.967	0.205	157.058	0.737	148.494	1.797	130.530	2.521	111.558	0.036

Table 4.3: Eigenfrequencies given in $[Hz]$ for the new modeling approach along with the relative deviation from the conforming discretization depicted on the left hand side of Figure 4.4.

All computations are carried out with a polynomial degree of $k = 10$. We observe that the new model is able to reproduce the eigenvalues to an accuracy of at least 4%. Not only the eigenvalues but also the eigenmodes of the two different discreti-

zation models are required to match closely. Figure 4.6 shows selected eigenvectors of elastomer 5. The upper row provides the eigenvectors, as computed by an explicit modeling of the elastomer, while the lower row represents the corresponding eigenvectors of the new mortar method.

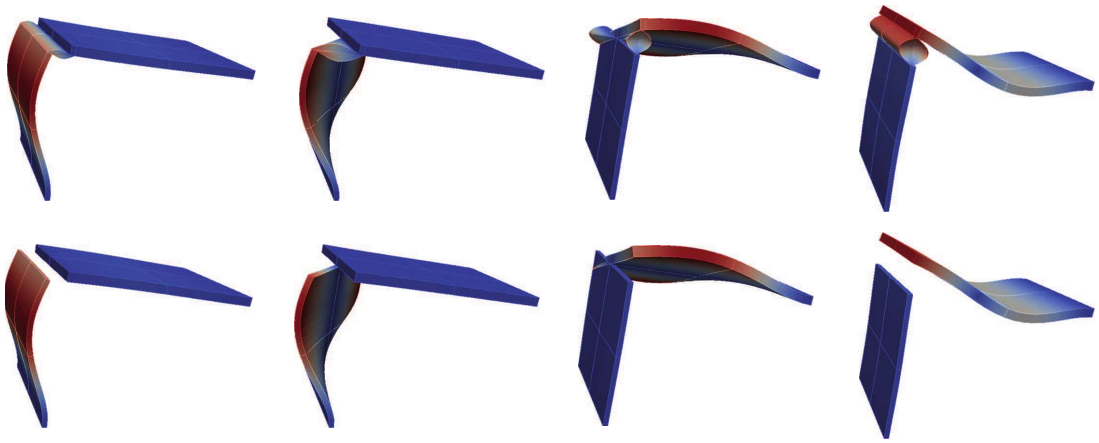

Figure 4.6: Comparison between eigenmodes 1, 3, 4 and 7. Top row: Conforming, hexahedral discretization. Bottom row: New mortar method. Note that the greyscale shows the displacement.

Obviously, different types of modes, such as lateral and transversal shear modes as well as pure compression and traction modes, are equally well represented. While in the upper row the elastomer undergoes severe deformations, these are approximated by the coupling conditions at the interface between wall and slab in the lower row. Note that the missing elements for the elastomeric layer result from the reduction of the dimension. Moreover, the sequence of the eigenmodes remains the same in both models.

We also analyse the eigenmodes by a modal assurance criterion as it is described in [120], which determines the correlation of the eigenmodes. For a good correlation, the resulting matrix should have a diagonal with values greater than 0.9. Diagonal values close to 0 mean a poor correlation. The modal assurance criterion matrices show very good results for all investigated practically relevant elastomers. We show as an example the modal assurance criterion matrix for elastomer 5 in Table 4.4. Together with the eigenmodes depicted in Figure 4.6, this confirms the good results for the newly developed coupling condition. Furthermore, it is pointed out that the number of elements is reduced by one third even in this small example. Herein, the boundary conforming model requires 12 hexahedral elements while only 8 hexahedral elements suffice for the new mortar approach. However,

$MAC_{E51.2[cm]}=$

	u_1	u_2	u_3	u_4	u_5	u_6	u_7	u_8
u_1	1.000	0.000	0.004	0.000	0.002	0.000	0.000	0.000
u_2	0.000	1.000	0.000	0.000	0.000	0.000	0.000	0.000
u_3	0.003	0.000	0.999	0.000	0.000	0.000	0.003	0.000
u_4	0.000	0.000	0.000	0.999	0.000	0.000	0.000	0.000
u_5	0.001	0.000	0.000	0.000	1.000	0.000	0.000	0.000
u_6	0.000	0.000	0.000	0.000	0.000	1.000	0.002	0.000
u_7	0.000	0.000	0.000	0.000	0.000	0.000	0.998	0.000
u_8	0.000	0.000	0.000	0.000	0.000	0.000	0.000	1.000

Table 4.4: Modal assurance criterion for the modeling of elastomer 5 split in x, y and z direction.

and most importantly, the mesh generation is simpler using the reduced model in the sense that each wall or slab can now be meshed separately before the discretized components are glued back together.

A key assumption of the new approach is that the displacement field varies only linearly in the direction perpendicular to the two opposite interfaces of the elastomer with adjacent structures. In order to investigate the validity of this assumption, we vary the thickness of the elastomer and show its influence on the corresponding eigenvalues. At this point it is noted that the thickness of the elastomers for typical wall-slab configurations is below 3$[cm]$. In practical applications, thicknesses range from 1$[cm]$ to 1.5$[cm]$. The reference solution is again computed using the conforming finite element method. We perform our simulation with two further thicknesses of the elastomer. The first thickness is 3$[cm]$, which is the maximum relevant thickness and the second thickness is 4$[cm]$, which is beyond the typical application range. The corresponding results for the investigation for the two elastomer thicknesses are depicted in Table 4.5 and Table 4.6, respectively. The tables also show the relative deviation between the new model and the explicitly modeled

	Elast 1			Elast 3			Elast 5		
EV	Conform Method	New Method	% diff	Conform Method	New Method	% diff	Conform Method	New Method	% diff
1	46.873	46.828	0.096	42.043	42.282	0.568	29.716	30.419	2.367
2	51.223	51.504	0.549	47.783	48.655	1.825	36.608	37.718	3.033
3	60.827	61.081	0.416	50.929	51.658	1.432	37.274	39.155	5.047
4	76.991	78.028	1.347	65.466	68.104	4.031	48.848	51.360	5.143
5	103.857	104.722	0.833	88.359	89.365	1.139	76.357	76.166	0.251
6	138.595	139.275	0.491	101.474	103.915	2.406	79.253	79.477	0.283
7	151.783	152.988	0.794	119.491	121.222	1.449	84.601	88.684	4.826
8	153.680	156.466	1.813	119.571	127.398	6.546	103.182	102.752	0.416

Table 4.5: Eigenfrequencies given in $[Hz]$ for the conform and the new method with the corresponding relative deviation for the elastomer thickness 3[cm].

	Elast 1			Elast 3			Elast 5		
EV	Conform Method	New Method	% diff	Conform Method	New Method	% diff	Conform Method	New Method	%diff
1	46.100	46.001	0.215	39.931	40.471	1.354	26.683	27.634	3.562
2	50.780	51.115	0.661	46.091	47.664	3.413	32.869	35.531	8.098
3	59.252	59.736	0.817	47.753	48.835	2.266	35.046	36.449	4.004
4	75.331	76.804	1.956	61.409	65.291	6.323	45.903	48.787	6.283
5	100.661	102.266	1.594	85.356	86.606	1.464	73.943	73.419	0.707
6	132.275	134.570	1.735	93.278	96.202	3.135	78.124	78.372	0.317
7	145.499	148.266	1.902	108.759	115.437	6.140	80.538	84.663	5.122
8	148.833	153.236	2.959	113.584	119.391	5.113	101.426	100.758	0.658

Table 4.6: Eigenfrequencies given in $[Hz]$ for the conform and the new method with the corresponding deviation in [%] for the elastomer thickness 4[cm].

elastomer layer.

While it can be observed that the thicker the elastomer, the bigger the error, the error does not rise above engineering accuracy for practical applications. Table 4.7 and Table 4.8 show the modal assurance criterion matrices for the eigenmodes for the corresponding 3$[cm]$ and 4$[cm]$ elastomer simulations.

$MAC_{E53cm}=$

	u_1	u_2	u_3	u_4	u_5	u_6	u_7	u_8
u_1	1.000	0.000	0.000	0.000	0.000	0.001	0.000	0.000
u_2	0.000	1.000	0.000	0.000	0.000	0.000	0.000	0.000
u_3	0.000	0.000	0.996	0.000	0.000	0.000	0.003	0.000
u_4	0.000	0.000	0.000	0.999	0.000	0.000	0.000	0.000
u_5	0.001	0.000	0.000	0.000	0.998	0.000	0.006	0.000
u_6	0.002	0.000	0.000	0.000	0.002	0.999	0.001	0.000
u_7	0.000	0.000	0.004	0.000	0.000	0.000	0.994	0.000
u_8	0.000	0.000	0.000	0.000	0.000	0.000	0.000	1.000

Table 4.7: Modal assurance criterion for the modeling of elastomer 5 with thickness 3[cm], split in x, y and z direction.

$MAC_{E54cm}=$

	u_1	u_2	u_3	u_4	u_5	u_6	u_7	u_8
u_1	1.000	0.000	0.000	0.000	0.000	0.001	0.000	0.000
u_2	0.000	1.000	0.000	0.000	0.000	0.000	0.000	0.000
u_3	0.000	0.000	0.994	0.000	0.000	0.000	0.003	0.000
u_4	0.000	0.000	0.000	0.999	0.000	0.000	0.000	0.000
u_5	0.002	0.000	0.000	0.000	0.998	0.000	0.008	0.000
u_6	0.002	0.000	0.000	0.000	0.002	0.999	0.001	0.000
u_7	0.000	0.000	0.008	0.000	0.000	0.000	0.990	0.000
u_8	0.000	0.000	0.000	0.000	0.000	0.000	0.000	1.000

Table 4.8: Modal assurance criterion for the modeling of elastomer 5 with thickness 4[cm], split in x, y and z direction.

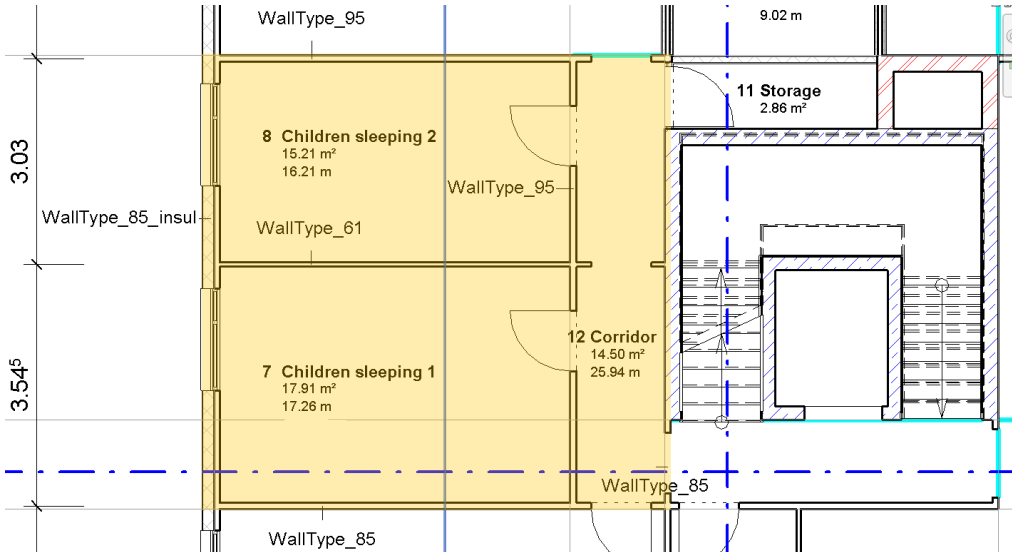

Figure 4.7: Detail of the ground floor plan considered for acoustical analysis.

The good performance of the new mortar method carries over to larger examples of engineering relevance, where an orthotropic material law is used for the elastically connected building parts. Figure 4.7 depicts a floor plan of the model timber building along with a $2\frac{1}{2}$D submodel consisting of three rooms.

This model forms the basis of the three-dimensional computational solid model comprising all conforming hexahedral elements depicted in Figure 4.8.

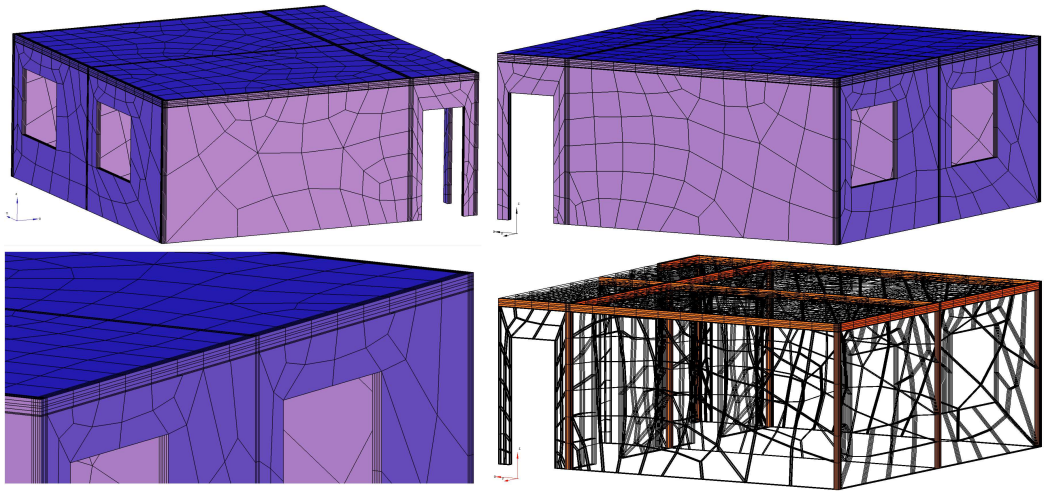

Figure 4.8: Conforming hexahedral discretization.

Note that walls and slabs consist of several layers of wood, as depicted in Figure 4.9. The thickness of the layers is given in Table 4.9. In this example, each layer is explicitly modeled with the characteristic orthotropic material parameters

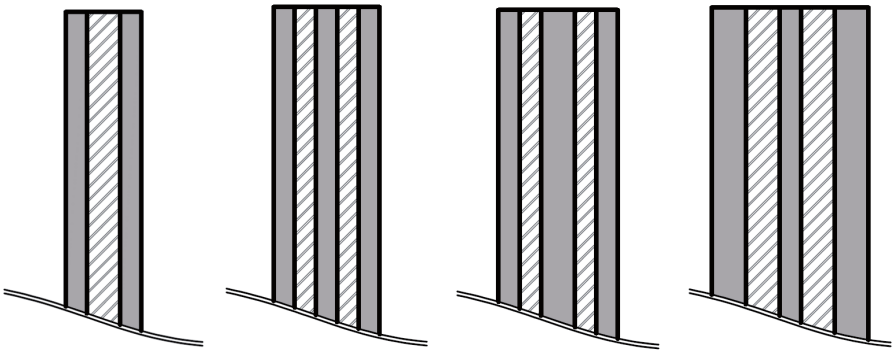

Figure 4.9: Wall types from left to right: Wall type 61, 85, 95 and slab 125.

type	layering $[mm]$
61	17*–27–17*
85	17*–17–17*–17–17*
95	17*–17–27*–17–17*
125	27*–27–17*–27–27*

Table 4.9: Layer thicknesses of walls and slab 125.

of timber. We set the Young's moduli in fiber direction to $E_x = 137 \times 10^6[N/m^2]$, in-plane orthogonal $E_y = 1424 \times 10^6[N/m^2]$, and perpendicular to the plane $E_z = 10211 \times 10^6[N/m^2]$. The Poisson's ratios are $\nu_{xz} = 0.035$, $\nu_{yz} = 0.045$ and $\nu_{xy} = 0.037$. In addition, we apply the shear moduli $G_{xz} = 459 \times 10^6[N/m^2]$, $G_{yz} = 102 \times 10^6[N/m^2]$ and $G_{xy} = 171 \times 10^6[N/m^2]$. The density is assumed to be $\rho = 450[kg/m^3]$ for all layers.

Although the individual layers have the same material properties, their fiber orientation in plane is orthogonal in adjacent layers in such a way that the orientation is equal on every other layer only. This situation is accurately resolved by the finite element mesh. The elastomer is situated only at the interface, where the slab rests on the walls and possesses the isotropic material properties of elastomer 5, as given in Table 4.1. The conforming model is depicted in Figure 4.8. In total, the mesh consists of 7578 hexahedral elements.

In contrast, the computational mesh for the mortar method is depicted in Figure 4.10, consisting of only 2475 hexahedral elements. It is evident how the components wall and slab were meshed independently of one another and are nonconforming at their interface.

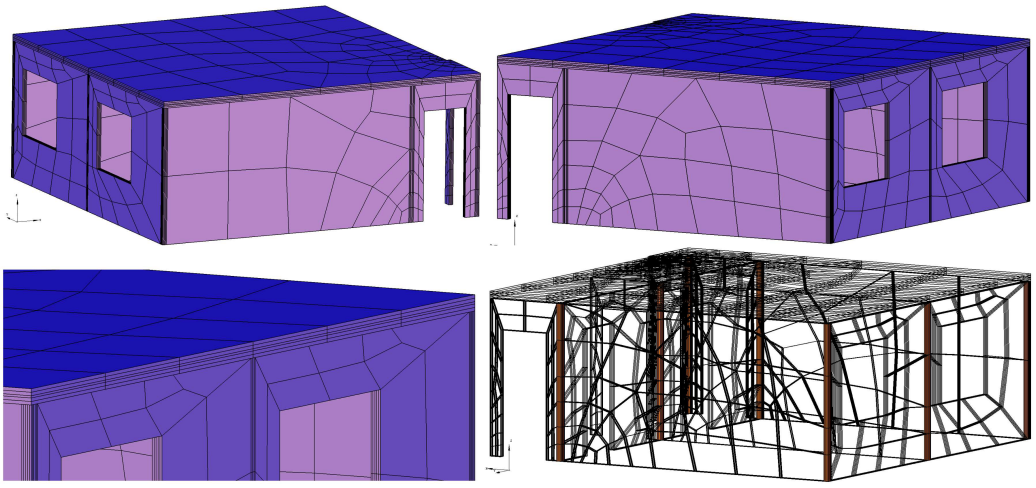

Figure 4.10: Non-conforming hexahedral discretization.

Not only does this greatly simplify the mesh generation process itself, it also avoids the generation of hexahedral elements due to continuity constraints at the interfaces of walls and slabs. A further reduction of hexahedral elements is possible by choosing mesh densities individually for all involved components. Also note that local refinements do not branch out to other walls. The elastomer where the slab rests on the walls is now modeled using the new mortar method derived above.

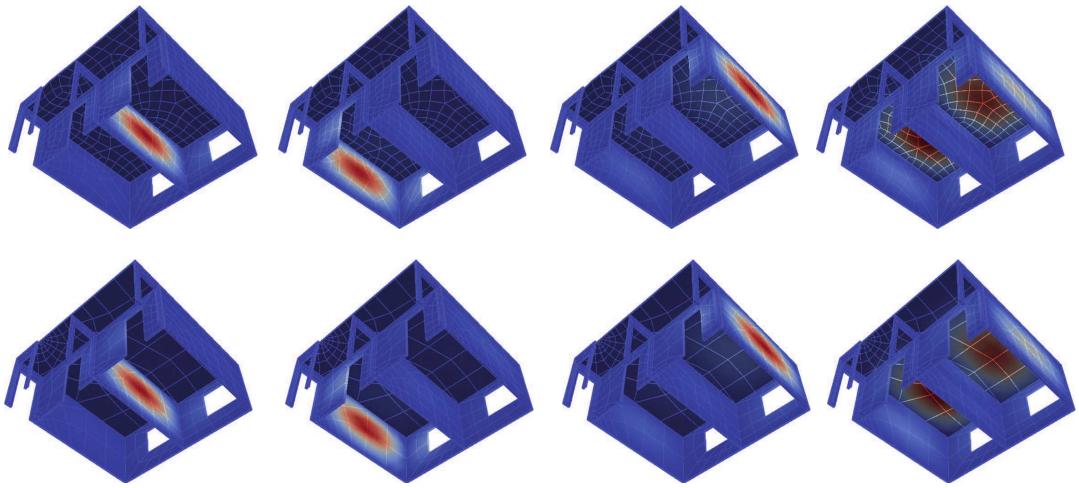

Figure 4.11: Comparison between eigenmodes 1, 2, 3 and 4. Top row: Resulting from the conforming discretization corresponding to Figure 4.8. Bottom row: Non-conforming discretization corresponding to Figure 4.10.

Table 4.10 summarizes the comparison for the first eight eigenvalues and then selected higher eigenvalues up to one hundred.

EV	Conform No Elast	Mortar No Elast	% diff	Conform Elast	New coupling Elast	% diff
1	11.357	11.471	1.007	9.883	9.960	0.779
2	13.738	13.861	0.899	12.439	12.496	0.459
3	14.347	14.425	0.547	13.302	13.346	0.330
4	15.807	15.947	0.884	13.938	14.067	0.926
5	16.988	17.133	0.856	14.980	15.134	1.030
6	21.070	21.329	1.227	19.256	19.398	0.737
7	21.832	21.988	0.715	20.765	20.833	0.325
8	24.038	24.265	0.947	21.072	21.165	0.437
...	...	...	...	...	...	...
20	36.868	37.071	0.552	34.033	34.437	1.189
...	...	...	...	...	...	...
30	48.414	48.769	0.732	43.329	43.850	1.202
...	...	...	...	...	...	...
40	61.815	62.479	1.073	53.238	53.574	0.631
...	...	...	...	...	...	...
50	69.224	70.028	1.162	60.897	61.468	0.938
...	...	...	...	...	...	...
60	77.711	78.402	0.889	66.702	67.982	1.919
...	...	...	...	...	...	...
70	86.225	86.443	0.253	76.123	76.488	0.479
...	...	...	...	...	...	...
80	93.425	93.893	0.501	83.881	84.382	0.597
...	...	...	...	...	...	...
90	101.063	101.673	0.603	88.875	89.558	0.769
...	...	...	...	...	...	...
100	108.871	109.382	0.469	94.814	95.145	0.349

Table 4.10: Computed eigenfrequencies given in $[Hz]$ for the building example.

Note that the modeling error introduced by the new mortar approach remains below two percent for all investigated eigenvalues. In comparison to the conforming method, the error obtained when using the mortar method with the new coupling condition is comparable to the error obtained when using the standard mortar method. The upper row of Figure 4.11 depicts selected eigenvectors resulting from the conforming discretization given in Figure 4.8, while the lower half depicts the corresponding eigenvectors of the mortar discretization of Figure 4.10. All eigenvectors match within an accuracy which is considered sufficient for engineering applications.

Chapter III.
Reduced basis methods for eigenvalue problems

The vibro-acoustical analysis of cross-laminated timber structures constitutes a parameter dependent eigenvalue problem in linear elasticity, where the input parameters are the material properties of different structural components. This problem has to be solved many times during a design and optimization phase and thus our aim in this chapter is to develop a model reduction framework for the corresponding elliptic parameter dependent eigenvalue problems (μEVP).

5. Eigenvalue reduced basis methods for elliptic eigenvalue problems

Since the main part of a vibro-acoustical analysis is the modal analysis, which not only takes the first eigenvalue into account, but all eigenvalues lower than a certain frequency, depending on the problem under investigation, the outputs of interest are the K smallest eigenvalues with corresponding eigenfunctions. A characteristic feature of the considered μEVP is the possible appearance of multiple eigenvalues. In particular, the multiplicities depend on the parameters. Furthermore another characteristic of the considered μEVP is the rather large number of outputs of interest K, which in our exemplary case ranges from two to twenty.

The Sections 5.2–5.5 contain results published by the author with B. Wohlmuth and T. Dickopf in the paper entitled "Simultaneous reduced basis approximation of parameterized elliptic eigenvalue problems" in the journal ESAIM: Mathematical Modelling and Numerical Analysis in 2016, [80].

5.1. Introduction to reduced basis methods

In the following, we introduce the principal ideas on which the reduced basis method for right-hand side problems is founded. Reduction methods are of crucial importance whenever a calculation becomes complex or has to be performed several times. The large computation times required for this can be reduced significantly

by performing once a very general calculation and then deducting the particular solutions from it.

To this end, reduced basis methods have been developed over the last decade; see, e. g., [128, Chapter 19] or [129, 141] for comprehensive reviews, with the first reduced basis problem being investigated in the 1980's [117]. Reduced basis methods have been successfully applied to many different problem classes both in the real-time and the many-query context. Among those are finite element discretizations of elliptic equations [141], parabolic equations [66, 139, 165] and hyperbolic equations [42, 68]. Furthermore the reduced basis method has been extended to Stokes problems [87, 102, 140, 142] and variational inequalities [65, 69]. In addition the reduced basis method was used in the context of stochastic processes in [54, 167] and in the context of a finite volume scheme of a parameterized and highly nonlinear convection-diffusion problem with discontinuous solutions in [51].

Let us assume that an input-output relation for a parameterized partial differential equation (μPDE) has an input parameter vector μ belonging to the input-parameter domain $\mathcal{P}$, i.e., $\mu \in \mathcal{P} \subset \mathbb{R}^P$. Then the solution u of a general elliptic problem depends on the parameter vector and the general problem formulation reads:
Given $\mu \in \mathcal{P}$, find $u(\mu) \in V$ such that

$$a(u(\mu), v; \mu) = l(v; \mu), \qquad v \in V,$$

where V denotes a suitably chosen Hilbert space and $a(\cdot, \cdot; \mu)$ and $l(\cdot; \mu)$ are the bilinear form and the linear functional, where the new argument μ indicates the parameter-dependence. Then the basic idea of the reduced basis method comes into play as we assume that the solutions $u(\mu)$ do not cover the entire space V, but rather lie on a curve or surface in V, which is assumed to be low-dimensional and smooth and which is called the parametrically induced manifold

$$\mathcal{M} = \{u(\mu) \in V : \mu \in \mathcal{P}\}.$$

We will approximate this manifold numerically and the best finite element approximation which can be achieved numerically is

$$\mathcal{M}^{\mathcal{N}} = \{u_h(\mu) \in V_h^k : \mu \in \mathcal{P}\},$$

where $V_h^k \subset V$ is a subspace of dimension $\mathcal{N} < \infty$. The larger $\mathcal{N}$, the bet-

ter the approximation, but also the more computation time is needed to perform the approximation. The reduced basis approach now allows us to build a lower-dimensional approximation $u_{\text{red}}(\mu) \in V_N$ of $u_h(\mu)$ of dimension $N \ll \mathcal{N}$. This is achieved by selecting several parameters from $\mathcal{P}$ and computing the corresponding solutions, which are called snapshots of the manifold $\mathcal{M}^{\mathcal{N}}$, then approximating the space V_h^k by its subspace V_N, composed of the linear combinations of the snapshots, and looking for u_{red} in V_N. The numerically built Lagrange reduced basis spaces corresponding to the Lagrange parameter samples $S_N = \{\mu^1, \ldots, \mu^N\}$ for $N = 1, \ldots, N_{max}$ are denoted by

$$V_N = \text{span}\{u_h(\mu^n), 1 \leq n \leq N\}$$

and are nested. This property is crucial for the memory efficiency of the reduced basis method. The reduced approximation $u_{\text{red}}(\mu)$ is computed using a Galerkin projection which, since the bilinear form is coercive and symmetric for any given μ, automatically selects the best snapshot combination. Then the use of a Gram-Schmidt orthogonalization allows us to achieve orthonormal basis functions ζ_n, $1 \leq n \leq N$, such that the reduced basis solution can be written as

$$u_{\text{red}}(\mu) = \sum_{i=1}^{N} u_{\text{red}_i}(\mu)\zeta_i$$

and the reduced basis problem now consists of finding the solution $u_{\text{red}}(\mu) \in V_N \subset V_h^k$ to the set of equations

$$\sum_{j=1}^{N} a(\zeta_j, \zeta_i; \mu) u_{\text{red}_j}(\mu) = l(\zeta_i; \mu), \qquad i \in \{1, \ldots, N\}.$$

A very important step in the reduced basis method is the sampling of the initial set of parameters from $\mathcal{P}$. There are two main procedures used for the sampling from $\mathcal{P}$, namely greedy algorithm strategies and the proper orthogonal decomposition (POD) method. The greedy algorithm gradually selects N possible parameter values $\mu^1, \ldots, \mu^N$ from the train sample Ξ_{train}. While doing this, in each iteration the parameter is added for which the solution $u_h(\mu)$ is worst approximated by the space V_{N-1} of the already retained snapshots. Thus an appropriate error estimator is required. In contrast, the proper orthogonal decomposition [90, 128, 129] aims at achieving the best possible reduced space in the sense that, for a given series of snapshots, the projection error w. r. t. the L^2-norm is minimized. Thus a set of

parameters is chosen into the sufficiently large train set Ξ_{train} and the snapshots are generated by solving the μPDE, which yields the set $S \subset V_h^k$ of all snapshots. Then the orthonormal functions $\{\zeta_1, \dots, \zeta_N\} \subset \text{span}(S)$ are chosen such that

$$\sum_{v \in S} \|v - \Pi_N v\|^2_{L^2(\Omega)}$$

is minimal, where Π_N denotes the L^2-orthogonal projection to span $\{\zeta_1, \dots, \zeta_N\}$.

The online-offline procedure is what enables the reduced basis method to be separated into two phases: The more costly offline computation of the space V_N and the very cheap online phase, in which the result to an imminent problem is derived from the offline phase results. This is made possible by the affine parameter dependence of the bilinear form $a(\cdot, \cdot; \mu)$ and the linear functional $l(\cdot; \mu)$, which can be expressed as

$$\begin{aligned} a(u, v; \mu) &= \textstyle\sum_{q=1}^{Q_a} \theta_a^q(\mu) a^q(u, v), \qquad u, v \in V, \mu \in \mathcal{P} \\ l(v; \mu) &= \textstyle\sum_{q=1}^{Q_l} \theta_l^q(\mu) l^q(v), \qquad v \in V, \mu \in \mathcal{P} \end{aligned}$$

for finite Q_a and Q_l and the μ-dependent functions $\theta_a^q : \mathcal{P} \to \mathbb{R}$ for $1 \leq q \leq Q_a$, $\theta_l^q : \mathcal{P} \to \mathbb{R}$ for $1 \leq q \leq Q_l$ as well as the μ-independent terms a^q and l^q. Inserting these forms into the set of linear algebraic equations obtained above yields

$$\sum_{j=1}^{N} \Big(\sum_{q=1}^{Q_a} \theta_a^q(\mu) a^q(\zeta_j, \zeta_i) \Big) u_{\text{red}_j}(\mu) = \sum_{q=1}^{Q_l} \theta_l^q(\mu) l^q(\zeta_i), \qquad i \in \{1, \dots, N\},$$

and thus a problem which can be separated into its parameter dependent and its parameter independent parts.

In several stages we want to assess the loss of accuracy in comparison to classical methods. Thus we employ *a posteriori* error estimators to facilitate the construction of reduced basis spaces by greedy algorithms as well as the certification of the outputs of the reduced models. Different greedy methods for reduced basis and error estimators are introduced in [106, 107, 166] and also a greedy method for eigenvalues is introduced in [34]. The convergence of greedy methods has been analyzed in [20, 32, 47]. Adequate *a posteriori* error estimators have to be rigorous, sharp as well as efficient and depend on N but not on $\mathcal{N}$ as will be seen in the following for parameterized elliptic eigenvalue problems.

5.2. Reduced basis for eigenvalue problems

In the following we consider the problem class of parameterized elliptic eigenvalue problems (μEVP), which is highly important but up to now only marginally investigated in the context of reduced basis methods. The first approach [104] from the year 2000, which is based on [105] among others, is restricted to the special case of an estimator for the first eigenvalue. In the publications [122, 123, 124], the method from [104] is developed further to include several eigenvalues.

However, both the analysis and the algorithms do not cover the case of multiple eigenvalues. Quite often, the "vectorial approach", i. e., the treatment of the eigenvectors $(u_i(\mu))_{1\leq i\leq K}$ as a (FE dimension $\cdot\, K$)-dimensional object and building the approximation space accordingly, see [123, Section 2.3.5], results in poor accuracy. This is due to the fact that the possible savings from reduced problems of smaller size seem marginal if achievable at all. In addition high-frequency information can and should be exploited for the approximation of low-frequency information, an effect that is expected to become more and more important with increasing number of desired eigenvalues. In [181], an elastic buckling problem is studied. While the model reduction is carried out primarily for a linear problem, the eigenvalue problem appears only in a second step. In [170] a non-rigorous *a posteriori* bound is computed by comparison with a reduced space approximation of double size. Furthermore a component based reduced basis method is studied for eigenvalue problems in [169]. Very recently a reduced basis method for the approximation of single eigenvalues in the context of parameterized elliptic eigenvalue problems has been investigated in [60]. The authors derive a bound for the error in the first eigenvalue which is assumed to be single.

We will now start by introducing reduced basis methods in a general eigenvalue context. Let the computational domain $\Omega \subset \mathbb{R}^d$, with $d \in \{2, 3\}$, be bounded and polygonal. As an elliptic eigenvalue model problem, we consider the linear elasticity case. We recall the eigenvalue problem in linear elasticity, which is given by

$$-\text{div}\ \sigma(u) = \lambda \rho u \quad \text{in } \Omega,$$

with boundary conditions prescribed as Dirichlet conditions on a closed non-trivial subset Γ^D of $\partial\Omega$ and homogeneous Neumann conditions on $\partial\Omega \setminus \Gamma^D$. In addition, the linearized stress and strain tensors are defined as in Section 2.3. We set the

density ρ to 1 for simplicity. As above, the set of admissible parameters is denoted by $\mathcal{P} \subset \mathbb{R}^P$ and $\mu \in \mathcal{P}$ stands for a vector of parameters. Then $\mathbb{C}(\mu)$ denotes the parameter dependent Hooke's tensor, which we assume to be uniformly positive definite. To this end let Ω be decomposed into non-overlapping subdomains such that $\overline{\Omega} = \bigcup_s \overline{\Omega}_s$. We assume that the material parameters are piecewise constant w. r. t. this decomposition. In the isotropic case, the parameters may be chosen as Young's modulus E and Poisson's ratio ν such that P equals two times the number of structural components, i. e., subdomains. More precisely, we set $\mu_{2s-1} = E|_{\Omega_s}$ and $\mu_{2s} = \nu|_{\Omega_s}$ in this case. The anisotropic case is treated analogously.

Let the parameter dependent bilinear forms $a(\cdot,\cdot;\mu) : (H^1(\Omega))^d \times (H^1(\Omega))^d \to \mathbb{R}$ and $m(\cdot,\cdot) : (L^2(\Omega))^d \times (L^2(\Omega))^d \to \mathbb{R}$ be given by

$$(u,v) \mapsto a(u,v;\mu) := \int_\Omega \mathbb{C}(\mu)\epsilon(u) : \epsilon(v)\,\mathrm{d}x$$

and

$$(u,v) \mapsto m(u,v) := (u,v)_{L^2(\Omega)} := \int_\Omega u \cdot v\,\mathrm{d}x,$$

where $a(\cdot,\cdot;\mu)$ depends on the parameter vector μ, whereas $m(\cdot,\cdot)$ and Ω do not.

Remark 5.1. *The equations of linear elasticity are used as a model problem as we are interested in the applications of vibro-acoustics. However this does not pose any restriction to the theoretical results shown in the following. Thus we could replace $a(\cdot,\cdot,\mu)$ by any H^1-elliptic bilinear form.*

Let now $V_h^k \subset \left\{v \in (H^1(\Omega))^d : v|_{\Gamma_D} = 0\right\}$ be a fixed conforming finite element space of order k with dimension $\mathcal{N}$. For the ease of notation, in this section we define $V_h := V_h^k$. Then, the discrete variational formulation of (3) reads: Find the eigenvalues $\lambda(\mu) \in \mathbb{R}$ and the eigenfunctions $u(\mu) \in V_h$ such that

$$a(u(\mu), v; \mu) = \lambda(\mu) m(u(\mu), v), \qquad v \in V_h \tag{11}$$

for given $\mu \in \mathcal{P}$. We assume that the eigenvalues are positive and numbered as

$$0 < \lambda_1(\mu) \leq \ldots \leq \lambda_{\mathcal{N}}(\mu).$$

The corresponding eigenfunctions are denoted by $u_i(\mu) \in V_h$ for $i = 1, \ldots, \mathcal{N}$ with the normalization

$$m(u_i(\mu), u_j(\mu)) = \delta_{ij} \text{ for } 1 \leq i, j \leq \mathcal{N}.$$

In the present context, the error of the finite element solution is assumed to be very small. This is achieved by a fine mesh size leading to a large dimension $\mathcal{N}$. The discretization error analysis can be found, e. g., in [8, 9, 10].

Let $L \geq 1$ be the number of distinct eigenvalues of (11). For multiple eigenvalues, we use the standard notation from [10] and denote the lowest index of the i-th distinct eigenvalue by k_i and its multiplicity by q_i, $i = 1, \ldots, L$. We write $\mathcal{K}_i := \{k_i, \ldots, k_i + q_i - 1\}$. Here and in the following, the dependency of the index notations on μ is suppressed as it is always clear from the context. The corresponding eigenspaces are denoted by

$$U_i(\mu) := \operatorname{span}\{u_{k_i}(\mu), \ldots, u_{k_i+q_i-1}(\mu)\}.$$

Now, the goal is to find a computationally inexpensive but accurate surrogate model that can be used in the many-query or real-time context.

We consider a variational approximation of the μEVP in an N-dimensional reduced space

$$V_N := \operatorname{span}\{\zeta_n : n = 1, \ldots, N\} \subset V_h, \tag{12}$$

with $N \ll \mathcal{N}$. As a matter of fact, the choice of V_N highly depends on the algorithmic methodology. Several (snapshot-based) possibilities are investigated in Section 5.4. Now, the reduced eigenvalue problem reads as

$$\begin{aligned} (u_{\mathrm{red}}(\mu), \lambda_{\mathrm{red}}(\mu)) &\in V_N \times \mathbb{R}, \\ a(u_{\mathrm{red}}(\mu), v; \mu) = \lambda_{\mathrm{red}}(\mu) m(u_{\mathrm{red}}(\mu), v), &\quad v \in V_N \end{aligned} \tag{13}$$

for given $\mu \in \mathcal{P}$. Let us emphasize that all eigenpairs of interest are approximated in the same space V_N. As before, we assume a numbering $\lambda_{\mathrm{red},i}(\mu)$, $i = 1, \ldots, N$ of the "reduced eigenvalues". The minimum-maximum principles guarantee that $\lambda_i(\mu) \leq \lambda_{\mathrm{red},i}(\mu)$ for $i = 1, \ldots, N$; see [10, Sect. 8]. Note that the multiplicity of the finite element eigenvalues is not necessarily reflected in the reduced basis eigenvalues. The corresponding eigenfunctions are denoted by $u_{\mathrm{red},i}(\mu) \in V_N$ for $i = 1, \ldots, N$, again with the normalization

$$m(u_{\mathrm{red},i}(\mu), u_{\mathrm{red},j}(\mu)) = \delta_{ij}, \quad 1 \leq i, j \leq N.$$

In practice, as mentioned before, one is only interested in the first K eigenvalues for

any chosen parameter. We expect that the dimension N required to achieve a certain accuracy will depend not only on the smoothness of the parameter-dependency of the μPDE but also on the number of outputs K.

As above, $a(\cdot,\cdot;\mu)$ is affine w. r. t. the parameter μ, i. e.,

$$a(u,v;\mu) = \sum_{q=1}^{Q_a} \theta_a^q(\mu) a^q(u,v) \tag{14}$$

for suitable parameter independent bilinear forms $a^q : (H^1(\Omega))^d \times (H^1(\Omega))^d \to \mathbb{R}$ and coefficients $\theta_a^q : \mathcal{P} \to \mathbb{R}$, which are readily derived from the constitutive equations. For instance, we have two terms per subdomain in the isotropic case. This leads to a fast online evaluation as the cost of the assembly of the parameter dependent reduced systems, i. e., matrices in $\mathbb{R}^{N\times N}$ associated with (13), is independent of $\mathcal{N}$. Note that the expansion (14) will also be exploited for an online-offline decomposition of the error estimators.

Apart from greedy methods, as already mentioned, POD techniques which yield the best reduced space, can be used in the context of parameter dependent eigenvalue problems with multiple output values. A detailed description of the usage of POD methods in the present context, can be found e. g. in [90, 128, 129].

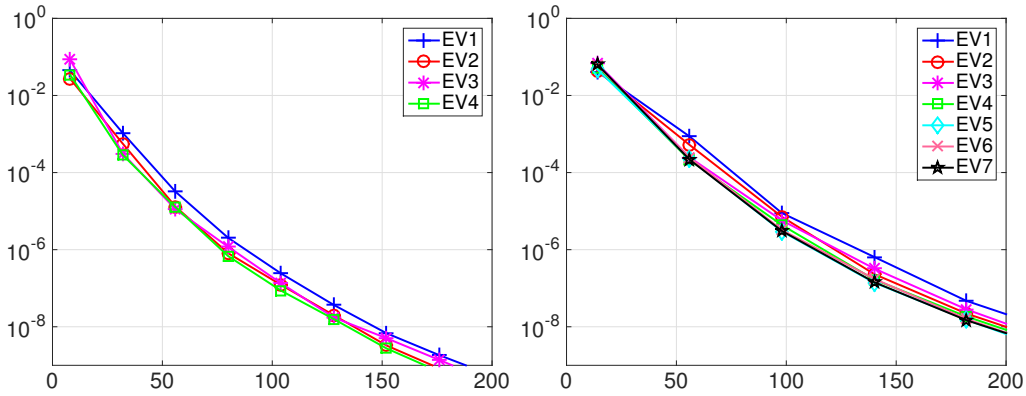

Figure 5.1: Convergence of POD methods ($0 < N \leq 200$) for the described μEVP with different numbers of outputs of interest: Average relative errors in the eigenvalues $\lambda_1, \ldots, \lambda_K$ for $K = 4$ (left) and $K = 7$ (right).

Figure 5.1 illustrates the convergence of the POD method for $K = 4$ and $K = 7$. The details of the underlying numerical experiment are elaborated in Section 5.4, where the numerical results are presented. On the one hand, the results show that it

is in principle possible to construct one single reduced space that effectively captures the parameter dependent behavior of the first K eigenfunctions simultaneously. On the other hand, it is evident that the reduced basis dimension N required for a certain accuracy increases with K. More precisely, the asymptotic decay of the error is approximately $C_4\,\mathrm{e}^{-0.0513\cdot N}$ for $K = 4$ and $C_7\,\mathrm{e}^{-0.0477\cdot N}$ for $K = 7$ for some constants C_4 and C_7. From the cost point of view the POD is quite expensive, and thus we focus on computationally efficient greedy strategies in combination with *a posteriori* error bounds.

In the following we will establish the analysis of an asymptotically reliable error estimator including the case of multiple eigenvalues and a series of algorithmic advancements. This constitutes a significant difference to the approach introduced in [60] as our goal is a reduced basis approximation not only of one eigenvalue, but of a series of eigenvalues, including eigenvalues with multiplicity greater than one. Furthermore our numerical results demonstrate that tailored greedy strategies yield very efficient reduced basis spaces for the simultaneous approximation of many eigenvalues for the considered problem class. In this context, the parameter dependence of the multiplicity of the eigenvalues constitutes a major challenge and is included into both our analysis and our algorithms.

Our experiments show that, in a greedy algorithm, it is usually not optimal to include the first K eigenfunctions for a particular parameter, neither is it advisable to choose the same number of eigenfunctions for different eigenvalues. This may be attributed to the fact that the smoothness of the input-output relation can vary strongly with the different outputs of interest, i. e., the eigenvalues. We rather suggest to choose maximizing parameters for K different error estimators. The reduced approximation should be of comparable quality for a broad range of frequencies, although in structural acoustics the accuracy requirements might decrease with increasing frequency. Note that, for the application scenario at hand, the number of desired eigenpairs is typically in the order of ten for simple components and even larger for geometrically more complex structures. We are interested in approximating the smallest eigenvalues "simultaneously" in the sense that a single reduced space is constructed for the variational approximation of the eigenvalue problem and that the individual *a posteriori* error estimators for the eigenvalues use the online components provided offline. This allows us to generate an efficient and accurate simultaneous reduced basis approximation. The large number of outputs of interest K justifies an increased computational effort by an increased dimension

N as compared to the standard single output case. In particular, any decent, i. e., sufficiently accurate, approximation needs $N \gg K$.

5.3. Error estimators

We will now establish *a posteriori* error estimators for our output quantities, in this case the eigenvalues. As mentioned above, it is important to determine such estimators in order to find out which basis functions should be selected by the greedy method. In particular, their computational evaluation must only depend on the basis size N but not on the dimension of the finite element space $\mathcal{N}$. To this end, we first derive error bounds that still depend on the finite element eigenvalues, and in particular on their multiplicities. Then, we focus on a computable approximation yielding the desired error estimators.

We will now introduce a generalized error bound. To this end let the parameter dependent energy norm be defined as $\|\cdot\|_{\mu;V_h} := a(\cdot,\cdot;\mu)^{\frac{1}{2}}$. In addition to a parameter dependent norm we are using a parameter independent norm defined as $\|\cdot\|_{\widehat{\mu};V_h} := \widehat{a}(\cdot,\cdot)^{\frac{1}{2}} := a(\cdot,\cdot;\widehat{\mu})^{\frac{1}{2}}$. For a linear functional $r : V_h \to \mathbb{R}$, we define the corresponding dual norms by

$$\|r\|_{\mu;V_h'} := \sup_{0\neq v\in V_h} \frac{r(v)}{\|v\|_{\mu;V_h}} \quad \text{and} \quad \|r\|_{\widehat{\mu};V_h'} := \sup_{0\neq v\in V_h} \frac{r(v)}{\|v\|_{\widehat{\mu};V_h}},$$

respectively. The analysis and the practical implementation employ different error representations, namely the so-called reconstructed errors w. r. t. the bilinear forms $a(\cdot,\cdot;\mu)$ and $\widehat{a}(\cdot,\cdot)$. Using the residual

$$v \mapsto r_i(v;\mu) := a(u_{\mathrm{red},\,i}(\mu), v;\mu) - \lambda_{\mathrm{red},\,i}(\mu)\, m(u_{\mathrm{red},\,i}(\mu), v)$$

for $i = 1,\ldots,N$, we define $e_i(\mu) \in V_h$ and $\widehat{e}_i(\mu) \in V_h$ by

$$a(e_i(\mu), v;\mu) = r_i(v;\mu), \quad v \in V_h \tag{15}$$

and

$$\widehat{a}(\widehat{e}_i(\mu), v) = r_i(v;\mu), \quad v \in V_h. \tag{16}$$

In particular, $\|r_i(\cdot;\mu)\|_{\mu;V_h'} = \|e_i(\mu)\|_{\mu;V_h}$ and $\|r_i(\cdot;\mu)\|_{\widehat{\mu};V_h'} = \|\widehat{e}_i(\mu)\|_{\widehat{\mu};V_h}$. For any $\mu \in \mathcal{P}$, assume that $g(\mu) > 0$ is a generalized coercivity constant such that $g(\mu)\hat{a}(v,v) \leq a(v,v;\mu)$ for all $v \in V_h$. Technically speaking, $g(\mu)$ is the parameter

dependent coercivity constant of $a(\cdot,\cdot;\mu)$ w. r. t. $\|\cdot\|_{\widehat{\mu};V_h}$. This implies

$$\|r\|_{\mu;V_h'} \leq g(\mu)^{-\frac{1}{2}} \|r\|_{\widehat{\mu};V_h'} \tag{17}$$

for any $r \in V_h'$ and

$$\|v\|_{\widehat{\mu};V_h} \leq g(\mu)^{-\frac{1}{2}} \|v\|_{\mu;V_h}$$

for any $v \in V_h$.

We are now ready to prove the error bounds. The following theorem, combined with the computational/algorithmic aspects in Section 5.4, generalizes the results of [104, 122, 123, 124] for the case of multiple eigenvalues.

Theorem 3. *Let $1 \leq i \leq L$ such that $k_i + q_i - 1 \leq N$. For $j = 1, \ldots, q_i$, set*

$$\tilde{d}_{k_i+j-1}(\mu) := \min_{\mathcal{N} \geq l > k_i+q_i-1} \left| \frac{\lambda_l(\mu) - \lambda_{\mathrm{red},\, k_i+j-1}(\mu)}{\lambda_l(\mu)} \right|. \tag{18}$$

Then,

$$0 \leq \lambda_{\mathrm{red},\, k_i+j-1}(\mu) - \lambda_{k_i}(\mu) \leq \frac{\|r_{k_i+j-1}(\cdot;\mu)\|^2_{\mu;V_h'}}{\tilde{d}_{k_i+j-1}(\mu)} \left(1 + \frac{\|r_{k_i+j-1}(\cdot;\mu)\|_{\mu;V_h'}}{\tilde{d}_{k_i+j-1}(\mu)^2 \sqrt{\lambda_{k_i}}}\right). \tag{19}$$

Proof. Fix $\mu \in \mathcal{P}$, $1 \leq i \leq L$ and $1 \leq j \leq q_i$. Let $u_{\mathrm{red},\, k_i+j-1}(\mu) = \sum_{l=1}^{\mathcal{N}} \alpha_l u_l(\mu)$ and $e_{k_i+j-1}(\mu) = \sum_{l=1}^{\mathcal{N}} \beta_l u_l(\mu)$. By (15), we find

$$\beta_l = \alpha_l \frac{\lambda_l(\mu) - \lambda_{\mathrm{red},\, k_i+j-1}(\mu)}{\lambda_l(\mu)}.$$

Therefore, we get

$$\begin{aligned}
\|r_{k_i+j-1}(\cdot;\mu)\|^2_{\mu;V_h'} &= \sum_{l=1}^{\mathcal{N}} \alpha_l^2 \left(\frac{\lambda_l(\mu) - \lambda_{\mathrm{red},\, k_i+j-1}(\mu)}{\lambda_l(\mu)} \right)^2 \lambda_l(\mu) \\
&\geq \sum_{l > k_i+q_i-1} \alpha_l^2 \left(\frac{\lambda_l(\mu) - \lambda_{\mathrm{red},\, k_i+j-1}(\mu)}{\lambda_l(\mu)} \right)^2 \lambda_l(\mu) \\
&\geq \tilde{d}_{k_i+j-1}(\mu)^2 \sum_{l > k_i+q_i-1} \alpha_l^2 \lambda_l(\mu).
\end{aligned} \tag{20}$$

Using the fact that $\sum_l \alpha_l^2 = 1$, $\lambda_l(\mu) \leq \lambda_{k_i}(\mu)$ for $l \leq k_i + q_i - 1$, we find for the

difference between approximated and detailed eigenvalue

$$\begin{aligned}
\Delta\lambda_{k_i} := \lambda_{\mathrm{red},\,k_i+j-1}(\mu) - \lambda_{k_i}(\mu) &= a(u_{\mathrm{red},\,k_i+j-1}(\mu), u_{\mathrm{red},\,k_i+j-1}(\mu);\mu) - \lambda_{k_i}(\mu) \\
&= \sum_{l=1}^{\mathcal{N}} \alpha_l^2 \lambda_l(\mu) - \lambda_{k_i}(\mu) \\
&= \sum_{l \le k_i+q_i-1} \alpha_l^2(\lambda_l(\mu) - \lambda_{k_i}(\mu)) \\
&\quad + \sum_{l > k_i+q_i-1} \alpha_l^2(\lambda_l(\mu) - \lambda_{k_i}(\mu)) \\
&\le \sum_{l > k_i+q_i-1} \alpha_l^2(\lambda_l(\mu) - \lambda_{k_i}(\mu)). \qquad (21)
\end{aligned}$$

From this we obtain two upper bounds for $\Delta\lambda_{k_i}$. The first one follows trivially from the fact that $\lambda_{k_i}(\mu) > 0$ and (20)

$$\Delta\lambda_{k_i} \le \sum_{l > k_i+q_i-1} \alpha_l^2 \lambda_l(\mu) \le \frac{\|r_{k_i+j-1}(\cdot;\mu)\|^2_{\mu;V_h'}}{\tilde{d}_{k_i+j-1}(\mu)^2}.$$

The second bound is based on the Cauchy-Schwarz inequality and on Young's inequality. In terms of

$$(\lambda_l(\mu) - \lambda_{k_i}(\mu))^2 \le (1+\epsilon)(\lambda_l(\mu) - \lambda_{\mathrm{red},\,k_i+j-1}(\mu))^2 + (1+\frac{1}{\epsilon})(\Delta\lambda_{k_i})^2$$

for $\epsilon > 0$, we get from (20) and (21)

$$\begin{aligned}
\Delta\lambda_{k_i} &= \sum_{l > k_i+q_i-1} \alpha_l \frac{\lambda_l(\mu) - \lambda_{k_i}(\mu)}{\lambda_l(\mu)} \sqrt{\lambda_l(\mu)} \alpha_l \sqrt{\lambda_l(\mu)} \\
&\le \left(\sum_{l > k_i+q_i-1} \alpha_l^2 (\frac{\lambda_l(\mu) - \lambda_{k_i}(\mu)}{\lambda_l(\mu)})^2 \lambda_l(\mu) \right)^{\frac{1}{2}} \left(\sum_{l > k_i+q_i-1} \alpha_l^2 \lambda_l(\mu) \right)^{\frac{1}{2}} \\
&\le \frac{1}{\tilde{d}_{k_i+j-1}(\mu)} \|r_{k_i+j-1}(\cdot;\mu)\|_{\mu;V_h'} \cdot \\
&\quad \sqrt{(1+\epsilon)\|r_{k_i+j-1}(\cdot;\mu)\|^2_{\mu;V_h'} + (1+\frac{1}{\epsilon})\Delta\lambda_{k_i}^2 \sum_{l > k_i+q_i-1} \alpha_l^2 \frac{1}{\lambda_l(\mu)}} \\
&\le \frac{1}{\tilde{d}_{k_i+j-1}(\mu)} \|r_{k_i+j-1}(\cdot;\mu)\|_{\mu;V_h'} \sqrt{(1+\epsilon)\|r_{k_i+j-1}(\cdot;\mu)\|^2_{\mu;V_h'} + (1+\frac{1}{\epsilon})\frac{\Delta\lambda_{k_i}^2}{\lambda_{k_i}(\mu)}} \\
&\le \frac{1}{\tilde{d}_{k_i+j-1}(\mu)} \|r_{k_i+j-1}(\cdot;\mu)\|^2_{\mu;V_h'} \sqrt{1+\epsilon+(1+\frac{1}{\epsilon})\frac{\|r_{k_i+j-1}(\cdot;\mu)\|^2_{\mu;V_h'}}{\tilde{d}_{k_i+j-1}(\mu)^4 \lambda_{k_i}(\mu)}}.
\end{aligned}$$

Setting $\epsilon = \frac{\left\|r_{k_i+j-1}(\cdot;\mu)\right\|_{\mu;V_h'}}{\tilde{d}_{k_i+j-1}(\mu)^2\sqrt{\lambda_{k_i}(\mu)}}$ gives the upper bound in (19). The lower bound follows directly from [10, Sect. 8].

□

Besides the generalization to multiple eigenvalues, let us point out that our bounds are sharper than the ones, e. g., in [124, Prop. 1], as the lowest order term in (19) is of the form $\frac{\left\|r_{k_i+j-1}(\cdot;\mu)\right\|^2_{\mu;V_h'}}{\tilde{d}_{k_i+j-1}(\mu)}$ rather than $\frac{\left\|r_{k_i+j-1}(\cdot;\mu)\right\|^2_{\mu;V_h'}}{\tilde{d}_{k_i+j-1}(\mu)^2}$. Note that the error bounds in Theorem 3 still depend on the finite element solution via the eigenvalues $\lambda_l(\mu)$ in (18).

Remark 5.2. *It is also possible to give an upper bound for the eigenvectors by replacing $\tilde{d}_{k_i+j-1}(\mu)$ by $\hat{d}_{k_i+j-1}(\mu)$ defined as*

$$\hat{d}_{k_i+j-1}(\mu) := \min_{\mathcal{N}\geq l>k_i+q_i-1 \vee l<k_i} \left|\frac{\lambda_l(\mu)-\lambda_{\mathrm{red},\,k_i+j-1}(\mu)}{\lambda_l(\mu)}\right|.$$

Using now $\Pi_i : V_h \to U_i(\mu)$ as the orthogonal projection w. r. t. the L^2-inner product, we define $\bar{v} := \Pi_i(u_{\mathrm{red},\,k_i+j-1}(\mu)) = \sum_{\mathcal{N}\geq l>k_i+q_i-1 \vee l<k_i} \alpha_l u_l(\mu)$ and give the upper bound as

$$\begin{aligned}\|u_{\mathrm{red},\,k_i+j-1}(\mu)-\bar{v}\|^2_{\mu;V_h} &= \left\|\sum_{\mathcal{N}\geq l>k_i+q_i-1 \vee l<k_i} \alpha_l u_l(\mu)\right\|^2_{\mu;V_h} \\ &= \sum_{\mathcal{N}\geq l>k_i+q_i-1 \vee l<k_i} \alpha_l^2\lambda_l(\mu) \leq \frac{\|r_{k_i+j-1}(\cdot;\mu)\|^2_{\mu;V_h'}}{\hat{d}_{k_i+j-1}(\mu)^2}.\end{aligned}$$

We now derive approximate error bounds that are computable in the sense that they do not depend on the finite element solution. To achieve this, it remains to approximate $\tilde{d}_i$, which may be interpreted as a measure for the relative distance between neighboring eigenvalues, particularly to decide which of the indices to exclude from the minimum. We point out that the dimension of the (detailed) eigenspace is not accessible. The application scenario we have in mind features multiple eigenvalues with their multiplicities depending on the parameter. It is therefore impossible to determine the structure of the spectrum, i. e., the indices k_i or the index sets $\mathcal{K}_i$, *a priori*.

Recall that the first K eigenvalues are the output quantities of interest. Assume that the reduced basis method converges in the following sense: For $\mu \in \mathcal{P}$ and $1 \leq i \leq K$,

$$\lambda_{\mathrm{red},\,i}(\mu) \to \lambda_i(\mu) \text{ for } N \to \mathcal{N}.$$

In particular, $\lambda_{\mathrm{red},\,j}(\mu) \to \lambda_{k_i}(\mu)$ for $N \to \mathcal{N}$ for $j \in \mathcal{K}_i$. Given the eigenvalues $\lambda_{\mathrm{red},\,i}(\mu)$, $i = 1, \ldots, K$, of (13), we replace $\lambda_l(\mu)$ in (18) by $\lambda_{\mathrm{red},\,l}(\mu)$ and approximate $\mathcal{K}_i$ by

$$\mathcal{K}_{\mathrm{red},\,i} := \left\{ 1 \leq j \leq K + \mathfrak{r};\ \left| \frac{\lambda_{\mathrm{red},\,j}(\mu) - \lambda_{\mathrm{red},\,i}(\mu)}{\lambda_{\mathrm{red},\,j}(\mu)} \right| < \varepsilon_\lambda \right\}$$

for a chosen tolerance $\varepsilon_\lambda > 0$ and with $\mathfrak{r}$ as the difference between the index of the first eigenvalue after the multiplicity of the K-th eigenvalue and the K-th eigenvalue itself. In the case that we know *a priori* the maximal multiplicity of all relevant eigenvalues for all parameters, we set $\mathfrak{r}$ equal to this value. Otherwise we select it adaptively during the initialization phase of the greedy method. More precisely, we start with $\mathfrak{r} = 1$ and increase it by one as long as $K + \mathfrak{r} \in \mathcal{K}_{\mathrm{red},\,i}$. Thus $\#\mathcal{K}_{\mathrm{red},\,i}$ will be our best guess for the multiplicity of the eigenvalue to which $\lambda_{\mathrm{red},\,i}(\mu)$ converges. Then for $1 \leq i \leq K$,

$$d_i(\mu) := \min_{\substack{l \notin \mathcal{K}_{\mathrm{red},\,i} \\ K+\mathfrak{r} \geq l > i}} \left| \frac{\lambda_{\mathrm{red},\,l}(\mu) - \lambda_{\mathrm{red},\,i}(\mu)}{\lambda_{\mathrm{red},\,l}(\mu)} \right| \tag{22}$$

is the relative distance of $\lambda_{\mathrm{red},\,i}(\mu)$ to the reduced eigenvalues that are further away than the chosen tolerance ε_λ. The adaptive selection of $\mathfrak{r}$ guarantees that, even for $i = K$ and multiple eigenvalues, $d_i(\mu)$ is easily computable and does not severely underestimate $\tilde{d}_i(\mu)$.

Finally, since we are looking for an asymptotic estimator for the relative error in the eigenvalues which is cheaply computable in the online-phase, we neglect the higher order term in (19). In addition, the parameter dependent norm $\|\cdot\|_{\mu;V_h'}$ is replaced by the parameter independent norm $\|\cdot\|_{\widehat{\mu};V_h'}$ by (17), which introduces an additional factor $g(\mu)^{-1}$.

To summarize we can state the following corollary:

Corollary 5.3. *Let $i = 1, \ldots, K$ and $\lambda_{\mathrm{red},\,i}(\mu) \to \lambda_i(\mu)$ for $N \to \mathcal{N}$. Furthermore let $\mathcal{K}_{\mathrm{red},\,i}$ be defined as above and the distance between neighboring eigenvalues $d_i(\mu)$ be given as in (22). Then the error estimator given by*

$$\mu \mapsto \eta_i(\mu) := \frac{\|r_i(\cdot;\mu)\|^2_{\widehat{\mu};V_h'}}{g(\mu) \cdot d_i(\mu) \cdot \lambda_{\mathrm{red},\,i}(\mu)} \tag{23}$$

is asymptotically reliable in the sense that

$$0 \leq \frac{\lambda_{\mathrm{red},\,k_i+j-1}(\mu) - \lambda_{k_i}(\mu)}{\lambda_{k_i}} \leq C\eta_i(\mu),$$

with C tending to one as N tends to $\mathcal{N}$.

Note that the approximation in (22) is, in general, less accurate for $i = K$. This is because the space V_N is built to approximate well the K outputs, but for the K-th estimator we need the $(K+\mathfrak{r})$-th outputs with $\mathfrak{r} \geq 1$, which are approximated only roughly. The tolerance ε_λ has to be selected such that it reflects the desired accuracy of the reduced basis approximation.

All error estimator contributions may be decomposed as already outlined in [104]. Let $(\zeta_n)_{1\leq n\leq N}$ be the orthonormal basis (w. r. t. $m(\cdot,\cdot)$) of V_N. For $0 \leq q, p \leq Q$ let $\widehat{A}^{q,p} \in \mathbb{R}^{N\times N}$ with $\widehat{A}^{q,p}_{n,m} := \widehat{a}(\xi^q_n, \xi^p_m)$ for $1 \leq n, m \leq N$ where

$$\widehat{a}(\xi^q_n, v) = a^q(\zeta_n, v), \quad v \in V_h,\ 1 \leq n \leq N,\ 1 \leq q \leq Q, \tag{24}$$

and

$$\widehat{a}(\xi^0_n, v) = m(\zeta_n, v), \quad v \in V_h,\ 1 \leq n \leq N. \tag{25}$$

In the following, we identify the function $u_{\mathrm{red},\,i}(\mu) \in V_N$ and its vector representation w. r. t. the basis $(\zeta_n)_{1\leq n\leq N}$ such that $(u_{\mathrm{red},\,i}(\mu))_n$ denotes the n-th coefficient. Then, given a reduced eigenpair $(u_{\mathrm{red},\,i}(\mu), \lambda_{\mathrm{red},\,i}(\mu))$, we have the error representation

$$\widehat{e}_i(\mu) = \sum_{n=1}^{N}\sum_{q=1}^{Q_a} \theta^q_a(\mu)\,(u_{\mathrm{red},\,i}(\mu))_n\,\xi^q_n - \lambda_{\mathrm{red},\,i}(\mu)\sum_{n=1}^{N}(u_{\mathrm{red},\,i}(\mu))_n\,\xi^0_n$$

by (16). Consequently, the main contribution of $\eta_i(\mu)$ decomposes into

$$\begin{aligned}\|r_i(\cdot;\mu)\|^2_{\widehat{\mu};V_h'} = &\sum_{n=1}^{N}\sum_{m=1}^{N}\sum_{q=1}^{Q_a}\sum_{p=1}^{Q_a}(u_{\mathrm{red},\,i}(\mu))_n\,(u_{\mathrm{red},\,i}(\mu))_m\,\theta^q_a(\mu)\theta^p_a(\mu)\,\widehat{A}^{q,p}_{n,m}\\ &+\lambda^2_{\mathrm{red},\,i}(\mu)\sum_{n=1}^{N}\sum_{m=1}^{N}(u_{\mathrm{red},\,i}(\mu))_n\,(u_{\mathrm{red},\,i}(\mu))_m\,\widehat{A}^{0,0}_{n,m}\\ &-2\,\lambda_{\mathrm{red},\,i}(\mu)\sum_{n=1}^{N}\sum_{m=1}^{N}\sum_{q=1}^{Q_a}(u_{\mathrm{red},\,i}(\mu))_n\,(u_{\mathrm{red},\,i}(\mu))_m\,\theta^q_a(\mu)\,\widehat{A}^{q,0}_{n,m}.\end{aligned}$$

We recall that only a single reduced space is built for the approximation of all eigenvectors simultaneously. Thus the above decomposition uses the same offline

ingredients for all $1 \leq i \leq K$. In particular, the number K of desired eigenpairs does not directly influence the complexity (only via the reduced space dimension N).

5.4. Algorithms

In this section, we present different greedy strategies that employ the error estimators of Section 5.3 to build the reduced space in (12). The advantage compared to the POD method is that only relatively few finite element solutions of the μEVP need to be computed. Since we use a single space for the approximation of multiple outputs, we have several natural possibilities which are investigated in the following. Furthermore an extension that takes into account multiple eigenvalues is presented and a remedy for the potential unreliability of the error estimators for small N is discussed.

Recall that the K smallest eigenvalues are the quantities of interest, where K is typically $2 - 20$ for our application scenario. In principle, given a reduced space, one could try to identify a suitable $\mu \in \mathcal{P}$ and then include the first K eigenfunctions for this parameter value. In each greedy step, this would require the detailed finite element solution of (11) for one parameter only. However, numerical studies clearly show that this naive choice is far from optimal as the generated reduced spaces tend to be much too large. This is because the errors in the individual eigenvalues and eigenfunctions are only very weakly correlated, if at all. There are at least the following two much more natural options: Let a sufficiently rich training set $\Xi_{\text{train}} \subset \mathcal{P}$ be given. Then, in Algorithm 1, the individual $\arg\max$ for each $1 \leq i \leq K$ is chosen separately. In contrast, Algorithm 2 chooses only one single $\arg\max$. Note that both Algorithm 1 (line 7) and Algorithm 2 (line 6) require the evaluation of all error estimators at all parameters in Ξ_{train} to determine the choice of μ. This does not lead to large computations since the calculations are only performed with the reduced space of size N, such that we obtain K reduced eigenpairs for any $\mu \in \Xi_{\text{train}}$, see also Section 5.3. However, Algorithm 1 (line 10) and Algorithm 2 (line 8) require also finite element solutions which then determine the reduced basis space. The multi-choice variant rests on the intuition that the individual eigenfunctions can and should be approximated separately. In contrast, the single choice variant takes into account that the approximation power of eigenfunctions to large eigenvalues can be exploited also for eigenfunctions to smaller eigenvalues. During the greedy procedure, we orthonormalize the selected

Algorithm 1 Multi-choice greedy

1: **for** $i = 1, \dots, K$ **do**
2: $\quad \zeta_i \leftarrow u_i(\widehat{\mu})$
3: **end for**
4: $N \leftarrow K$
5: **while** $N < N_{\max}$ **do**
6: $\quad$ **for** $i = 1, \dots, K$ **do**
7: $\quad\quad \mu_{\max,i} \leftarrow \arg\max_{\mu \in \Xi_{\text{train}}} \eta_i(\mu)$
8: $\quad\quad$ **if** $\eta_i(\mu_{\max,i}) > \varepsilon_{\text{tol}}$ **then**
9: $\quad\quad\quad N \leftarrow N + 1$
10: $\quad\quad\quad \zeta_N \leftarrow u_i(\mu_{\max,i})$ (orthonormalized)
11: $\quad\quad$ **end if**
12: $\quad$ **end for**
13: $\quad$ **if** $\max_{\mu \in \Xi_{\text{train}}, 1 \le i \le K} \eta_i(\mu) < \varepsilon_{\text{tol}}$ **then**
14: $\quad\quad$ **break**
15: $\quad$ **end if**
16: **end while**

Algorithm 2 Single-choice greedy

1: **for** $i = 1, \dots, K$ **do**
2: $\quad \zeta_i \leftarrow u_i(\widehat{\mu})$
3: **end for**
4: $N \leftarrow K$
5: **while** $N < N_{\max}$ **do**
6: $\quad (\mu_{\max}, i_{\max}) \leftarrow \arg\max_{\mu \in \Xi_{\text{train}}, 1 \le i \le K} \eta_i(\mu)$
7: $\quad N \leftarrow N + 1$
8: $\quad \zeta_N \leftarrow u_{i_{\max}}(\mu_{\max})$ (orthonormalized)
9: $\quad$ **if** $\max_{\mu \in \Xi_{\text{train}}, 1 \le i \le K} \eta_i(\mu) < \varepsilon_{\text{tol}}$ **then**
10: $\quad\quad$ **break**
11: $\quad$ **end if**
12: **end while**

basis functions. Not only does this yield small condition numbers of the reduced systems, it is also beneficial for the special treatment of multiple eigenvalues described in the next section.

In Algorithm 1 (line 10) and Algorithm 2 (line 8), an orthonormalization is performed. For this purpose, let $\Pi_N : V_h \to V_N$ be the L^2-orthogonal projection to the current reduced space. For a snapshot candidate $\zeta \in V_h$, i.e., one of the eigenfunctions chosen as described above, we compute $\tilde{\zeta} := \zeta - \Pi_N \zeta$. Then, if $\|\tilde{\zeta}\|_0$ is sufficiently large ($\ge \varepsilon_{\text{proj}}$), the new contribution $\frac{\tilde{\zeta}}{\|\tilde{\zeta}\|_0}$ is included in the reduced basis. In case of multiple eigenvalues, the greedy method needs to be modified as follows: Assume an index $1 \le \tilde{\imath} \le K$ and a parameter μ^* have been selected by

means of the eigenvalue-based estimators $(\eta_i)_{i=1,\dots,K}$, in Algorithm 2 (line 6), or several parameters μ^* have been selected in Algorithm 1 (line 7), such that the span of $u_{\tilde{\imath}}(\mu^*)$ is to be included in the reduced space. However, a large value of $\eta_{\tilde{\imath}}(\mu^*)$ merely indicates that the corresponding (fine) eigenspace $U_{\tilde{\imath}}(\mu^*)$ contains functions that are badly approximated by the current reduced space. Nevertheless the eigenspace might also contain other functions that are already well approximated. Consequently, if the detailed eigenvalue associated with a chosen snapshot has multiplicity greater than one, we aim to add all the eigenfunctions for the multiple eigenvalue, except the ones which are already approximated well enough. A motivation for exploring the whole eigenspace for multiple eigenvalues is to guarantee that we take the correct eigenvalue/eigenfunction, since we cannot ensure that the indexed eigenvalue/eigenfunction in the reduced space is the same as in the detailed calculation. This is due to the fact that there is no prescribed ordering for the eigenfunctions corresponding to a multiple eigenvalue.

As for the definition of $d_i(\mu)$, one has to compute a sufficient number $K' > K$ of eigenfunctions of the finite element problem μEVP (11) such that

$$\lambda_{K'}(\mu^*)/\lambda_K(\mu^*) > 1 + \varepsilon_\lambda.$$

Then, lines 9–10 in Algorithm 1 are replaced by:

---

for all $j \geq 1$ **with** $|\lambda_j(\mu_{\max,i}) - \lambda_i(\mu_{\max,i})|/\lambda_i(\mu_{\max,i}) \leq \varepsilon_\lambda$ **do**
  if $\|u_j(\mu_{\max,i}) - \Pi_N u_j(\mu_{\max,i})\|_{L^2(\Omega)} \geq \varepsilon_{\text{proj}}$ **then**
    $N \leftarrow N + 1$
    $\zeta_N \leftarrow u_j(\mu_{\max,i})$ (orthonormalized)
  end if
end for

Analogously, lines 7–8 in Algorithm 2 now read as:

---

for all $j \geq 1$ **with** $|\lambda_j(\mu_{\max}) - \lambda_{i_{\max}}(\mu_{\max})|/\lambda_{i_{\max}}(\mu_{\max}) \leq \varepsilon_\lambda$ **do**
  if $\|u_j(\mu_{\max}) - \Pi_N u_j(\mu_{\max})\|_{L^2(\Omega)} \geq \varepsilon_{\text{proj}}$ **then**
    $N \leftarrow N + 1$
    $\zeta_N \leftarrow u_j(\mu_{\max})$ (orthonormalized)
  end if
end for

Here, $\Pi_N : V_h \to V_N$ denotes the L^2-orthogonal projection. The parameter $\varepsilon_{\text{proj}}$ is a small tolerance that prevents the selection of functions that are already approximated sufficiently well.

In our calculations, we need as already mentioned an error estimator for the K-th eigenvalue. For the computation of this estimator, we need a rough approximation of the $(K + \mathfrak{r})$-th eigenvalue. In order to ensure that our reduced space has the ability to roughly approximate this $(K+\mathfrak{r})$-th eigenvalue, we use an initial approximation space in which we include the corresponding components. We suggest to include components using the proper orthogonal decomposition method described in Section 5.1 (with $N = N_{\text{init}}$) applied to a small number of snapshots. Here, the snapshots $S \subset V_h$ are associated with a training set $\Xi_{\text{train}}^{\text{POD}}$ typically of size 2^P, taking into account the extension described above. This initial approximation space of dimension N_{init}, which is constructed as an initialization step for the greedy algorithm, should be sufficiently large as the reliability of the error estimators analyzed in Section 5.3 can depend on the dimension of the reduced space. To make sure that we are able to calculate and to approximate the $(K + \mathfrak{r})$-th eigenvalues, we choose our N_{init} to be at least $(K + \mathfrak{r})$ times a factor ≥ 1.5.

In the following, the performance of the proposed algorithms is illustrated by numerical examples, in two and in three dimensions. For the two-dimensional calculations we use plane strain elasticity while for the three-dimensional simulations we use linear elasticity. The implementation is performed in MATLAB based on the RBmatlab library [50]. We investigate the individual components and highlight their benefits in several steps. All following examples contain multiple eigenvalues.

First we choose Ω as a rectangle of size 3.0×1.0 with Dirichlet boundary on the left and on the right. Let Ω be split into three subdomains of size 1.0×1.0. The material parameters E and ν used for these subdomains are in the range of $10 - 100$ and $0.1 - 0.4$, respectively; we have $P = 6$ and $Q = 6$. We choose a uniform random sample of size 10000 as set of training parameters $\Xi_{\text{train}} \subset \mathcal{P}$. To evaluate the errors, another sufficiently rich set of parameters $\Xi_{\text{test}} \subset \mathcal{P}$ is used of size 1000. For our initial space we choose $N_{\text{init}} \leq 40$, depending on the desired number of eigenvalues K. We always report the average errors of the reduced approximations given by

$$\frac{1}{\#\Xi_{\text{test}}} \sum_{\mu \in \Xi_{\text{test}}} \frac{\lambda_{\text{red},\,i}(\mu) - \lambda_i(\mu)}{\lambda_i(\mu)}$$

and comment on the standard deviation in Remark 5.4.

For the generalized coercivity estimate, we exploit the affine decomposition of the

bilinear form and set

$$g(\mu) := \min_{q=1,\dots,Q_a} \frac{\theta_a^q(\mu)}{\theta_a^q(\widehat{\mu})}. \tag{26}$$

We emphasize that $g(\mu)$ merely relates the bilinear forms $a(\cdot,\cdot;\mu)$ and $\widehat{a}(\cdot,\cdot)$; a coercivity estimate for $a(\cdot,\cdot;\mu)$ itself is not required in the present context. Note that (26) indeed yields an admissible parameter dependent constant provided the bilinear forms $a^q(\cdot,\cdot)$ in (14) are positive semi-definite and the coefficient functions $\theta^q(\cdot)$ in (14) are positive; see, e. g., [121, Sect. 4.2.2]. This is true for our application. Better results, i. e., a larger lower bound, could be obtained by the more expensive successive constraint method [86]. In the present setting, the estimate (26) is typically smaller than the exact solution of the corresponding generalized eigenvalue problem by a factor ranging from 0.7 to 0.98.

We first illustrate the necessity of the extended selection for multiple eigenvalues. Figure 5.2 shows the behavior of a POD method with (left) and without (right) the extended selection for the first two eigenvalues ($K = 2$). Figure 5.3 shows the same comparison for the greedy method (Algorithm 2). For both the POD method and the greedy method, we observe that in the variants without extension the convergence for the second eigenvalue becomes slower after a certain number of basis functions has been included. In contrast, the extended selection yields convergence curves that approximately coincide. The shortcomings of the non-extended methods may be explained by the fact that the second eigenvalue has multiplicity two for certain parameters and in these cases, for the multiple eigenvalue, the correct eigenfunction is not necessarily chosen. Note that the effect is more significant for a smaller POD training size (Figure 5.2, second row) as it is less likely that all directions of an eigenspace are present in the snapshot set. The convergence of the second reduced eigenvalue possibly improves drastically if, incidentally, the missing component is added during the greedy method.

Next, we illustrate the benefit of Algorithm 2 in comparison to Algorithm 1. In Figure 5.4, for $K = 4$, one can see that with Algorithm 1 (left) the convergence behavior varies over the course of the greedy method while with Algorithm 2 (right) all desired eigenvalues exhibit similar convergence. This also holds true for the errors in the eigenfunctions not shown here. The poor convergence of the third eigenvalue only improves rapidly at $N \approx 170$, after the other three eigenvalues have reached an accuracy in the order of the target tolerance, and thus the algorithm only chooses eigenvalue 3. This effect, namely an imbalanced resolution of the rele-

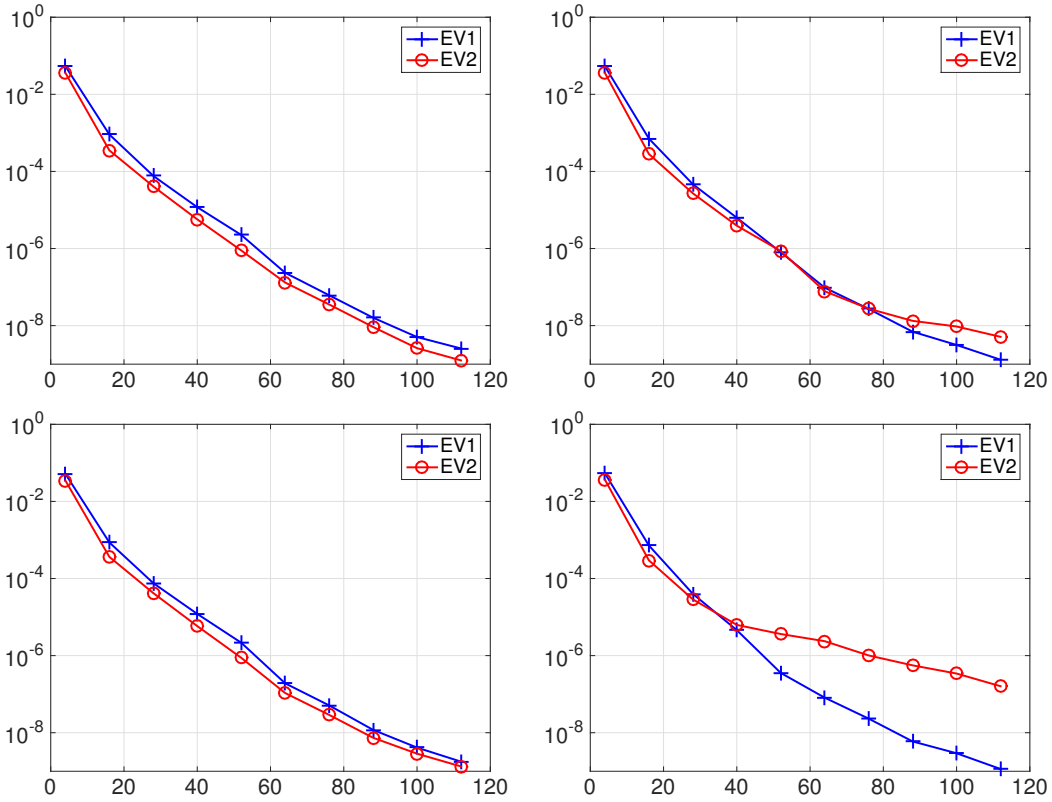

Figure 5.2: Error decay for the eigenvalues with the POD method: Extended (left) vs. non-extended (right). First row: Training size 10000. Second row: Training size 1000.

vant eigenspaces during the greedy method, is directly related to the inappropriate *a priori* assumption of Algorithm 1 that roughly the same number of snapshots corresponding to the first K eigenvalues should be included in the reduced space. At this point it should also be noted that in general Algorithm 1 creates a larger reduced basis space than Algorithm 2 as soon as more eigenvalues have a poor convergence.

To further illustrate the behavior of the single-choice greedy method, in Figure 5.5, we report the accumulated numbers of chosen eigenfunctions corresponding to $\lambda_1, \ldots, \lambda_K$ over the course of Algorithm 2 for $K = 4$ and $K = 7$ (first row), as selected by the error estimators in line 6. The reason for the greedy algorithm not selecting any eigenfunctions before a basis size of 40 is that this is the size of our initial space. The respective error decay for $K = 7$ is depicted in Figure 5.5 (second row). Note that the good convergence (in particular, similar rates for all outputs of interest simultaneously) is achieved by a rather uneven distribution. The diagrams indicate that, for both values of K, larger eigenvalues as well as possibly double

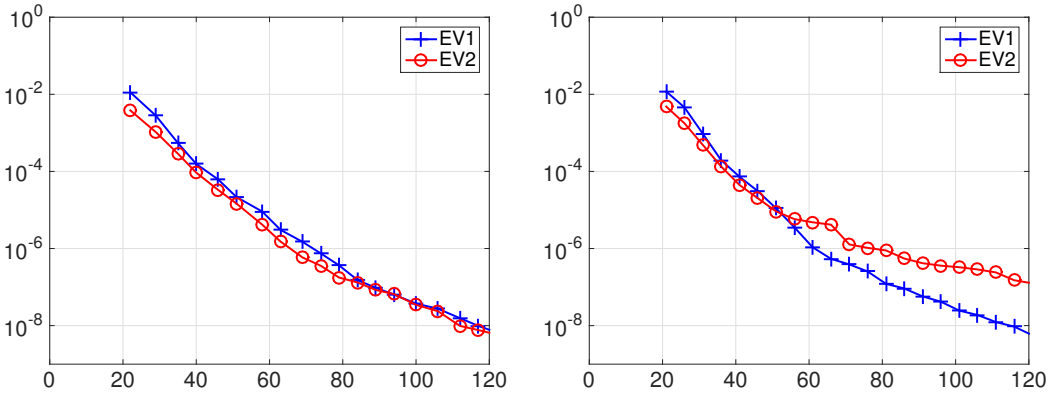

Figure 5.3: Error decay for eigenvalues with the greedy method. Extended (left) vs. non-extended (right): Training size 1000.

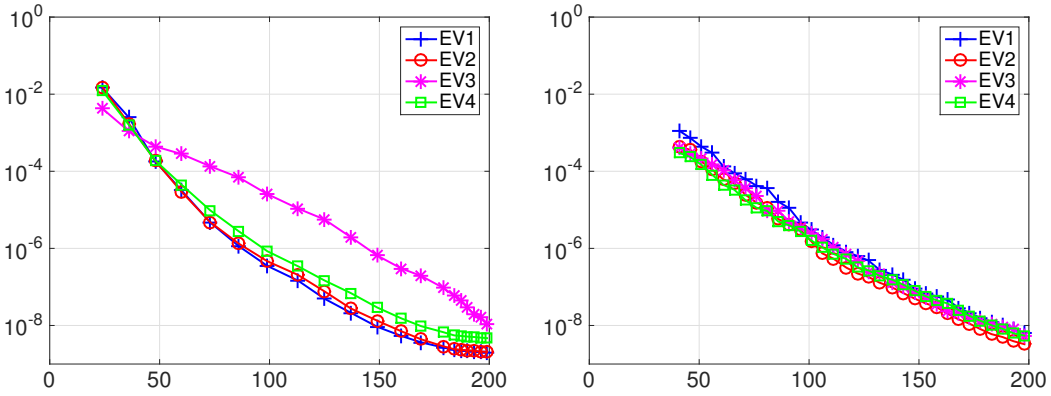

Figure 5.4: RB error decay: Comparison of Algorithm 1 (left) and Algorithm 2 (right) for $K = 4$.

eigenvalues are preferred by the algorithm. This and the fact that, although fewer eigenfunctions are included for the smaller eigenvalues than for the larger ones, but nevertheless the error decay is equal, mean that the eigenfunctions corresponding to larger eigenvalues are effectively used to approximate the ones corresponding to smaller eigenvalues.

We now investigate the performance of the greedy method in more detail. For this purpose, we also consider the effectivity numbers γ_i, $1 \leq i \leq K$, of the error estimators and its maximal ratio R defined by

$$\gamma_i := \frac{1}{\#\Xi_{\text{test}}} \sum_{\mu \in \Xi_{\text{test}}} \frac{\eta_i(\mu) \cdot \lambda_i(\mu)}{\lambda_{\text{red},\,i}(\mu) - \lambda_i(\mu)}, \qquad R := \frac{\max_{i=1,\ldots,K} \gamma_i}{\min_{i=1,\ldots,K} \gamma_i}.$$

As already mentioned, the estimators derived in Section 5.3 are of asymptotic character and therefore generally not reliable for small N. To prevent a misleading

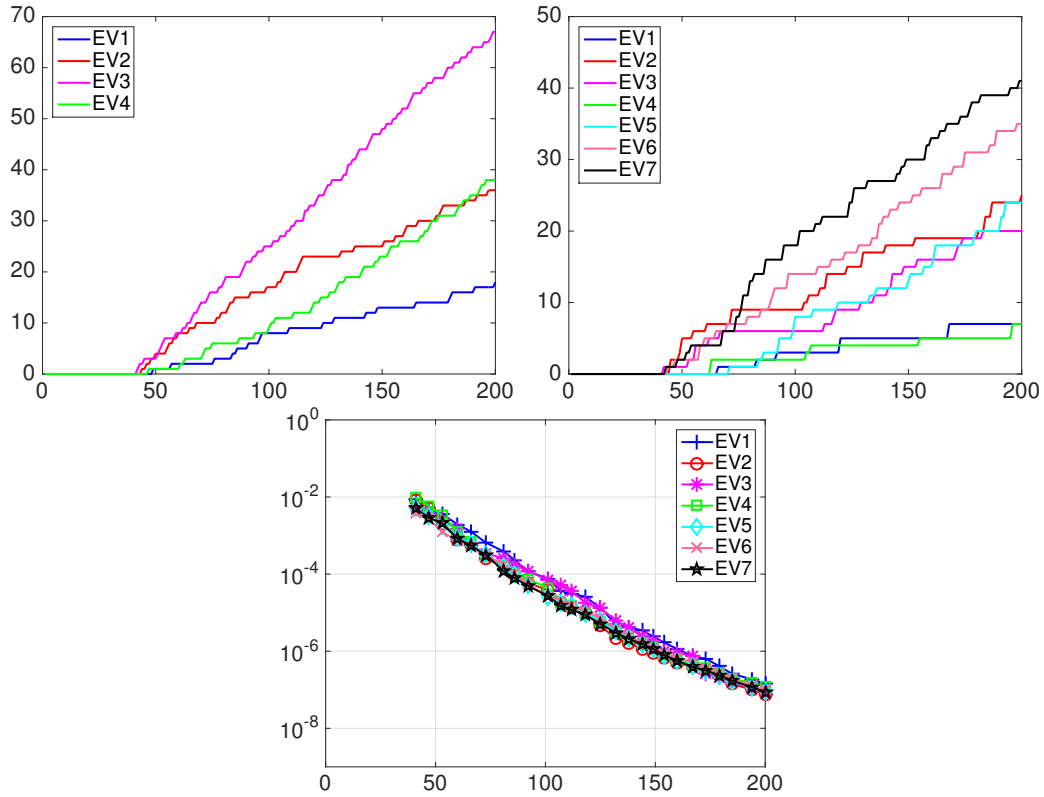

Figure 5.5: First row: Accumulated numbers of chosen eigenfunctions over the course of Algorithm 2 for $K = 4$ and $K = 7$. Second row: Error decay for $K = 7$.

selection of basis functions in the first few greedy steps, the initialization is used to generate an initial basis.

Figure 5.6 shows the error decay (left), the effectivity numbers of the *a posteriori* estimators (center) and the accumulated index counts (right) for $K = 5$ with and without the initialization. In this case, a similar convergence is achieved for both algorithms, and the index count plots also show a similar behavior. In the pre-asymptotic range, we observe a difference in the effectivity numbers. Without initialization these numbers possibly depend sensitively on the selected snapshots. While this does not influence the overall performance for $K = 5$, for $K = 7$ we do get extremely poor results if we start directly with the greedy algorithm. This is caused by the fact that the approximation of $\tilde{d}_i(\mu)$ by $d_i(\mu)$ is then not reliable. Thus we always include the initialization step in our adaptive algorithms. In our experiments, the described initialization always prevents the effectivity numbers from having jumps and leads to good convergence of the greedy methods. For instance, Figure 5.7 shows the effectivity measures corresponding to the error curves

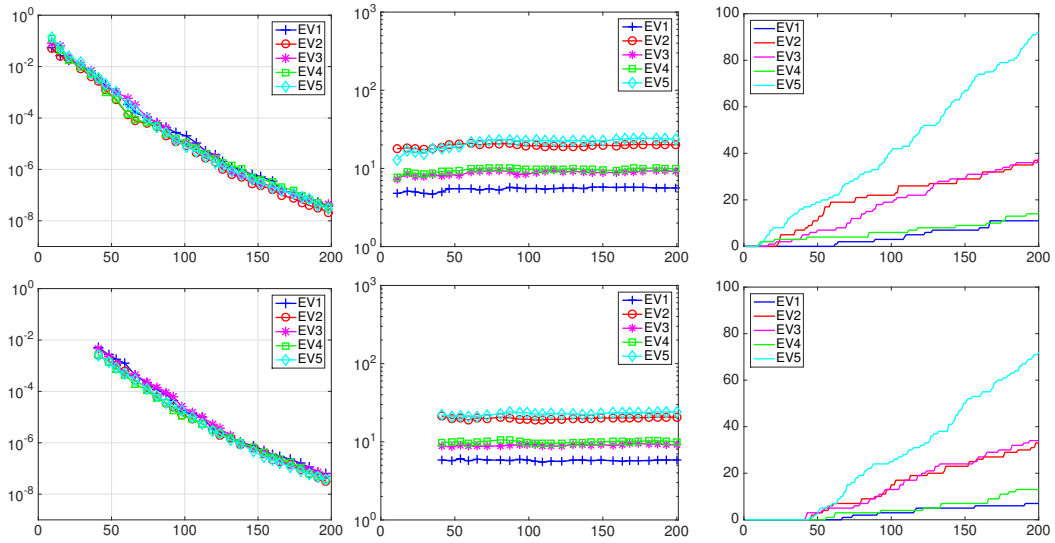

Figure 5.6: Comparison of Algorithm 2 without (top) and with (bottom) the initialization described above for $K = 5$ for a selected case in which the greedy algorithm without initialization does not fail. RB error decay (left), effectivity numbers (center) and accumulated index counts (right).

from Figure 5.4 (right) and Figure 5.5 (second row). The effectivities are virtually constant and close together, which is reflected in a small value of R. This is of crucial importance for the performance of our Algorithm 2. In all our settings R is below five, e. g., $R = 3.41$ for $K = 4$. Note that for $K = 4$ and $K = 7$, the same eigenvalues show similar effectivities. A high effectivity ratio R possibly leads to an oversampling of the eigenfunctions associated with the indices of a high effectivity and thus a loss in the performance. At this point, although our error estimators are for eigenvalues, we want to show that also the effectivities for the eigenvectors are constant and close together. To do so we depict the results in Figure 5.8.

After having demonstrated the performance of the single components of our algorithm, let us compare the results of our greedy method using the error estimator and the best components with the convergence of the POD method. Comparing the error plots in Figure 5.1 with the ones in Figure 5.4 (right) and Figure 5.5 (right), we see that we achieve very similar convergence behavior. In particular, the error curves of our simultaneous reduced basis approximation for the individual eigenvalues are similarly close to each other. Moreover, the accuracy reached at $N \approx 200$ differs only by a factor of roughly ten. We recall that the POD method uses the full training set (namely 10000 finite element solutions in this case which leads to a computation time of over 10 h) to reach this accuracy while the greedy

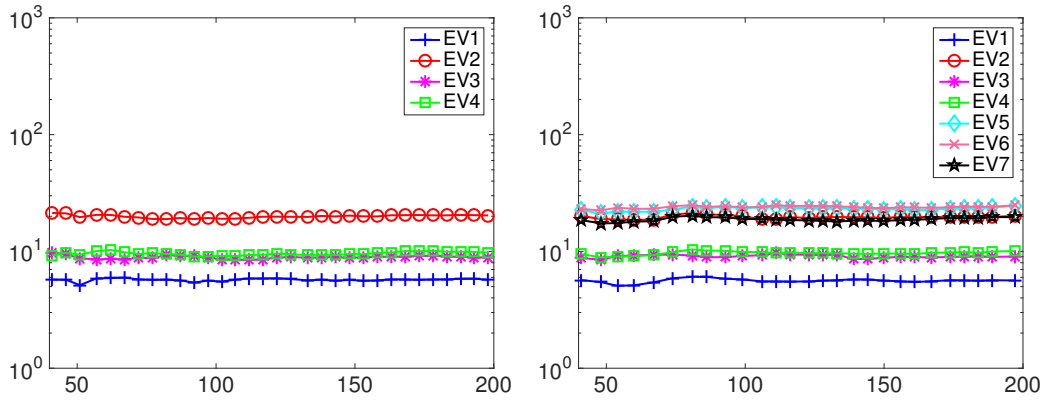

Figure 5.7: Effectivity numbers of the estimators for $K = 4$ (left) and $K = 7$ (right).

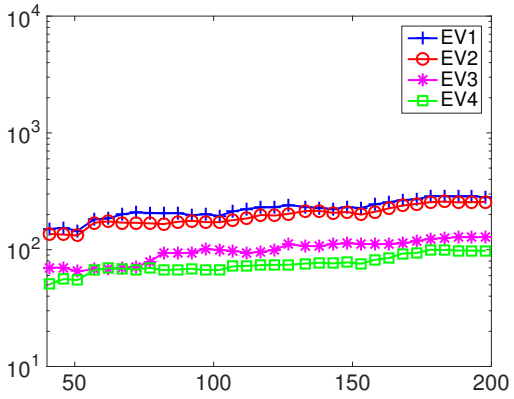

Figure 5.8: Effectivity numbers for the eigenfunctions for $K = 4$.

method only needs a couple of hundred detailed simulations and the evaluation of the estimator, which leads in this case to a computation time of 6-7 h. It should be noted that this gap in computation time between POD and greedy increases further with the complexity of the detailed solution. Let us emphasize that the bounds from [124], i.e., $d_i(\mu)^2$ in the denominator of (23) instead of $d_i(\mu)$, lead to a large ratio of the maximal and minimal effectivity value and thus to poorer results in the multiple output case. Highly different effectivity numbers result in an over-selection of eigenfunctions associated with the largest effectivity numbers and thus in a performance loss, hence, to a much less attractive greedy algorithm.

Remark 5.4 (Error evaluation)**.** *For completeness, Figure 5.9 shows a convergence plot including the standard deviation for $K = 6$. In the semilogarithmic plots, one can see that the standard deviation is always in the order of the (relative) discretization error itself.*

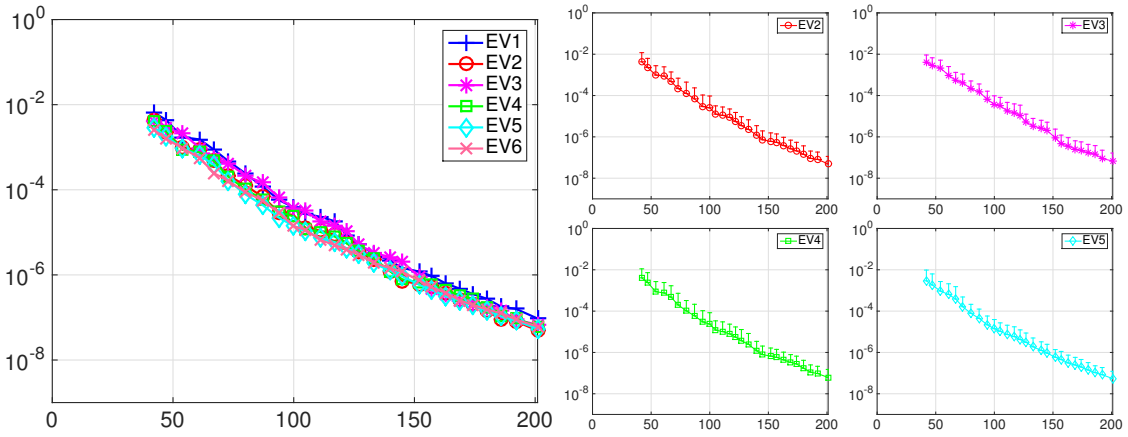

Figure 5.9: RB discretization error for $K = 6$ with standard deviation (as unidirectional error bar) for EV 2 to EV 5.

In the following, we show the speed-up, which is calculated serially using MATLAB on a Macbook laptop; the standard routine *eigs*, which is based on ARPACK [99], was used for solving the eigenvalue problems. We used linear finite elements for the discretization space V_h. With our greedy method as introduced above, a significant speed-up in the computation of eigenvalues can be achieved, as is shown for the settings of $K = 2$ to $K = 7$ eigenvalues in Table 5.1. Here, the calculation of the detailed solutions takes in the range of 3.5 to 3.6 seconds, while the calculation of the reduced solution is possible in 0.021 to 0.078 seconds, resulting in a speed-up of 140 to 43. The higher the value of N, the longer the reconstruction time, but in this case the increase is approximately linear in N. Moreover, it should be noted that the more accurately the detailed solution is calculated, the more expensive the detailed calculation becomes while the cost for the calculation of the reduced basis solution will stay in the same range, such that we would achieve even higher speed-ups. In computations of practical relevance, the detailed and the reduced accuracies have to be adjusted as it is described in [180]. Here we are mostly interested in the performance of the reduced basis algorithm, and thus we work with a fixed moderate finite element resolution of 15402 DoFs.

As can be seen in Table 5.2, the computation times for the error estimators (η) as well as for the required offline components for the error estimators, i. e., solutions of (24) and (25) ("assembly") and computation of $\widehat{A}$, increase for increasing values of N. In the case of $\widehat{A}$, the increase is approximately linear. Note that these longer computations will only have to be performed in the offline phase and will not have any impact on the computation times for the online phase. The computation of $g(\mu)$ as defined in (26) is necessary for the error estimator and takes 0.0042 seconds.

K	2				4				7			
N	50	100	150	200	50	100	150	200	50	100	150	200
Detailed solution	3.5				3.5				3.6			
Reduced solution	0.025	0.028	-	-	0.037	0.043	0.050	0.055	0.057	0.067	0.075	0.082
Reconstruction	0.009	0.011	-	-	0.009	0.012	0.016	0.019	0.010	0.013	0.018	0.021
Speed-up	140	125	-	-	94	81	70	63	63	53	48	43

Table 5.1: Timings for the detailed solution and the online calculations (reduced solution including error estimation; reconstruction of the finite element solution from the reduced solution) in seconds and speed-up numbers.

N	η	$\widehat{A}$	Assembly
50	0.0028	1.3672	6.076
100	0.0037	2.7640	6.156
150	0.0040	4.1144	6.272
200	0.0046	5.5995	6.312

Table 5.2: Timings for single components of the offline phase in seconds.

5.5. Application to complex geometries

Furthermore we show the ability of the newly developed reduced basis method to approximate multiple eigenvalues in a two-dimensional wall-slab configuration with a thin elastomer layer in between. The first domain shape is an L-shape with three non-overlapping subdomains representing the wall, the elastomer and the slab, denoted by Ω_1, Ω_2 and Ω_3, respectively. The corresponding domains are chosen as $\Omega_1 = [0,1] \times [0,2.8]$, $\Omega_2 = [0,1] \times [2.8,3]$ and $\Omega_3 = [0,3] \times [3,4]$. We again used standard linear finite elements with 30702 DoFs for these calculations. The material parameters E and ν are chosen as $E \in [10,100]$ and $\nu \in [0.1,0.4]$. Since we aim for large numbers of eigenvalues, we perform our simulations for $K = 20$. Figure 5.10 shows that we do not only obtain very good convergence for the eigenvalues (left) but also for the corresponding eigenfunctions (right). The error curves chosen to be represented in Figure 5.10 are representative examples for the eigenvalue and eigenfunction errors in the wall-slab configuration, while the black lines denote the minimum and the maximum of the averaged errors over the $\mu \in \Xi_{\text{test}}$, respectively. The speed-up is similar to the one analyzed in detail above. For the wall-slab configuration, we show in Table 5.3 the computation times in the case of $K = 20$ eigenvalues. As can be seen, the computation of the detailed solution takes 14.03 seconds, while the computations of the reduced solutions take between 0.14 and 0.24 seconds, depending on the basis size N. This results in a speed-up of 100 for $N = 50$ to 58 if we take $N = 300$ for an accuracy of 10^{-7}.

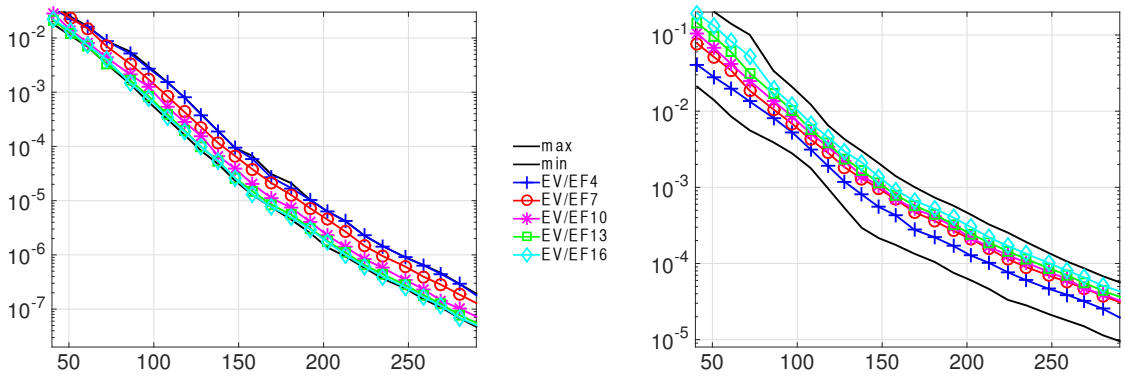

Figure 5.10: Wall-slab configuration with thin elastomer: Reduced basis error of eigenvalues (left) and eigenfunctions (right).

K	20					
N	50	100	150	200	250	300
Detailed solution	14.03					
Reduced solution	0.14	0.16	0.18	0.19	0.22	0.24
Reconstruction	0.027	0.035	0.041	0.049	0.054	0.065
Speed-up	100	87	78	73	63	58

Table 5.3: Timings for the detailed solution and the online calculations (reduced solution including error estimation; reconstruction of the finite element solution from the reduced solution) for a slab-wall configuration in seconds.

As the second domain we consider now a more complex one, targeted towards our modeling application. Since we aim to apply our results to the modal analysis for vibro-acoustics of laminated timber structures, as they occur in modern timber buildings, we test the performance of our method on a three-dimensional geometry representing the first floor of a building. Although wooden structures consist of orthotropic materials, we will use isotropic material parameters for the ease of computation. Usually different materials are used in the construction of a building. In this case, we have three different materials for the walls. More precisely, we assume that the outer walls are subdomain one, which consists of one material and that the interior walls can be divided into two more subdomains, namely ordinary walls and load-bearing walls. Figure 5.11 depicts our geometry and the corresponding domains. The material parameters E and ν range from $100 - 1000$ and $0.1 - 0.4$. We perform our simulations for $K = 10$ and use standard finite elements with 20994 degrees of freedom.

The first row in Figure 5.12 represents the first eigenfunctions for three different

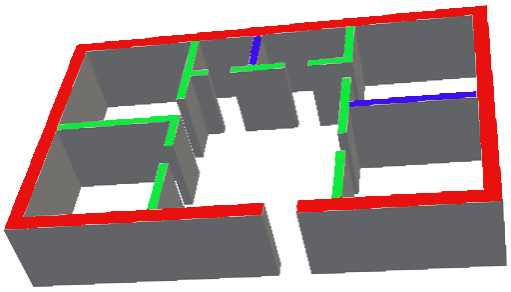

Figure 5.11: Geometry and subdomains: Outer walls in red, inner load-bearing walls in green, inner ordinary walls in blue.

parameter sets, while the second row represents the corresponding fourth eigenfunctions. We used the parameter sets

$$\begin{aligned} \mu^1 &= (200, 0.1, 800, 0.3, 400, 0.2), \\ \mu^2 &= (650, 0.36, 150, 0.25, 900, 0.11), \\ \mu^3 &= (800, 0.3, 500, 0.1, 200, 0.4). \end{aligned}$$

It can be observed that the eigenfunctions change significantly depending on the parameters while still being approximated very well by our method. Figure 5.13 shows the error decay for selected eigenvalues (left) and the corresponding eigenfunctions (right), as well as the minimum and maximum averaged errors. We again obtain very good convergence.

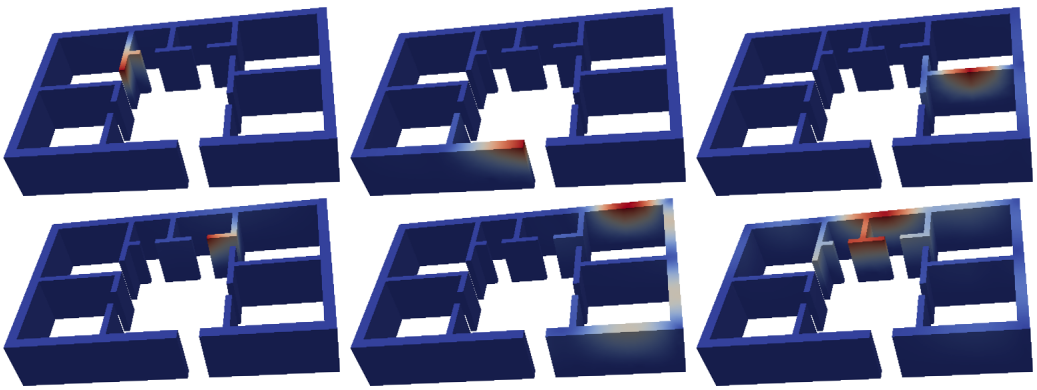

Figure 5.12: Behavior of the eigenfunctions depending on parameter variations. Top row depicts the first eigenfunction and bottom row the fourth eigenfunction.

The speed-up in the three-dimensional setting is even more significant. For the first floor of the building, we show in Table 5.4 the computation times for $K = 10$

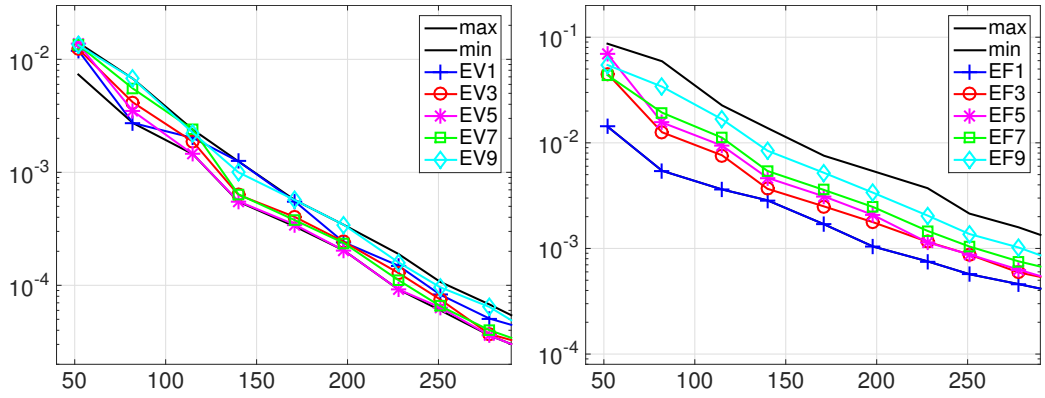

Figure 5.13: First floor configuration: Reduced basis error of eigenvalues (left) and eigenfunctions (right).

eigenvalues. We observe that the computation of the detailed solution takes 31.59 seconds, while the computations of the reduced solutions take between 0.084 and 0.142 seconds, depending on the basis size N. This results in a speed-up of 376 for $N = 50$ to 222 if we take $N = 300$ for an accuracy of 10^{-5}.

K	10					
N	50	100	150	200	250	300
Detailed solution	31.59					
Reduced solution	0.084	0.096	0.102	0.111	0.125	0.142
Reconstruction	0.021	0.027	0.031	0.035	0.040	0.046
Speed-up	376	329	309	284	252	222

Table 5.4: Timings for the detailed solution and the online calculations for the first floor in seconds.

6. Isogeometric mortar reduced basis method for elliptic eigenvalue problems

This section contains results from the publication "Reduced basis isogeometric mortar approximations for eigenvalue problems in vibroacoustics", which is submitted by the author, B. Wohlmuth and L. Wunderlich, 2016, [81].

In vibro-acoustical applications, often complicated curved domains are of special interest. Besides large constructions, such as bridges and buildings, also music instruments are investigated. An important part of a violin is the wooden violin bridge, depicted in Figure 6.1. The eigenvalues of a violin bridge play a crucial

role in transmitting the vibration of the strings to the violin body and hence influence the sound of the instrument, see [59, 178]. Not only the material but also the thickness plays an important role. Therefore we include the thickness as an additional tenth parameter.

6.1. Isogeometric mortar method with geometry parameter

Due to the complicated curved domain and improved eigenvalue approximations compared to finite element methods, see [83], we consider an isogeometric discretization. Flexibility for the tensor product spline spaces is gained by a weak domain decomposition of the non-convex domain. Isogeometric analysis, introduced in 2005 by Hughes et al. in [82], is a family of methods that uses B-splines and non-uniform rational B-splines (NURBS) as basis functions to construct numerical approximations of partial differential equations, see also [15, 38]. We have seen above that mortar methods are a popular tool for the weak coupling of non-matching meshes, originally introduced for spectral and finite element methods [16, 17, 19]. An early contribution to isogeometric elements in combination with domain decomposition techniques can be found in [48, 73]. A rigorous mathematical analysis of the *a priori* error in combination with uniform stability results for different Lagrange multiplier spaces is given in [31] and applications of isogeometric mortar methods can be found in [49, 151].

As mentioned before, we find mortar formulations as an indefinite saddle point-problem. The additional degrees of freedom for the Lagrange multiplier as well as the need for a uniform inf-sup condition to achieve stability make mortar methods, in general, more challenging than simple conforming approaches. Theoretically, the Lagrange multiplier can be eliminated. However this often results in a global process and is not carried out directly. While this concerns the detailed solution, the reduced basis can be purely based on a primal space and results in a non-conforming but positive definite approach. Then the saddle point structure becomes redundant and we gain the efficiency of a positive definite reduced system. In the following we start by describing the geometric setup and the isogeometric mortar discretization for the violin bridge.

We recall the eigenvalue problem of elasticity

$$-\operatorname{div}\sigma(u) = \lambda\rho u,$$

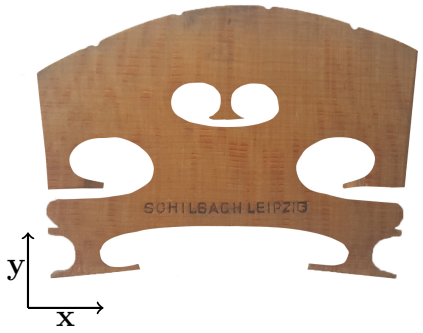

Figure 6.1: Example of a violin bridge.

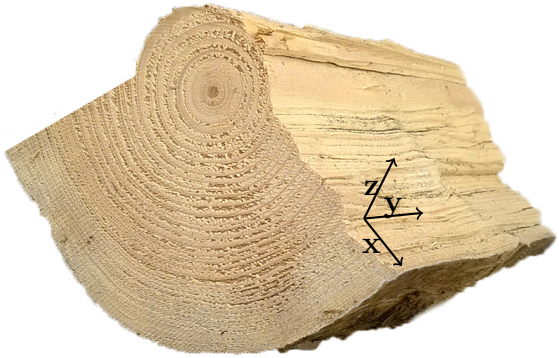

Figure 6.2: Illustration of the orthotropic structure of wood.

where $\rho > 0$ is the mass density and $\sigma(u)$ depends on the material law of the structure under consideration. In our case, linear orthotropic materials are appropriate since, as depicted in Figure 6.2, wood consists of three different axes and only small deformations are considered. Note that besides the cylindrical structure of a tree trunk, we consider Cartesian coordinates due to the comparably small size of the bridge. In the following let thus y denote the fiber direction, z the plane orthogonal direction and x the radial direction. The curved domain of the violin bridge can be very precisely described by a spline curve. Since it is not suitable for a single-patch description, we decompose it into 16 three-dimensional spline patches shown in Figure 6.3. While the description of the geometry could also be done with fewer patches, the number of 16 patches Ω_i gives us regular geometry mappings and a reasonable flexibility of the individual meshes.

The decomposed geometry is solved using an equal order isogeometric mortar method as described in [31]. A trivariate B-spline space V_i is considered on each patch Ω_i. The broken ansatz space $V_h = \prod_i V_i$ is weakly coupled on each of the 16 interfaces. For each interface $\Gamma_{s,m}$ the two adjacent domains are labeled as one slave and one master domain (i.e. $\Gamma_{s,m} = \partial\Omega_s \cap \partial\Omega_m$) and the coupling space $M_{(s,m)}$ is set as the trace space of the spline spaces on the slave domain and $M_h = \prod_{(s,m)} M_{(s,m)}$. Several crosspoints are present in the decomposition, where an appropriate local degree reduction is performed as described in [31, Section 4.3] to guarantee stability.

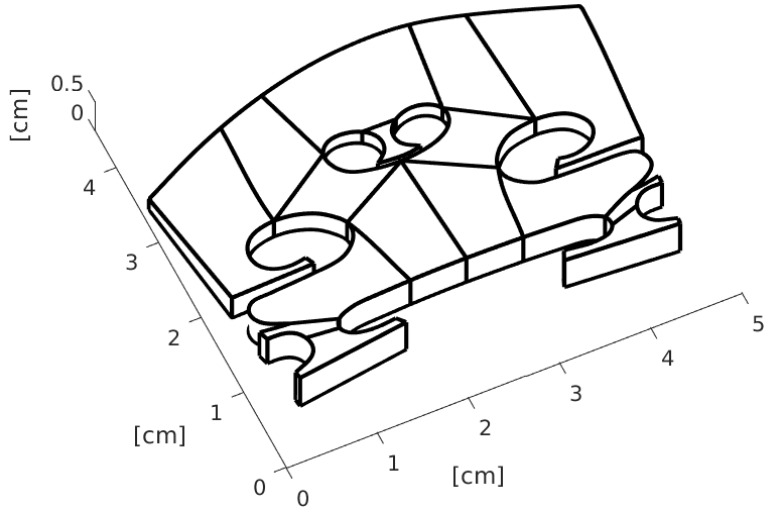

Figure 6.3: Decomposition of the three-dimensional geometry into 16 patches and 16 interfaces.

We use the standard bilinear forms for mortar techniques in linear elasticity

$$\begin{aligned} a(u,v) &= \sum_i \int_{\Omega_i} \sigma(u) : \varepsilon(v)\, dx, \quad m(u,v) = \sum_i \int_{\Omega_i} \rho u v\, dx, \\ b(v,\widehat{\tau}) &= \sum_{(s,m)} \int_{\Gamma_{s,m}} [v]_{(s,m)} \widehat{\tau}\, dx, \end{aligned}$$

where $[v]_{(s,m)} = v_s|_{\Gamma_{s,m}} - v_m|_{\Gamma_{s,m}}$ denotes the jump across the interface $\Gamma_{s,m}$. We note that no additional variational crime by different non-matching geometrical resolutions of $\Gamma_{s,m}$ enters. The detailed eigenvalue problem is defined as $(u,\tau) \in V_h \times M_h$, $\lambda \in \mathbb{R}$, such that

$$\begin{aligned} a(u,v) + b(v,\tau) &= \lambda m(u,v), \quad v \in V_h, \\ b(u,\widehat{\tau}) &= 0, \qquad\quad \widehat{\tau} \in M_h. \end{aligned}$$

As already mentioned, in addition to the nine material parameters E_i, G_{ij}, ν_{ij}, we consider a geometry parameter μ_{10}, describing the thickness of the violin bridge. Transforming the geometry to a reference domain, we can interpret the thickness parameter as one more material parameter.

We now execute the transformation of the geometrical parameters to the corresponding material parameter. For this purpose let the parameter dependent geometry $\Omega(\mu)$ be a unidirectional scaling of a reference domain $\widehat{\Omega}$, i.e., a transformation by $F(\cdot;\mu) : \widehat{\Omega} \to \Omega(\mu)$, $\mathbf{x} = F(\widehat{x};\mu) = (\widehat{x}, \widehat{y}, \mu_{10}\widehat{z})$, with $\widehat{x} = (\widehat{x}, \widehat{y}, \widehat{z}) \in \widehat{\Omega}$. Transfor-

ming the unknown displacement and rescaling it as $\widehat{u}(\widehat{x}) = DF(\widehat{x};\mu)^T\, u(F(\widehat{x};\mu))$ allows us to define a symmetric strain variable on the reference domain as

$$\widehat{\varepsilon}(\widehat{u}(\widehat{x})) = DF(\widehat{x};\mu)^T\, \epsilon(u(F(\widehat{x};\mu)))\, DF(\widehat{x};\mu).$$

The orthotropic stiffness tensor is then transformed to

$$\widehat{\mathbb{C}}(\mu) = \begin{pmatrix} A_{11} & A_{12} & \mu_{10}^{-2} A_{13} & & & \\ A_{21} & A_{22} & \mu_{10}^{-2} A_{23} & & & \\ \mu_{10}^{-2} A_{31} & \mu_{10}^{-2} A_{32} & \mu_{10}^{-4} A_{33} & & & \\ & & & \mu_{10}^{-2} G_{yz} & & \\ & & & & \mu_{10}^{-2} G_{zx} & \\ & & & & & G_{xy} \end{pmatrix}.$$

In terms of this coordinate transformation, the eigenvalue problem in the continuous H^1-setting reads, since $\det DF(\widehat{x};\mu) = \mu_{10}^{-1}$ is constant, as

$$\int_{\widehat{\Omega}} \widehat{\varepsilon}(\widehat{u})\ \widehat{\mathbb{C}}(\mu)\ \widehat{\varepsilon}(\widehat{v})\ \mathrm{d}\widehat{x} = \lambda \int_{\Omega} \rho\ \widehat{u}^{\top} \begin{pmatrix} 1 & & \\ & 1 & \\ & & \mu_{10}^{-2} \end{pmatrix} \widehat{v}\ \mathrm{d}\widehat{x}.$$

In our mortar case, the coupling conditions across the interfaces have to be transformed as well. However due the affine mapping with respect to x, y and z, the parameter dependence on $b(\cdot,\cdot)$ can be removed. Another material parameter of interest for applications is the constant mass density ρ. However any change in the constant ρ does not influence the eigenvectors. Only the eigenvalue is rescaled, yielding a trivial parameter dependence. For this reason, the density is kept constant in the reduced basis computations and can be varied as a postprocess by rescaling the eigenvalues. The described material parameters allow for an affine parameter dependence of the mass and the stiffness, with $Q_a = 10$, $Q_m = 2$,

$$a(\cdot,\cdot;\mu) = \sum_{q=1}^{Q_a} \theta_a^q(\mu) a^q(\cdot,\cdot), \quad m(\cdot,\cdot;\mu) = \sum_{q=1}^{Q_m} \theta_m^q(\mu) m^q(\cdot,\cdot).$$

6.2. Reduced basis for the saddle point problem

Reduced basis methods for the simultaneous approximation of eigenvalues and eigenvectors have been analyzed in the previous section. Here, we apply these methods to the previously described setting. An important difference to the previous

example is that we wish to approximate a saddle point problem instead of a positive definite matrix. Previous works on saddle point problems construct a reduced basis for both the primal and the dual space. This is necessary for example for variational inequalities or when the coupling i.e. $b(\cdot,\cdot)$, is parameter dependent, see [63, 69, 116]. To ensure the inf-sup stability of the discrete saddle point problem, supremizers should be added to the primal space, additionally increasing the size of the reduced system.

In order to perform the reduction of the saddle point problem, we note that due to the parameter independence of $b(\cdot,\cdot)$, which is an important but restrictive assumption, we can reformulate the detailed saddle point problem (6.1) in a purely primal form posed on the constraint space

$$X_h = \{v \in V_h, b(v,\widehat{\tau}) = 0, \widehat{\tau} \in M_h\}.$$

Also note that this formulation is not suitable for solving the detailed solution, since, in general, it is costly to construct a basis of X_h and severely disturbs the sparsity of the detailed matrices. Only in the case of so-called dual Lagrange multiplier spaces, a local static condensation can be carried out and the constrained basis functions do have local support. However, in the reduced basis context the constructed basis functions do automatically satisfy the weak coupling properties and thus the saddle-point problem is automatically reduced to a positive definite one.

Our reduced space is defined by $X_N := \{\zeta_n \in X_N, n = 1,\dots,N\}$, where the reduced basis functions ζ_n are selected using the greedy method presented before. Then the reduced eigenvalue problem for the first K eigenpairs is given by:
Find the eigenvalues $\lambda_{\mathrm{red},i}(\mu) \in \mathbb{R}$ and the eigenfunctions $u_{\mathrm{red},i}(\mu) \in X_N$ for $i = 1,\dots,K$, such that

$$a(u_{\mathrm{red},i}(\mu), v; \mu) = \lambda_{\mathrm{red},i}(\mu)\; m(u_{\mathrm{red},i}(\mu), v; \mu), \quad v \in X_N.$$

Nevertheless, adaptations for the online-offline decomposition of the error estimator will have to be performed in the following. The main contribution of the estimator is the residual

$$r_i(\cdot;\mu) = a(u_{\mathrm{red},i}(\mu), \cdot; \mu) - \lambda_{\mathrm{red},i}(\mu)\, m(u_{\mathrm{red},i}(\mu), \cdot; \mu).$$

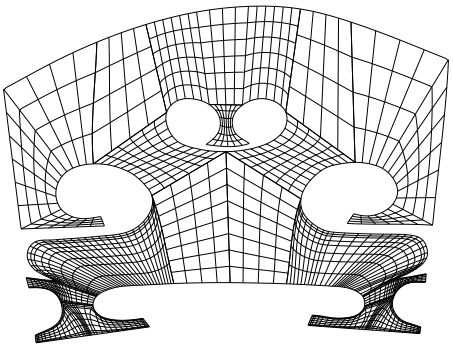

Figure 6.4: Non-matching isogeometric mesh of the violin bridge.

To adapt the online-offline decomposition from Section 5.3, we add additional terms corresponding to the mass components m_q. Let $(\zeta_n)_{1\leq n\leq N}$ be the orthonormal basis (w. r. t. $m(\cdot,\cdot;\widehat{\mu})$) of X_N and let us define $\xi_n^q \in X_N$ and $\xi_n^{m,q} \in X_N$ by

$$\begin{aligned}\widehat{a}(\xi_n^q, v) &= a^q(\zeta_n, v), \quad v \in X_h,\ 1 \leq n \leq N,\ 1 \leq q \leq Q_a,\\ \widehat{a}(\xi_n^{m,q}, v) &= m^q(\zeta_n, v), \quad v \in X_h,\ 1 \leq n \leq N,\ 1 \leq q \leq Q_m.\end{aligned}$$

In the following, we identify the function $u_{\mathrm{red},\,i}(\mu) \in V_N$ and its vector representation w. r. t. the basis $(\zeta_n)_{1\leq n\leq N}$ such that $\left(u_{\mathrm{red},\,i}(\mu)\right)_n$ denotes the n-th coefficient. Then, given a reduced eigenpair $(u_{\mathrm{red},\,i}(\mu), \lambda_{\mathrm{red},\,i}(\mu))$, we have the error representation

$$\widehat{e}_i(\mu) = \sum_{n=1}^{N}\sum_{q=1}^{Q_a} \theta_a^q(\mu)\left(u_{\mathrm{red},\,i}(\mu)\right)_n \xi_n^q - \lambda_{\mathrm{red},\,i}(\mu)\sum_{n=1}^{N}\sum_{q=1}^{Q_m} \theta_m^q(\mu)\left(u_{\mathrm{red},\,i}(\mu)\right)_n \xi_n^{m,q}.$$

Consequently, the main contribution of $\eta_i(\mu)$ can be decomposed using that we have $\|r_i(\cdot;\mu)\|^2_{\widehat{\mu};X_h'} = \widehat{a}(\widehat{e}_i(\mu), \widehat{e}_i(\mu))$ as before.

Now in the numerical simulations, the performance of the proposed algorithm is illustrated by numerical examples. The detailed computations were performed using geoPDEs [44], a Matlab toolbox for isogeometric analysis, the reduced computations are based on RBmatlab [50]. For the detailed problem, we use an anisotropic discretization. In plane, we use splines of degree three on the non-matching mesh shown in Figure 6.4. The mesh has been adapted locally to better resolve corner singularities of the solution. In the z-direction a single element of degree four is used. The resulting equation system has 45960 degrees of freedom for the displacement, whereas the surface traction on the interfaces is approximated by 2025 degrees of freedom. We consider the ten parameters described in the problem set-

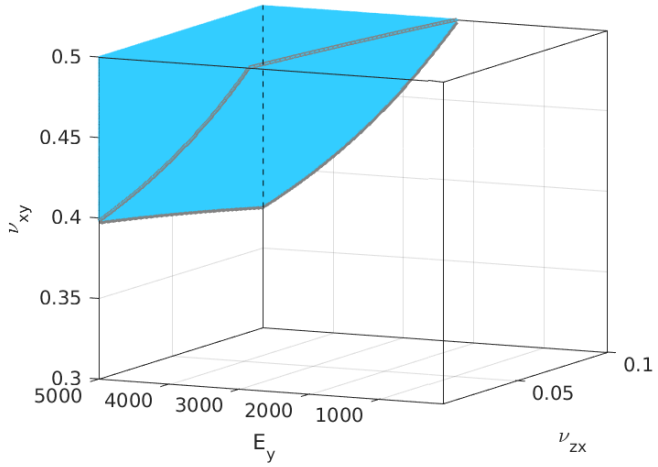

Figure 6.5: Illustration of non-admissible parameter values in a lower-dimensional excerpt of $\mathcal{P}_2$, varying $\nu_{zx} \in (0.01, 0.1), \nu_{xy} \in (0.3, 0.5), E_y \in (100, 5000)$ and fixing $E_x = 1000, E_z = 2000$ and $\nu_{yz} = 0.5$.

ting, $\mu = (\mu_1, \ldots, \mu_{10})$ with the elastic moduli $\mu_1 = E_x$, $\mu_2 = E_y$, $\mu_3 = E_z$, the shear moduli $\mu_4 = G_{yz}$, $\mu_5 = G_{xz}$, $\mu_6 = G_{xy}$, Poisson's ratios $\mu_7 = \nu_{yz}$, $\mu_8 = \nu_{xz}$, $\mu_9 = \nu_{yz}$ and the scaling of the thickness μ_{10}. The considered parameter values were chosen according to real parameter data given in [136, Table 7-1]. We consider two different scenarios. In the first setting, we fix the wood type and take into account only the natural variations, see [136, Section 7.10]. To capture the sensitivity of the violin bridge, one can choose a rather small parameter range around a reference parameter. We choose the reference data of *fagus sylvatica*, the common beech, as given in Table 6.1, as well as the parameter range $\mathcal{P}_1$. The mass density is fixed in all cases as $720 kg/m^3$.

In our second test setting, we also consider different wood types. Hence we also consider a larger parameter set, including the parameters for several types of wood. Based on a selection of some wood types, we choose the parameter range $\mathcal{P}_2$, see Table 6.1. We note that not all parameters in this large range are admissible for the orthotropic elasticity as they do not fulfill the conditions for the positive definiteness of the elastic tensor. Thus, we constrain the tensorial parameter space by

$$1 - \nu_{yz}^2 E_z/E_y + \nu_{xy}^2 E_y/E_x + 2\nu_{xy}\nu_{yz}\nu_{zx}E_z/E_x + \nu_{zx}^2 E_z/E_x \geq c_0,$$

as well as $E_x/E_y - \nu_{xy}^2 \geq c_1$, where the tolerances c_0 and c_1 are chosen according to several wood types. For example, in Figure 6.5 we depict a lower-dimensional excerpt of $\mathcal{P}_2$ which includes non-admissible parameter values.

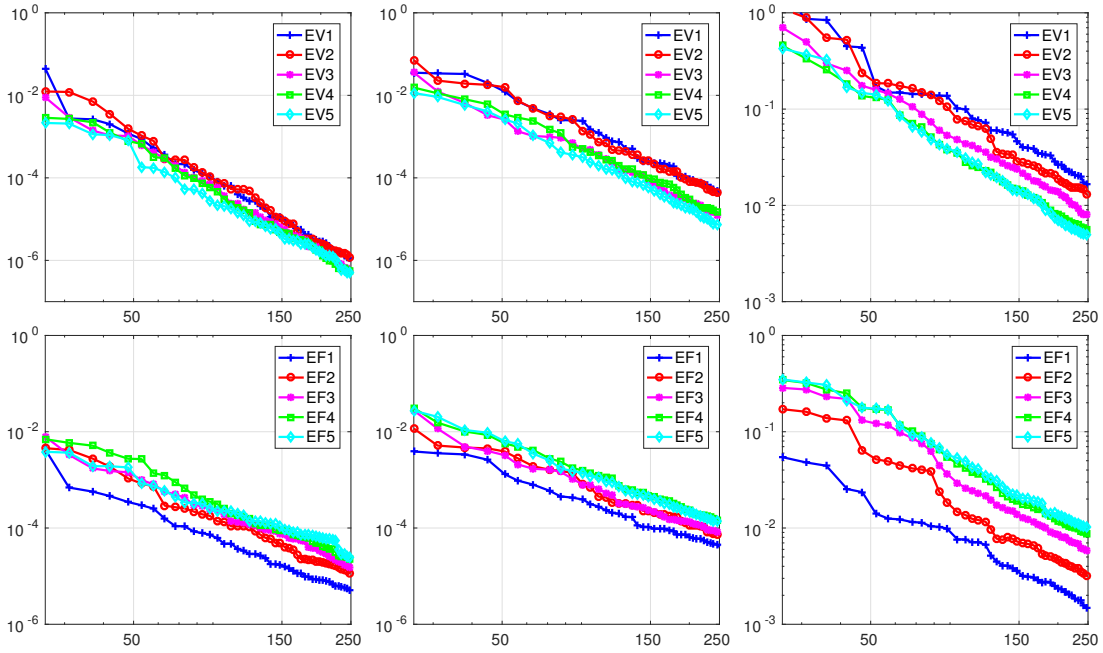

Figure 6.6: Convergence of the eigenvalues (top) and eigenfunctions (bottom). Parameter range $\mathcal{P}_1$ with a fixed thickness (left), with varying thickness (middle) and parameter range $\mathcal{P}_2$ with varying thickness (right).

	E_x $[MPa]$	E_y $[MPa]$	E_z $[MPa]$	G_{yz} $[MPa]$	G_{zx} $[MPa]$	G_{xy} $[MPa]$	ν_{yz}	ν_{zx}	ν_{xy}
$\widehat{\mu}$	$14,000$	$2,280$	$1,160$	465	$1,080$	$1,640$	0.36	0.0429	0.448
$\mathcal{P}_1$	$13,000$ $-\ 15,000$	$1,500$ $-\ 3,000$	750 $-\ 1,500$	100 $-\ 1,000$	500 $-\ 1,500$	$1,000$ $-\ 2,000$	0.3 $-\ 0.4$	0.03 $-\ 0.06$	0.4 $-\ 0.5$
$\mathcal{P}_2$	$1,000$ $-\ 20,000$	100 $-\ 5,000$	100 $-\ 2,000$	10 $-\ 5,000$	100 $-\ 2,500$	100 $-\ 5,000$	0.1 $-\ 0.5$	0.01 $-\ 0.1$	0.3 $-\ 0.5$

Table 6.1: Reference parameter and considered parameter ranges.

First, we consider the effect of the varying thickness parameter on the solution of our model problem. In Table 6.2 the first eigenvalues are listed for different values of the thickness, where we observe a notable and nonlinear parameter dependence. A selection of the corresponding eigenfunctions is depicted in Figure 6.10, where the strong influence becomes even more evident, since in some cases the shape of the eigenfunction changes when varying the thickness. In the following reduced basis tests, the relative error values are computed as the mean value over a large amount of random parameters. The L^2-error of the normed eigenfunctions is evaluated as the residual of the L^2-projection onto the corresponding detailed eigenspace. This takes into account possible multiple eigenvalues and the invariance with respect to a scaling by (-1).

The first reduced basis test is the simultaneous approximation of five eigenpairs

EV	$\mu_{10} = 0.5$	$\mu_{10} = 1.0$	$\mu_{10} = 2.0$	ratio 0.5/1.0	ratio 1.0/2.0
1	0.4057	1.3238	3.6954	0.3065	0.3582
2	1.1613	3.8870	10.8071	0.2988	0.3597
3	4.4096	12.9562	26.5621	0.3403	0.4878
4	6.1371	19.3254	30.0050	0.3176	0.6441
5	13.5564	27.3642	53.2657	0.4954	0.5137
6	19.2229	46.2521	93.9939	0.4156	0.4921
7	27.6118	65.0940	111.6075	0.4242	0.5832
8	39.3674	96.8069	129.3406	0.4067	0.7485
9	57.8266	107.6749	189.6090	0.5370	0.5679
10	68.0131	130.8876	241.7695	0.5196	0.5414

Table 6.2: Smallest eigenvalues for different thickness parameters.

on both parameter-sets $\mathcal{P}_1$ and $\mathcal{P}_2$ with the thickness parameter $\mu_{10} \in [0.5, 2]$. We use an initial basis of the size 25 computed by a POD, which is enriched by the greedy algorithm up to a basis size of 250. In Figure 6.6, the error decay for the

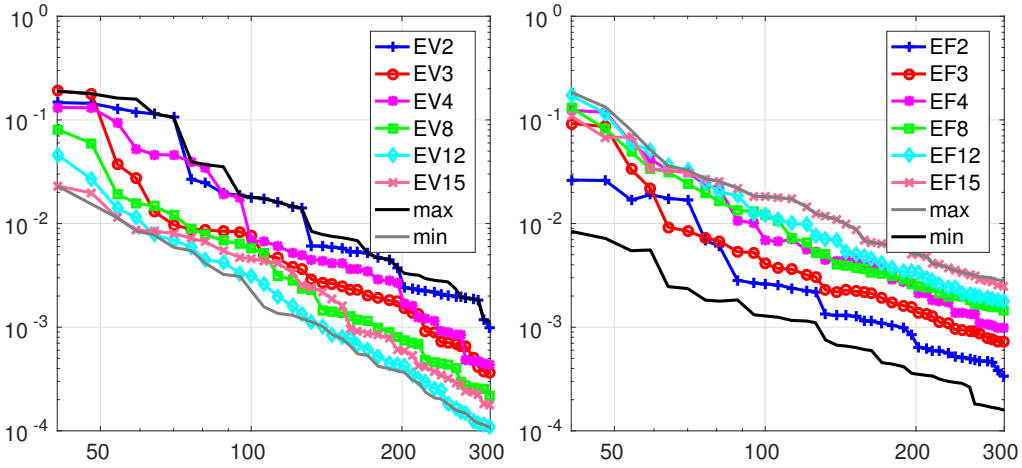

Figure 6.7: Convergence of the eigenvalues (left) and eigenfunctions (right). Parameter range $\mathcal{P}_1$ with varying thickness, simultaneously approximating 15 eigenpairs.

eigenvalue and the eigenfunction is presented. We observe very good convergence, with a similar rate in all cases. As expected the magnitude of the error grows with the complexity of the parameter range. Also an approximation of a larger number of eigenpairs does not pose any unexpected difficulties. Error values for the eigenvalue and eigenfunction are shown in Figure 6.7 for an approximation of the first 15 eigenpairs in the parameter-set $\mathcal{P}_1$, showing a good convergence behavior. The reduced basis size necessary for a given accuracy increases compared to the previous cases of five eigenpairs, due to the higher amount of eigenfunctions which are, for a fixed parameter, orthogonal to each other. When considering the relative error for the eigenvalues, see Figure 6.6 and Figure 6.7, we note that for a fixed ba-

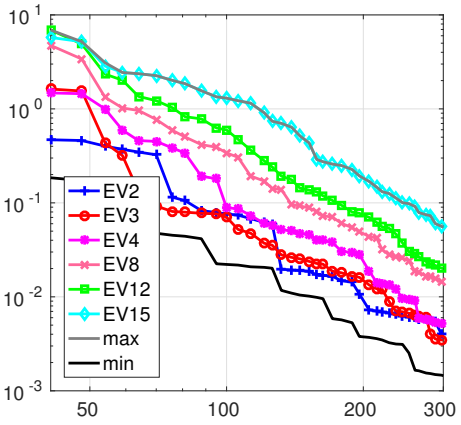

Figure 6.8: Convergence of the absolute error value for the eigenvalues. Parameter range $\mathcal{P}_1$ with varying thickness, simultaneously approximating 15 eigenpairs.

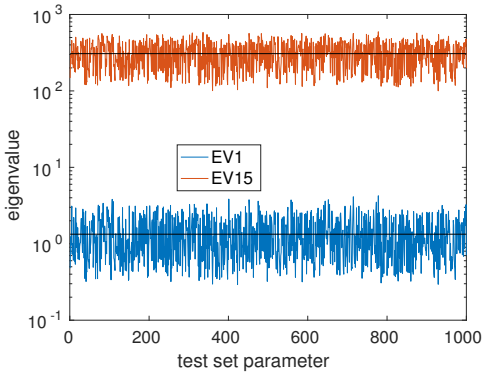

Figure 6.9: Sampling of the first and 15th eigenvalue within the parameter set $\mathcal{P}_1$ as used in the test set. Extremal values: $\min \lambda_1 = 0.29$, $\max \lambda_1 = 4.24$, $\min \lambda_{15} = 100.19$, $\max \lambda_{15} = 593.65$.

sis size, the higher eigenvalues have a better relative approximation than the lower ones. In contrast, considering the eigenfunctions, the errors of the ones associated with the lower eigenvalues are smaller compared to the ones associated with the higher eigenvalues. In Figure 6.8, we see the same effect, when considering absolute error values for the eigenvalue compared to the relative values. The error in the eigenfunctions has the same ordering as the absolute error in the eigenvalue. For the parameters under consideration, the lower and higher ones of the considered eigenvalues differ by magnitudes as illustrated in Figure 6.9. Hence when computing the relative error from the absolute ones, the error values of the high eigenvalues are divided by a large number and become small compared to the lower eigenvalues.

Thus our eigenvalue reduced basis approximation of a violin bridge yields a good approximation quality as well as a significant complexity reduction to a positive-definite system of less than 300 degrees of freedom. Furthermore, the geometry parameter representing the thickness of the violin bridge has a significant influence on the eigenvalues and eigenfunctions, without posing further difficulties to the reduced basis approximation.

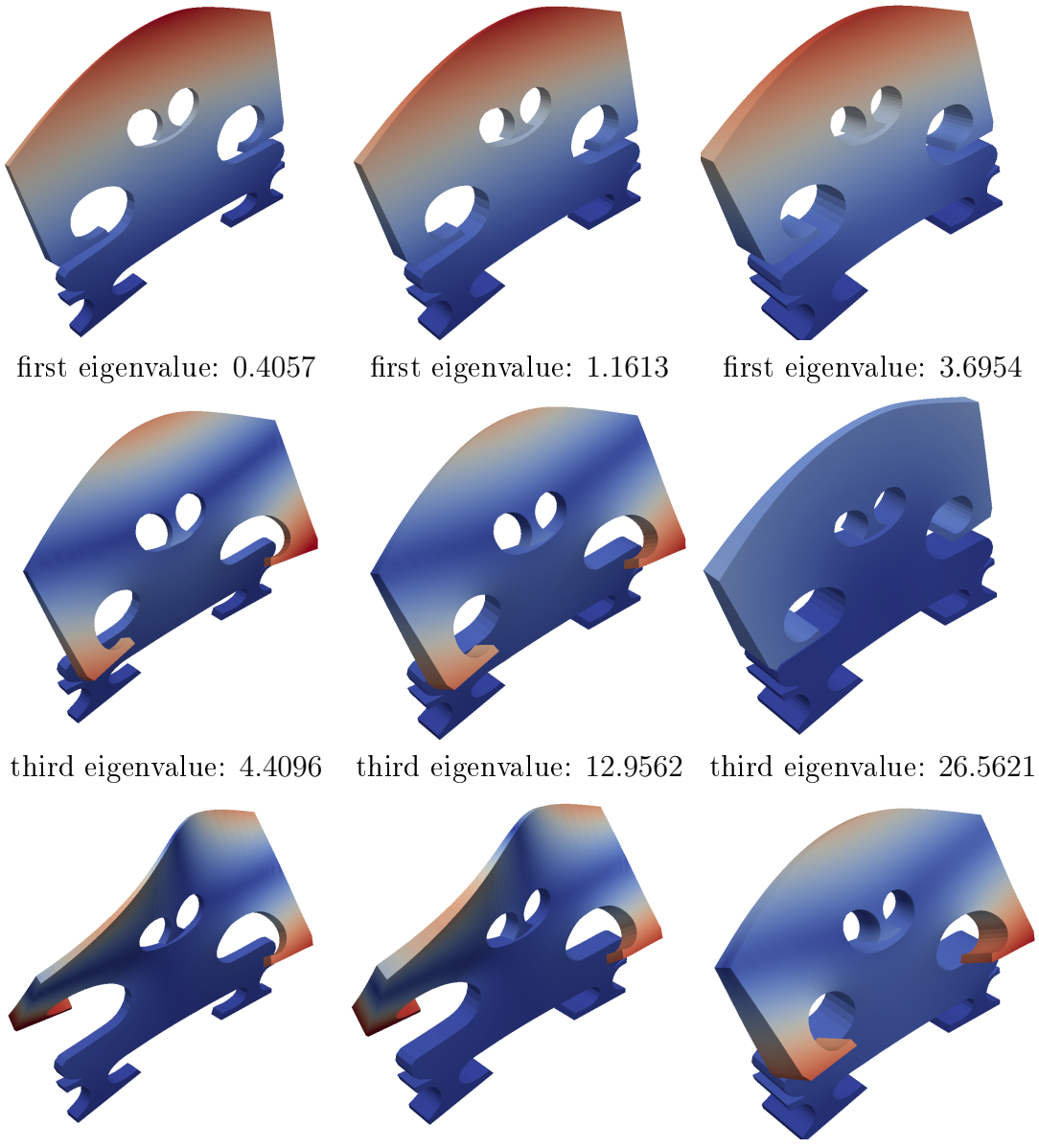

Figure 6.10: Influence of the thickness of the bridge on several eigenmodes.

7. Reduced basis component mode synthesis for elliptic eigenvalue problems

In this chapter, we have so far discussed reduced basis methods for eigenvalue problems and derived the corresponding error estimators, showing that we can approximate several, even multiple, eigenvalues simultaneously. Nevertheless the considered approaches present possible remaining challenges. It is possible that the required detailed solutions for the greedy algorithm cannot be computed due to hardware or time restrictions. If the calculation is feasible, it can become very costly in the offline phase since for a certain required accuracy the basis becomes very large. Another possibility is that when, e.g. in the context of a building construction, each component is assigned its own orthotropic material parameters, the reduced basis space has to be built in a way that allows to accomodate the nine orthotropic material parameters per component for all K eigenvalues.

7.1. Introduction to component mode synthesis

The component mode synthesis method [39, 40, 84] represents an alternative to overcome these challenges for eigenvalue problems. A similar method used in general for linear problems is the static condensation reduced basis method, see e.g. [52, 85, 154]. It was also applied to eigenvalue problems in [169]. The component mode synthesis allows to approximate eigenmodes and eigenvalues of a vibro-acoustical problem, while dissecting the structure under consideration into its single components, even when the generalized eigenvalue problem of the whole system is not available. After the frequency and modal analysis of the single components, the entire structure is considered as an assembly of the components. A review of component mode synthesis methods and their origins as well as appropriate error measures can be found in [45]. An important procedure in this context is the Craig-Bampton method [41]. The origin of component mode synthesis methods lies in applications in aerospace engineering [161]. Nevertheless the numerous fields of interest for these methods include fluid-structure interactions [114] and buckling [168]. Furthermore hybrid methods have been presented in [46, 88, 103, 160, 162]. Recent methods involve coupling modes, which correspond to the eigenfunctions of the Poincaré-Steklov operator [25, 26, 27].

For the component mode synthesis we again consider the parameter μ-dependent eigenvalue problem given by:

Find the eigenvalue $\lambda \in \mathbb{R}$ and the eigenfunctions $u \in V_h$ such that

$$a(u(\mu), v; \mu) = \lambda(\mu) m(u(\mu), v), \qquad v \in V_h,$$

which can be written in matrix notation as

$$Ax = \lambda M x.$$

Then the idea is to split the global domain Ω into p non-overlapping subdomains, i.e. $\bar{\Omega} = \bigcup_j \bar{\Omega}_j$, and calculate bubble modes as well as static modes on the respective subdomains, and finally to set up the reduced eigenvalue problem. An example of such a domain decomposition is shown in Figure 7.1 with the corresponding notations, where a three-dimensional L-shape domain is decomposed into 3 subdomains. For ease of notation we denote the interfaces $\Gamma_k := \Gamma_{s,m} = \partial\Omega_s \cap \partial\Omega_m$ in the following with k as a global numbering.

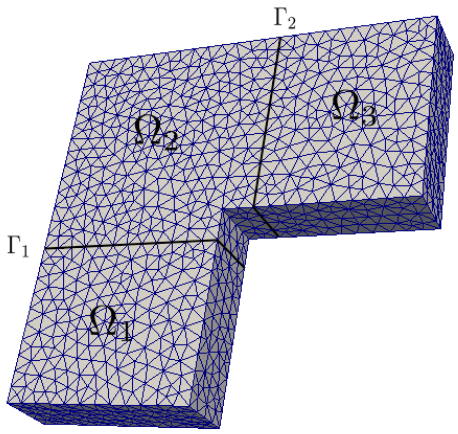

Figure 7.1: L-shape domain for component mode synthesis with domain split into three subdomains.

The stiffness matrix $A \in \mathbb{R}^{n \times n}$ and the mass matrix $M \in \mathbb{R}^{n \times n}$ of a component are partitioned as follows with the indices I related to the internal and the indices Γ related to the interface degrees of freedom

$$A = \begin{pmatrix} A_{II} & A_{I\Gamma} \\ A_{\Gamma I} & A_{\Gamma\Gamma} \end{pmatrix} \qquad \text{and} \qquad M = \begin{pmatrix} M_{II} & M_{I\Gamma} \\ M_{\Gamma I} & M_{\Gamma\Gamma} \end{pmatrix}.$$

We find the coordinate transformation with the matrix

$$\Psi = \begin{pmatrix} \Phi_{II} & \Psi_{I\Gamma} \\ 0 & I_{\Gamma\Gamma} \end{pmatrix},$$

where Φ_{II} contains the bubble modes and $\Psi_{I\Gamma}$ contains the static modes. Note that the static and bubble modes do not necessarily span the whole V_h. Then the mass and stiffness matrices transform to the reduced ones given by

$$\widetilde{A} = \Psi^T A \Psi, \qquad \widetilde{M} = \Psi^T M \Psi$$

and the reduced eigenvalue problem to be solved can be written as

$$\widetilde{A}x = \lambda \widetilde{M} x,$$

where the matrices are given according to [14, 25, 119] with the static modes $s_i^{\Gamma_k}$ and the bubble modes $b_i^{\Omega_j}$ as

$$\widetilde{A} = \begin{pmatrix} \begin{pmatrix} \lambda_{\Omega_1,1} & & & & & & 0 \\ & \ddots & & & & & \\ & & \lambda_{\Omega_1,K} & & & & \\ & & & \ddots & & & \\ & & & & \lambda_{\Omega_p,1} & & \\ & & & & & \ddots & \\ 0 & & & & & & \lambda_{\Omega_p,K} \end{pmatrix} & \begin{matrix} 0 \\ \\ \\ \\ \\ \\ [a(s_i^{\Gamma_k}, s_j^{\Gamma_l})] \end{matrix} \\ \begin{matrix} 0 & & & & & & \end{matrix} & \end{pmatrix},$$

and

$$\widetilde{M} = \begin{pmatrix} \begin{pmatrix} 1 & & & & & & 0 \\ & \ddots & & & & & \\ & & 1 & & & & \\ & & & \ddots & & & \\ & & & & 1 & & \\ & & & & & \ddots & \\ 0 & & & & & & 1 \end{pmatrix} & \begin{matrix} [m(b_i^{\Omega_k}, s_j^{\Gamma_l})] \\ \\ \\ \\ \\ \\ [m(s_i^{\Gamma_k}, s_j^{\Gamma_l})] \end{matrix} \\ \begin{matrix} [m(b_j^{\Omega_l}, s_i^{\Gamma_k})] & & & & & & \end{matrix} & \end{pmatrix}.$$

These matrices are not diagonal, but since the stiffness matrix $\widetilde{A}$ exhibits a clearer sparsity than the mass matrix $\widetilde{M}$, this method is said to act through mass coupling.

Now since we know how the reduced system looks like it remains open how the respective bubble and static modes are built. For each subdomain Ω_j, let us define the approximate bubble modes $b_i^{\Omega_j} \in \mathring{V}_h(\Omega_j)$, where $\mathring{V}_h(\Omega_j)$ is the space of functions on Ω_j, such that the trival extension on Ω is in V_h. The bubble modes $b_i^{\Omega_j}$ are obtained as the first K eigenfunctions of the variational eigenvalue problem:
Find $(\lambda_{\Omega_j,i}, b_i^{\Omega_j}) \in \mathbb{R} \times \mathring{V}_h$ such that

$$a_{\Omega_j}(b_i^{\Omega_j}, v) = \lambda_{\Omega_j,i} m_{\Omega_j}(b_i^{\Omega_j}, v), \qquad v \in \mathring{V}_h(\Omega_j). \tag{27}$$

The eigenfunctions $b_i^{\Omega_j}$ are extended by zero outside Ω_j and thus defined on the whole domain Ω.

As the next step we have to define the static modes on each subdomain by

$$s_i^{\Omega_j,\Gamma_k} \in V_h(\Omega_j, \Gamma_k),$$

where

$$V_h(\Omega_j, \Gamma_k) := \{v_{j,k} = v|_{\Omega_j}, v \in V_h, \text{ with } v|_{\Gamma_l} = 0, l \neq k\},$$

for Γ_k being an interface of Ω_j. We choose the static modes to be discrete harmonic, hence we can define it by the value on the interface Γ_k. The values on Γ_k are called port modes $p_i^k \in V_h(\Gamma_k)$ with

$$V_h(\Gamma_k) := \{v_k = v|_{\Gamma_k}, v \in V_h\}.$$

The port modes are then lifted harmonically into the neighboring domain Ω_j by

$$\begin{aligned} &a(s_i^{\Omega_j,\Gamma_k}, v) = 0, \qquad v \in V_h(\Omega_j, \Gamma_k), \\ &s_i^{\Omega_j,\Gamma_k} = p_i^{\Gamma_k}, \qquad \text{on } \Gamma_k, \end{aligned} \tag{28}$$

which then yield according to [84] our static modes on each domain Ω_j. We now associate the static modes on the neighboring subdomains Ω_l and Ω_r belonging to the same port mode, i.e.

$$s_i^{\Gamma_k} := \begin{cases} s_i^{\Omega_l,\Gamma_k}, & \text{on } \Omega_l \\ s_i^{\Omega_r,\Gamma_k}, & \text{on } \Omega_r \end{cases}.$$

There are several ways to define the port modes. Some of them are discussed in the following. At this point we only give a short description of two possible methods to

compute port modes, for more detailed reviews we refer to [28] and the references therein.

The first method described here is the Craig-Bampton method [41]. This method takes all interface DoFs into account. It fixes all DoFs to zero, except the i-th boundary degree of freedom, which is set to unity and then, as already described above, harmonically lifted into the domain to obtain the static modes.

The next method is based on the Poincaré-Steklov operator method [25, 28], which solves an adapted eigenvalue problem on the interface. Given the mesh dependent Poincaré-Steklov operator S_h^Γ, we solve the eigenvalue problem

$$S_h^{\Gamma_k} p^{\Gamma_k} = \lambda p^{\Gamma_k}.$$

A realization of this eigenvalue problem is given by solving the following eigenvalue problem:
Find the eigenvalue $\lambda \in \mathbb{R}$ and the eigenfunctions $\tilde{u} \in V_h(\Omega_l \cup \Omega_r)$ such that

$$a_{\Omega_l}(\tilde{u}, v) + a_{\Omega_r}(\tilde{u}, v) = \lambda \int_{\Gamma_k} \tilde{u} v \, dx, \qquad v \in V_h(\Omega_l \cup \Omega_r)$$

and restrict $\tilde{u}$ to the interface Γ_k: $p_i^{\Gamma_k} := \tilde{u}|_{\Gamma_k}$.

As already mentioned, the Craig-Bampton method generates a port mode for each degree of freedom on the interface Γ_k, and therefore leads to many static modes on each component when using a fine mesh of the domain Ω_j. In comparison, methods like the Poincaré-Steklov method use only few port modes, which thus allows to build and use only few static modes as well, while nevertheless obtaining a certain accuracy. The lower amount of static mode constructions benefits our reduced basis approach, as we will see later.

7.2. Application to complex geometries

In the following we present an L-shape domain decomposed into three subdomains with two interfaces as depicted in Figure 7.1. The problem under investigation is again the linear elasticity eigenvalue problem (5). For simplicity we again choose the material to be isotropic. The parameters for this simulation and the next two examples are $E = 1000$ and $\nu = 0.25$ for the whole domain. In this setting we calculate the first 20 eigenvalues. Figure 7.3 shows the results for the first, third,

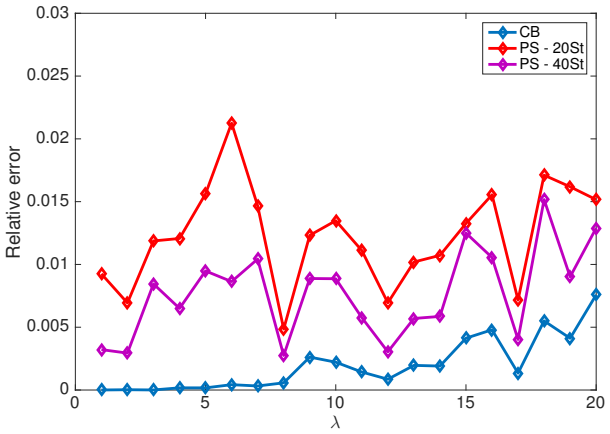

Figure 7.2: Comparison of the Craig-Bampton and Poincaré-Steklov methods for 20 and 40 static modes.

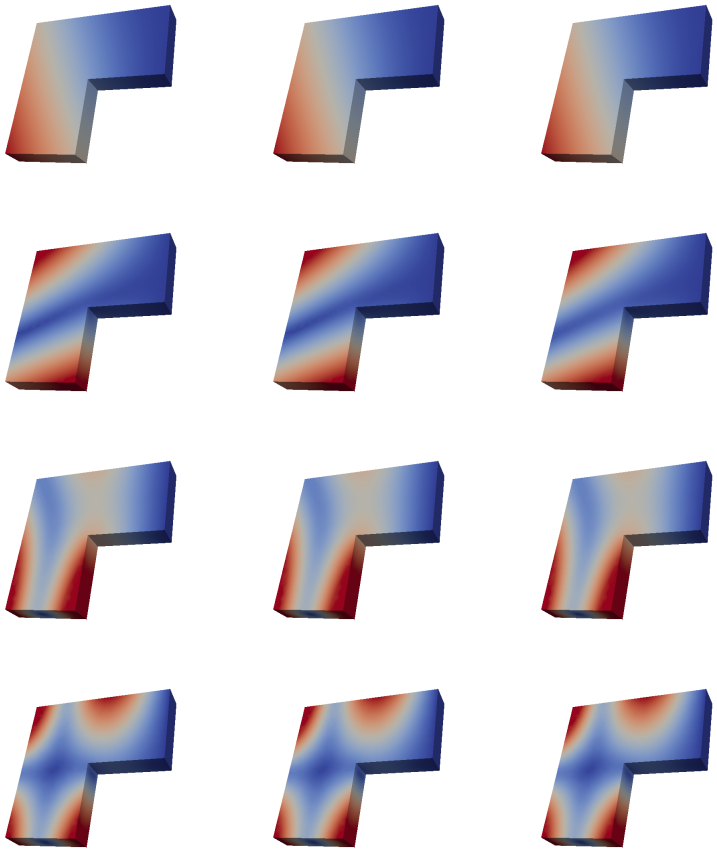

Figure 7.3: Comparison of the first, third, fifth and seventh (from top to bottom) eigenmodes of the detailed solution and Craig-Bampton and Poincaré-Steklov methods (from left to right) on the L-shape domain.

fifth and seventh eigenfunctions, where we compare the exact solutions calculated

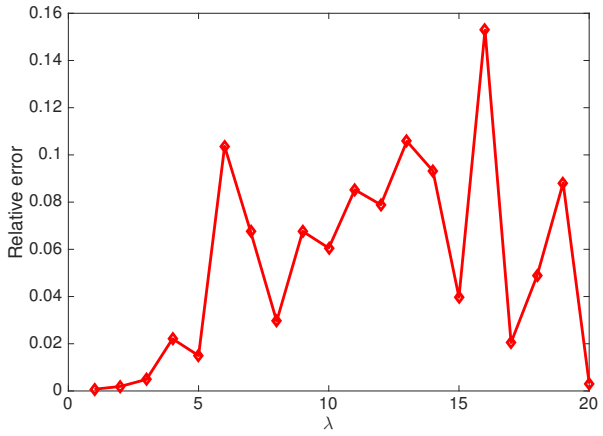

Figure 7.4: Relative error in the eigenvalues for the reduced basis component mode synthesis for the L-shape domain.

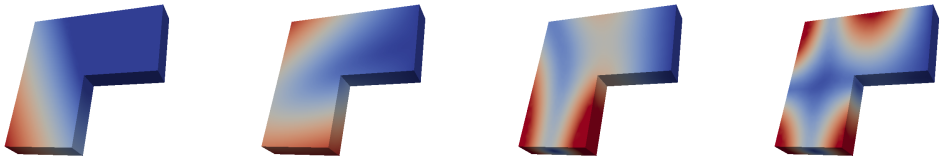

Figure 7.5: Eigenfunctions 1, 3, 5 and 7 on the L-shape domain calculated with the reduced basis component mode synthesis.

on the global domain at once, the Craig-Bampton method and then the Poincaré-Steklov method with 40 static modes. In both cases good agreement of the modes is observed.

In Figure 7.2 we depict the results for the eigenvalues. This time we show the accuracy of the Craig-Bampton and Poincaré-Steklov methods with 20 and 40 static modes compared to the detailed solution solved on a global domain. Thereby we see that the Craig-Bampton method is the more accurate method but also, as des-

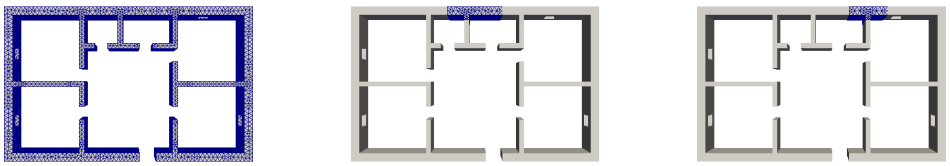

Figure 7.6: First floor domain decomposed into 33 subdomains. Full domain on the left and example subdomains in the middle and on the right.

EV	λ	λ_{cms}	%	EV	λ	λ_{cms}	%
1	15.75	15.71	0.25	11	36.66	36.60	0.16
2	18.46	18.47	0.05	12	40.95	40.81	0.34
3	24.69	24.56	0.53	13	41.25	41.16	0.22
4	27.71	27.64	0.25	14	42.12	42.02	0.24
5	28.41	28.19	0.77	15	44.09	43.87	0.50
6	29.23	29.17	0.21	16	44.27	44.08	0.43
7	30.73	30.63	0.33	17	49.38	49.33	0.10
8	32.57	32.46	0.34	18	51.13	51.08	0.10
9	33.75	33.53	0.65	19	52.18	52.20	0.04
10	35.45	35.20	0.71	20	59.15	59.09	0.10

Table 7.1: Comparison of the eigenvalues obtained using the Poincaré-Steklov method with 40 static modes to the detailed solution.

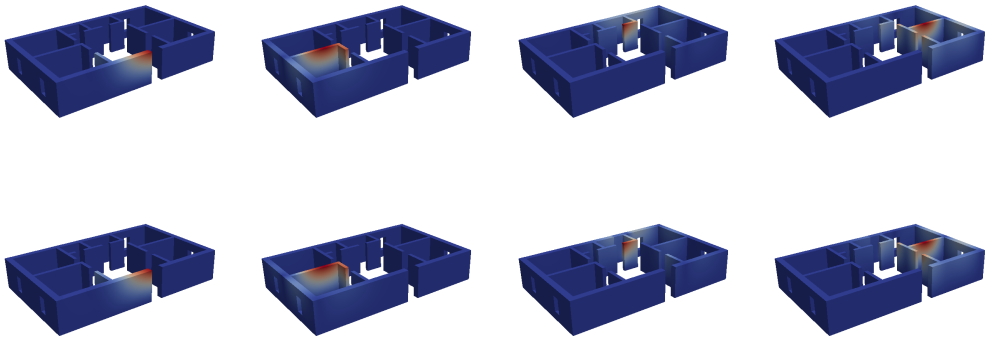

Figure 7.7: Comparison of the first, third, fifth and seventh (from left to right) eigenmodes on the first floor domain. The detailed solution is depicted in the first row and the component mode solution in the second row.

cribed above, uses many static modes per component, while the Poincaré-Steklov method only uses 20 or 40 static modes in this case. We further observe the influence of the number of used static modes for the Poincaré-Steklov method, where the accuracy is improved for 40 static modes but nevertheless in all cases we obtain relative errors of less than 2%. Furthermore it should be noted that when using the Poincaré-Steklov method with 40 static modes, we have a complexity reduction from 6705 DoFs to 140 DoFs.

Even though the global problem is split into several small local ones it is still very costly to solve the detailed solutions on a subdomain when they are resolved with a fine mesh size. Since we have a parameter μ-dependent problem, with $\mu = (E, \nu)$ where $E \in [500, 1500]$ and $\nu \in [0.2, 0.3]$, the problem has to be solved several times. Therefore at this point it is adequate to couple the already well-known component

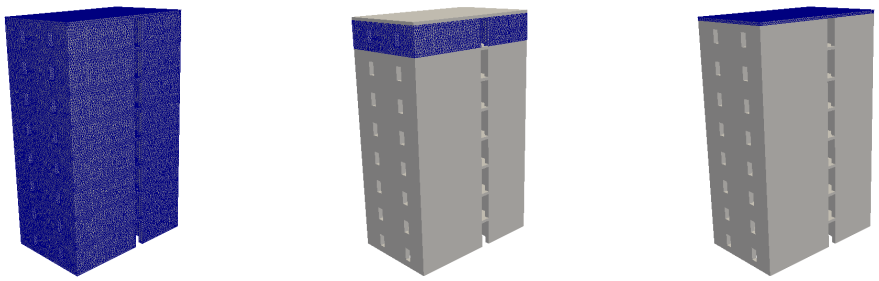

Figure 7.8: Eight story building decomposed into 16 subdomains. Full domain on the left and the subdomains in the middle and on the right.

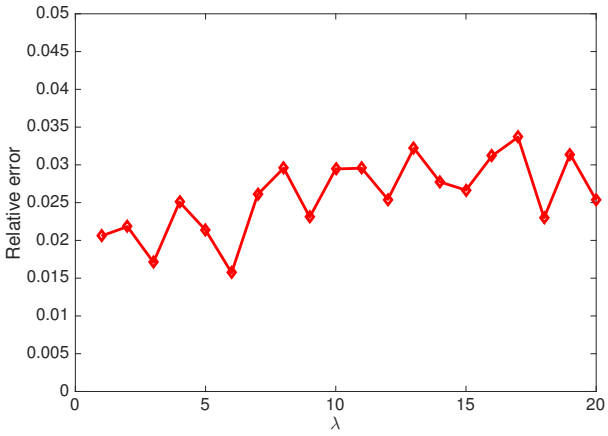

Figure 7.9: Relative error of the component mode synthesis method for the eight story building example.

mode synthesis described above with the reduced basis methods. To solve the eigenvalue problem given by (27) for the bubble modes and for the calculation of the eigenfunctions on the interface Γ_k, it is possible to use the newly derived reduced basis eigenvalue problem from Section 6. Furthermore for the harmonic lifting (29), which is a simple right-hand-side problem, well-known reduced basis methods can be employed, where the basis is either built with a greedy method or with a POD as for example in [129, 141] and in the references therein.

Now we couple the component mode synthesis with our reduced basis eigenvalue method to generate the bubble functions. The reduced basis size for these simulations is 40 for 20 eigenvalues and we use the Poincaré-Steklov method with 40 static modes. As seen in the sections before, for obtaining an accurate approximation for such a large number of eigenvalues, usually larger reduced spaces are employed. Nevertheless with this rough approximation, we obtain the results for the eigenvalues depicted in Figure 7.4 and the results in Figure 7.5 for the eigen-

EV	λ_{cms}	EV	λ_{cms}	EV	λ_{cms}	EV	λ_{cms}
1	0.16	6	3.12	11	11.01	16	16.04
2	0.26	7	5.16	12	12.61	17	16.64
3	0.72	8	6.68	13	14.39	18	16.85
4	1.86	9	7.56	14	14.79	19	17.08
5	2.71	10	8.58	15	15.13	20	17.13

Table 7.2: First 20 eigenvalues of the eight story building.

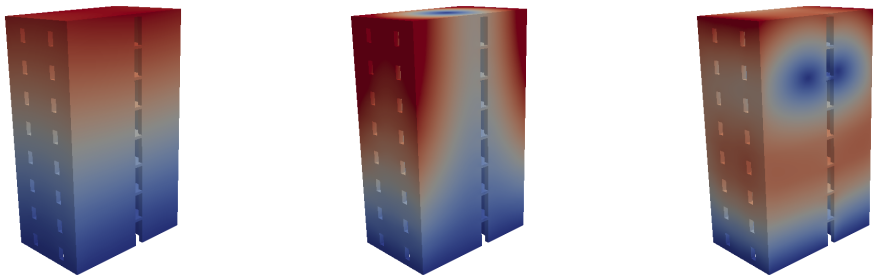

Figure 7.10: Exemplary resulting eigenfunctions 1, 3 and 5 (from left to right) of the eight story building.

functions. Except for the outlier case corresponding to eigenvalue 16, we lie in the engineering tolerance of less than 10%. Furthermore the eigenfunctions are in very good accordance with the ones depicted above in Figure 7.3. Increasing the reduced basis size will lead to a decrease of the error and finally results similar to the ones depicted in Figure 7.2 are obtained.

Finally we want to show the potential of the proposed method for an example with more engineering relevance and perform calculations on a first floor domain. It is decomposed into 33 subdomains with 28 interfaces as depicted in Figure 7.6. The resulting differences between the eigenvalues obtained by the Poincaré-Steklov method with 40 static modes and the ones from the detailed solution are found in Table 7.1. There we observe a very good accordance between the component mode synthesis and the detailed solution. In all cases, we see a very good accuracy with a relative error of less than 1%.

In Figure 7.7 the first, third, fifth and seventh eigenmodes for the first floor domain are depicted. We observe very good accordance of the eigenfunctions, while the number of degrees of freedom is reduced from 33912 DoFs in the full model to 1700 DoFs in the component mode model.

To demonstrate the benefits of this component mode method, we consider an even

more complex geometry, namely an eight story building as depicted in Figure 7.8. For the component mode synthesis, we only use the two subdomains which are depicted in the middle and on the right of the figure to build the entire model. These subdomains are then used several times each. For this simulation 300 static modes are used per component, since the interface is now the entire ground plan of the first floor example, which is larger and much more complex than in the previous cases, where the interface consisted of simple rectangles. In Figure 7.9 we depict the relative error of the component mode synthesis in the example of the eight story building. It can be seen that even though we are using large components with complex interfaces, a very good accuracy is achieved, with relative errors under 3.5%. The resulting first 20 eigenvalues are shown in Table 7.2 and several representative eigenfunctions in particular associated with the first, third and fifth eigenvalues are depicted in Figure 7.10.

Chapter IV.
Energy correction methods for corner domains

In this chapter we deal with domains with reentrant corners and possible methods to obtain optimal convergence rates despite the pollution effect caused by the corner singularities.

8. Domains with reentrant corners

The building structures under investigation in this thesis constitute a special challenge since in several places non-smooth structures arise, for example when building components such as walls and ceilings or door frames meet. In these cases corner singularities are found which have to be treated accordingly in our numerical setting. The equation of main interest for our vibro-acoustic analysis is the linear elasticity equation, which is an elliptic problem. We will thus in the following consider elliptic problems in non-smooth domains.

8.1. Introduction to corner singularities and the pollution effect

As demonstrated in Section 2.2, in order to prove optimal convergence in the L^2-norm, one usually uses the full elliptic regularity of the dual problem. The drawback of this procedure is that if the H^2-regularity does not hold, such as in the case of polygonal domains with reentrant corners, the optimal convergence is lost.

In the following chapter, if not stated otherwise, we will consider as a model problem the Poisson equation with homogeneous boundary conditions

$$-\Delta u = f \quad \text{in } \Omega, \qquad u = 0 \quad \text{on } \partial\Omega \tag{29}$$

on the domain $\Omega \subset \mathbb{R}^2$ defined as above, which has a single reentrant corner. Its solution consists of a regular and a singular part, where the singularity is only due to the reentrant corner with interior angle $\pi < \omega < 2\pi$, as depicted in Figure 8.1. The arguments in the following chapters will be local ones, thus allowing us to

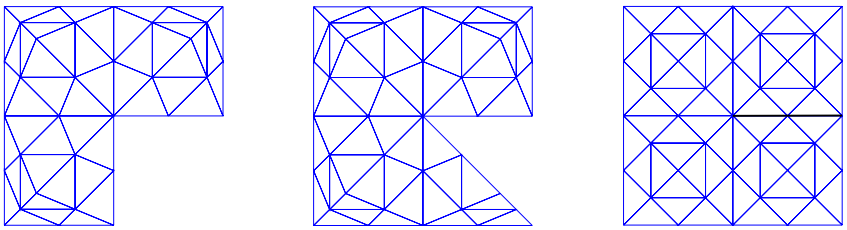

Figure 8.1: Domains with reentrant corners.

easily extend our considerations to the case of several reentrant corners.

As mentioned above and according to [96], it is possible to expand the solution of the Poisson equation into its regular and singular parts by the following lemma.

Lemma 8.1 (Expansion of the solution)**.** *Let Ω be a polygonal with a single reentrant corner of an angle $\omega \in (\pi, 2\pi)$, $m \in \mathbb{N}_0$, and $f \in H^m_{-\gamma}(\Omega)$ for $\gamma > 1 + m - \frac{\pi}{\omega}$. Also, let $N_\omega \in \mathbb{N}$ be such that*

$$i = 1, ..., N_\omega : \quad \frac{i\pi}{\omega} < 1 + m + \gamma, \qquad \text{and} \qquad \frac{(N_w + 1)\pi}{\omega} > 1 + m + \gamma.$$

Then the unique solution $u \in H^1_0(\Omega)$ of (29) belongs also to $H^{m+2}_\gamma(\Omega)$ and it can be decomposed into

$$u = \sum_{i=1}^{N_w} k_i s_i + W, \tag{30}$$

where $W \in H^{m+2}_{-\gamma}(\Omega) \cap H^1_0(\Omega)$ and $k_n \in \mathbb{R}$. Moreover, it satisfies the following a priori estimates:

$$\|u\|_{m+2,\gamma} \lesssim \|f\|_{m,-\gamma}, \qquad \sum_{n=1}^{N_\omega} |k_i| + \|W\|_{m+2,-\gamma} \lesssim \|f\|_{m,-\gamma}.$$

In Lemma 8.1, the singular parts consist of the singular functions for $i \in \mathbb{N}$ given in polar coordinates (r, φ) as

$$s_i(r, \varphi) = \eta(r) r^{\frac{i\pi}{\omega}} \sin(\frac{i\pi}{\omega}\varphi),$$

where the smooth cut-off function $\eta(r)$ is one in a neighborhood $\Omega' \subset \Omega$ of the singularity and the coefficients k_i are called the stress intensity factors, as detailed in [21]. For further details we refer to the works of Kondratiev [96] and Maz´ja, Plamenevskii [109] as well as to the works of Grisvard [67] and Blum, Dobrowol-

ski [21]. Since the first singular function s_1 is not in $H^2(\Omega)$ or higher, also the solution of the Poisson equation (29) is in general not in $H^2(\Omega)$. Thus in the presence of reentrant corners, optimal convergence in the L^2-norm can in general not be achieved by standard methods with quasi-uniform refinement since the solution does not lie in $H^2(\Omega)$.

The results in Table 8.1 show this behavior in case of the exact solution given by $u = s_1(r,\phi) + s_2(r,\phi)$ and $f = 0$ on the L-shape domain depicted in Figure 8.1. It can also be observed that the change to higher order ansatz functions does not influence the convergence rate.

	$k=1$		$k=2$	
level	$\|u-u_h\|_0$	rate	$\|u-u_h\|_0$	rate
1	1.1606e-01	-	1.7134e-02	-
2	4.1410e-02	1.49	7.0661e-03	1.28
3	1.5316e-02	1.44	2.7236e-03	1.38
4	5.8013e-03	1.40	1.0453e-03	1.38
5	2.2296e-03	1.38	4.0414e-04	1.37
6	8.6488e-04	1.37	1.5751e-04	1.36
7	3.3764e-04	1.36	6.1766e-05	1.35
8	1.3242e-04	1.35	2.4323e-05	1.34

Table 8.1: Convergence rates on an L-shape domain for order one and two ansatz functions.

The following result will show that even employing a weighted Sobolev norm, which reduces the influence of the neighborhood of the singularity, does not help to overcome the pollution effect [11, 21, 22, 155].

Lemma 8.2 (Pollution effect)**.** *Let u be the solution of (29) with $f \in H^0_{-\alpha}(\Omega)$ for some $\alpha > -1$. If $k_1 \neq 0$ in (30), then*

$$\|u-u_h\|_{0,\alpha} \gtrsim \|\nabla(u-u_h)\|_0^2 \gtrsim h^{\frac{2\pi}{\omega}}.$$

Proof. The first inequality is given by

$$\begin{aligned}\|\nabla(u-u_h)\|_0^2 &= |a(u,u) - a(u_h,u_h)| \\ &= |f(u) - f(u_h)| \leq \|f\|_{0,-\alpha}\|u-u_h\|_{0,\alpha},\end{aligned}$$

where we use that f is in $H^0_{-\alpha}(\Omega)$. For the second inequality we refer to [53].

□

When performing the calculations from Table 8.1 again, but this time with the

weighted Sobolev norm, we still observe suboptimal convergence rates for the solution on the whole domain in Table 8.2. This is independent of the particular choice of the weight α. Thus only changing the norm does not improve our convergence rates.

	$k=1$		$k=1$		$k=2$		$k=2$	
level	$\|u-u_h\|_{0,\alpha}$	rate	$\|u-u_h\|_{0,\alpha}$	rate	$\|u-u_h\|_{0,\alpha}$	rate	$\|u-u_h\|_{0,\alpha}$	rate
1	9.5228e-02	-	5.8391e-02	-	8.6233e-03	-	6.0284e-03	-
2	2.9239e-02	1.70	1.4086e-02	2.05	1.9374e-03	2.15	1.0526e-03	2.52
3	9.6829e-03	1.59	4.2196e-03	1.74	6.1894e-04	1.65	3.7698e-04	1.48
4	3.4360e-03	1.49	1.4528e-03	1.54	2.3724e-04	1.38	1.4885e-04	1.34
5	1.2798e-03	1.42	5.3821e-04	1.43	9.3743e-05	1.34	5.9031e-05	1.33
6	4.9065e-04	1.38	2.0664e-04	1.38	3.7180e-05	1.33	2.3422e-05	1.33
7	1.9108e-04	1.36	8.0687e-05	1.36	1.4753e-05	1.33	9.2944e-06	1.33
8	7.5045e-05	1.35	3.1757e-05	1.35	5.8546e-06	1.33	3.6884e-06	1.33

Table 8.2: Rates in weighted norms of the Poisson equation with $\alpha = 0.3333$ and $\alpha = 1.3333$ for the first two columns with linear ansatz functions and $\alpha = 1.3333$ and $\alpha = 2.3333$ for the last two columns with second order ansatz functions.

The above results do not only hold for the "simple" case of the Poisson equation, but are also valid for all other elliptic equations, such as the elasticity equation given by Equation (3) with u composed of singular functions as stated in [138] and $f = 0$. This is shown by the results depicted in Table 8.3 for ansatz functions of order $k = 1$ and $k = 2$.

	$k=1$		$k=2$	
level	$\|u-u_h\|_0$	rate	$\|u-u_h\|_0$	rate
2	2.0194e-01	-	4.1246e-02	-
3	8.0865e-02	1.32	1.6494e-02	1.32
4	3.3635e-02	1.27	6.9601e-03	1.24
5	1.4310e-02	1.23	3.0019e-03	1.21
6	6.1613e-03	1.22	1.3046e-03	1.20
7	2.6693e-03	1.21	5.6847e-04	1.20

Table 8.3: Convergence rates for the isotropic elasticity equation on an L-shape domain with ansatz functions of order one and two.

Also in the case of eigenvalue problems the pollution effect can be observed, and the results also enlight that the eigensolutions can have different regularities. This can be seen in Table 8.4 and Table 8.5, where the eigenvalues show different convergence rates for ansatz functions of order one and two, respectively. The non-optimal rates are written in bold.

	1.EV		2.EV		3.EV		4.EV		5.EV	
level	$\lvert\lambda - \lambda_h\rvert$	rate	$\lvert\lambda - \lambda_h\rvert$	rate	$\lvert\lambda - \lambda_h\rvert$	rate	$\lvert\lambda - \lambda_h\rvert$	rate	$\lvert\lambda - \lambda_h\rvert$	rate
1	0.4798	-	0.4392	-	1.6788	-	2.1304	-	4.4007	-
2	0.1449	**1.73**	0.1555	1.50	1.0362	0.70	1.1693	0.87	1.6094	1.45
3	0.0493	**1.55**	0.0439	1.82	0.2984	1.80	0.3161	1.89	0.4384	1.88
4	0.0178	**1.47**	0.0116	1.92	0.0787	1.92	0.0804	1.97	0.1133	1.95
5	0.0067	**1.42**	0.0030	1.96	0.0201	1.97	0.0202	1.99	0.0287	1.98

Table 8.4: Convergence rates for the Laplace eigenvalue problem on an L-shape domain for ansatz functions of order one.

	1.EV		2.EV		3.EV		4.EV		5.EV	
level	$\lvert\lambda - \lambda_h\rvert$	rate	$\lvert\lambda - \lambda_h\rvert$	rate	$\lvert\lambda - \lambda_h\rvert$	rate	$\lvert\lambda - \lambda_h\rvert$	rate	$\lvert\lambda - \lambda_h\rvert$	rate
1	0.0414	-	0.0547	-	0.7611	-	0.9702	-	0.7921	-
2	0.0173	**1.26**	0.0046	**3.56**	0.0457	4.06	0.0498	4.28	0.0658	**3.59**
3	0.0070	**1.30**	0.0005	**3.26**	0.0031	3.89	0.0033	3.93	0.0048	**3.78**
4	0.0028	**1.32**	6.08e-05	**2.99**	0.0002	3.96	0.0002	3.97	0.0004	**3.76**
5	0.0011	**1.33**	8.61e-06	**2.82**	1.23e-05	4.00	1.31e-05	4.00	2.90e-05	**3.60**

Table 8.5: Convergence rates for the Laplace eigenvalue problem on an L-shape domain for ansatz functions of order two.

8.2. Basic methods for singularities: graded mesh technique

Corner singularities, as introduced before, pollute the solution, destroy the optimal convergence behavior and therefore require special numerical treatment. As also seen before in Section 8.1, quasi-uniform mesh refinements or weighted spaces are not sufficient to overcome the pollution effect. Several methods have been developed to improve the energy approximation in the neighborhood of a singularity. Among them are graded meshes as described in [2, 3, 4] and adaptive meshes such as in [3, 6, 148]. For adaptive meshes error estimators play an important role, which leads to an increased computational cost. It is also possible to add suitable singular functions to the finite element space [7, 21, 155].

In the following section we introduce graded meshes, following [2]. As mentioned above, singularities in the geometry of a domain constitute an important challenge on the accuracy of our numerical approximations. In this context, local mesh grading allows for mesh refinement where it is required while, in contrast to uniform mesh refinement, keeping the computation cost at a reasonable level. We consider local mesh grading in two dimensions, where the singular part s_i of the solution is

written in a polar coordinate representation as described in Section 8.1

$$s_i = k_i \eta(r) r^{\frac{i\pi}{\omega}} \sin(\frac{i\pi}{\omega}\varphi),$$

with the stress intensity factor k_i and the smooth cut-off function $\eta(r)$. We need to find a coordinate transformation, such that the points x with distance to the corner C, which is for simplicity reasons assumed to lie in $(0,0)$, less than R_0 will be transformed onto themselves. We use the transformation from r, φ to ρ, φ

$$\left(\frac{r}{R_0}\right)^{\mathcal{G}} = \frac{\rho}{R_0}, \qquad \mathcal{G} \in (0,1], \tag{31}$$

as introduced in [2]. We can now express s_i in terms of ρ and φ as

$$s_i = s_i(\rho,\varphi) = \bar{k}_i \bar{\eta}(\rho) \rho^{\frac{i\pi}{\omega\mathcal{G}}} \sin(\frac{i\pi}{\omega}\varphi),$$

obtaining the derivatives $\frac{\partial^{k+1} s_i}{\partial \rho^{k+1}} \in L^2$ for $k \geq 1$ and

$$\mathcal{G} < \frac{\pi}{k\omega}. \tag{32}$$

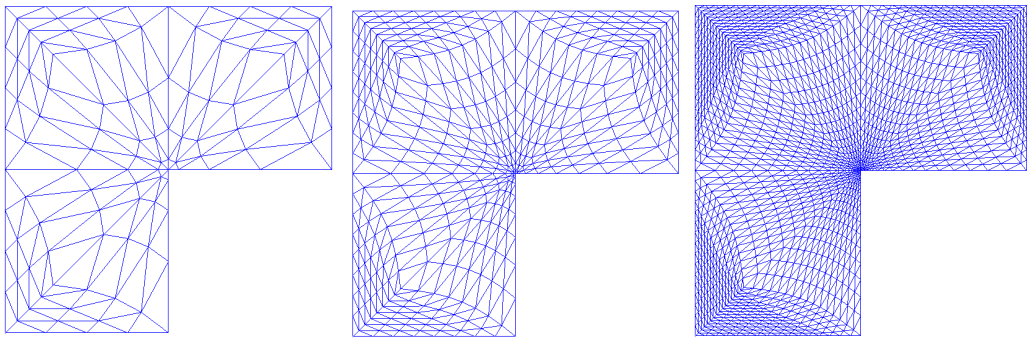

Figure 8.2: Graded meshes with different mesh sizes and grading parameter 1/2.

The smooth solution of the transformed problem still requires several calculations to be performed, for example an adequate transformation of input data. Thus we would like to reduce the computational cost and instead of transforming the problem, we rather transform the mesh by an inverse mapping.In order to do that, the mesh around the corner is created in the coordinates transformed by (31), then the coordinates are transformed back on the domain of computation and all calculations are performed in the original coordinate system. The transformed element diameter diam(e) depends on the distance of an element e to the corner

coordinate point C. We distinguish between elements which have a vertex at the corner and those who do not. For the elements that have a vertex in the corner the derivation of the relationship yields

$$\operatorname{diam}(e) \sim h^{\frac{1}{\mathcal{G}}}$$

since in the transformed domain these are contained in the circle with radius $\rho = h$. For the other elements $\rho_o - \rho_i \sim h$, with ρ_o and ρ_i the outer and inner radius of the elements, respectively. Thus with $r_o^{\mathcal{G}} = \rho_o$, $r_i^{\mathcal{G}} = \rho_i$ and $r_o - r_i \sim \operatorname{diam}(e)$ we have

$$\frac{h}{\operatorname{diam}(e)} \sim \frac{r_o^{\mathcal{G}} - r_i^{\mathcal{G}}}{r_o - r_i} = \mathcal{G} r_*^{\mathcal{G}-1}$$

for $r_* \in (r_i, r_o)$ and $r_* \sim \operatorname{dist}(e, C)$. All in all we obtain for the grid width h and the refinement parameter $\mathcal{G}$ that

$$\operatorname{diam}(e) \sim \begin{cases} h^{\frac{1}{\mathcal{G}}}, & C \in \bar{e} \\ h \operatorname{dist}(e, C)^{1-\mathcal{G}}, & C \notin \bar{e} \end{cases}.$$

For the error estimates in the H^1 and L^2 norms we find according to [2] that for $\mathcal{G}$ as in (32) it holds that

$$\|u - u_h\|_1 \lesssim h, \qquad \text{and} \qquad \|u - u_h\|_0 \lesssim h^2.$$

An easy way to construct these meshes is to use the transformation given by

$$\begin{aligned} r &:= [(x_1 - X_1)^2 + (x_2 - X_2)^2]^{1/2}, \\ x_1 &:= X_1 + (x_1 - X_1)(r/R_0)^{-1+1/\mathcal{G}}, \\ x_2 &:= X_2 + (x_2 - X_2)(r/R_0)^{-1+1/\mathcal{G}}. \end{aligned}$$

In the following we want to show the influence of graded meshes with different grading parameters in Table 8.6 and Table 8.7. We highlight the importance of the grading parameter and condition (32). For the simulation we again use the model problem of the Poisson equation and the setting as in the simulations of Section 8.1, where we obtain the suboptimal convergence rates. The only difference in the underlying setting is the graded mesh depicted in Figure 8.2. We depict the influence of the grading parameter in Table 8.6. It is obvious that if condition (32) for the grading factor is valid, we obtain optimal rates as expected from the theory. Otherwise we obtain slightly improved (in comparison to the untreated meshes)

		$\mathcal{G} = 1/4$		$\mathcal{G} = 2/4$		$\mathcal{G} = 3/4$	
level	DoFs	$\|u - u_h\|_0$	rate	$\|u - u_h\|_0$	rate	$\|u - u_h\|_0$	rate
1	11	1.1606e-01	-	1.1606e-01	-	1.1606e-01	-
2	33	8.3587e-02	0.47	4.2787e-02	1.44	3.5589e-02	1.71
3	113	3.5642e-02	1.23	1.2558e-02	1.77	1.0954e-02	1.70
4	417	1.1566e-02	1.62	3.3742e-03	1.90	3.3690e-03	1.70
5	1601	3.2601e-03	1.83	8.7588e-04	1.95	1.0337e-03	1.70
6	6273	8.5712e-04	1.93	2.2377e-04	1.97	3.1582e-04	1.71
7	24833	2.1886e-04	1.97	5.6678e-05	1.98	9.5988e-05	1.72
8	98817	5.5263e-05	1.99	1.4284e-05	1.99	2.9024e-05	1.73

Table 8.6: L^2-error for the simulations performed using the graded mesh with grading parameters 1/4, 2/4 and 3/4.

but still suboptimal convergence rates. In Table 8.7 we obtain the same results using weighted norms, which means again that the weighted norm does not help to obtain better rates. Furthermore it should be noted that the numbers of elements

		$\mathcal{G} = 1/4$		$\mathcal{G} = 2/4$		$\mathcal{G} = 3/4$	
level	DoFs	$\|u - u_h\|_{0,\alpha}$	rate	$\|u - u_h\|_{0,\alpha}$	rate	$\|u - u_h\|_{0,\alpha}$	rate
1	11	9.5228e-02	-	9.5228e-02	-	9.522803e-02	-
2	33	6.7712e-02	0.49	3.5065e-02	1.44	2.6564e-02	1.84
3	113	2.9564e-02	1.20	1.0202e-02	1.78	7.6703e-03	1.79
4	417	9.8350e-03	1.59	2.7176e-03	1.91	2.2542e-03	1.77
5	1601	2.8243e-03	1.80	7.0119e-04	1.95	6.6930e-04	1.75
6	6273	7.5094e-04	1.91	1.7841e-04	1.97	1.9953e-04	1.75
7	24833	1.9295e-04	1.96	4.5065e-05	1.99	5.9526e-05	1.75
8	98817	4.8891e-05	1.98	1.1337e-05	1.99	1.7741e-05	1.75

Table 8.7: Weighted L^2-error for the simulations performed using the graded mesh with grading parameters 1/4, 2/4 and 3/4.

and nodes are not increased. Only the positions of the already existing nodes have been changed. Thus we do not observe an increase in the degrees of freedom, there is only an increased cost for the generation of the graded mesh. It should also be noted that the graded mesh also modifies the shape of the elements.

9. Energy correction methods

Several numerical schemes have been developed to overcome the pollution, such as graded meshes as depicted above or adaptive meshes. A drawback of these methods is that they employ a deep change in the meshes, such as grading the mesh towards the singular point or evaluating an error estimator for the adaptive mesh generation in order to set up the mesh refinement. Furthermore, all these proce-

dures are costly and either require good expertise in mesh generation or increase the implementation cost when adaptive procedures are used.

A further possible scheme to obtain optimal convergence rates is the energy correction method, which will be presented in the following.

9.1. Introduction to the energy correction method

The energy correction method was first used in the context of the finite difference scheme [182], where a local modification with a scalar value was used to correct the energy defect. This was then developed further by [144, 146] and then extended to finite elements in the papers [53, 145] on the Laplace equation with linear ansatz functions. Using this procedure only requires a small change, namely a small local modification of the bilinear form in the vicinity of the singular point, which can be interpreted as a relaxation of the stiffness in the area. The local modification will be denoted by $c_h(u, v)$ and the neighborhood of the singularity is defined as

$$\mathcal{S}_h := \bigcup \bar{T} \qquad \text{for } T \in \mathcal{T}_h \text{ with } \operatorname{dist}(T, 0) \leq \kappa h,$$

using the constant parameter $\kappa > 0$ which determines the amount of element rings in the chosen neighborhood. The modification term $c_h(\cdot, \cdot)$ is defined only on a

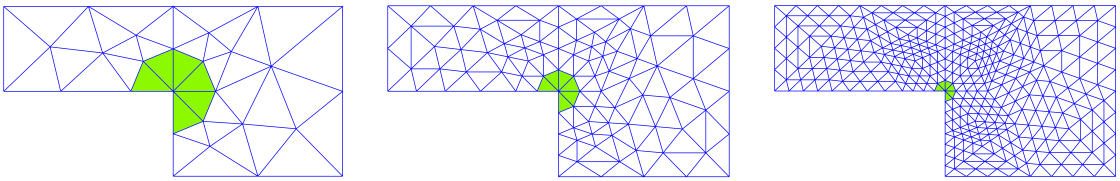

Figure 9.1: Graphical illustration of the local uniformness of the initial mesh and two sequent refinements. By the green area we depict the $\mathcal{S}_h$-surrounding whose support shrinks with $h \to 0^+$.

h-surrounding of the reentrant corner $\mathcal{S}_h$, see Figure 9.1, i.e., its support shrinks with decreasing h.

The modified bilinear form can be stated as

$$a_h(u, v) = a(u, v) - c_h(u, v)$$

and recovers optimal convergence in the weighted norm while only using a uniform mesh refinement. Furthermore using post-processing, it is also possible to achieve

optimal convergence in the L^2-norm [53].

Using the modified bilinear form with linear order, we now obtain a modified Galerkin approximation of the form:
Find $u_h^{\mathrm{m}} \in V_h^1$ such that

$$a_h(u_h^{\mathrm{m}}, v_h) = (f, v_h), \qquad v_h \in V_h^1.$$

The standard Galerkin approximation u_h is included as the special case $c_h(\cdot,\cdot) \equiv 0$ in the bilinear form.

A standard modification $c_h(\cdot,\cdot)$ has to satisfy the properties coercivity, continuity and symmetry:

(C1) $a(u,u) - c_h(u,u) \gtrsim \|u\|_1^2$ for all $u \in H_0^1(\Omega)$.

(C2) $c_h(u,v) \lesssim \|\nabla u\|_{L^2(\mathcal{S}_h)} \|\nabla v\|_{L^2(\mathcal{S}_h)}$ for all $u, v \in H_0^1(\Omega)$.

(C3) $c_h(u,v) = c_h(v,u)$ for all $u, v \in H_0^1(\Omega)$.

We also need the mesh to be symmetric around the corner singularity if $\omega > 3/2\pi$, see e.g. Figure 9.3, which is expressed in the condition

(G2) The set of elements $T \subset \mathcal{T}_H$ for which $0 \in \bar{T}$ constitutes a symmetric partition, i.e. the coarse mesh $\mathcal{T}_H$ is locally symmetric around the singular point.

The following theorem on the convergence is stated in [53] and shows that full convergence in weighted Sobolev norms can be recovered using a modified bilinear form as introduced above:

Theorem 4. *Let $f : H^0_{-\alpha}(\Omega)$ for some $1 - \frac{\pi}{\omega} < \alpha < 1$, and assume that (C1)–(C3) are valid and that (G2) holds if $\frac{3}{2}\pi < \omega < 2\pi$. If, in addition, the modification satisfies*

$$a(s_1 - s_{1,h}^{\mathrm{m}}, s_1 - s_{1,h}^{\mathrm{m}}) - c_h(s_{1,h}^{\mathrm{m}}, s_{1,h}^{\mathrm{m}}) = \mathcal{O}(h^2), \tag{33}$$

then convergence rates of optimal order hold i.e.

$$\|\nabla(u - u_h^{\mathrm{m}})\|_{0,\alpha} \lesssim h\|f\|_{0,-\alpha} \qquad \textit{and} \qquad \|u - u_h^{\mathrm{m}}\|_{0,\alpha} \lesssim h^2\|f\|_{0,-\alpha}.$$

A possible choice of the modification of the bilinear form is also introduced in [53] as

$$c_h(u,v) = \gamma \int_{\mathcal{S}_h} \nabla u \cdot \nabla v \, dx,$$

where the correction parameter γ has to fulfill $0 \leq \gamma \leq \frac{1}{2}$ such that the ellipticity of $a_h(\cdot,\cdot)$ is preserved. This allows us to define the pollution function $\mathrm{g}_{h,1}(\gamma)$ for the linear case as

$$\mathrm{g}_{h,1}(\gamma) := a(s_1 - R_h^{\mathrm{m}}(\gamma)s_1, s_1 - R_h^{\mathrm{m}}(\gamma)s_1) - c_h(R_h^{\mathrm{m}}(\gamma)s_1, R_h^{\mathrm{m}}(\gamma)s_1) \tag{34}$$

where $R_h^{\mathrm{m}}(\gamma)s_1 \in V_h^1$ denotes the modified Galerkin approximation of s_1, which is taken to be

$$a(R_h^{\mathrm{m}}(\gamma)s_1, v_h) - c_h(R_h^{\mathrm{m}}(\gamma)s_1, v_h) = a(s_1, v_h), \quad v_h \in V_h^1.$$

There are now two possibilities to obtain the correction parameter γ from the pollution function, namely computing γ as the root of an implicitely given function and using a nested-Newton method as described in [145]. For every mesh $\mathcal{T}_h$, an optimal γ_h can be found using the condition $g_{h,1}(\gamma_h) = 0$. Furthermore it is shown in [53] that there is an asymptotic $\gamma^\star$ such that (33) is fulfilled on all levels.

Let us now recall the L-shape domain $\Omega := (-1,1)^2 \setminus ([0,1] \times [-1,0])$ with the singularity in $(0,0)$ and the interior angle $\omega = 3/2\pi$, which has been simulated without correction in Section 8.1 and with graded mesh in Section 8.2. We again consider numerically the Poisson problem with Dirichlet boundary conditions on Ω given as

$$-\Delta u = 0 \text{ in } \Omega, \qquad u = s \text{ on } \partial\Omega, \tag{35}$$

where $s := s_1(r,\phi) + s_2(r,\phi) := r^{\frac{2}{3}}\sin(\frac{2\phi}{3}) + r^{\frac{4}{3}}\sin(\frac{4\phi}{3})$.

		$\gamma^\star = 0.1194$		$\gamma^\star = 0.1194$		$\gamma = 0.1$		$\gamma = 0.1$	
level	DoFs	$\|u - u_h^{\mathrm{m}}\|_0$	rate	$\|u - u_h^{\mathrm{m}}\|_{0,\alpha}$	rate	$\|u - u_h^{\mathrm{m}}\|_0$	rate	$\|u - u_h^{\mathrm{m}}\|_{0,\alpha}$	rate
1	11	1.1336e-01	-	8.8439e-02	-	1.1317e-01	-	8.8240e-02	-
2	33	3.6735e-02	1.63	2.5048e-02	1.82	3.6684e-02	1.63	2.4827e-02	1.83
3	113	1.0880e-02	1.76	6.2414e-03	2.00	1.1127e-02	1.72	6.3627e-03	1.96
4	417	3.2021e-03	1.76	1.5050e-03	2.05	3.3915e-03	1.71	1.6308e-03	1.96
5	1601	9.6287e-04	1.73	3.6594e-04	2.04	1.0617e-03	1.68	4.4065e-04	1.89
6	6273	2.9529e-04	1.71	9.0338e-05	2.02	3.4122e-04	1.64	1.2919e-04	1.77
7	24833	9.1684e-05	1.69	2.2566e-05	2.00	1.1228e-04	1.60	4.1572e-05	1.64
8	98817	2.8661e-05	1.68	5.6770e-06	1.99	3.7814e-05	1.57	1.4523e-05	1.52

Table 9.1: Energy-corrected L-shaped domain with linear order ansatz functions, errors in the L^2- and weighted L^2-norm.

Table 9.1 depicts the results obtained with the energy correction method. In the first two columns a fixed optimal correction parameter is used, such that

$g_{h,1}(\gamma^\star) = O(h^2)$ holds on all the refinement levels. In the last two columns a too rough correction parameter approximation was chosen, such that $g_{h,1}(\gamma) = O(h^2)$ is not fulfilled. As it can be seen, optimal convergence rates are achieved with an adequate parameter given by $\gamma^\star$, and without such a parameter the rates collapse on the finer levels.

Let us at this point shortly compare the presented method to the graded mesh method. Both do not change the amount of degrees of freedom, see Tables 8.6 and 9.1, and both are very sensible to the correction and grading parameter. An advantage of the energy correction method is the trivial change in the stiffness matrix, while the mesh grading is more complex and changes the element shapes. In contrast, the estimation of the correction parameter is more complex for the energy correction and it demands knowledge of the singular functions of the problem. Nevertheless it should be noted that the energy correction method has a smaller error on the same refinement level with the same amount of degrees of freedom and it does not change the shape of the elements.

Remark 9.1. *The results from above can be extended to three-dimensional domains, as long as these are obtained from the two-dimensional ones by an extension in z-direction. Such geometries can be L- or T-shape domains. In these cases the correction is performed on a cylinder-shaped domain around the reentrant edge and the correction parameters from the two-dimensional case can be used. For the three-dimensional L-shape domain we depict our results in Table 9.2 for the Poisson equation (35). In contrast to the two dimensional case, where we use a triangular mesh, we use a hexahedral mesh, which results in the different correction parameter.*

		$\gamma = 0.0$		$\gamma^\star = 0.065710$	
level	DoFs	$\|u - u_h\|_{0,\alpha}$	rate	$\|u - u_h^{\mathrm{m}}\|_{0,\alpha}$	rate
1	160	0.0016164	-	0.0011503	-
2	1408	0.00056148	1.46	0.00027464	1.98
3	11776	0.0002111	1.38	6.7132e-05	1.99
4	96256	8.1853e-05	1.35	1.6674e-05	1.99
5	778240	3.2139e-05	1.34	4.1739e-06	1.99
6	6258688	1.269e-05	1.34	1.0488e-06	1.99

Table 9.2: L^2-errors and convergence rates for the energy-corrected three-dimensional L-shape domain.

Remark 9.2. *Energy correction methods are not only adequate for the Laplace problem, but also a good tool for other equations such as the linear elasticity equation,*

which is used in our timber building application. The method presented above would have to be adapted to the specific singular functions of the linear elasticity [138]. Thus in Table 9.3 we only depict that optimal convergence rates can be obtained after the successful application of the energy correction method for the isotropic case. For comparison the uncorrected results can be found in Table 8.3.

level	$\|u - u_h^{\mathrm{m}}\|_{0,\alpha}$	rate
2	1.8270e-01	-
3	4.7118e-02	1.96
4	1.1721e-02	2.01
5	2.9297e-03	2.00
6	7.3294e-04	2.00
7	1.8308e-04	2.00

Table 9.3: L^2-errors and convergence rates after application of the energy correction method on the isotropic linear elasticity equation.

9.2. Energy correction method with high order ansatz functions

The considerations presented in this section can be found in "Higher order energy-corrected finite element methods" by the author together with P. Pustejovska and B. Wohlmuth, in preparation, 2016, [79].

In this section, an extension of the results for linear ansatz functions above to higher order ansatz functions will be presented. We expect the order of convergence to increase. To be precise the full h^{k+1} convergence order of the approximation can be reproduced in certain weighted norms (see Theorem 9.3) or by a post-processing in the standard L^2-norm (see Corollary 9.4). One can show that the pollution effect is contained in the scheme if and only if the defect function given by (34) converges suboptimally. More on the pollution effect and its relation to the pollution function can be found in all previous energy correction method literature, e.g. [53, 145].

If we set

$$\tilde{g}_h(w_1, w_2) := a(w_1 - w_{1h}^{\mathrm{m}}, w_2 - w_{2h}^{\mathrm{m}}) - c_h(w_{1h}^{\mathrm{m}}, w_{2h}^{\mathrm{m}}),$$

we can define our pollution function as $g_h(w) := \tilde{g}_h(w, w)$. Nevertheless, not all parts of the pollution function of $g_h(u)$ are of a decreased order. To see this, we refer to the expansion Lemma 8.1, which is also an important ingredient of the

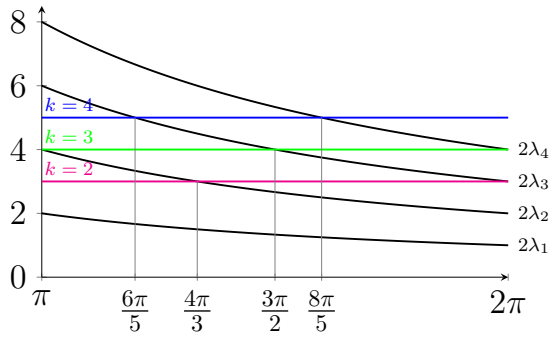

Figure 9.2: Graphical illustration of the total number of essential pollutions $g_h(s_i)$. Namely, the value $\mathcal{K}$ is determined by the number of thick lines below the horizontal approximation line. For example, in the case of the approximation order $k=4$, we have: $\mathcal{K}=2$ for $\omega \in (\pi, \frac{6}{5}\pi]$, $\mathcal{K}=3$ for $\omega \in (\frac{6}{5}\pi, \frac{8}{5}\pi]$, and $\mathcal{K}=4$ for $\omega \in (\frac{8}{5}\pi, 2\pi]$. The colored lines represent $k+1$ bounds.

proof of our main Theorem 9.3.

Assuming the expansion of the solution u and the approximative solution u_h^{m} with the limit N_u, we define a correction order $\mathcal{K}$ for the approximative order k and angle ω as:

$$\mathcal{K} := \max_{i\in\mathbb{N},\ i<(k+1)\frac{\omega}{2\pi}} i \leqslant k. \tag{36}$$

Now we can decompose the pollution function $g_h(u)$ as:

$$g_h(u) = \sum_{i=1}^{\mathcal{K}} (k_i^u)^2 g_h(s_i) + \sum_{i\neq j=1}^{N_u} k_i^u k_j^u\, \tilde{g}_h(s_i, s_j) + \text{regular terms}. \tag{37}$$

Here $g_h(s_i)$ are called the essential pollutions due to their unconditionally reduced convergence order. The possible pollution of $\tilde{g}_h(s_i, s_j)$ is non-essential in the sense that it can be balanced by some local symmetry properties of the mesh. Either way, we aim to construct the modification $c_h(\cdot,\cdot)$ in such a way that the pollution in the error of approximation of all terms in (37) will diminish. The number $\mathcal{K}$ introduced above gives the number of correction parameters needed for the energy correction and it can be easily determined from Figure 9.2.

Furthermore for the correction we need additional assumptions on the mesh. Where in the linear case we only needed the (G2) mirror symmetry of the mesh, here we need further assumptions. In the following, we distinguish between several cases of combinations between ω and the approximation order k and assign to them

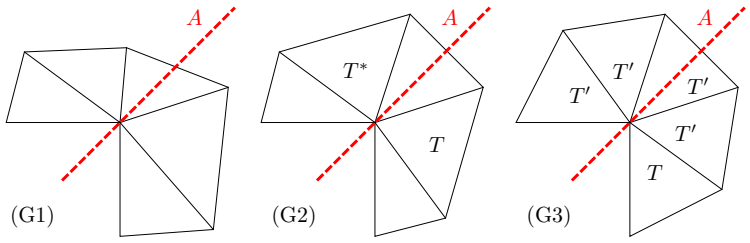

Figure 9.3: Symmetry conditions of the local mesh at the reentrant corner. For simplicity, we depict only a first layer of elements. The dashed line A represents the bisectional axis of the angle ω, element T^* represents the mirror image across A of T, and T' represent the rotation of T around the reentrant corner.

three different mesh properties (G1)–(G3), which are schematically represented in Figure 9.3 for a typical example $\omega = 3/2\pi$. Note that (G1)–(G3) are assumed on the local neighborhood $\mathcal{S}_h$ of the coarsest refinement level and thus, by uniform refinement, they will automatically hold on each $\mathcal{S}_h$. More precisely, (G1) represents a general mesh without any specific symmetry properties, (G2) stands for a mesh with a local mirror-symmetry, i.e., to each element $T \in \mathcal{S}_h$ exists another $T^* \in \mathcal{S}_h$ which is a mirror image of T across the bisectional axis A. The last property (G3) represents a full local symmetry at the singular corner in the sense that $\mathcal{S}_h$ is composed of one base element which is then rotated around the reentrant corner. We say that an initial mesh has the (U)-property which depends on k and ω if

$$\begin{cases} k = 1 \quad \text{and} \quad \omega < \frac{3}{2}\pi : & \text{(G1)}, \\ k = 1 \quad \text{and} \quad \omega \geqslant \frac{3}{2}\pi, \ \text{or } k = 2 \text{ and } \omega < \frac{4}{3}\pi : & \text{(G2)}, \\ k = 2 \quad \text{and} \quad \omega \geqslant \frac{4}{3}\pi, \ \text{or } k \geqslant 3 : & \text{(G3)}. \end{cases} \tag{U}$$

Associated with the (U)-property of a mesh, we make here an assumption on the interpolation property. If the mesh satisfies the (U)-property, we assume that for $i\pi/\omega + j\pi/\omega < k + 1$ we find

$$\int_\Upsilon \nabla s_j \cdot \nabla I_h^k s_i \, dx = \int_\Upsilon \nabla s_j \cdot \nabla s_i \, dx = 0, \qquad i \neq j, \tag{38}$$

where Υ is the domain $\mathcal{S}_h$ of the coarsest refinement level. We call this assumption (U)-assumption. We point out that Equation (38) does not hold for arbitrary shaped meshes at the re-entrant corner. However, all our numerical study tests have shown that the (U)-property is sufficient for Equation (38) to hold, see Table 9.8. Later we will show numerically that under the (U)-assumption the mixed

terms $\tilde{g}_h(s_i, s_j)$, $i \neq j = 1, ..., N_u$, converge optimally, and thus, the global pollution in the error originates strictly from $g_h(s_i)$ terms, $i \leqslant \mathcal{K}$. Hence, we call $\mathcal{K}$ the correction order, since it represents the number of conditions we lay on the modification. As it was already mentioned its value can be simply read out from Figure 9.2. Now, we are ready to formulate the main theorem on the order of convergence.

Theorem 9.3 (Main theorem)**.** *Let $k \in \mathbb{N}$ denote the polynomial degree of the modified scheme, $f \in H^{k-1}_{-\tilde{\alpha}}(\Omega)$ for some $\tilde{\alpha} > 1 - \frac{\pi}{\omega}$, and let ω be the angle of the reentrant corner. Also, let us assume that (C1)–(C3) and the* (U)*-assumption hold and moreover that the modification $c_h(\cdot, \cdot)$ satisfies:*

$$g_h(s_i) = \mathcal{O}(h^{k+1}) \qquad \text{for all } i \leqslant \mathcal{K}. \tag{39}$$

Then, we have the following optimal convergence results of the modified approximation in the weighted norms with $\alpha = \tilde{\alpha} + k - 1$:

$$\|u - u_h^{\mathrm{m}}\|_{0,\alpha} \lesssim h^{k+1} \|f\|_{k-1,-\tilde{\alpha}} \quad \text{and} \quad \|\nabla(u - u_h^{\mathrm{m}})\|_{0,\alpha} \lesssim h^{k} \|f\|_{k-1,-\tilde{\alpha}}.$$

Proof. For the proof of these properties, we use techniques introduced for example in [53] concerning energy corrections. For the detailed proof we again refer to the final version of [79]. □

Furthermore it is possible to obtain by a post-processing step full order of convergence in the standard L^2-norm. This is stated by the following corollary from [79], where we define by

$$k_{h,i}^{u,\mathrm{m}} := \frac{1}{i\pi} \int_\Omega (f s_i + u_h^{\mathrm{m}} \Delta s_{-i})\, dx$$

the stress intensity factor.

Corollary 9.4. *Let us assume that the assumptions of Theorem 9.3 hold. Then, the post-processed solution defined as*

$$u_h^{pos} := u_h^{\mathrm{m}} + \sum_{i=1}^{\mathcal{K}} k_{h,i}^{u,\mathrm{m}} (s_i - s_{i,h}^{\mathrm{m}})$$

converges in standard L^2-norm as

$$\|u - u_h^{pos}\|_0 \lesssim h^{k+1}.$$

In the following we will illustrate how the correction term $c_h(\cdot,\cdot)$ could be constructed. The main assumption of Theorem 9.3 was (39), namely $g_h(s_i) = \mathcal{O}(h^{k+1})$, $i < (k+1)\frac{\omega}{2\pi}$. This means choosing a correction term $c_h(\cdot,\cdot)$ in such a way that (39) is satisfied guarantees the optimal convergence rates of the modified scheme. We recall that $\mathcal{K}$ from (36) refers to the total number of essential pollutions $g_h(s_i)$ contributing to the total pollution. Also, we define the radial element layers $\mathcal{S}_h^i$ with respect to the reentrant corner placed at $\mathbf{0}$ as:

$$\mathcal{S}_h^1 := \{T \in \mathcal{T}_h : \ \mathbf{0} \in \partial T\}, \qquad \mathcal{S}_h^i := \{T \in \mathcal{T}_h : \ \partial T \cap \partial \mathcal{S}_h^{i-1} \neq \emptyset\}, \ i = 2, ..., \mathcal{K}.$$

Following the basic concept from previous studies on energy correction methods, we can simply adapt the construction of $c_h(\cdot,\cdot)$ to our higher order case and define

$$c_h^R(u,v) := \sum_{i=1}^{\mathcal{K}} \int_{\mathcal{S}_h^i} \gamma_i^R \nabla u \cdot \nabla v \, dx, \qquad \mathcal{S}_h^R := \operatorname{int}\left(\cup_{i=1}^{\mathcal{K}} \overline{\mathcal{S}_h^i}\right), \tag{40}$$

where the constants γ_i^R are called correction parameters. We also call the scheme with c_h^R a method with (radial) layer correction, since $\mathcal{K}$-layers of elements $\mathcal{S}_h^i$ are involved in the definition of the modification. It is clear that with higher k the support of $c_h^R(\cdot,\cdot)$ is significantly larger, which can cause some difficulties by the initial mesh generation with the U-property. We also present an alternative approach of a function correction for which, in contrast to the layer-modification, we need only a single layer-support, independent of k or ω. Namely, we define:

$$c_h^F(u,v) := \sum_{i=1}^{\mathcal{K}} \int_{\mathcal{S}_h^1} \gamma_i^F \hat{r}^{i-1} \nabla u \cdot \nabla v \, dx, \qquad \mathcal{S}_h^F = \mathcal{S}_h^1, \tag{41}$$

where $\hat{r} \in [0,1]$ is the h-scaled distance from the origin, i.e., $\hat{r} = r/h$.

We shortly denote the correction parameters by a vector valued

$$\boldsymbol{\gamma}^{\#} = (\gamma_1^{\#}, \ldots, \gamma_K^{\#})^\top \in \mathbb{R}^{\mathcal{K}}, \qquad \# \in \{R, F\}.$$

For example, in the case of the layer correction, a sufficient condition is that $\boldsymbol{\gamma}^R \in \mathcal{B}_{\mathcal{R}}^{\infty}(0) = \{\mathbf{y} \in \mathbb{R}^{\mathcal{K}} : \ \|\mathbf{y}\|_{l^\infty} < \mathcal{R}\}$ with a fixed $\mathcal{R} < 1$. Furthermore we show in our numerics that both types of modification are good choices, if optimal parameters $\boldsymbol{\gamma}^R$, $\boldsymbol{\gamma}^F$ are known. Then the basic question which remains is how to obtain the optimal correction parameters. Let us describe this topic briefly for the layer correction $c_h^R(\cdot,\cdot)$ and, for the better readability, skip the index R. For the

function correction, we use the same strategy.

We follow the same technique as proposed in [53] and proven in [145] for the linear elements for the Poisson problem. This means, we construct a sequence $\{\boldsymbol{\gamma}_h\}_{h>0} \subset \mathcal{B}_R^\infty(0)$ satisfying certain conditions, such that it converges to a unique asymptotic value $\boldsymbol{\gamma}^\star \in \mathcal{B}_R^\infty(0)$, being the optimal correction parameter. Namely, for each admissible $\boldsymbol{\gamma} = (\gamma_1, \ldots, \gamma_\mathcal{K})^\top$, we define the vector valued pollution function for $i = 1, ..., \mathcal{K}$ as $\mathbf{g}_h : \mathcal{B}_R^\infty(0) \to \mathbb{R}^\mathcal{K}$ by its components:

$$g_{h,i}(\boldsymbol{\gamma}) = a(s_i - R_h^{\mathrm{m}}(\boldsymbol{\gamma})s_i, s_i - R_h^{\mathrm{m}}(\boldsymbol{\gamma})s_i) - c_h(R_h^{\mathrm{m}}(\boldsymbol{\gamma})s_i, R_h^{\mathrm{m}}(\boldsymbol{\gamma})s_i), \tag{42}$$

where $R_h^{\mathrm{m}}(\boldsymbol{\gamma})s_i$ represents the modified-approximative solution to s_i, this time explicitly dependent on the choice of $\boldsymbol{\gamma}$. If we construct $\{\boldsymbol{\gamma}_h\}_{h>0}$ such that

$$\mathbf{g}_h(\boldsymbol{\gamma}_h) = \mathbf{0}, \quad h > 0,$$

we can possibly generalize the proof of [145] and show the convergence $\boldsymbol{\gamma}_h$ to $\boldsymbol{\gamma}^\star$ for $k \to \infty$ with a certain rate. Under the assumption on the convergence of $\boldsymbol{\gamma}_h$, we can show that for the asymptotic vector $\boldsymbol{\gamma}^\star$, the necessary condition (39) on the modification $c_h(\cdot, \cdot)$ on each level is satisfied. For this we also refer to [79].

After having introduced how the modification $c_h(\cdot, \cdot)$ can be constructed, we show in the following the numerical results for problem (35) using higher order finite elements with and without energy correction. We illustrate our theoretical results for schemes up to order four, and we always assume an exact solution given by:

$$u := s_1 + s_2 + s_3 + s_4 = \sum_{i=1}^{4} r^{\lambda_i} \sin(\lambda_i \theta).$$

We note that each term contributes to the total energy with the same magnitude. The convergence rates and the γ-convergence studies for the second, third and fourth order scheme are performed on the geometries as depicted in Figure 9.4.
In the following, for a better readability, we skip the index R and F in the notation of the asymptotic values $\boldsymbol{\gamma}^\star$ and their components $\gamma_i^\star$, $i \leqslant \mathcal{K}$. Also, the specific values of $\boldsymbol{\gamma}^\star$ are stated in the following only up to a certain precision.

Before we start with the numerical tests, we show that our local modification of the finite element method does not increase the condition number of the stiffness

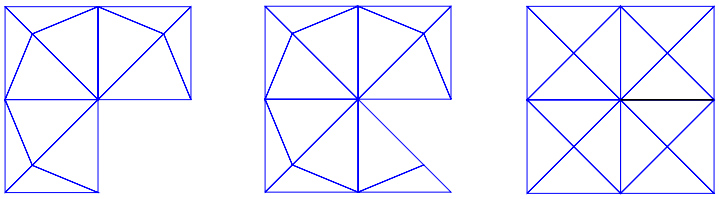

Figure 9.4: Initial meshes, level= 1 for $\omega = 3/2\pi,\ 7/4\pi,\ 2\pi$ used for $k = 2, 3, 4$ approximations.

matrix. Namely, in Table 9.4 we give the ratios $\frac{(\lambda_{\min})_h^{\mathrm{m}}}{(\lambda_{\min})_h}$ and $\frac{(\lambda_{\max})_h^{\mathrm{m}}}{(\lambda_{\max})_h}$ between eigenvalues of the stiffness matrix which belong to the modified scheme $(\cdot)_h^{\mathrm{m}}$ and the standard scheme $(\cdot)_h$, for both correction methods $c_h^R(\cdot,\cdot)$ and $c_h^F(\cdot,\cdot)$.

	layer correction $c_h^R(\cdot,\cdot)$			function correction $c_h^F(\cdot,\cdot)$		
level	2	3	4	2	3	4
$\frac{(\lambda_{\min})_h^{\mathrm{m}}}{(\lambda_{\min})_h}$	0.9886	0.9891	0.9952	0.9806	0.9901	0.9954
$\frac{(\lambda_{\max})_h^{\mathrm{m}}}{(\lambda_{\max})_h}$	1.0007	1.0000	1.0000	1.0000	1.0000	1.0000

Table 9.4: Comparison of the condition numbers of the stiffness matrices belonging to corrected and standard scheme; $\omega = 7/4\pi$, $k = 2$.

We now present the results for the energy correction with the layer-modification (40). After this a more detailed study is performed for the second order case, showing convergence results for the modified scheme. An important part of the energy correction method is an accurate approximation of the correction parameter $\boldsymbol{\gamma}^\star = (\gamma_1^\star, \ldots, \gamma_K^\star)$, as an asymptotic value of the series $\{\boldsymbol{\gamma}_h\}_{h>0}$. In our study, we use two different possibilities to estimate $\boldsymbol{\gamma}_h$. The first one is purely based on existing FEniCS routines and uses *fsolve* to compute an approximation of γ_h as the root of an implicitely given function. The second one uses the nested-Newton method of [145] adapted to the higher order case. The implementation of this method in FEniCS is, in comparison to the *fsolve* routine, cheaper in terms of computation time.

With the obtained γ_h, a fit is performed in MATLAB [108] for the approximation of $\boldsymbol{\gamma}^\star$ as the limit value of $\gamma_h, h \to 0$, by exploiting the asymptotic

$$\boldsymbol{\gamma}^\star + c\, h^{2(k-\lambda_K)},$$

where c is a constant, differing for the fits to data obtained by *fsolve* (c_f) or by

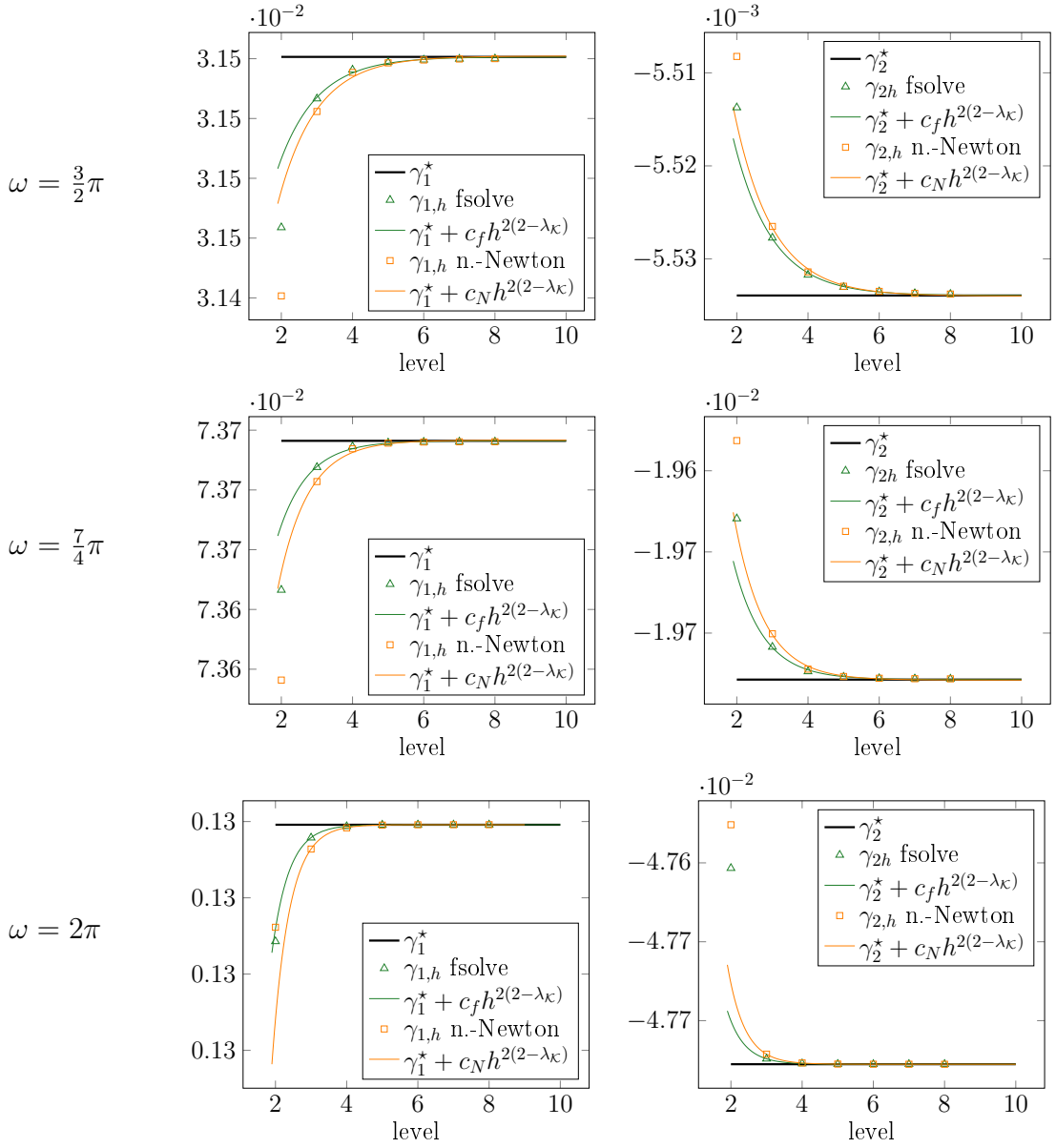

Figure 9.5: Best fits of $\gamma_{i,h}$ obtained by *fsolve* and the nested-Newton scheme, with respect to the theoretical expected rates. First column: Fits of $\gamma_1^\star$. Second column: Fits of $\gamma_2^\star$. Different reentrant corners are shown from left to right.

the nested Newton (c_N). At this point it should be noted that the calculated $\boldsymbol{\gamma}^\star$ slightly differs depending on the underlying fit data.

Figure 9.5 depicts the resulting fits of $\gamma_i^\star$ for both *fsolve* and nested Newton method. We also show the results for all three basic scenarios of reentrant corners: $\omega = 3/2\pi$, $7/4\pi$ and 2π. In the first column of the figure, we present fits for the first component of $\boldsymbol{\gamma}^\star$, in the second column, the fits for the second one. For both

methods we obtain the same convergence rate for the correction parameters. Both methods tend, as it is expected from our theory, to the same $\boldsymbol{\gamma}^\star$. In our case the above mentioned difference between the approximated $\boldsymbol{\gamma}^\star$ is less than 10^{-6}. For our further calculations we use the $\boldsymbol{\gamma}^\star$ obtained with the *fsolve* routine. To obtain the same convergence results, it would also be possible to use $\boldsymbol{\gamma}^\star$ obtained with the nested-Newton method, or alternatively also the first six digits of $\boldsymbol{\gamma}^\star$.

With the asymptotic values $\boldsymbol{\gamma}^\star$, we illustrate in Table 9.5 and Table 9.6 the convergence rates with and without energy correction. Our numerical results are in excellent agreement with the theory, see Theorem 9.3. The errors are measured for both, the L^2- and the L^2_α- norms. In this part, we focus on the cases of $\omega = 3/2\pi$ and $\omega = 7/4\pi$. In comparison to the linear approximations, as studied in [53], the error in gradients for the second order also has a reduced convergence order. Therefore, we present also the convergence rates for the gradient, see Table 9.5 and Table 9.6. As one can see, standard finite elements exhibit $2\pi/\omega$ and π/ω convergence rates for the L^2-error in the solution and the gradient, respectively. Furthermore, optimal rates three and two in the weighted L^2_α-norm can be achieved using energy-correction.

	$\boldsymbol{\gamma} = (0,0)^\top$				$\boldsymbol{\gamma}^\star = (0.031521, -0.005534)^\top$			
level	$\|u-u_h\|_0$	rate	$\|u-u_h\|_{0,\alpha}$	rate	$\|u-u_h^{\mathrm{m}}\|_0$	rate	$\|u-u_h^{\mathrm{m}}\|_{0,\alpha}$	rate
2	7.0709e–03	-	1.9465e–03	-	5.6222e–03	-	1.8330e–03	-
3	2.7238e–03	1.38	6.1921e–04	1.65	1.5194e–03	1.89	1.8777e–04	3.29
4	1.0452e–03	1.38	2.3725e–04	1.38	4.4752e–04	1.76	1.8210e–05	3.37
5	4.0414e–04	1.37	9.3743e–05	1.34	1.3749e–04	1.70	1.9942e–06	3.19
6	1.5751e–04	1.36	3.7180e–05	1.33	4.2897e–05	1.68	2.3592e–07	3.08
7	6.1766e–05	1.35	1.4753e–05	1.33	1.3461e–05	1.67	2.8883e–08	3.03
8	2.4323e–05	1.34	5.8546e–06	1.33	4.2339e–06	1.67	3.5837e–09	3.01
level	$\|\nabla(u-u_h)\|_0$	rate	$\|\nabla(u-u_h)\|_{0,\alpha}$	rate	$\|\nabla(u-u_h^{\mathrm{m}})\|_0$	rate	$\|\nabla(u-u_h^{\mathrm{m}})\|_{0,\alpha}$	rate
2	3.8901e–02	-	1.2469e–02	-	4.3263e–02	-	1.6682e–02	-
3	2.4482e–02	0.67	3.6263e–03	1.78	2.4334e–02	0.83	3.2480e–03	2.36
4	1.5461e–02	0.66	1.2070e–03	1.59	1.4871e–02	0.71	7.3695e–04	2.14
5	9.7522e–03	0.66	4.4090e–04	1.45	9.2795e–03	0.68	1.7799e–04	2.05
6	6.1468e–03	0.67	1.6891e–04	1.38	5.8257e–03	0.67	4.3872e–05	2.02
7	3.8731e–03	0.67	6.6080e–05	1.35	3.6651e–03	0.67	1.0900e–05	2.01
8	2.4401e–03	0.67	2.6074e–05	1.34	2.3077e–03	0.67	2.7175e–06	2.00

Table 9.5: $\omega = 3/2\pi$: Errors and convergence rates of the solution and the gradients with (u_h^{m}) and without energy correction (u_h), $k = 2$, and $\alpha = 1.3333$. Layer-modification c_h^R with correction parameter $\boldsymbol{\gamma}^\star$.

In the proof of our main Theorem 9.3, see [79], we assume (U)-property of the mesh

	$\boldsymbol{\gamma} = (0,0)^\top$				$\boldsymbol{\gamma}^\star = (0.073696, -0.019675)^\top$			
level	$\|u-u_h\|_0$	rate	$\|u-u_h\|_{0,\alpha}$	rate	$\|u-u_h^{\mathrm{m}}\|_0$	rate	$\|u-u_h^{\mathrm{m}}\|_{0,\alpha}$	rate
2	1.4688e–02	-	4.0231e–03	-	1.4058e–02	-	5.5315e–03	-
3	6.5058e–03	1.17	1.5652e–03	1.36	3.5969e–03	1.97	6.4029e–04	3.11
4	2.8727e–03	1.18	6.9520e–04	1.17	1.0173e–03	1.82	6.0880e–05	3.39
5	1.2781e–03	1.17	3.1399e–04	1.15	3.1468e–04	1.69	6.0667e–06	3.33
6	5.7257e–04	1.16	1.4210e–04	1.14	1.0189e–04	1.63	6.4267e–07	3.24
7	2.5768e–04	1.15	6.4335e–05	1.14	3.3693e–05	1.60	7.1739e–08	3.16
8	1.1628e–04	1.15	2.9132e–05	1.14	1.1248e–05	1.58	8.3485e–09	3.10
level	$\|\nabla(u-u_h)\|_0$	rate	$\|\nabla(u-u_h)\|_{0,\alpha}$	rate	$\|\nabla(u-u_h^{\mathrm{m}})\|_0$	rate	$\|\nabla(u-u_h^{\mathrm{m}})\|_{0,\alpha}$	rate
2	7.2533e-02	-	2.1898e-02	-	9.7586e-02	-	4.2072e-02	-
3	4.9699e-02	0.55	7.7725e-03	1.49	5.3057e-02	0.88	7.3131e-03	2.52
4	3.3713e-02	0.56	3.1786e-03	1.29	3.3087e-02	0.68	1.4913e-03	2.29
5	2.2769e-02	0.57	1.3896e-03	1.19	2.1653e-02	0.61	3.4514e-04	2.11
6	1.5347e-02	0.57	6.2221e-04	1.16	1.4407e-02	0.59	8.3736e-05	2.04
7	1.0335e-02	0.57	2.8078e-04	1.15	9.6473e-03	0.58	2.0675e-05	2.02
8	6.9573e-03	0.57	1.2701e-04	1.14	6.4780e-03	0.57	5.1410e-06	2.01

Table 9.6: $\omega = 7/4\pi$: Errors and convergence rates of the solution and the gradients with (u_h^{m}) and without energy correction (u_h), $k = 2$, and $\alpha = 1.4286$. Layer-modification c_h^R with correction parameter $\boldsymbol{\gamma}^\star$.

to derive *a priori* convergence rates for

$$\tilde{g}_h(s_i, s_j) = a(s_i - s_{i,h}^{\mathrm{m}}, s_j - s_{j,h}^{\mathrm{m}}) - c_h(s_{i,h}^{\mathrm{m}}, s_{j,h}^{\mathrm{m}}) \lesssim h^{k+1}, \qquad i \neq j. \tag{43}$$

We now demonstrate that these conditions are necessary. Hence, we perform two types of computations, first, using a fully non-symmetric mesh, and a mesh which is locally mirror-symmetric, but not satisfying the (G3)-property, see the meshes on the left side of Table 9.7, for the case of $k = 2$ and $\omega = 7/4\pi > 4/3\pi$. Thus for this combination of k and ω, the (U)-property of the mesh is not satisfied. Again, since we consider the second order approximations, we require for the optimal convergence rates of the solution, i.e., $\|u - u_h^{\mathrm{m}}\|_{0,\alpha} = \mathcal{O}(h^3)$, the convergence rate in (43) to be also $O(h^3)$ for both pairings (s_1, s_2) and (s_1, s_3), see Figure 9.2.

In Table 9.7, we present the numerical results computed on the above mentioned meshes demonstrating that (G1)- or (G2)-properties of the local mesh are not sufficient. As one can see in the case of a locally mirror-symmetric mesh, the necessary condition (43) is violated only for the (s_1, s_3) pairing, while the (s_1, s_2) pairing has even higher convergence order than we require. This comes from the fact that s_1 is symmetric and s_2 is anti-symmetric in the θ-direction, and thus the integral of the product of their gradients on a mirror-symmetric mesh vanishes. The violation of the local symmetry of the mesh then results in the fact that also this pairing does

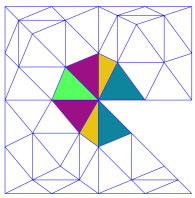

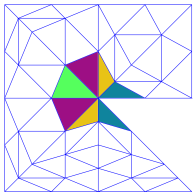

	(G1) non-symmetric			
level	$\tilde{g}_h(s_1, s_2)$	rate	$\tilde{g}_h(s_1, s_3)$	rate
2	1.7836e–04	–	1.9118e–04	–
3	5.3969e–05	1.72	3.8239e–05	2.32
4	1.6437e–05	1.72	7.8252e–06	2.29
5	5.0081e–06	1.71	1.6040e–06	2.29
6	1.5260e–06	1.71	3.2887e–07	2.29
7	4.6503e–07	1.71	6.7436e–08	2.29
8	1.4172e–07	1.71	1.3829e–08	2.29
	(G2) mirror-symmetric			
level	$\tilde{g}_h(s_1, s_2)$	rate	$\tilde{g}_h(s_1, s_3)$	rate
2	3.4985e–06	–	1.3550e–04	–
3	3.6461e–07	3.26	2.8173e–05	2.27
4	2.3000e–08	3.99	5.7796e–06	2.29
5	1.4154e–09	4.02	1.1833e–06	2.29
6	8.7613e–11	4.01	2.4236e–07	2.29
7	5.4420e–12	4.01	4.9666e–08	2.29
8	3.5838e–13	3.92	1.0181e–08	2.29

Table 9.7: Two examples of $\omega = 7/4\pi$ meshes which do not satisfy (G3), but the property (G1) for the first row and the property (G2) for the second row.

not exhibit the required convergence rate.

We would also like to remark that the full symmetry (G3) is a too strong assumption and it can be relaxed to more general cases. For example, classical criss-cross meshes, see the case for $\omega = 2\pi$ in Figure 9.4, would be enough. To demonstrate the plausibility of this assumption, we include Table 9.8, where $\int_\Upsilon \nabla s_1 \cdot \nabla I_h^2 s_3 \, dx$ is evaluated on different refinement levels, with Υ-domains as depicted on the left of the tables.

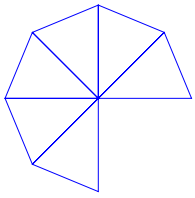

level	(G3) mesh
1	-2.636780e–15
2	-3.774758e–15
3	-3.734860e–15
4	-3.631210e–15
5	-3.642052e–15

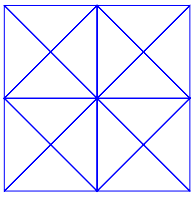

level	criss-cross
1	-2.636780e–15
2	-3.774758e–15
3	-3.734860e–15
4	-3.631210e–15
5	-3.642052e–15

Table 9.8: Values of $\int_\Upsilon \nabla s_1 \cdot \nabla I_h^2 s_3 \, dx$ for the depicted meshes for different refinement levels.

We now turn our attention to the results for the third and fourth order approximations, again for the layer correction, and concentrate on two reentrant corner cases: $3/2\pi$ (Table 9.9) and 2π (Table 9.10). In all cases, the optimal rates are obtained in the L^2_α-norm if a sufficient number of correction parameters is used.

They can be read out from Figure 9.2. Note also, that the weight α increases with the approximation order k, namely $\alpha = k - \lambda_1$.

	$k=3$				$k=4$			
level	$\|u-u_h\|_{0,\alpha}$	rate	$\|u-u_h^{\mathrm{m}}\|_{0,\alpha}$	rate	$\|u-u_h\|_{0,\alpha}$	rate	$\|u-u_h^{\mathrm{m}}\|_{0,\alpha}$	rate
2	3.6458e–04	-	4.7531e–04	-	1.4972e–04	-	4.3849e–04	-
3	1.4914e–04	1.29	3.5013e–05	3.76	5.6715e–05	1.40	1.4127e–05	4.96
4	5.9232e–05	1.33	1.9895e–06	4.14	2.2495e–05	1.33	2.9706e–07	5.57
5	2.3504e–05	1.33	1.1977e–07	4.05	8.9263e–06	1.33	7.2456e–09	5.36
6	9.3270e–06	1.33	7.4012e–09	4.02	3.5423e–06	1.33	1.9010e–10	5.25
7	3.7013e–06	1.33	4.5990e–10	4.01				

Table 9.9: $\omega = 3/2\pi$: Errors and convergence rates with (u_h^{m}) and without energy correction (u_h), for $k = 3, 4$, and $\alpha_3 = 2.3333$, $\alpha_4 = 3.3333$. Layer-modification c_h^R with correction parameters for third $(\boldsymbol{\gamma}_3)$ and fourth $(\boldsymbol{\gamma}_4)$ order. $\boldsymbol{\gamma}_3 = (0.012891, -0.002367)^\top$, $\boldsymbol{\gamma}_4 = (0.007703, -0.002478, 0.000452)^\top$.

	$k=3$				$k=4$			
level	$\|u-u_h\|_{0,\alpha_3}$	rate	$\|u-u_h^{\mathrm{m}}\|_{0,\alpha_3}$	rate	$\|u-u_h\|_{0,\alpha_4}$	rate	$\|u-u_h^{\mathrm{m}}\|_{0,\alpha_4}$	rate
2	1.6938e–03	-	7.3218e–03	-	7.8234e–04	-	8.2906e–03	-
3	8.4536e–04	1.00	4.0724e–04	4.17	3.8899e–04	1.01	5.0596e–04	4.03
4	4.2165e–04	1.00	1.9310e–05	4.40	1.9423e–04	1.00	9.1646e–06	5.79
5	2.1059e–04	1.00	1.0565e–06	4.19	9.7052e–05	1.00	2.0680e–07	5.47
6	1.0524e–04	1.00	6.2341e–08	4.08	4.8510e–05	1.00	6.2929e–09	5.04
7	5.2604e–05	1.00	3.7994e–09	4.04				

Table 9.10: $\omega = 2\pi$: Errors and convergence rates with (u_h^{m}) and without energy correction (u_h), for $k = 3$, $k = 4$ and $\alpha_3 = 2.5$, $\alpha_4 = 3.5$. Layer-modification c_h^R with correction parameters for third $(\boldsymbol{\gamma}_3)$ and fourth $(\boldsymbol{\gamma}_4)$ order. $\boldsymbol{\gamma}_3 = (0.083770, -0.057179, 0.015783)^\top$, $\boldsymbol{\gamma}_4 = (0.059374, -0.060325, 0.033989, -0.008364)^\top$.

We finally also compare the qualitative behavior of the layer and function correction, namely, the influence of the choice of the modification $c_h(\cdot,\cdot)$ on the quantitative error. As described before, higher order approximations require an increased number of correction parameters γ_i, $i = 1, \ldots, \mathcal{K} \leqslant k$. This means that *a priori*, the correction by rings $c_h^R(\cdot,\cdot)$ needs a larger support, constructed by $\mathcal{K}$-layers of elements around the singular point. To have a possibility to avoid this fact, we have suggested a correction by a function, $c_h^F(\cdot,\cdot)$, see (41). Its support is always restricted to a single element layer at the singular points.

In Figure 9.6, we graphically illustrate the comparison of the convergence rates of the standard scheme and the two corrections, for all studied scenarios, i.e., approximation orders $k = 2, 3, 4$ and $\omega = 3/2\pi, 7/4\pi, 2\pi$. The first three plots demonstrate

the recovered optimal rates $k+1$ of the error $\|u-u_h^{\mathrm{m}}\|_{0,\alpha}$, $\alpha = k - \frac{\pi}{\omega}$, where the y-label of the plots represents the error, i.e., $\|u-u_h^{\mathrm{m}}\|_{0,\alpha}$ and $\|u-u_h\|_{0,\alpha}$, respectively. As one can see, both corrections are qualitatively comparable, nevertheless, the function correction $c_h^F(\cdot,\cdot)$ is quantitatively significantly better for higher k. This observation is depicted in the last plot of Figure 9.6, showing the ratio between the errors caused by the approximations computed with $c_h^R(\cdot,\cdot)$ and $c_h^F(\cdot,\cdot)$. Note the clustering of the ratios by the number of the correction parameters $\mathcal{K}$. We present the asymptotic correction function $\sum_{i=1}^{\mathcal{K}} \gamma_i^{F\star}\, \hat{r}^{i-1}$ for all the considered mesh and approximation order settings, see Figure 9.7. Note here the bound of the maximum of the correction function, guaranteeing the ellipticity of $a_h(\cdot,\cdot)$.

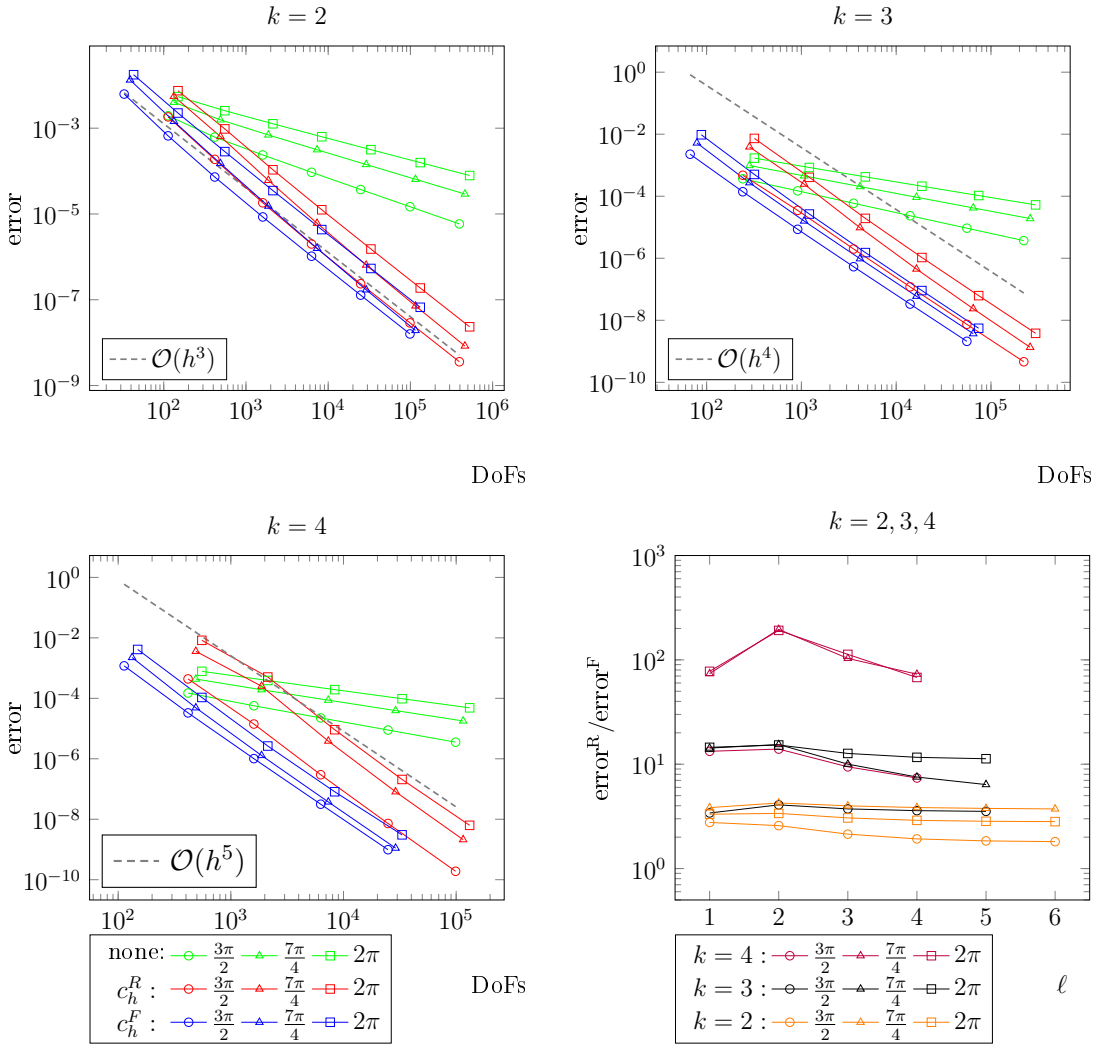

Figure 9.6: Comparison of the standard and modified finite elements with energy corrections c_h^R and c_h^F for approximation orders $k = 2, 3, 4$. The last plot represents the ratio between the errors produced by the layer correction and function correction.

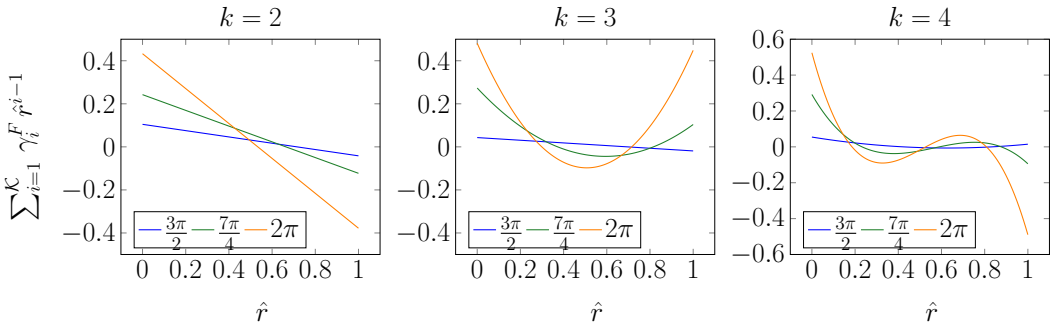

Figure 9.7: Asymptotic correction functions $\sum_{i=1}^{\mathcal{K}} \gamma_i^F \hat{r}^{i-1}$ for three different approximation orders and three different angles. These function corrections were used for the computations presented in Figure 9.6.

9.3. Energy correction method for the Poisson eigenvalue problem

This section contains results which were previously published by the author with M. Huber, U. Rüde, C. Waluga and B. Wohlmuth in the year 2014 in Numerical Mathematics and Advanced Applications - ENUMATH 2013 proceedings, Volume 103 of the series Lecture Notes in Computational Science and Engineering, under the title "Energy-corrected finite element methods for scalar elliptic problems", [74].

Reasoned by our interest in the vibro-acoustic analysis of domains with reeantrant corners, in this section we extend the linear energy correction method to eigenvalue problems. In the following we consider the eigenvalue problem with homogeneous Neumann boundary conditions

$$\Delta u_l = \lambda_l u_l \qquad \text{in } \Omega$$

on the L-shaped domain $\Omega := (-1,1)^2 \backslash ([0,1] \times [-1,0])$ and the slit-domain $\Omega := (-1,1)^2 \backslash ([0,1] \times \{0\})$. We construct our meshes such that we obtain perfectly symmetric isosceles triangles around the singular points, see Figure 9.8. Furthermore we use different meshes for the comparison with reference values given in the literature [23, 43] and present results for a domain with multiple reentrant corners, in which case we compute a fine mesh reference solution. It is well-known [8, 9, 10, 23, 101] that the pollution effect occurs only for eigenfunctions and eigenvalues with a non-smooth singular component. For sufficiently smooth eigenfunctions, a quadratic convergence rate for the eigenvalues can be observed in case of linear finite elements, i.e. $k = 1$.

Our modified finite element formulation reads:
Find the discrete eigenvalues $\lambda_{h,l}^{\mathrm{m}} \in \mathbb{R}$ and the eigenfunctions $u_{h,l}^{\mathrm{m}}(\gamma) \in V_h^1$ such that

$$a_h(u_{h,l}^{\mathrm{m}}, v) = \lambda_{h,l}^{\mathrm{m}} \, (u_{h,l}^{\mathrm{m}}, v), \quad v \in V_h^1,$$

where $0 \leq \lambda_{h,1}^{\mathrm{m}} \leq \lambda_{h,2}^{\mathrm{m}} \leq \ldots$.

In the convergence analysis of the discrete eigenvalues $\lambda_{h,l}^{\mathrm{m}}$ we follow the lines of [137] in the conforming setting and introduce the eigenvalue problem:
Find $\lambda \in \mathbb{R}$ and $w \in H^1(\Omega)$ such that $a(w, z) = \lambda \, (w, z)$ for all $z \in H^1(\Omega)$.

The non-negative eigenvalues are ordered such that $0 \leq \lambda_1 \leq \lambda_2 \leq \ldots$, and the associated eigenfunctions are denoted by w_i with the normalization $(w_i, w_j) = \delta_{i,j}$. We now define the l-dimensional space V_l by $V_l := \mathrm{span}\{w_i, i \leq l\}$. Further for each $v \in V_l$ let the modified Galerkin projection $R_h^{\mathrm{m}} := R_h^{\mathrm{m}}(\gamma)$ onto V_h^1 be defined by

$$a_h(R_h^{\mathrm{m}} v, v_h) = a(v, v_h)$$

for all $v_h \in V_h^1$. We recall that R_h^{m} depends on the specific choice of γ. In terms of R_h^{m}, we define $E_{l,h} := R_h^{\mathrm{m}} V_l$ and note that $\dim E_{l,h} = l$ for $h \leq h_0$ small enough.
For the sake of presentation, let us first state the main result and subsequently develop the ingredients needed for its proof.

Theorem 5. *Let $1 - \frac{\pi}{\omega} < \alpha < 1$. If the energy correction for linear finite elements is used with $\gamma^\star$, the following upper and lower bound for $\lambda_{h,l}^{\mathrm{m}}$ hold,*

$$\lambda_l(1 - Ch^2\lambda_l^{1+\alpha}) \leq \lambda_{h,l}^{\mathrm{m}} \leq \lambda_l(1 + Ch^2\lambda_l^{\alpha+1}).$$

Our proof is based on the following two technical results which are provided without a detailed proof.

Lemma 9.5. *Let $1 - \frac{\pi}{\omega} < \widetilde{\alpha} < \alpha < 1$. Then it holds that*

$$\|r^{-\tilde{\alpha}} v\|_0 \leq C \|v\|_0^{1-\alpha} \|v\|_1^{\alpha}, \quad v \in H^1(\Omega).$$

The upper bound in Lemma 9.5 can be obtained by using the Hölder inequality in combination with interpolation arguments and standard Sobolev embedding results. Combining Lemma 9.5 with [137, Lemma 6.4-2], [53, Theorem 2.4] and some straightforward computations yields the following bounds:

Lemma 9.6. *Let $v \in V_l$ with $(v,v) = 1$. Then $v = \sum_{i=1}^{l} \beta_i w_i$ with $\sum_{i=1}^{l} \beta_i^2 = 1$, and it satisfies $a(v,z) = (f_v, z)$ for all $z \in H^1(\Omega)$ with $f_v := \sum_{i=1}^{l} \beta_i \lambda_i w_i$. Moreover, we have $r^{-\alpha} f_v \in L^2(\Omega)$ for $1 - \frac{\pi}{\omega} < \alpha < 1$, and the following bounds hold with constants independent of the mesh-size*

$$\begin{aligned} |a(v,v) - a_h(R_h^{\mathrm{m}} v, R_h^{\mathrm{m}} v)| &\leq C h^2 \lambda_l^{2+\alpha}, \\ (R_h^{\mathrm{m}} v, R_h^{\mathrm{m}} v) &\geq 1 - C h^2 \lambda_l^{\alpha+1}. \end{aligned}$$

Now we are prepared to provide the proof of the main result.

Proof. The proof of Theorem 5 is based on the characterization of the eigenvalues by the Rayleigh quotient. We start with the upper bound. Using $E_{l,h}$ as defined above together with Lemma 9.6, we get the following upper bound:

$$\begin{aligned} \lambda_{h,l}^{\mathrm{m}} &\leq \max_{v \in E_{l,h}} \frac{a_h(v,v)}{(v,v)} = \max_{v \in V_l} \frac{a_h(R_h^{\mathrm{m}} v, R_h^{\mathrm{m}} v)}{(R_h^{\mathrm{m}} v, R_h^{\mathrm{m}} v)} \\ &= \max_{v \in V_l} \frac{a(v,v) + a_h(R_h^{\mathrm{m}} v, R_h^{\mathrm{m}} v) - a(v,v)}{(R_h^{\mathrm{m}} v, R_h^{\mathrm{m}} v)} \\ &= \max_{v \in V_l} \frac{a(v,v)}{(v,v)} \max_{v \in V_l} \frac{(v,v)}{(R_h^{\mathrm{m}} v, R_h^{\mathrm{m}} v)} + \max_{v \in V_l} \frac{a_h(R_h^{\mathrm{m}} v, R_h^{\mathrm{m}} v) - a(v,v)}{(R_h^{\mathrm{m}} v, R_h^{\mathrm{m}} v)} \\ &\leq \lambda_l \frac{1 + C h^2 \lambda_l^{2+\alpha}}{1 - C h^2 \lambda_l^{\alpha+1}} \lesssim \lambda_l (1 + C h^2 \lambda_l^{\alpha+1}) + C h^2 \lambda_l^{2+\alpha} (1 + C h^2 \lambda_l^{\alpha+1}). \end{aligned}$$

In the next step, it remains to show the lower bound. In contrast to the uncorrected scheme, we do not have the trivial bound $\lambda_l \leq \lambda_{h,l}^{\mathrm{m}}$. The proof of the lower bound follows basically the lines of the upper bound but requires the use of a different l-dimensional space. Firstly we define a new space given by $E_l := \operatorname{span}\{\widetilde{w}_i, i \leq l\}$ where $\widetilde{w}_i \in H^1(\Omega)$ is defined by $a(\widetilde{w}_i, z) = (w_{i,h}, z)$ for all $z \in H^1(\Omega)$. Secondly, we note that $R_h^{\mathrm{m}} E_l = E_{l,h}$ and thus for h small enough we have $\dim E_l = l$. Now, similar arguments as before yield

$$\begin{aligned} \lambda_l &\leq \max_{v \in E_l} \frac{a(v,v)}{(v,v)} = \max_{v \in E_l} \frac{a_h(R_h^{\mathrm{m}} v, R_h^{\mathrm{m}} v) + a(v,v) - a_h(R_h^{\mathrm{m}} v, R_h^{\mathrm{m}} v)}{(v,v)} \\ &= \max_{v \in E_l} \frac{a_h(R_h^{\mathrm{m}} v, R_h^{\mathrm{m}} v)}{(R_h^{\mathrm{m}} v, R_h^{\mathrm{m}} v)} \max_{v \in E_l} \frac{(R_h^{\mathrm{m}} v, R_h^{\mathrm{m}} v)}{(v,v)} + \max_{v \in E_l} \frac{a(v,v) - a_h(R_h^{\mathrm{m}} v, R_h^{\mathrm{m}} v)}{(v,v)} \\ &\leq \lambda_{h,l}^{\mathrm{m}} (1 + C h^2 (\lambda_{h,l}^{\mathrm{m}})^{1+\alpha}). \end{aligned}$$

Combining the upper bounds for λ_l and $\lambda_{h,l}^{\mathrm{m}}$ yields the lower bound for $\lambda_{h,l}^{\mathrm{m}}$. □

The steps outlined in this section show the flexibility and potential of the ideas of [53, 145] to eigenvalue problems. We conduct convergence studies for the eigen-

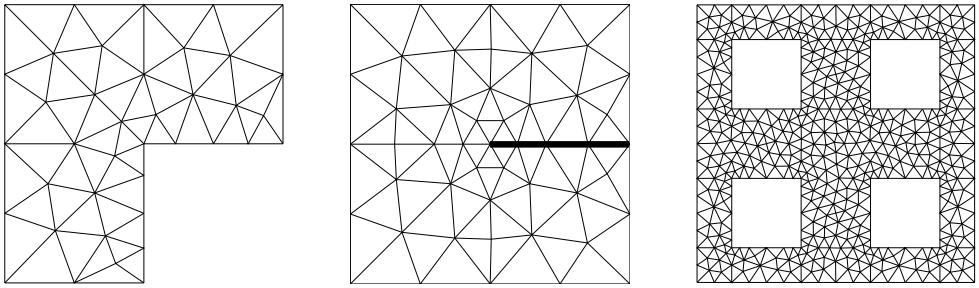

Figure 9.8: L-shape, slit and domain with multiple reentrant corners.

No Correction $\gamma = 0$:

	1.EV		2.EV		3.EV		4.EV		5.EV	
	exact: 1.47562		exact: 3.53403		exact: 9.86960		exact: 9.86960		exact: 11.38948	
level	value	rate	value	rate	value	rate	value	rate	value	rate
1	1.55008	-	3.63939	-	10.79641	-	10.90447	-	12.67323	-
2	1.50014	**1.60**	3.56116	1.96	10.10623	1.97	10.12814	2.00	11.71975	1.96
3	1.48402	**1.55**	3.54091	1.98	9.92994	1.97	9.93496	1.98	11.47442	1.96
4	1.47861	**1.49**	3.53576	1.99	9.88483	1.99	9.88604	1.99	11.41101	1.98
5	1.47672	**1.44**	3.53447	2.00	9.87342	2.00	9.87372	2.00	11.39489	1.99

Correction $\gamma^\star = 0.147850426060652$:

	1.EV		2.EV		3.EV		4.EV		5.EV	
	exact: 1.47562		exact: 3.53403		exact: 9.86960		exact: 9.86960		exact: 11.38948	
level	value	rate	value	rate	value	rate	value	rate	value	rate
1	1.51075	-	3.62603	-	10.78432	-	10.89390	-	12.64990	-
2	1.48457	**1.97**	3.55913	1.87	10.10560	1.95	10.12758	1.99	11.71674	1.95
3	1.47785	**2.00**	3.54060	1.93	9.92990	1.97	9.93493	1.98	11.47396	1.95
4	1.47617	**2.03**	3.53571	1.96	9.88482	1.99	9.88604	1.99	11.41094	1.98
5	1.47575	**2.06**	3.53446	1.98	9.87342	2.00	9.87372	2.00	11.39488	1.99

Table 9.11: Convergence rates for eigenvalues in the L-shaped domain with and without energy correction.

value problem defined on the geometries depicted in Figure 9.8. First the numerical results obtained without correction are compared to those obtained with a suitable modification parameter. In this we make use of the Neumann fit tabulated in [145, Table 5.3], which provides a simple heuristic approach to determine modification parameters in case of meshes consisting of isosceles triangles around the singularity. The purely geometric assumption is satisfied for our meshes by construction, see Figure 9.8. The correction parameter $\gamma^\star$ for the L-shape and the multiple reentrant corners domain is given by $\gamma^\star \approx 0.1478$. We note that in each case four isosceles triangles are attached to the singularity, and thus the correction parameter is the same for all reentrant corners. For the slit domain we count six adjacent elements at the singular vertex, and hence we determine our correction parameter to be $\gamma^\star \approx 0.2716$. In Tables 9.11, 9.12 and 9.13 we list the results for our convergence study for the L-shape, the slit domain and the domain with multiple reentrant corners, respectively. Without correction, we observe suboptimal rates

No Correction $\gamma = 0$:

	1.EV		2.EV		5.EV		7.EV		8.EV	
	exact: 1.03407		exact: 2.46740		exact: 9.86960		exact: 12.26490		exact: 12.33701	
level	value	rate	value	rate	value	rate	value	rate	value	rate
1	1.14032	-	2.52918	-	10.78301	-	13.97705	-	14.17015	-
2	1.07951	**1.23**	2.48307	1.98	10.10730	1.94	12.75729	**1.80**	12.81216	1.95
3	1.05478	**1.13**	2.47135	1.99	9.93045	1.97	12.43849	**1.50**	12.44434	2.15
4	1.04392	**1.07**	2.46839	2.00	9.88497	1.99	12.32633	**1.50**	12.36411	1.99
5	1.03887	**1.04**	2.46765	2.00	9.87346	1.99	12.28924	**1.34**	12.34381	1.99

Correction $\gamma = 0.271607294328175$:

	1.EV		2.EV		5.EV		7.EV		8.EV	
	exact: 1.03407		exact: 2.46740		exact: 9.86960		exact: 12.26490		exact: 12.33701	
level	value	rate	value	rate	value	rate	value	rate	value	rate
1	1.06167	-	2.49235	-	10.76626	-	13.85168	-	13.88581	-
2	1.04116	**1.96**	2.47377	1.97	10.10651	1.92	12.66340	**1.99**	12.73749	1.95
3	1.03583	**2.01**	2.46902	1.97	9.93041	1.96	12.36581	**1.98**	12.43961	1.96
4	1.03449	**2.06**	2.46781	1.99	9.88497	1.98	12.29021	**1.99**	12.36294	1.98
5	1.03417	**2.14**	2.46750	1.99	9.87346	1.99	12.27120	**2.01**	12.34352	1.99

Table 9.12: Convergence rates for eigenvalues in the slit domain with and without energy correction.

No Correction $\gamma = 0$:

	1.EV		2.EV		3.EV		4.EV		5.EV	
	exact: 0.11422		exact: 0.11422		exact: 0.23460		exact: 0.31626		exact: 0.31626	
level	value	rate	value	rate	value	rate	value	rate	value	rate
1	0.11609	-	0.11609	-	0.23841	-	0.32303	-	0.32323	-
2	0.11489	**1.48**	0.11489	**1.48**	0.23595	**1.51**	0.31861	**1.53**	0.31867	**1.53**
3	0.11446	**1.46**	0.11446	**1.46**	0.23509	**1.47**	0.31709	**1.49**	0.31711	**1.50**
4	0.11431	**1.42**	0.11431	**1.42**	0.23478	**1.44**	0.31656	**1.45**	0.31657	**1.45**
5	0.11425	**1.39**	0.11425	**1.39**	0.23467	**1.40**	0.31637	**1.41**	0.31637	**1.42**

Correction $\gamma = 0.147850426060652$:

	1.EV		2.EV		3.EV		4.EV		5.EV	
	exact: 0.11422		exact: 0.11422		exact: 0.23460		exact: 0.31626		exact: 0.31626	
level	value	rate	value	rate	value	rate	value	rate	value	rate
1	0.11472	-	0.11473	-	0.23574	-	0.31869	-	0.31887	-
2	0.11435	**1.85**	0.11436	**1.85**	0.23492	**1.85**	0.31690	**1.92**	0.31695	**1.92**
3	0.11425	**1.97**	0.11425	**1.96**	0.23469	**1.96**	0.31642	**1.99**	0.31643	**1.99**
4	0.11422	**2.04**	0.11422	**2.03**	0.23462	**2.02**	0.31630	**2.04**	0.31630	**2.03**
5	0.11422	**2.11**	0.11422	**2.10**	0.23461	**2.09**	0.31627	**2.09**	0.31627	**2.08**

Table 9.13: Convergence rates for eigenvalues in the domain with multiple reentrant corners with and without correction.

for some eigenvalues in each of the three cases. However, using the modified method, the asymptotically optimal convergence of $\mathcal{O}(h^2)$ for all given eigenvalues is obtained in the three cases. Note that we excluded the results for some eigenvalues for the slit domain in Table 9.12. This is because the corresponding eigenfunctions do not include singular components strong enough to affect the optimal rate for linear elements. Hence, for these eigenvalues, a convergence rate of $\mathcal{O}(h^2)$ can be reached already by using the non-corrected method.

10. Duality techniques for smooth solutions in non-smooth domains

In this section we present some results which were already published in the paper "On optimal L^2- and surface flux convergence in FEM." by the author together with M. Melenk and B. Wohlmuth in Computing and Visualization in Science, Volume 16, 2015, [77].

In the last sections we have considered modification techniques to obtain optimal convergence rates in the presence of reentrant corners. In the following we show theoretically that under additional regularity of the solution, optimal convergence rates in L^2 are obtained, even if the dual problem lacks full regularity. Numerical examples in a variety of settings confirm the results.

10.1. Finite element method L^2-error analysis

Of importance will be the distance function δ_Γ and the regularized distance function $\widetilde{\delta}_\Gamma$ with $\Gamma = \partial\Omega$ given by

$$\delta_\Gamma(x) := \operatorname{dist}(x, \Gamma), \qquad \widetilde{\delta}_\Gamma(x) := h + \operatorname{dist}(x, \Gamma).$$

Later on, the parameter $h > 0$ will be the mesh size of the quasi-uniform triangulation. Also of importance will be neighborhoods S_D of the boundary $\partial\Omega$ given by

$$S_D := \{x \in \Omega \,|\, \delta_\Gamma(x) < D\},$$

with particular emphasis on the case $D = O(h)$.

For this section our model problem is as stated in Section 2.2, Equation (1) with the weak form given by

$$a(u, v) := \int_\Omega \mathbf{A}\nabla u \cdot \nabla v = \langle f, v\rangle, \qquad v \in H_0^1(\Omega). \tag{44}$$

We denote by $T : (H_0^1(\Omega))' \to H_0^1(\Omega)$ the solution operator. We emphasize that the choice of homogeneous Dirichlet boundary conditions is not essential for our purposes. Essential, however, is the following assumption:

Assumption 6. *There exists $s_0 \in (1/2, 1]$ such that the solution operator $f \mapsto Tf$*

for (44) satisfies

$$\|Tf\|_{H^{1+s_0}(\Omega)} \leq C\|f\|_{(H_0^{1-s_0}(\Omega))'} \leq C\|f\|_{L^2(\Omega)}.$$

Here and in the following $0 < c, C < \infty$ denote generic constants that do not depend on the mesh-size but possibly depend on s_0. Since our problem is symmetric, certain dual problems that will be needed below coincide with the primal problem, thus simplifying the presentation. Inspection of the procedure below shows that we need Assumption 6 for the dual problem and the bidual problem with weighted right-hand side. Let now $\mathcal{T}$ be an affine simplicial quasi-uniform triangulation of Ω with mesh size h and $V_h^k := V_h^k(\Omega) \subset H_0^1(\Omega)$ the continuous space of piecewise polynomials of degree k.

We restrict ourselves to simplicial triangulations since then the space V_h^k has the approximation properties, the inverse estimates, and moreover it has the "superapproximation property" that underlies the local error analysis as presented in [172, Sec. 5.4]. This restriction is however not essential. In the space V_h^k the Scott-Zhang operator $I_h^k : H^1(\Omega) \to V_h^k(\Omega)$ of [150] constitutes a quasi-local and stable approximation operator, such that

$$\|\nabla I_h^k u\|_{L^2(K)} \lesssim \|\nabla u\|_{L^2(\omega_K)},$$

where ω_K is the patch of elements sharing a node with K. Furthermore if $u \in H_0^1(\Omega)$ then $I_h^k u \in V_h^k$ and I_h^k satisfies the approximation properties

$$\|\nabla^j (u - I_h^k u)\|_{L^2(K)} \lesssim h^{l+1-j} \|\nabla^{l+1} u\|_{L^2(\omega_K)}, \quad j \in \{0, 1\}, \quad 0 \leq l \leq k.$$

With an interpolation argument using the K-method, it follows from above that for every $v \in B_{2,\infty}^{3/2}(\Omega) \cap H_0^1(\Omega)$ it holds that

$$\inf_{z \in V_h^k} \|v - z\|_{H^1(\Omega)} \leq h^{1/2} \|v\|_{B_{2,\infty}^{3/2}(\Omega)}.$$

Furthermore for integer $0 \leq j \leq m \leq k$ the space V_h^k satisfies the standard elementwise inverse estimates

$$|v|_{H^m(K)} \leq C h^{-(m-j)} |v|_{H^j(K)}, \qquad v \in V_h^k.$$

The Galerkin method for (44) is then:

Find $u_h \in V_h^k$ such that

$$a(u_h, v) = \langle f, v \rangle, \qquad v \in V_h^k.$$

The following embedding theorem is a key mechanism in our arguments that will allow us to exploit additional regularity of a function.

Lemma 10.1. *The following estimates hold, if $\Omega \subset \mathbb{R}^d$ is a bounded Lipschitz domain and z sufficiently regular.*

$$\begin{aligned}
\|\widetilde{\delta}_\Gamma^{-1/2+\varepsilon} z\|_{L^2(\Omega)} &\leq \|\delta_\Gamma^{-1/2+\varepsilon} z\|_{L^2(\Omega)} \leq C_\varepsilon \|z\|_{H^{1/2-\varepsilon}(\Omega)}, \quad \varepsilon \in (0, 1/2], && (45)\\
\|\widetilde{\delta}_\Gamma^{-1/2} z\|_{L^2(\Omega)} &\leq C|\ln h|^{1/2} \|z\|_{B^{1/2}_{2,1}(\Omega)}, && (46)\\
\|\widetilde{\delta}_\Gamma^{-1/2-\varepsilon} z\|_{L^2(\Omega)} &\leq C_\varepsilon h^{-\varepsilon} \|z\|_{B^{1/2}_{2,1}(\Omega)}, \qquad \varepsilon > 0, && (47)\\
\|z\|_{L^2(S_h)} &\leq C h^{1/2} \|z\|_{B^{1/2}_{2,1}(\Omega)}, \qquad h > 0, && (48)\\
\|z\|_{L^2(\Gamma)} &\leq C \|z\|_{B^{1/2}_{2,1}(\Omega)}. && (49)
\end{aligned}$$

Proof. The estimate involving δ_Γ in (45) can be found, e.g., in [67, Thm. 1.4.4.3] and (48) is shown in [100, Lemma 2.1]. The estimates (46), (47), (49) follow from one-dimensional Sobolev embedding theorems for L^∞ and locally flattening the boundary Γ in the same way as it is done in the proof of [100, Lemma 2.1]. For example, for (49) we note that a local flattening of the boundary Γ and the 1D embedding $\|v\|^2_{L^\infty(0,1)} \lesssim \|v\|_{L^2(0,1)} \|v\|_{H^1(0,1)}$ imply $\|z\|^2_{L^2(\Gamma)} \lesssim \|z\|_{L^2(\Omega)} \|z\|_{H^1(\Omega)}$. This implies the estimate $\|z\|_{L^2(\Gamma)} \lesssim \|z\|_{B^{1/2}_{2,1}(\Omega)}$ by [159, Lemma 25.3]. □

One of several applications of Lemma 10.1 is that it allows us to transform negative norms into weighted L^2-estimates as shown in the following lemma.

Lemma 10.2. *For $\varepsilon \in (0, 1/2]$ and sufficiently regular z there holds*

$$\begin{aligned}
\|\delta_\Gamma^\beta z\|_{(H^{1/2-\varepsilon}(\Omega))'} &\leq C_\varepsilon \|\delta_\Gamma^{\beta+1/2-\varepsilon} z\|_{L^2(\Omega)}, \quad -1 + 2\varepsilon \leq \beta \leq 0, && (50)\\
\|\widetilde{\delta}_\Gamma^{-1} z\|_{(B^{1/2}_{2,1}(\Omega))'} &\leq C|\ln h|^{1/2} \|\widetilde{\delta}_\Gamma^{-1/2} z\|_{L^2(\Omega)}. && (51)
\end{aligned}$$

Proof. We show the first inequality (50) using in the first step a standard duality argument and in the last step (45) of Lemma 10.1 to obtain

$$\begin{aligned}
\|\delta_\Gamma^\beta z\|_{(H^{1/2-\varepsilon}(\Omega))'} &= \sup_{v \in H^{1/2-\varepsilon}(\Omega)} \frac{\langle \delta_\Gamma^\beta z, v \rangle}{\|v\|_{H^{1/2-\varepsilon}(\Omega)}} \\
&= \sup_{v \in H^{1/2-\varepsilon}(\Omega)} \frac{\langle \delta_\Gamma^{\beta+1/2-\varepsilon} z, \delta_\Gamma^{-1/2+\varepsilon} v \rangle}{\|v\|_{H^{1/2-\varepsilon}(\Omega)}} \overset{(45)}{\leq} C_\varepsilon \|\delta_\Gamma^{\beta+1/2-\varepsilon} z\|_{L^2(\Omega)}.
\end{aligned}$$

Secondly, (51) follows by the same type of arguments, where the application of (45) is replaced with that of (46).

$$\begin{aligned}
\|\widetilde{\delta}_\Gamma^{-1} z\|_{(B^{1/2}_{2,1}(\Omega))'} &= \sup_{v\in B^{1/2}_{2,1}(\Omega)} \frac{\langle \tilde{\delta}_\Gamma^{-1} z, v\rangle}{\|v\|_{B^{1/2}_{2,1}(\Omega)}} = \sup_{v\in B^{1/2}_{2,1}(\Omega)} \frac{\langle \tilde{\delta}_\Gamma^{-1+1/2} z, \tilde{\delta}_\Gamma^{-1/2} v\rangle}{\|v\|_{B^{1/2}_{2,1}(\Omega)}} \\
&\leq \|\tilde{\delta}_\Gamma^{-1/2} z\|_{L^2(\Omega)} \sup_{v\in B^{1/2}_{2,1}(\Omega)} \frac{\|\tilde{\delta}_\Gamma^{-1/2} v\|_{L^2(\Omega)}}{\|v\|_{B^{1/2}_{2,1}(\Omega)}} \\
&\overset{(46)}{\leq} \|\tilde{\delta}_\Gamma^{-1/2} z\|_{L^2(\Omega)} \sup_{v\in B^{1/2}_{2,1}(\Omega)} \frac{C|\ln h|^{1/2}\|v\|_{B^{1/2}_{2,1}(\Omega)}}{\|v\|_{B^{1/2}_{2,1}(\Omega)}} \\
&= C|\ln h|^{1/2} \|\widetilde{\delta}_\Gamma^{-1/2} z\|_{L^2(\Omega)}
\end{aligned}$$

□

The following lemma is a variant of interior regularity of elliptic problems and will be required for the proof of Theorem 9.

Lemma 10.3. *Let Ω be a bounded Lipschitz domain and $z \in H^{1+\beta}(\Omega)$, $\beta \in (0,1]$, solve*

$$-\nabla\cdot(\mathbf{A}\nabla z) = f \quad \text{in } \Omega.$$

Then, for a constant $C>0$ depending only on $\|\mathbf{A}\|_{C^{0,1}(\overline{\Omega})}$, α_0, β, and Ω

$$\|\delta_\Gamma^{1-\beta}\nabla^2 z\|_{L^2(\Omega)} \leq C\left(\|\delta_\Gamma^{1-\beta} f\|_{L^2(\Omega)} + \|z\|_{H^{1+\beta}(\Omega)}\right).$$

Proof. The upper bound follows from local interior regularity for elliptic problems (see [115, Lemma 5.7.2] or [64, Thm. 8.8]) and a Besicovitch covering argument, see, e.g., [55, Section 1.5.2] and [110, Chapter 5]. We refer also to [94, Lemma A.3], where a closely related result is worked out in detail. We use the Besicovitch covering theorem to construct a covering of Ω by the countable collection $\mathcal{B} = \{B_i | i \in \mathbb{N}\}$ of closed balls B_i where $B_i = B_{r_i}(x_i)$ with the following properties:

1. We have $r_i = c'\mathrm{dist}(x_i, \partial\Omega)$ for a fixed $c' \in (0,1)$.
2. There is an $N \in \mathbb{N}$ such that for all $x \in \Omega$ $|\{i \in \mathbb{N} | x \in B_i\}| \leq N$.
3. There exists a $c \in (0,1)$ such that $\Omega \subset \cup_{i\in\mathbb{N}} B_{cr_i}(x_i)$.

We set

$$C_i^2 = \|f\|^2_{B_{\delta_{\mathcal{E}}}(x)}$$

and use the Besicovitch covering and [94, Lemma A.3] with $p = 0$ to obtain

$$\begin{aligned}
\|\delta_{\mathcal{E}}^{1-\beta}\nabla^2 z\|_{L^2(\Omega)}^2 &\leq C\sum_i \delta_{\mathcal{E}}^{2(1-\beta)}\|\nabla^2 z\|_{L^2(B_{\delta_{\mathcal{E}}}(x))}^2 \\
&\overset{[94,\text{Lemma A.3}]}{\leq} C\sum_i \|\delta_{\mathcal{E}}^{(1-\beta)} f\|_{L^2(B_{\delta_{\mathcal{E}}}(x))}^2 + \|z\|_{H^1(B_{\delta_{\mathcal{E}}}(x))}^2 \\
&\quad + |\nabla z|_{H^\beta(B_{\delta_{\mathcal{E}}}(x))}^2 \\
&\leq C\left(\|\delta_{\mathcal{E}}^{1-\beta} f\|_{L^2(\Omega)}^2 + \|z\|_{H^{1+\beta}(\Omega)}^2\right)
\end{aligned}$$

with a suitable constant C. □

It is worth pointing out that neither the structure of the boundary Γ nor the kind of boundary conditions play a role in Lemma 10.3. One possible interpretation of Lemma 10.3 is that z could lose the H^2-regularity anywhere near Γ. For certain boundary conditions such as homogeneous Dirichlet conditions and piecewise smooth geometries Γ the solution fails to be in H^2 only near the points of non-smoothness of the geometry. With methods similar to those of Lemma 10.3 one can show the following, stronger result:
For the proof of Lemma 10.3 we had to employ a standard Besicovitch covering argument. For the stronger result, which will be stated in Lemma 10.8, we have to employ the following coverings, introduced by Theorems 7 and 8. In order to be able to prove these theorems, we introduce several concepts in the following. Note that for the distance $\operatorname{dist}(x, M)$ to some set M, we set $\operatorname{dist}(x, \emptyset) = 1$ to include the degenerate case $M = \emptyset$. We quote from [113, Lemma A.1]:

Lemma 10.4. *Let $\Omega \subset \mathbb{R}^d$ be bounded open and $M = \overline{M}$ be a closed set. Fix $c \in (0, 1)$ and $\varepsilon \in (0, 1)$ such that*

$$1 - c(1 + \varepsilon) =: c_0 > 0.$$

For each $x \in \Omega$, let $B_x := \overline{B}_{c\operatorname{dist}(x,M)}(x)$ be the closed ball of radius $c\operatorname{dist}(x, M)$ centered at x, and let $\widehat{B}_x := \overline{B}_{(1+\varepsilon)c\operatorname{dist}(x,M)}(x)$ denote the stretched (closed) ball of radius $(1 + \varepsilon)c\operatorname{dist}(x, M)$ also centered at x.
Then there exists a countable set $x_i \in \Omega$, $i \in \mathbb{N}$, and a constant $N \in \mathbb{N}$ depending solely on the spatial dimension d with the following properties:

1. *(covering property) $\cup_{i\in\mathbb{N}} B_{x_i} \supset \Omega$;*
2. *(finite overlap on Ω) for each $x \in \Omega$, there holds $\operatorname{card}\{i \,|\, x \in \widehat{B}_{x_i}\} \leq N$.*

Proof. See [77]. □

Before we proceed with variants of the covering result of Lemma 10.4, we can now state the notation of sectorial neighborhoods relative to a singular set M:

Definition 10.5 (Sectorial neighborhood)**.** *Let e, $M \subset \mathbb{R}^d$ and $\widetilde{c} > 0$. Then*

$$S_{e,M,\widetilde{c}} := \cup_{x \in e} B_{\widetilde{c}\,\mathrm{dist}(x,M)}(x)$$

is a sectorial neighborhood of the set e relative to the singular set M.

We are interested in coverings of lower dimensional manifolds by balls whose centers are located on these manifolds:

Lemma 10.6. *Let $d \in \mathbb{N}$ and $1 \leq d' < d$. Let $\omega \subset \mathbb{R}^{d'}$ and let $\Omega \subset \mathbb{R}^d$ be the canonical embedding of ω into $\mathbb{R}^d$, i.e., $\Omega := \omega \times \{0\} \times \cdots \times \{0\} \subset \mathbb{R}^d$. Assume the hypotheses and notation of Lemma 10.4. Then there are $\widetilde{c} > 0$, $N > 0$, and a collection of balls B_{x_i}, $i \in \mathbb{N}$, as described in Lemma 10.4 such that*

(i) (covering property for Ω) $\cup_{i\in\mathbb{N}} B_{x_i} \supset \Omega$.

(ii) (covering property for a sectorial neighborhood of Ω) $\cup_{i\in\mathbb{N}} B_{x_i} \supset S_{\Omega,M,\widetilde{c}}$.

(iii) (finite overlap property on $\mathbb{R}^d$) for each $x \in \mathbb{R}^d$, there holds

$$\mathrm{card}\{i \,|\, x \in \widetilde{B}_{x_i}\} \leq N.$$

Proof. We employ the result of Lemma 10.4 for the lower-dimensional manifold ω noting that $B_x \cap \omega$ is a ball in $\mathbb{R}^{d'}$. In order to be able to ensure the covering condition for the sectorial neighborhood of Ω stated in (iii), we introduce the auxiliary balls $B'_x := \overline{B}_{c/2\,\mathrm{dist}(x,M)}(x)$ of half the radius. Applying Lemma 10.4 with these balls B'_x and the stretched balls $\widehat{B}_x$ therefore produces a collection of centers $x_i \in \Omega$, $i \in \mathbb{N}$, such that

1. $B'_{x_i} \cap \Omega$ covers Ω;
2. for the stretched balls $\widehat{B}_{x_i}$, we have a finite overlap property on Ω:

$$x \in \Omega: \quad \mathrm{card}\{i \,|\, x \in \widehat{B}_{x_i}\} \leq N. \tag{52}$$

We next see that the balls $\widehat{B}_{x_i}$ even have the following, stronger finite overlap property:

$$x \in \mathbb{R}^d: \quad \mathrm{card}\{i \,|\, x \in \widehat{B}_{x_i}\} \leq N.$$

To see this, define the infinite cylinders $\widehat{C}_{x_i} := \{x \,|\, \pi_{d'}(x) \in \widehat{B}_{x_i} \cap \Omega\}$, where $\pi_{d'}$ is the canonical projection onto the hyperplane $\{x = (x_1, \dots, x_d) \in \mathbb{R}^d \,|\, x_{d'+1} = \cdots = x_d = 0\}$. Clearly, $\widehat{B}_{x_i} \subset \widehat{C}_{x_i}$. These infinite cylinders have a finite overlap property by (52) as can be seen by writing any $x \in \mathbb{R}^d$ in the form $x = (\pi_{d'}(x), x')$ for some $x' \in \mathbb{R}^{d-d'}$ and then noting that $x \in \widehat{C}_{x_i}$ implies $\pi_{d'}(x) \in \widehat{B}_{x_i} \cap \Omega$.
It remains to see that the balls B_{x_i} cover a sectorial neighborhood of Ω. To that end, we note that the balls B'_{x_i} cover Ω. Furthermore, for each $x \in \Omega$, we pick x_i such that $x \in B'_{x_i} \subset B_{x_i}$. Since the radius of B_{x_i} is twice that of B'_{x_i}, we even have $B_{c/2\,\mathrm{dist}(x_i,M)}(x) \subset B_{x_i}$. Furthermore, by $c \in (0,1)$, we have

$$0 < (1 - c/2)\,\mathrm{dist}(x_i, M) \leq \mathrm{dist}(x, M) \leq (1 + c/2)\,\mathrm{dist}(x_i, M).$$

Therefore, there is $\widetilde{c} > 0$ such that $B_{\widetilde{c}\,\mathrm{dist}(x,M)}(x) \subset B_{x_i}$ and thus

$$\cup_{x\in\Omega} B_{\widetilde{c}\,\mathrm{dist}(x,M)}(x) \subset \cup_i B_{x_i}.$$

□

We next show covering theorems for polygons and polyhedra. In the interest of clarity of presentation, we formulate two separate results. Before doing so, we point out that the intersection of balls with center located on the boundary of the polygon/polyhedron Ω with the domain Ω will be of interest. We therefore introduce the following notions:

Definition 10.7 (Solid angles and dihedral angles)**.** *1. Let $\Omega \subset \mathbb{R}^2$ be a Lipschitz polygon. Let A be a vertex where the edges e_1, e_2 meet. We say that the set $B_\varepsilon(A) \cap \Omega$ is a solid angle, if $\partial(B_\varepsilon(A) \cap \Omega) \cap \partial\Omega$ is contained in $\{A\} \cup e_1 \cup e_2$.*

2. Let $\Omega \subset \mathbb{R}^3$ be a Lipschitz polyhedron. Let A be a vertex of Ω. We say that the set $B_\varepsilon(A) \cap \Omega$ is a solid angle*, if $\partial(B_\varepsilon(A) \cap \Omega) \cap \partial\Omega$ is contained in the union of $\{A\}$ and the edges and faces meeting at A.*

3. Let $\Omega \subset \mathbb{R}^3$ be a Lipschitz polyhedron. Let e be an edge of Ω, which is shared by the faces f_1, f_2. Let $x \in e$. We say that the set $B_\varepsilon(x) \cap \Omega$ is a dihedral angle*, if $\partial(B_\varepsilon(x) \cap \Omega) \cap \partial\Omega$ is contained in $e \cup f_1 \cup f_2$.*

We are now ready to introduce a two-dimensional covering theorem for polygons.

Theorem 7. *Let $\Omega \subset \mathbb{R}^2$ be a bounded Lipschitz polygon with vertices A_j, $j = 1, \dots, J$, and edges $\mathcal{E}$. Let $M \subset \{A_1, \dots, A_J\}$. Set $\mathcal{A}' := \{A_1, \dots, A_J\} \setminus M$ and fix $\varepsilon \in (0,1)$.*

(i) *There is a sectorial neighborhood* $S_{\mathcal{A}',M,\widetilde{c}}$ *of the vertices* $\mathcal{A}'$ *and a constant* $c \in (0,1)$ *such that* $S_{\mathcal{A}',M,\widetilde{c}}$ *is covered by balls* $B_i := \overline{B}_{c\,\mathrm{dist}(x_i,M)}(x_i)$ *with centers* $x_i \in \mathcal{A}'$. *Furthermore, the stretched balls* $\widehat{B}_i := \overline{B}_{(1+\varepsilon)c\,\mathrm{dist}(x_i,M)}(x_i)$ *are solid angles and satisfy a finite overlap property on* $\mathbb{R}^2$.

(ii) *Fix a sectorial neighborhood* $\mathcal{U} := S_{\mathcal{A}',M,c'}$ *of the vertices* $\mathcal{A}'$. *For each edge* $e \in \mathcal{E}$, *there is a sectorial neighborhood* $S_{e,M,\widetilde{c}}$ *and a constant* $c \in (0,1)$ *such that* $S_{e,M,\widetilde{c}} \setminus \mathcal{U}$ *is covered by balls* $B_i = \overline{B}_{c\,\mathrm{dist}(x_i,M)}(x_i)$ *whose centers* x_i *are located on* e. *Furthermore, the stretched balls* $\widehat{B}_i = \overline{B}_{(1+\varepsilon)c\,\mathrm{dist}(x_i,M)}(x_i)$ *satisfy a finite overlap property on* $\mathbb{R}^2$ *and are such that each* $\widehat{B}_i \cap \Omega$ *is a half-disk.*

(iii) *Fix a sectorial neighbood* $\mathcal{U} := S_{\mathcal{E},M,c'}$ *of the edges* $\mathcal{E}$. *There is* $c \in (0,1)$ *such that* $\Omega \setminus \mathcal{U}$ *is covered by balls* $B_i = \overline{B}_{c\,\mathrm{dist}(x_i,M)}(x_i)$ *such that the stretched balls* $\widehat{B}_i = \overline{B}_{(1+\varepsilon)c\,\mathrm{dist}(x_i,M)}(x_i)$ *are completely contained in* Ω *and satisfy a finite overlap property on* $\mathbb{R}^2$.

Proof. The assertion (i) is almost trivial and only included to emphasize the structure of the arguments. Assertions (ii), (iii) follow from suitable applications of Lemmas 10.6 and 10.4. □

The three-dimensional version of Theorem 7 is formulated in Theorem 8. We emphasize that the "singular" set M does not need to be the union of *all* edges and vertices but can be just a subset. We also emphasize that it is not necessarily related to the notion of "singular set" in Definition 10.9, although it is used in this way. The key property of the covering balls is again such that the centers are either a) in Ω (in which case the stretched ball is contained in Ω); or b) on a face (in which case the stretched ball $\widehat{B}_i$ is such that $\widehat{B}_i \cap \Omega$ is a half-ball); or c) on an edge in which case $\widehat{B}_i \cap \Omega$ is a dihedral angle (see Definition 10.7); or d) in a vertex in which case $\widehat{B}_i \cap \Omega$ is a solid angle (see Definition 10.7).

Theorem 8. *Let* $\Omega \subset \mathbb{R}^3$ *be a Lipschitz polyhedron with faces* $\mathcal{F}$, *edges* $\mathcal{E}$, *and vertices* $\mathcal{A}$. *Let* $M_{\mathcal{A}} \subset \mathcal{A}$ *and* $M_{\mathcal{E}} \subset \mathcal{E}$. *Let* $M = \overline{M} = \overline{M_{\mathcal{A}} \cup M_{\mathcal{E}}}$ *and fix* $\varepsilon \in (0,1)$. *Let* $\mathcal{A}' := \{A \in \mathcal{A} \,|\, A \notin M\}$ *be the vertices not in* M *and* $\mathcal{E}' := \{e \in \mathcal{E} \,|\, \overline{e} \cap M = \emptyset\}$ *be the edges not abutting* M. *Then:*

(i) *(non-singular vertices) There is a sectorial neighborhood* $S_{\mathcal{A}',M,\widetilde{c}}$ *of the vertices in* $\mathcal{A}'$ *and a constant* $c \in (0,1)$ *such that* $S_{\mathcal{A}',M,\widetilde{c}}$ *is covered by balls* $B_i := \overline{B}_{c\,\mathrm{dist}(x_i,M)}(x_i)$ *with centers* $x_i \in \mathcal{A}'$. *Furthermore, the stretched balls* $\widehat{B}_i := \overline{B}_{(1+\varepsilon)c\,\mathrm{dist}(x_i,M)}(x_i)$ *are solid angles and satisfy a finite overlap property on* $\mathbb{R}^3$.

(ii) *(non-singular edges) Fix a sectorial neighborhood* $\mathcal{U} := S_{\mathcal{A}',M,c'}$ *of* $\mathcal{A}'$. *For each edge* $e \in \mathcal{E}'$, *there is a sectorial neighborhood* $S_{e,M,\widetilde{c}}$ *and a constant* $c \in (0,1)$ *such that* $S_{e,M,\widetilde{c}} \setminus \mathcal{U}$ *is covered by balls* $B_i = \overline{B}_{c\,\mathrm{dist}(x_i,M)}(x_i)$ *whose centers* x_i *are located on* e. *Furthermore, the stretched balls* $\widehat{B}_i = \overline{B}_{(1+\varepsilon)c\,\mathrm{dist}(x_i,M)}(x_i)$ *satisfy a finite overlap property on* $\mathbb{R}^3$ *and* $\widehat{B}_i \cap \Omega$ *is a dihedral angle.*

(iii) *(faces) Fix a sectorial neighbood* $\mathcal{U} := S_{\mathcal{E},M,c'}$ *of* $\mathcal{E}$. *There is a sectorial neighborhood* $S_{\mathcal{F},M,\widetilde{c}}$ *and a constant* $c \in (0,1)$ *such that* $S_{\mathcal{F},M,\widetilde{c}} \setminus \mathcal{U}$ *is covered by balls* $B_i = \overline{B}_{c\,\mathrm{dist}(x_i,M)}(x_i)$ *with centers* $x_i \in \partial\Omega$. *Furthermore, the stretched balls* $\widehat{B}_i = \overline{B}_{(1+\varepsilon)c\,\mathrm{dist}(x_i,M)}(x_i)$ *satisfy a finite overlap property on* $\mathbb{R}^3$ *and* $\widehat{B}_i \cap \Omega$ *is a half-ball.*

(iv) *(interior) Fix a sectorial neighbood* $\mathcal{U} := S_{\mathcal{F},M,c'}$ *of* $\mathcal{F}$, *where* $\mathcal{F}$ *is the set of faces. Then there is* $c \in (0,1)$ *such that* $\Omega \setminus \mathcal{U}$ *is covered by balls* $B_i = \overline{B}_{c\,\mathrm{dist}(x_i,M)}(x_i)$ *with centers* $x_i \in \Omega$. *Furthermore, the stretched balls* $\widehat{B}_i = \overline{B}_{(1+\varepsilon)c\,\mathrm{dist}(x_i,M)}(x_i)$ *satisfy a finite overlap property on* $\mathbb{R}^3$ *and* $\widehat{B}_i \subset \Omega$.

Proof. Follows from Lemmas 10.6 and 10.4. □

Now finally we have the adequate tools to state and to prove the stronger result of Lemma 10.3.

Lemma 10.8. *Let* Ω *be a (curvilinear) polygon in 2D or a (curvilinear) polyhedron in 3D. Denote by* $\mathcal{E}$ *the set of all vertices of* Ω *in 2D and the set of all edges of* Ω *in 3D. Let* $\delta_{\mathcal{E}}$ *be the distance from* $\mathcal{E}$. *Let* $z \in H^{1+\beta}(\Omega)$, $\beta \in (0,1]$, *solve (1). Then, for a constant* C *depending on* α_0, $\|\mathbf{A}\|_{C^{0,1}(\overline{\Omega})}$, β, *and* Ω,

$$\|\delta_{\mathcal{E}}^{1-\beta}\nabla^2 z\|_{L^2(\Omega)} \leq C_\beta \left(\|\delta_{\mathcal{E}}^{1-\beta} f\|_{L^2(\Omega)} + \|z\|_{H^{1+\beta}(\Omega)} \right).$$

Proof. Follows from local considerations as in Lemma 10.3. The novel aspect is the behavior near the boundary away from the vertices (in two dimensions) and the edges (in three dimensions). This is achieved with an adapted covering theorem of the type described in Theorems 7, 8. The key feature of these coverings is that they allow us to reduce the considerations to balls $B = B_r(x)$ and stretched balls $\widehat{B} = B_{(1+\varepsilon)r}(x)$ (with fixed $\varepsilon > 0$) with $r \sim \mathrm{dist}(x, \mathcal{E})$ and the following properties: either $x \in \Omega$ with $\widehat{B}_r(x) \subset \Omega$ or $x \in \Gamma$ and $\widehat{B} \cap \Omega$ is a half-ball. Local elliptic regularity assertions can then be employed for each ball B. □

Lemma 10.8 assumes that a loss of H^2-regularity occurs at any point of non-smoothness of Γ. However, the set of "singular" vertices or edges can be further

reduced. For example, in two dimensions for $\mathbf{A} = \mathrm{Id}$, it is well-known that only the vertices of Ω with interior angle greater than π lead to a loss of full H^2-regularity. It will therefore be useful to introduce the closed set M_s of boundary points associated with a loss of H^2-regularity. Before introducing this set, we point out that this set is a subset of the vertices and edges:

Definition 10.9 (H^2-regular part and singular part of the boundary)**.** *Let Ω be a polygon (in 2D) or a polyhedron (in 3D) with vertices $\mathcal{A}$ and edges $\mathcal{E}$.*

1. *A vertex $A \in \mathcal{A}$ of Ω is said to be H^2-regular, if there is a ball $B_\varepsilon(A)$ of radius $\epsilon > 0$ such that the solution u of (1) satisfies $u|_{B_\varepsilon(A)\cap\Omega} \in H^2(\Omega)$ whenever $f \in L^2(\Omega)$ together with the* a priori *estimate $\|u\|_{H^2(B_\varepsilon(A)\cap\Omega)} \leq C\|f\|_{L^2(\Omega)}$.*

2. *In three dimensions, an edge $e \in \mathcal{E}$ of Ω with endpoints A_1, A_2 is said to be H^2-regular if the following condition is satisfied: There is $c > 0$ such that for the neighborhood $S = \cup_{x\in e} B_{c\,\mathrm{dist}(x,\{A_1,A_2\})}(x)$ of the edge e we have the regularity assertion $u|_{S\cap\Omega} \in H^2$ for the solution u of (1) whenever $f \in L^2(\Omega)$ together with the* a priori *estimate $\|u\|_{H^2(S\cap\Omega)} \leq C\|f\|_{L^2(\Omega)}$.*

Denote by $\mathcal{A}_r \subset \mathcal{A}$ the set of H^2-regular vertices and by $\mathcal{E}_r \subset \mathcal{E}$ the set of H^2-regular edges. Correspondingly, let $\mathcal{A}_s := \mathcal{A} \setminus \mathcal{A}_r$ and $\mathcal{E}_s := \mathcal{E} \setminus \mathcal{E}_r$ be the set of vertices and edges, respectively, associated with a loss of H^2-regularity. Define the singular set M_s *as*

$$M_s := \mathcal{A}_s \bigcup \mathcal{E}_s \subset \Gamma.$$

With the notion of the singular set in hand, we can formulate the following regularity result:

Lemma 10.10. *Let Ω be a polygon or a polyhedron. Let M_s be the singular set as defined in Definition 10.9. Then the following is true for any solution $z \in H^1_0(\Omega)$ of (1): If $z \in H^{1+\beta}(\Omega)$ for some $\beta \in (0, 1]$, then with $\delta_{M_s} := \mathrm{dist}(\cdot, M_s)$, there holds for some $C > 0$ depending only on α_0, $\|\mathbf{A}\|_{C^{0,1}(\overline{\Omega})}$, β, and Ω,*

$$\|\delta_{M_s}^{1-\beta}\nabla^2 z\|_{L^2(\Omega)} \leq C_\beta \left(\|\delta_{M_s}^{1-\beta} f\|_{L^2(\Omega)} + \|z\|_{H^{1+\beta}(\Omega)}\right).$$

Proof. The proof is based on local considerations as in Lemma 10.8. We recall that not all vertices and edges (in 3D) are included in the singular set M_s. This is accounted for by a further refinement of the covering employed. We restrict ourselves to the 3D situation. Using finite coverings provided by Theorem 8, one may restrict the attention to balls $B_r = B_r(x)$ and stretched balls $\widehat{B} = B_{(1+\varepsilon)r}(x)$ (with

fixed $\varepsilon > 0$) with $r \sim \operatorname{dist}(x, \mathcal{E})$ where one of the following additional properties is satisfied: a) $x \in \Omega$ with $\widehat{B}_r(x) \subset \Omega$; b) $x \in \mathcal{A}_r$ and $\widehat{B} \cap \Omega$ is a solid angle; c) $x \in \cup \mathcal{E}_r$ and $\widehat{B} \cap \Omega$ is a dihedral angle; d) x lies in the interior of a face and $\widehat{B} \cap \Omega$ is a half-ball. We emphasize that we do not need to consider balls $B_r(x)$ with $x \in \mathcal{A}_s$ or $x \in \mathcal{E}_s$ since the covering provided by Theorem 8 is such that for every such x there is a neighborhood $\mathcal{U}_x$ of x that is covered by (countably many) balls whose radii tend to 0 as their centers approach x.

□

We have the following continuity results for the solution operator T for our model problem (1) with locally supported right-hand sides:

Lemma 10.11. *Let Assumption 6 be valid. Then $T : (H_0^1(\Omega))' \to H_0^1(\Omega)$ satisfies*

$$\begin{aligned} \|Tf\|_{B^{3/2}_{2,\infty}(\Omega)} &\leq C\|f\|_{(B^{1/2}_{2,1}(\Omega))'}, && (53)\\ \|Tf\|_{H^{3/2+\varepsilon}(\Omega)} &\leq C_\varepsilon \|\delta_\Gamma^{1/2-\varepsilon} f\|_{L^2(\Omega)}, \qquad 0 < \varepsilon \leq s_0 - 1/2. && (54) \end{aligned}$$

In particular, if $f \in L^2(\Omega)$ with $\operatorname{supp} f \subset \overline{S_h}$, then

$$\begin{aligned} \|Tf\|_{B^{3/2}_{2,\infty}(\Omega)} &\leq Ch^{1/2}\|f\|_{L^2(\Omega)}, && (55)\\ \|Tf\|_{H^{3/2+\varepsilon}(\Omega)} &\leq C_\varepsilon h^{1/2-\varepsilon}\|f\|_{L^2(\Omega)}, \qquad 0 < \varepsilon \leq s_0 - 1/2. && (56) \end{aligned}$$

Proof. We follow the arguments of [113, Lemma 5.2]. The starting point for the proof of (53) is that interpolation and Assumption 6 yield with $\theta \in (0,1)$

$$T : ((H_0^{1-s_0}(\Omega))', (H_0^1(\Omega))')_{\theta,\infty} \to (H^{1+s_0}(\Omega), H^1(\Omega))_{\theta,\infty} = B^{1+s_0(1-\theta)}_{2,\infty}(\Omega).$$

Next, we recognize as in [113, Lemma 5.2] (cf. [163, Thm. 1.11.2] or [159, Lemma 41.3])

$$\begin{aligned} ((H_0^{1-s_0}(\Omega))', (H_0^1(\Omega))')_{\theta,\infty} &= ((H_0^{1-s_0}(\Omega), H_0^1(\Omega))_{\theta,1})' \\ &\supset ((H^{1-s_0}(\Omega), H^1(\Omega))_{\theta,1})' = (B^{1-s_0(1-\theta)}_{2,1}(\Omega))'. \end{aligned}$$

Setting $\theta = 1 - 1/(2s_0) \in (0, 1/2]$, we get $(B^{1-s_0(1-\theta)}_{2,1}(\Omega))' = (B^{1/2}_{2,1}(\Omega))'$ and $B^{1+s_0(1-\theta)}_{2,\infty}(\Omega) = B^{3/2}_{2,\infty}(\Omega)$.
The assertion (54) follows from the Assumption 6 and (50) with $\beta = 0$.

$$\begin{aligned} \|Tf\|_{H^{1+(1/2+\varepsilon)}(\Omega)} &\leq C\|f\|_{(H_0^{1-(1/2+\varepsilon)}(\Omega))'} \\ &\overset{(50)}{\leq} C_\varepsilon \|\delta_\Gamma^{1/2-\varepsilon} f\|_{L^2(\Omega)}, \end{aligned}$$

For the bound (55), we argue as in the proof of Lemma 10.2 and use (48), see also [113, Lemma 5.2].

$$\begin{aligned}
\|Tf\|_{B^{3/2}_{2,\infty}(\Omega)} &\leq C\|f\|_{B^{1/2}_{2,1}(\Omega)'} \\
&= C \sup_{z\in B^{1/2}_{2,1}(\Omega)} \frac{(f,z)_{L^2(S_h)}}{\|z\|_{B^{1/2}_{2,1}(\Omega)}} \\
&\leq C\|f\|_{L^2(\Omega)} \sup_{z\in B^{1/2}_{2,1}(\Omega)} \frac{\|z\|_{L^2(S_h)}}{\|z\|_{B^{1/2}_{2,1}(\Omega)}} \\
&\overset{(48)}{\leq} C\sqrt{h}\|f\|_{L^2(\Omega)}
\end{aligned}$$

Finally, the proof of (56) follows from (54) and the assumed support properties of f as

$$\|Tf\|_{H^{3/2+\varepsilon}(\Omega)} \leq C_\varepsilon \|\delta_\Gamma^{1/2-\varepsilon} f\|_{L^2(\Omega)} \leq C_\varepsilon h^{1/2-\varepsilon}\|f\|_{L^2(\Omega)}.$$

□

We will also require mapping properties of the solution operator T in weighted spaces:

Lemma 10.12. *Let Assumption 6 be valid. Then for $v \in L^2(\Omega)$*

$$\|T(\widetilde{\delta}_\Gamma^{-1} v)\|_{B^{3/2}_{2,\infty}(\Omega)} \leq C|\ln h|^{1/2}\|\widetilde{\delta}_\Gamma^{-1/2} v\|_{L^2(\Omega)}, \tag{57}$$

$$\|T(\widetilde{\delta}_\Gamma^{-1} v)\|_{H^{3/2+\varepsilon}(\Omega)} \leq C_\varepsilon h^{-\varepsilon}\|\widetilde{\delta}_\Gamma^{-1/2} v\|_{L^2(\Omega)}, \quad \varepsilon \in (0, s_0 - 1/2], \tag{58}$$

$$\|T(\delta_\Gamma^{-1+2\varepsilon} v)\|_{H^{3/2+\varepsilon}(\Omega)} \leq C_\varepsilon \|\delta_\Gamma^{-1/2+\varepsilon} v\|_{L^2(\Omega)}, \quad \varepsilon \in (0, s_0 - 1/2]. \tag{59}$$

Proof. The results follow by combining Lemmas 10.2 and 10.11. To prove the first inequality, we employ the Equations (53) and (51) to obtain

$$\begin{aligned}
\|T(\widetilde{\delta}_\Gamma^{-1} v)\|_{B^{3/2}_{2,\infty}(\Omega)} &\overset{(53)}{\leq} C\|\tilde{\delta}_\Gamma^{-1} v\|_{(B^{1/2}_{2,1}(\Omega))'} \\
&\overset{(51)}{\leq} C|\ln h|^{1/2}\|\widetilde{\delta}_\Gamma^{-1/2} v\|_{L^2(\Omega)}.
\end{aligned}$$

Then with Equation (54) we can state that

$$\begin{aligned}\|T(\widetilde{\delta}_\Gamma^{-1}v)\|_{H^{3/2+\varepsilon}(\Omega)} &\overset{(54)}{\leq} C_\varepsilon\|\delta_\Gamma^{1/2-\varepsilon}\tilde{\delta}_\Gamma^{-1}v\|_{L^2(\Omega)}\\ &\leq C_\varepsilon\|\tilde{\delta}_\Gamma^{1/2-\varepsilon}\tilde{\delta}_\Gamma^{-1}v\|_{L^2(\Omega)}\\ &\leq C_\varepsilon h^{-\varepsilon}\|\widetilde{\delta}_\Gamma^{-1/2}v\|_{L^2(\Omega)}.\end{aligned}$$

For the last inequality we can show using (54) that

$$\begin{aligned}\|T(\delta_\Gamma^{-1+2\varepsilon}v)\|_{H^{3/2+\varepsilon}(\Omega)} &\overset{(54)}{\leq} C_\varepsilon\|\delta^{1/2-\varepsilon}\delta_\Gamma^{-1+2\varepsilon}v\|_{L^2(\Omega)}\\ &= C_\varepsilon\|\delta^{-1/2+\varepsilon}v\|_{L^2(\Omega)}.\end{aligned}$$

□

The standard workhorse for L^2-error analysis of the FEM approximation u_h with the error $e = u - u_h$ is the Galerkin orthogonality given by

$$a(e,v) = a(u-u_h,v) = 0, \qquad v \in V_h^k.$$

We start with a weighted L^2-error:

Lemma 10.13. *Let Assumption 6 be valid. Assume that a function $z \in H_0^1(\Omega)$ satisfies the Galerkin orthogonality*

$$a(z,v) = 0, \qquad v \in V_h^k.$$

Then

$$\|\delta_\Gamma^{-1/2+\varepsilon}z\|_{L^2(\Omega)} \leq C_\varepsilon h^{1/2+\varepsilon}\|z\|_{H^1(\Omega)}, \qquad \varepsilon \in (0, s_0 - 1/2], \tag{60}$$

$$\|\widetilde{\delta}_\Gamma^{-1/2}z\|_{L^2(\Omega)} \leq Ch^{1/2}|\ln h|^{1/2}\|z\|_{H^1(\Omega)}. \tag{61}$$

Proof. The proof follows standard lines. Define $\psi = T(\delta_\Gamma^{-1+2\varepsilon}z)$, which solves

$$\langle v, \delta_\Gamma^{-1+2\varepsilon}z\rangle = a(v,\psi), \qquad v \in H_0^1(\Omega).$$

Then we have by Galerkin orthogonality for arbitrary $I\psi \in V_h^k$

$$\|\delta_\Gamma^{-1/2+\varepsilon}z\|_{L^2(\Omega)}^2 = a(z,\psi) = a(z,\psi - I\psi) \leq C\|z\|_{H^1(\Omega)}\|\psi - I\psi\|_{H^1(\Omega)}.$$

From (59) in Lemma 10.12, we have $\|\psi\|_{H^{3/2+\varepsilon}(\Omega)} \leq C_\varepsilon\|\delta_\Gamma^{-1/2+\varepsilon}z\|_{L^2(\Omega)}$ so that with

the approximation properties of V_h^k we get

$$\inf_{I\psi\in V_h^k} \|\psi - I\psi\|_{H^1(\Omega)} \leq C_\varepsilon h^{1/2+\varepsilon} \|\delta_\Gamma^{-1/2+\varepsilon} z\|_{L^2(\Omega)}.$$

This shows (60). For (61), we proceed similarly using the regularity assertion (57) and the approximation property of V_h^k. Define $\psi = T(\widetilde{\delta}_\Gamma^{-1} z)$ as the solution of

$$\langle v, \tilde{\delta}_\Gamma^{-1} z\rangle = a(v,\psi), \qquad v \in H_0^1(\Omega).$$

Then using the Galerkin orthogonality for arbitrary $I\psi \in V_h^k$ it follows that

$$\begin{aligned}\|\widetilde{\delta}_\Gamma^{-1/2} z\|_{L^2(\Omega)} = a(\widetilde{\delta}_\Gamma^{-1/2} z, \widetilde{\delta}_\Gamma^{-1/2} z) = a(z, \widetilde{\delta}_\Gamma^{-1} z) = a(z,\psi) = a(z, \psi - I\psi) \\ \leq C\|z\|_{H^1(\Omega)} \|\psi - I\psi\|_{H^1(\Omega)}.\end{aligned}$$

Using (57) in Lemma 10.12, we obtain

$$\|\psi\|_{B^{3/2}_{2\infty}(\Omega)} \leq C_\epsilon |\ln h|^{1/2} \|\widetilde{\delta}_\Gamma^{-1/2} z\|_{L^2(\Omega)},$$

and thus it follows with the approximation properties of V_h^k that

$$\inf_{I\psi\in V_h^k} \|\psi - I\psi\|_{H^1(\Omega)} \leq h^{1/2} \|\psi\|_{B^{3/2}_{2,\infty}(\Omega)} \leq C_\epsilon h^{1/2} |\ln h|^{1/2} \|\widetilde{\delta}_\Gamma^{-1/2} z\|_{L^2(\Omega)}.$$

□

Corollary 10.14. *Let Assumption 6 be valid and the solution u be in $H^s(\Omega)$, $s \geq 1$. Then the FEM error $e = u - u_h$ satisfies for $\varepsilon \in (0, s_0 - 1/2]$*

$$\|\delta_\Gamma^{-1/2+\varepsilon} e\|_{L^2(\Omega)} \leq C_\varepsilon h^{\mu - 1/2 + \varepsilon} \|u\|_{H^\mu(\Omega)}, \qquad \mu := \min\{s, k+1\}.$$

If we can ensure that the solution has some additional regularity, L^2-convergence of the FEM can also be achieved on non-convex geometries, as will be seen in the following Theorem 9, which shows the optimal rate.

Theorem 9. *Let Assumption 6 be valid. Let the exact solution u satisfy the extra regularity $u \in H^{k+2-s_0}(\Omega)$. Then the FEM error $u - u_h$ satisfies*

$$\|u - u_h\|_{L^2(\Omega)} \lesssim h^{k+1} \|u\|_{H^{k+2-s_0}(\Omega)}. \tag{62}$$

More generally, if $u \in H^s(\Omega)$, $s \in [1, k+2-s_0]$, *then*

$$\|u - u_h\|_{L^2(\Omega)} \lesssim h^{s-1+s_0} \|u\|_{H^s(\Omega)}, \quad 1 \le s \le k+2-s_0. \tag{63}$$

Proof. of (62): We proceed along a standard duality argument. To begin with, we note that the case $s_0 = 1$ is classical so that we may assume $s_0 < 1$ for the remainder of the proof. Set $\varepsilon := s_0 - 1/2 \in (0, 1/2)$ by our assumption $1/2 < s_0 < 1$. Let $w = Te$ and let $w_h \in V_h^k$ be its Galerkin approximation. Quasi-optimality and the use of (50) give us the following energy error estimate:

$$\begin{aligned} \|w - w_h\|_{H^1(\Omega)} &\lesssim \inf_{v \in V_h^k} \|w - v\|_{H^1(\Omega)} \lesssim h^{1/2+\varepsilon} \|w\|_{H^{3/2+\varepsilon}(\Omega)} \\ &\lesssim h^{1/2+\varepsilon} \|e\|_{(H^{1/2-\varepsilon}(\Omega))'} \lesssim h^{1/2+\varepsilon} \|e\|_{L^2(\Omega)}. \end{aligned} \tag{64}$$

The Galerkin orthogonalities satisfied by e and $w - w_h$ and a weighted Cauchy-Schwarz inequality yield for the Scott-Zhang interpolant $I_h^k u$

$$\|e\|_{L^2(\Omega)}^2 = a(e, w) = a(e, w - w_h) = a(u - I_h^k u, w - w_h) \tag{65}$$

$$\le C \|\widetilde{\delta}_\Gamma^{-1/2+\varepsilon} \nabla(u - Iu)\|_{L^2(\Omega)} \|\widetilde{\delta}_\Gamma^{1/2-\varepsilon} \nabla(w - w_h)\|_{L^2(\Omega)}. \tag{66}$$

We get by a covering argument and (50) of Lemma 10.1

$$\begin{aligned} \|\widetilde{\delta}_\Gamma^{-1/2+\varepsilon} \nabla(u - I_h^k u)\|_{L^2(\Omega)} &\lesssim h^k \|\widetilde{\delta}_\Gamma^{-1/2+\varepsilon} \nabla^{k+1} u\|_{L^2(\Omega)} \\ &\lesssim h^k \|\nabla^{k+1} u\|_{H^{1/2-\varepsilon}(\Omega)}. \end{aligned} \tag{67}$$

It should also be noted at this point that in (67), the weight $\widetilde{\delta}_\Gamma^{-1/2+\varepsilon}$ can be considered as constant in each element K. For the contribution $\|\widetilde{\delta}_\Gamma^{1/2-\varepsilon} \nabla(w - w_h)\|_{L^2(\Omega)}$ in (66), we have to analyze the Galerkin error $w - w_h$ in more detail, which will be done with the techniques from the local error analysis of the FEM. We split Ω into $S_{ch} \cup (\Omega \setminus S_{ch})$ where $c > 0$ will be selected sufficiently large below. For fixed $c > 0$, the L^2-norm on S_{ch} can easily be bounded with (64) by

$$\|\widetilde{\delta}_\Gamma^{1/2-\varepsilon} \nabla(w - w_h)\|_{L^2(S_{ch})} \lesssim h^{1/2-\varepsilon} \|\nabla(w - w_h)\|_{L^2(\Omega)} \lesssim h \|e\|_{L^2(\Omega)}. \tag{68}$$

The term $\|\widetilde{\delta}_\Gamma^{1/2-\varepsilon} \nabla(w - w_h)\|_{L^2(\Omega \setminus S_{ch})}$ requires more care. Obviously, $\widetilde{\delta}_\Gamma^{1/2-\varepsilon} \lesssim \delta_\Gamma^{1/2-\varepsilon}$ on $\Omega \setminus S_{ch}$. We have to employ the tools from the local error analysis in FEM. The Galerkin orthogonality satisfied by $w - w_h$ allows us to use techniques as described in [172, Sec. 5.3], which yields the following estimate for arbitrary balls $B_r \subset B_{r'}$

with the same center (implicitly, $r' > r + O(h)$ is assumed in (69))

$$\|\nabla(w - w_h)\|_{L^2(B_r)} \lesssim \|\nabla(w - I_h^k w)\|_{L^2(B_{r'})} + \frac{1}{r' - r}\|w - w_h\|_{L^2(B_{r'})}. \tag{69}$$

By a covering argument (which requires $r' - r \sim c\delta_\Gamma(x)$, where x is the center of the ball B_r, and c is sufficiently small) these local estimates can be combined into a global estimate of the following form, where for sufficiently small $c_1 > 0$ (c_1 depends only on Ω and the shape regularity of the triangulation but is independent of h):

$$\begin{aligned} &\|\delta_\Gamma^{1/2-\varepsilon}\nabla(w - w_h)\|_{L^2(\Omega\setminus S_{ch})} \lesssim \\ &\qquad \|\delta_\Gamma^{1/2-\varepsilon}\nabla(w - I_h^k w)\|_{L^2(\Omega\setminus S_{cc_1h})} + \|\delta_\Gamma^{-1/2-\varepsilon}(w - w_h)\|_{L^2(\Omega\setminus S_{cc_1h})}. \end{aligned} \tag{70}$$

This estimate implicitly assumed $c_1 ch > 2h$, i.e., at least two layers of elements separate Γ from $\Omega \setminus S_{c_1ch}$. We now fix $c > 2/c_1$. The first term in (70) can easily be bounded by standard approximation properties of I_h^k, Lemma 10.3, and Assumption 6:

$$\begin{aligned} \|\delta_\Gamma^{1/2-\varepsilon}\nabla(w - I_h^k w)\|_{L^2(\Omega\setminus S_{cc_1h})} &\lesssim h\|\delta_\Gamma^{1/2-\varepsilon}\nabla^2 w\|_{L^2(\Omega)} \\ &\lesssim h\left[\|\delta_\Gamma^{1/2-\varepsilon}e\|_{L^2(\Omega)} + \|w\|_{H^{3/2+\varepsilon}(\Omega)}\right] \lesssim h\|e\|_{L^2(\Omega)}. \end{aligned}$$

In the last step, we have to deal with the term $\|\delta_\Gamma^{-1/2-\varepsilon}(w - w_h)\|_{L^2(\Omega\setminus S_{cc_1h})}$ of (70). Lemma 10.13 and (64) imply

$$\begin{aligned} \|\delta_\Gamma^{-1/2-\varepsilon}(w - w_h)\|_{L^2(\Omega\setminus S_{cc_1h})} &\lesssim h^{-2\varepsilon}\|\delta_\Gamma^{-1/2+\varepsilon}(w - w_h)\|_{L^2(\Omega)} \\ &\lesssim h^{-2\varepsilon}h^{1/2+\varepsilon}\|w - w_h\|_{H^1(\Omega)} \lesssim h\|e\|_{L^2(\Omega)}. \end{aligned} \tag{71}$$

Here we have used the quasi-optimality of the Galerkin approximation with respect to the H^1-norm.

Proof of (63): The above arguments show that the regularity of u enters in the bound (67). For $u \in H^1(\Omega)$, the stability properties of the Scott-Zhang operator I_h^k show

$$\|\widetilde{\delta}_\Gamma^{-1/2+\varepsilon}\nabla(u - I_h^k u)\|_{L^2(\Omega)} \lesssim h^{-1/2+\varepsilon}\|u\|_{H^1(\Omega)}. \tag{72}$$

Hence, a standard interpolation argument that combines (67) and (72) yields $\|\widetilde{\delta}_\Gamma^{-1/2+\varepsilon}\nabla(u - I_h^k u)\|_{L^2(\Omega)} \lesssim h^{-1/2+\varepsilon+s-1}\|u\|_{H^s(\Omega)}$ for $s \in [1, k + 2 - s_0]$. Combining this estimate with the above control of $\|\widetilde{\delta}_\Gamma^{1/2-\varepsilon}\nabla(w - w_h)\|_{L^2(\Omega)}$ yields the desired bound in the range $s \in [1, k + 2 - s_0]$. □

The convergence analysis of Theorem 9 did not make *explicit* use of the fact that a piecewise smooth geometry is considered; the essential ingredient was Assumption 6 (which, of course, is related to the geometry of the problem). This is reflected in our use of $\widetilde{\delta}_\Gamma$, which measures the distance from the boundary Γ. One interpretation of this procedure is that one assumes of the dual solution w (and, in fact, also of the solution of the "bidual" problem employed to estimate $\|\widetilde{\delta}_\Gamma^{-1/2+\varepsilon}(w-w_h)\|_{L^2(\Omega)}$ in Theorem 9) that it may lose H^2-regularity *anywhere* near Γ. However, for piecewise smooth geometries in conjunction with certain homogeneous boundary conditions (here: homogeneous Dirichlet conditions), this loss of H^2-regularity is restricted to a much smaller set, namely, a subset of vertices in 2D and a subset of the skeleton (i.e., the union of vertices and edges) in 3D. This set is given by M_s in Definition 10.9. For this set M_s, we introduce the distance function

$$\delta_{M_s} := \operatorname{dist}(\cdot, M_s), \qquad \widetilde{\delta}_{M_s} := h + \delta_{M_s}.$$

Theorem 10. *Let Ω be a polygon (in 2D) or a polyhedron (in 3D). Let M_s be the set of vertices (in 2D) or edges and vertices (in 3D) associated with a loss of H^2-regularity for (1) as given in Definition 10.9. Let Assumption 6 be valid. Let $Iu \in V_h^k$ be arbitrary. Then we have*

$$\|u-u_h\|_{L^2(\Omega)} \le h\|\widetilde{\delta}_{M_s}^{s_0-1}\nabla(u-Iu)\|_{L^2(\Omega)}.$$

Proof. We may assume $s_0 < 1$ since the case $s_0 = 1$ corresponds to the standard duality argument with full elliptic regularity and set $\varepsilon := s_0 - 1/2 \in (0, 1/2)$. The key observation is that, starting from the duality argument (65), one can replace the weight function $\widetilde{\delta}_\Gamma^{-1/2+\varepsilon}$ in (66) with *any* positive weight function. Taking as the weight function $\widetilde{\delta}_{M_s}^{-1/2+\varepsilon}$, we get

$$\|e\|_{L^2(\Omega)}^2 \le \|\widetilde{\delta}_{M_s}^{-1/2+\varepsilon}\nabla(u-Iu)\|_{L^2(\Omega)}\|\widetilde{\delta}_{M_s}^{1/2-\varepsilon}\nabla(w-w_h)\|_{L^2(\Omega)}. \tag{73}$$

The estimate of $w - w_h$ in the weighted norm is done similarly as in the proof of Theorem 9, taking into account the improved knowledge of the regularity of w. With $S_{M_s,ch} := \{x \in \Omega \,|\, \delta_{M_s}(x) < ch\}$ we have the trivial bound

$$\begin{aligned}&\|\widetilde{\delta}_{M_s}^{1/2-\varepsilon}\nabla(w-w_h)\|_{L^2(\Omega)} \\ &\quad\lesssim \|\widetilde{\delta}_{M_s}^{1/2-\varepsilon}\nabla(w-w_h)\|_{L^2(S_{M_s,ch})} + \|\widetilde{\delta}_{M_s}^{1/2-\varepsilon}\nabla(w-w_h)\|_{L^2(\Omega\setminus S_{M_s,ch})},\end{aligned} \tag{74}$$

where the parameter c will be selected sufficiently large below. The first term in

(74) is estimated in exactly the same way as in (68) and produces

$$\begin{aligned}\|\widetilde{\delta}_{M_s}^{1/2-\varepsilon}\nabla(w-w_h)\|_{L^2(S_{M_s,ch})} &\lesssim h^{1/2-\varepsilon}\|\nabla(w-w_h)\|_{L^2(\Omega)}\\ &= h^{1/2-\varepsilon}\|\nabla(w-w_h)\|_{H^1(\Omega)}\\ &\lesssim h^{1/2-\varepsilon}h^{1/2+\varepsilon}\|e\|_{L^2(\Omega)}\\ &\leq Ch\|e\|_{L^2(\Omega)}.\end{aligned}$$

The second term in (73) again requires the techniques from the local error analysis of the finite elements, this time with the appropriate modifications to account for the boundary conditions. Inspection of the arguments in [172, Sec. 5.3] shows that the key estimate (69) extends up to the boundary in the following sense:

$$\|\nabla(w-w_h)\|_{L^2(B_r\cap\Omega)} \lesssim \|\nabla(w-I_h^k w)\|_{L^2(B_{r'}\cap\Omega)} + \frac{1}{r'-r}\|w-w_h\|_{L^2(B_{r'}\cap\Omega)}.$$

Besides the implicit assumption $r' > r + O(h)$, the balls B_r and $B_{r'}$ are assumed to have the same center x and satisfy one of the following conditions:

1. $B_{r'} = B_{r'}(x) \subset \Omega$;
2. $x \in \partial\Omega$ and $B_{r'}(x) \cap \Omega$ is a half-disk;
3. x is a vertex of Ω;
4. (only for $d = 3$) x lies on an edge e and $B_{r'}(x) \cap \Omega$ is a dihedral angle (i.e., the intersection of $\partial(B_{r'}(x) \cap \Omega)$ with $\partial\Omega$ is contained in the two faces that share the edge e.

The reason for the restriction of the location of the centers of the balls is that the procedure presented in [172, Sec. 5.3] relies on Poincaré inequalities so that the number of possible shapes for the intersections $B_{r'} \cap \Omega$ should be finite. A covering argument (see Theorem 7 for the 2D case and Theorem 8 for the 3D situation) then leads to the following bound with an appropriate $c_1 > 0$ (here, $c > 0$ is implicitly assumed sufficiently large):

$$\begin{aligned}&\|\widetilde{\delta}_{M_s}^{1/2-\varepsilon}\nabla(w-w_h)\|_{L^2(\Omega\setminus S_{M_s,ch})} \lesssim \\ &\quad \|\widetilde{\delta}_{M_s}^{1/2-\varepsilon}\nabla(w-I_h^k w)\|_{L^2(\Omega\setminus S_{M_s,cc_1h})} + \|\widetilde{\delta}_{M_s}^{-1/2-\varepsilon}(w-w_h)\|_{L^2(\Omega\setminus S_{M_s,cc_1h})}.\end{aligned} \tag{75}$$

The first term in (75) can be estimated with the improved regularity assertion of Lemma 10.10 to produce (with appropriate $c_2 > 0$ and the implicit assumption on

c that $cc_1c_2 > 2$)

$$\begin{aligned}\|\widetilde{\delta}_{M_s}^{1/2-\varepsilon}\nabla(w - I_h^k w)\|_{L^2(\Omega\setminus S_{M_s,cc_1h})} &\lesssim h\|\widetilde{\delta}_{M_s}^{1/2-\varepsilon}\nabla^2 w\|_{L^2(\Omega\setminus S_{M_s,cc_1c_2h})}\\ &\lesssim h\left[\|\widetilde{\delta}_{M_s}^{1/2-\varepsilon}e\|_{L^2(\Omega)} + \|w\|_{H^{3/2+\varepsilon}(\Omega)}\right] \lesssim h\|e\|_{L^2(\Omega)}.\end{aligned}$$

For the second term in (75) we note that $-1/2-\varepsilon < 0$ so that $\widetilde{\delta}_{M_s}^{-1/2-\varepsilon} \le \widetilde{\delta}_{\Gamma}^{-1/2-\varepsilon}$. This leads to

$$\begin{aligned}\|\widetilde{\delta}_{M_s}^{-1/2-\varepsilon}(w - w_h)\|_{L^2(\Omega\setminus S_{M_s,cc_1h})} &\lesssim \|\widetilde{\delta}_{M_s}^{-1/2-\varepsilon}(w - w_h)\|_{L^2(\Omega)}\\ &\lesssim \|\widetilde{\delta}_{\Gamma}^{-1/2-\varepsilon}(w - w_h)\|_{L^2(\Omega)} \lesssim h^{-2\varepsilon}\|\widetilde{\delta}_{\Gamma}^{-1/2+\varepsilon}(w - w_h)\|_{L^2(\Omega)};\end{aligned}$$

the term $h^{-2\varepsilon}\|\widetilde{\delta}_{\Gamma}^{-1/2+\varepsilon}(w - w_h)\|_{L^2(\Omega)}$ has already been estimated in (71) in the desired form. □

The regularity requirements on the solution u can still be slightly weakened. As written, the exponent $s_0 - 1$ is related to the *global* regularity of the dual solution w. However, the developments above show that a *local* lack of full regularity of the dual solution w (and the bidual solution) needs to be offset by additional local regularity of the solution. To be more specific, we restrict our attention now to the 2D Laplacian, i.e., $\mathbf{A} = \mathrm{Id}$. In this case, the situation can be expressed as follows with the aid of the singular exponents $\alpha_j := \pi/\omega_j$, where $\omega_j \in (\pi, 2\pi)$ is the interior angle at the reentrant vertices A_j, $j = 1, \dots, J$.

Corollary 10.15. *Let $\Omega \subset \mathbb{R}^2$ be a polygon and let $\mathbf{A} = \mathrm{Id}$. Let $\delta_j := \mathrm{dist}(\cdot, A_j)$, $j = 1, \dots, J$, for the J reentrant corners. Set $\widetilde{\delta}_j := h + \delta_j$. Let ω_j be the interior angle at A_j and $\alpha_j = \pi/\omega_j$. Fix $\beta_j > 1 - \alpha_j$ arbitrary. Then for any $Iu \in V_h^k$*

$$\|u - u_h\|_{L^2(\Omega)} \lesssim h\sum_{j=1}^{J}\|\widetilde{\delta}_j^{-\beta_j}\nabla(u - Iu)\|_{L^2(\Omega)}.$$

Proof. The proof follows by an inspection of how the regularity of the solution $w = Te$ of the dual problem enters the proof of Theorem 10. By, e.g., [67] the solution $w = Te$ is in a weighted H^2-space with

$$\|\prod_{j=1}^{J}\delta_j^{\beta_j}\nabla^2 w\|_{L^2(\Omega)} \lesssim \|e\|_{L^2(\Omega)}, \tag{76}$$

and Assumption 6 holds with any $s_0 < \min_j \alpha_j$. The regularity assertion (76) suggests to choose $\prod_{i=1}^{J}\widetilde{\delta}_i^{\beta_i}$ as the weight in the proof of Theorem 9. Inspection of

the procedure in the proof of Theorem 10 then leads to the result. □

We extract from this result another corollary that we will prove useful in the numerical results. We formulate it in terms of (standard, unweighted) Sobolev regularity in order to emphasize the difference in regularity requirements of the solution near the reentrant corners and away from them:

Corollary 10.16. *Assume the hypotheses of Corollary 10.15. Let $s > 1$ and $s_i > 1$, $i = 1, \dots, J$. Let $\mathcal{U} := \Omega \setminus \cup \overline{\mathcal{U}}_i$, for some neighborhoods $\mathcal{U}_i$ of the reentrant vertices A_i. Let $u \in H^{s_i}(\mathcal{U}_i)$, $i = 1, \dots, J$ and $u \in H^s(\mathcal{U})$. Then for arbitrary $\varepsilon > 0$*

$$\|u - u_h\|_{L^2(\Omega)} \leq C_\varepsilon h^\tau, \quad \tau := \min(1 + k, s, \min_{j=1,\dots,J}(-1 + \alpha_j + s_j - \varepsilon)).$$

Proof. The approximant Iu in Corollary 10.15 may be taken as any standard nodal interpolant or the Scott-Zhang projection. Then standard estimates and Corollary 10.15 produce with the choice $\beta_j := 1 - \alpha_j + \varepsilon$ for arbitrary small but fixed $\varepsilon > 0$:

$$\begin{aligned} \|u - u_h\|_{L^2(\Omega)} &\lesssim h \min_{j=1,\dots,J}\{h^{\min\{k,s-1\}}, h^{-\beta_j + s_j - 1}\} \\ &\lesssim \min_{j=1,\dots,J}\{h^{\min\{k+1,s\}}, h^{\alpha_j + s_j - 1 - \varepsilon}\}. \end{aligned}$$

□

10.2. Numerical L^2-error investigation

In order to numerically demonstrate the derived theoretical results, we again consider the simple model equation $-\Delta u = f$ in $\Omega \subset \mathbb{R}^d$, $d \in \{2, 3\}$ with inhomogeneous Dirichlet boundary conditions, first in a two-dimensional setting. These are realized numerically by nodal interpolation of the prescribed exact solution u, and the data f is also computed from u. In the case of a non-smooth solution, we use a suitable quadrature formula on finer meshes to guarantee that the L^2-error is accurately evaluated. We use a sequence of uniformly refined triangular meshes, where each element is split into four triangles. We consider two typical domains for reentrant corners and start with the L-shaped domain $(-1, 1)^2 \setminus [0, 1] \times [-1, 0]$ and then consider a slit domain $(-1, 1)^2 \setminus ((0, 1) \times \{0\})$ using lowest order discretization. In both cases, the prescribed solution is given in polar coordinates by $u(r, \phi) = r^\alpha \sin(a\phi)$ where α, a are given parameters. For non-integer α, we have $u \in B^{1+\alpha}_{2,\infty}(\Omega)$ by [10, Thm. 2.1]. Moreover, we test the influence of the position (x_0, y_0) of the weak singularity at $r = 0$ by defining $r^2 := (x - x_0)^2 + (y - y_0)^2$. We

	$(x_0, y_0) = (0, 0)$ $a = \pi/2$		$(x_0, y_0) = (0.5, 0)$ $a = \pi$		$(x_0, y_0) = (0, 1)$ $a = \pi$	
DoFs	$\|u - u_h\|_{L^2(\Omega)}$	rate	$\|u - u_h\|_{L^2(\Omega)}$	rate	$\|u - u_h\|_{L^2(\Omega)}$	rate
81	6.1585e-03	-	6.8141e-03	-	6.2506e-03	-
289	2.6986e-03	1.19	2.5648e-03	1.41	2.1211e-03	1.56
1.089	1.1123e-03	1.28	8.8428e-04	1.54	6.7413e-04	1.65
4.225	4.4037e-04	1.34	2.9202e-04	1.60	2.0903e-04	1.69
16.641	1.7107e-04	1.36	9.4164e-05	1.63	6.4027e-05	1.71
66.049	6.5689e-05	1.38	2.9909e-05	1.65	1.9471e-05	1.72
263.169	2.5030e-05	1.39	9.4012e-06	1.67	5.8930e-06	1.72
1.050.625	9.4877e-06	1.40	2.9328e-06	1.68	1.7774e-06	1.73
4.198.401	3.5834e-06	1.40	9.0968e-07	1.69	5.3475e-07	1.73

Table 10.1: L–domain, $k = 1$: Influence of the position of singularity for $\alpha = 0.75$.

	$\alpha = 10/9$		$\alpha = 4/3$		$\alpha = 3/2$	
DoFs	$\|u - u_h\|_{L^2(\Omega)}$	rate	$\|u - u_h\|_{L^2(\Omega)}$	rate	$\|u - u_h\|_{L^2(\Omega)}$	rate
81	6.5660e-03	-	8.6776e-03	-	8.9932e-03	-
289	2.3309e-03	1.49	2.8523e-03	1.61	2.8151e-03	1.68
1.089	7.3413e-04	1.67	8.2870e-04	1.78	7.8034e-04	1.85
4.225	2.2257e-04	1.72	2.3073e-04	1.84	2.0751e-04	1.91
16.641	6.5650e-05	1.76	6.2539e-05	1.88	5.3910e-05	1.94
66.049	1.9056e-05	1.78	1.6688e-05	1.91	1.3835e-05	1.96
263.169	5.4810e-06	1.80	4.4099e-06	1.92	3.5256e-06	1.97
1.050.625	1.5690e-06	1.80	1.1580e-06	1.93	8.9467e-07	1.98
4.198.401	4.4822e-07	1.81	3.0279e-07	1.94	2.2641e-07	1.98

Table 10.2: L-domain, $k = 1$: Influence of exponent α for $a = 2/3\pi$ and $(x_0, y_0) = (0, 0)$.

note that irrespective of the location (x_0, y_0) of the singularity on the boundary Γ, we have $u \in B^{1+\alpha}_{2,\infty}(\Omega) \subset H^{1+\alpha-\varepsilon}(\Omega)$ for any $\varepsilon > 0$.

For the L-shaped domain, the shift parameter s_0 can be taken to be any $s_0 < 2/3$. From the theoretical results in this section, we therefore expect the error decay to have a rate of at least $\min(2, 1 + \alpha - 1/3)$ uniformly in the position (x_0, y_0) of the singularity. Table 10.1 shows the numerical results for $\alpha = 0.75$ and $a = \pi/2$, for which $\min(2, 1+\alpha-1/3) = 1.417$. As it can be seen for $(x_0, y_0) = (0, 0)$, we observe a good agreement with Theorem 9. However for the locations $(x_0, y_0) = (0.5, 0)$ and $(x_0, y_0) = (0, 1)$, the rates are substantially better. This can be explained by the more refined analysis of Corollary 10.16, where we expect an improved convergence rate of 1.75 for these cases. Table 10.2 shows the results for $(x_0, y_0) = (0, 0)$ and $\alpha \in \{10/9, 4/3, 3/2\}$. From Theorem 9, we expect convergence rates of 1.78, 2, and 2, respectively. The observed numerical rates of 1.81, 1.94, and 1.98 are quite close.

	$(x_0, y_0) = (0, 0)$ $a = \pi/2$		$(x_0, y_0) = (0.5, 0)$ $a = \pi$		$(x_0, y_0) = (0, 1)$ $a = \pi$	
DoFs	$\|u - u_h\|_{L^2(\Omega)}$	rate	$\|u - u_h\|_{L^2(\Omega)}$	rate	$\|u - u_h\|_{L^2(\Omega)}$	rate
81	4.6216e-03	-	1.8387e-04	-	1.6841e-04	-
289	1.6860e-03	1.45	6.0370e-05	1.61	5.0364e-05	1.74
1.089	5.4867e-04	1.62	1.8034e-05	1.74	1.3883e-05	1.86
4.225	1.7284e-04	1.67	5.1378e-06	1.81	3.6942e-06	1.91
16.641	5.2963e-05	1.71	1.4253e-06	1.85	9.6399e-07	1.94
66.049	1.5970e-05	1.73	3.8870e-07	1.87	2.4842e-07	1.96
263.169	4.7758e-06	1.74	1.0474e-07	1.89	6.3437e-08	1.97
1.050.625	1.4238e-06	1.75	2.7971e-08	1.90	1.6086e-08	1.98
4.198.401	4.2471e-07	1.75	7.4181e-09	1.91	4.0561e-09	1.99

Table 10.3: L–domain, $k = 1$: Influence of the position of singularity for $\alpha = 1.01$.

	$(x_0, y_0) = (0, 0)$ $a = \pi/2$		$(x_0, y_0) = (0.5, 0)$ $a = \pi$		$(x_0, y_0) = (0, 1)$ $a = \pi$	
DoFs	$\|u - u_h\|_{L^2(\Omega)}$	rate	$\|u - u_h\|_{L^2(\Omega)}$	rate	$\|u - u_h\|_{L^2(\Omega)}$	rate
81	8.6776e-03	-	3.8962e-03	-	3.6446e-03	-
289	2.8523e-03	1.61	1.1374e-03	1.78	1.0008e-03	1.86
1.089	8.2870e-04	1.78	3.0272e-04	1.91	2.5331e-04	1.98
4.225	2.3073e-04	1.84	7.7239e-05	1.97	6.2153e-05	2.03
16.641	6.2539e-05	1.88	1.9331e-05	2.00	1.5073e-05	2.04
66.049	1.6688e-05	1.91	4.7956e-06	2.01	3.6440e-06	2.05
263.169	4.4099e-06	1.92	1.1852e-06	2.02	8.8167e-07	2.05
1.050.625	1.1580e-06	1.93	2.9260e-07	2.02	2.1389e-07	2.04
4.198.401	3.0279e-07	1.94	7.2263e-08	2.02	5.2069e-08	2.04

Table 10.4: L–domain, $k = 1$: Influence of the position of singularity for $\alpha = 4/3$.

The situation for the next simulation is structurally similar to the one before. From Corollary 10.16, we expect the following convergence rates:

$$x_0 = (0,0) \implies \tau = \min\{2, 1+\alpha, -1+2/3+(1+\alpha)\} = \min\{2, 2/3+\alpha\},$$
$$x_0 \neq (0,0) \implies \tau = \min\{2, 1+\alpha, -1+2/3+\infty\} = \min\{2, 1+\alpha\}.$$

Also in this case the numerical rates depicted in Tables 10.3–10.4, where we show the results for $\alpha \in \{2/3, 1.01, 4/3\}$, are very close to the rates expected by our theory. The situation is similar for the slit domain, where the regularity of the dual problem is even further reduced. It corresponds to a limiting case of our theory, which, strictly speaking, we did not cover, since the parameter s_0 of Assumption 6 may be taken to be any $s_0 < 1/2$. Nevertheless, one expects from Theorem 9 a convergence rate close to $\min\{2, 1+\alpha-1/2\}$. For $\alpha = 0.75$ this is 1.25, which is visible in Table 10.5 for the case $(x_0, y_0) = (0, 0)$. Again, the better convergence behavior for $(x_0, y_0) = (0.5, 0)$ and $(x_0, y_0) = (0, 1)$ can be explained by the theory

	$(x_0, y_0) = (0, 0)$ $a = \pi/2$		$(x_0, y_0) = (0.5, 0)$ $a = \pi$		$(x_0, y_0) = (0, 1)$ $a = \pi$	
DoFs	$\|u - u_h\|_{L^2(\Omega)}$	rate	$\|u - u_h\|_{L^2(\Omega)}$	rate	$\|u - u_h\|_{L^2(\Omega)}$	rate
97	6.1391e-03	-	1.1088e-02	-	1.0692e-02	-
348	2.8187e-03	1.12	4.1329e-03	1.42	3.8553e-03	1.47
1.315	1.2351e-03	1.19	1.4164e-03	1.54	1.3388e-03	1.53
5.109	5.3338e-04	1.21	4.7830e-04	1.57	4.4562e-04	1.59
20.137	2.2846e-04	1.22	1.4725e-04	1.70	1.4420e-04	1.63
79.953	9.7267e-05	1.23	4.6683e-05	1.66	4.5843e-05	1.65
318.625	4.1233e-05	1.24	1.4761e-05	1.66	1.4401e-05	1.67
1.272.129	1.7428e-05	1.24	4.3773e-06	1.75	4.4861e-06	1.68
5.083.777	7.3524e-06	1.25	1.3285e-06	1.72	1.3889e-06	1.69

Table 10.5: Slit domain, $k = 1$: Influence of the position of singularity for $\alpha = 0.75$.

	$\alpha = 10/9$		$\alpha = 4/3$		$\alpha = 3/2$	
DoFs	$\|u - u_h\|_{L^2(\Omega)}$	rate	$\|u - u_h\|_{L^2(\Omega)}$	rate	$\|u - u_h\|_{L^2(\Omega)}$	rate
97	5.7534e-03	-	7.3549e-03	-	7.5901e-03	-
348	1.9412e-03	1.57	2.2414e-03	1.71	2.1664e-03	1.81
1.315	6.2583e-04	1.63	6.4849e-04	1.79	5.8638e-04	1.89
5.109	1.9689e-04	1.67	1.8251e-04	1.83	1.5450e-04	1.92
20.137	6.1446e-05	1.68	5.0718e-05	1.85	4.0197e-05	1.94
79.953	1.9191e-05	1.68	1.4021e-05	1.85	1.0396e-05	1.95
318.625	6.0229e-06	1.67	3.8699e-06	1.86	2.6803e-06	1.96
1.272.129	1.9023e-06	1.66	1.0682e-06	1.86	6.8978e-07	1.96
5.083.777	6.0474e-07	1.65	2.9514e-07	1.86	1.7730e-07	1.96

Table 10.6: Slit domain, $k = 1$: Influence of exponent α for $a = 1/2\pi$ and $(x_0, y_0) = (0, 0)$.

of Corollary 10.16, which predicts $1 + \alpha = 1.75$. Table 10.6 shows the results for $(x_0, y_0) = (0, 0)$ and $\alpha \in \{10/9, 4/3, 3/2\}$. From Theorem 9, we expect convergence rates of 1.61, 1.83 and 2, respectively. The observed numerical rates of 1.65, 1.86, and 1.96 are reasonably close to these predictions.

Furthermore for the following results we expect the convergence behavior detailed in Corollary 10.16 to be a good description of the actual convergence behavior. We assume that the global regularity of the solution u is described by $s = 1 + \alpha$ (actually, it is $1 + \alpha - \varepsilon$ for all $\varepsilon > 0$). Corollary 10.16 then lets us expect for the two cases $x_0 = (0, 0)$ and $x_0 \neq (0, 0)$ the following convergence rates:

$$x_0 = (0,0) \implies \tau = \min\{2, 1+\alpha, -1+1/2+(1+\alpha)\} = \min\{2, 1/2+\alpha\},$$
$$x_0 \neq (0,0) \implies \tau = \min\{2, 1+\alpha, -1+1/2+\infty\} = \min\{2, 1+\alpha\}.$$

In the following Tables 10.7–10.9, we vary the parameter α. In each table separa-

	$(x_0, y_0) = (0,0)$ $a = \pi/2$		$(x_0, y_0) = (0.5,0)$ $a = \pi$		$(x_0, y_0) = (0,1)$ $a = \pi$	
DoFs	$\|u - u_h\|_{L^2(\Omega)}$	rate	$\|u - u_h\|_{L^2(\Omega)}$	rate	$\|u - u_h\|_{L^2(\Omega)}$	rate
97	2.9124e-02	-	3.8405e-02	-	3.0468e-02	-
348	1.5745e-02	0.89	1.0451e-02	1.88	1.2883e-02	1.24
1.315	8.1422e-03	0.95	4.8926e-03	1.10	5.2831e-03	1.29
5.109	4.1322e-03	0.98	2.1508e-03	1.19	2.0814e-03	1.34
20.137	2.0799e-03	0.99	8.1046e-04	1.41	7.9896e-04	1.38
79.953	1.0430e-03	1.00	3.0969e-04	1.39	3.0187e-04	1.40
318.625	5.2221e-04	1.00	1.1780e-04	1.39	1.1288e-04	1.42
1.272.129	2.6125e-04	1.00	4.1750e-05	1.50	4.1903e-05	1.43
5.083.777	1.3066e-04	1.00	1.4985e-05	1.48	1.5472e-05	1.44

Table 10.7: Slit domain, $k = 1$: Influence of the position of singularity for $\alpha = 0.5$.

	$(x_0, y_0) = (0,0)$ $a = \pi/2$		$(x_0, y_0) = (0.5,0)$ $a = \pi$		$(x_0, y_0) = (0,1)$ $a = \pi$	
DoFs	$\|u - u_h\|_{L^2(\Omega)}$	rate	$\|u - u_h\|_{L^2(\Omega)}$	rate	$\|u - u_h\|_{L^2(\Omega)}$	rate
97	4.1949e-03	-	3.0111e-04	-	2.9784e-04	-
348	1.4605e-03	1.52	9.9257e-05	1.60	9.3618e-05	1.67
1.315	4.8756e-04	1.58	2.9679e-05	1.74	2.8033e-05	1.74
5.109	1.5909e-04	1.62	8.6201e-06	1.78	8.0205e-06	1.81
20.137	5.1667e-05	1.62	2.2994e-06	1.91	2.2266e-06	1.85
79.953	1.6874e-05	1.61	6.2533e-07	1.88	6.0606e-07	1.88
318.625	5.5687e-06	1.60	1.6832e-07	1.89	1.6270e-07	1.90
1.272.129	1.8596e-06	1.58	4.3035e-08	1.97	4.3240e-08	1.91
5.083.777	6.2798e-07	1.57	1.1235e-08	1.94	1.1403e-08	1.92

Table 10.8: Slit domain, $k = 1$: Influence of the position of singularity for $\alpha = 1.01$.

tely we vary the location. The locations under investigation are $(x_0, y_0) = (0,0)$, $(x_0, y_0) = (0.5,0)$ and $(x_0, y_0) = (0,1)$. We observe that the theoretical convergence rates are mostly achieved in our numerical simulations.

In the following we investigate the performance of quadratic finite elements for the L-shaped domain. We use the same type of solution as before and vary the parameter α for $(x_0, y_0) = (0,0)$, i.e., the reentrant corner. Here we expect from our theory a convergence rate of $\min(3, \alpha + 1 - 1/3)$. For $\alpha \in \{2.175, 2.275, 2.375\}$, the observed numerical rates, which are visible in Table 10.10, are very close to the theoretically predicted ones. Here, we expect the convergence rate

$$\tau = \min\{3, -1 + 2/3 + (1 + \alpha)\} = \min\{3, 2/3 + \alpha\}.$$

In the three-dimensional setting, we consider a Fichera corner $\Omega := (-1,1)^3 \setminus [0,1]^3$ and prescribe the smooth solution $u(x,y,z) := \sin((x+y)\pi)\cos(2\pi z)$. The inhomo-

	$(x_0, y_0) = (0, 0)$ $a = \pi/2$		$(x_0, y_0) = (0.5, 0)$ $a = \pi$		$(x_0, y_0) = (0, 1)$ $a = \pi$	
DoFs	$\|u - u_h\|_{L^2(\Omega)}$	rate	$\|u - u_h\|_{L^2(\Omega)}$	rate	$\|u - u_h\|_{L^2(\Omega)}$	rate
97	7.3549e-03	-	6.3401e-03	-	6.3849e-03	-
348	2.2414e-03	1.71	1.8792e-03	1.75	1.7790e-03	1.84
1.315	6.4849e-04	1.79	5.0365e-04	1.90	4.6905e-04	1.92
5.109	1.8251e-04	1.83	1.3007e-04	1.95	1.1878e-04	1.98
20.137	5.0718e-05	1.85	3.1798e-05	2.03	2.9443e-05	2.01
79.953	1.4021e-05	1.85	7.8665e-06	2.02	7.2227e-06	2.03
318.625	3.8699e-06	1.86	1.9356e-06	2.02	1.7642e-06	2.03
1.272.129	1.0682e-06	1.86	4.6924e-07	2.04	4.3055e-07	2.03
5.083.777	2.9514e-07	1.86	1.1524e-07	2.03	1.0519e-07	2.03

Table 10.9: Slit domain, $k = 1$: Influence of the position of singularity for $\alpha = 4/3$.

	$\alpha = 2/3$		$\alpha = 3/4$		$\alpha = 1.01$		$\alpha = 10/9$	
DoFs	$\|u - u_h\|_{L^2(\Omega)}$	rate	$\|u - u_h\|_{L^2(\Omega)}$	rate	$\|u - u_h\|_{L^2(\Omega)}$	rate	$\|u - u_h\|_{L^2(\Omega)}$	rate
289	3.1686e-03	-	1.6898e-03	-	4.8115e-04	-	5.9011e-04	-
1.089	1.2099e-03	1.39	6.0844e-04	1.47	1.4003e-04	1.78	1.5596e-04	1.92
4.225	4.6505e-04	1.38	2.1881e-04	1.48	3.7277e-05	1.91	3.8312e-05	2.03
16.641	1.8057e-04	1.36	8.0073e-05	1.45	9.9546e-06	1.90	9.3965e-06	2.03
66.049	7.0635e-05	1.35	2.9545e-05	1.44	2.6951e-06	1.89	2.3314e-06	2.01
263.169	2.7771e-05	1.35	1.0960e-05	1.43	7.4481e-07	1.86	5.8950e-07	1.98
1.050.625	1.0955e-05	1.34	4.0799e-06	1.43	2.1075e-07	1.82	1.5257e-07	1.95

	$\alpha = 4/3$		$\alpha = 3/2$		$\alpha = 2.175$		$\alpha = 2.275$	
DoFs	$\|u - u_h\|_{L^2(\Omega)}$	rate	$\|u - u_h\|_{L^2(\Omega)}$	rate	$\|u - u_h\|_{L^2(\Omega)}$	rate	$\|u - u_h\|_{L^2(\Omega)}$	rate
289	6.1433e-04	-	5.5363e-04	-	2.7565e-04	-	2.4570e-04	-
1.089	1.5136e-04	2.02	1.3540e-04	2.03	5.1121e-05	2.43	4.1696e-05	2.56
4.225	3.3604e-05	2.17	2.8521e-05	2.25	7.5320e-06	2.76	5.7319e-06	2.86
16.641	7.7002e-06	2.13	6.2123e-06	2.20	1.1051e-06	2.77	7.8407e-07	2.87
66.049	1.8014e-06	2.10	1.3642e-06	2.19	1.5938e-07	2.79	1.0553e-07	2.89
263.169	4.2916e-07	2.07	3.0106e-07	2.18	2.2723e-08	2.81	1.4044e-08	2.91
1.050.625	1.0374e-07	2.05	6.6649e-08	2.18	3.2138e-09	2.82	1.8538e-09	2.92

	$\alpha = 2.375$	
DoFs	$\|u - u_h\|_{L^2(\Omega)}$	rate
289	2.2177e-04	-
1.089	3.3912e-05	2.71
4.225	4.3221e-06	2.97
16.641	5.4888e-07	2.98
66.049	6.8762e-08	3.00
263.169	8.5292e-09	3.01
1.050.625	1.0497e-09	3.02

Table 10.10: L-shaped domain, $k = 2$: Influence of α for $a = 2/3\pi$ and $(x_0, y_0) = (0, 0)$.

geneous Dirichlet conditions are realized by nodal interpolation. The discretization is based on trilinear finite elements on hexahedra and uniform refinements. Alt-

DoFs	$\|u-u_h\|_{L^2(\Omega)}$	rate
316	0.0754	-
3.032	0.0172	1.96
26.416	0.0039	2.04
220.256	0.0009	2.02
1.798.336	0.0002	2.01
14.532.992	5.7491e-05	2.00

Table 10.11: Fichera corner, $k = 1$: L^2-error for a smooth solution.

	$x_0 = (-1,-1,-1)$, $\alpha = 0.55$		$x_0 = (0,0.5,0)$, $\alpha = 0.55$		$x_0 = (0,0.5,0)$, $\alpha = 2/3$	
DoFs	$\|u-u_h\|_{L^2(\Omega)}$	rate	$\|u-u_h\|_{L^2(\Omega)}$	rate	$\|u-u_h\|_{L^2(\Omega)}$	rate
316	0.0007	—	0.0007	—	0.0007	—
3.032	0.0002	2.00	0.0002	1.43	0.0002	1.55
26.416	3.9176e-05	1.98	6.8242e-05	1.72	6.2591e-05	1.80
22.0256	9.6835e-06	1.98	1.9077e-05	1.80	1.6589e-05	1.88
1.798.336	2.4305e-06	1.97	5.2412e-06	1.85	4.3418e-06	1.92
14.532.992	6.1407e-07	1.98	1.4423e-06	1.87	1.1264e-06	1.94

Table 10.12: Fichera corner: L^2-error.

hough the dual problem lacks full regularity, Theorem 9 asserts that this can be compensated by extra s_0-regularity of the primal solution to maintain full second order convergence in L^2.

Table 10.11 shows that we observe numerically already for coarse discretizations the predicted convergence order two, and the theoretical results are confirmed. For the last calculations of this section, the exact solution is given by

$$u = r^\alpha,$$

where $r = \operatorname{dist}(x, x_0)$ measures the distance from the point x_0, which is varied as depicted in Table 10.12. The L^2-error is computed with a tensor product Gauss rule (five points in each coordinate direction).

Remark 10.17. *Note that in the paper [77] we also consider the L^2-convergence of the normal derivative on the boundary. We show that the optimal rate $O(h^k)$ (up to a logarithmic factor in the lowest order case) can be achieved, if the solution is sufficiently smooth. The proof is based on a local error analysis of the FEM as discussed, e.g., in [171, 172]. In the paper we extract error bounds for the flux on the boundary from an optimal FEM estimate on a strip of width $O(h)$ near the boundary. Although we present the convergence of the flux for an H^1-conforming discretization, the techniques are applicable to mixed methods [112], FEM-BEM coupling [111],*

and mortar and DG methods [113, 173]. In fact, the results presented in [77] lead to a sharpening of [113], where convexity of the domain was assumed to avoid the analysis of a suitable additional dual problem.

Conclusion

In this thesis we have considered and developed complexity reduction techniques for finite element methods, which we have applied to eigenvalue problems for the vibro-acoustic analysis in the context of distinct problem settings as large as an eight story building and as small as a violin bridge.

We have started by demonstrating the benefits of the mortar method, which allows to mesh the single structures such as walls, floors and ceilings of a large building structure separately. This method is thus especially useful for our purpose of vibro-acoustic simulation of timber buildings using modular conception. Furthermore we have introduced a novel model reduction technique for elastomer modeling, which allows to replace the explicitely discretized elastomer by a coupling condition that fits into the implementational framework of mortar methods. We have demonstrated that it reduces the amount of degrees of freedom and the complexity of the mesh generation significantly while having a very good accuracy.

Then, in order to handle the extent of the numerical calculations performed when dealing with parameter-dependent calculations as they occur in our vibro-acoustic analysis, we have introduced an eigenvalue reduced basis method. We have presented a new error estimator and several greedy algorithms in order to construct a reduced basis space, which allows us to simultaneously approximate several eigenvalues of interest. Furthermore this error estimator is able to take into account multiple eigenvalues. These methods and the corresponding error estimators have first been considered in the context of conforming problems and then further extended to isogeometric mortar saddle point problems, where we have considered simulations on the curved domain of a violin bridge. Furthermore we have been able to eliminate the Lagrange multipliers from our detailed mortar solution in the reduced basis context and therefore to obtain a symmetric positive definite matrix. As an additional complexity reduction method we have considered the component mode synthesis in order to couple it with our reduced basis eigenvalue problem method. This has enabled us to approximate large complex geometries, such as an eight story building, adequately using modular conception in a fast and efficient way.

Due to the geometries under investigation, we have attended to elliptic problems in domains with reentrant corners. There we have presented several modification

techniques to overcome the resulting corner singularities and to obtain optimal L^2- convergence rates. First we have recalled the energy correction method, which constitutes a numerical tool to overcome the pollution effect with a trivial change in the stiffness matrix. For the first time we have extended and applied this method to higher order ansatz functions as well as to eigenvalue problems. Finally, we have shown by duality considerations that, under some additional regularity assumptions on the exact solution, it is possible to recover optimal L^2-convergence of the numerical approximation for right-hand side problems.

List of figures

List of tables

References

[1] R.A. Adams. *Sobolev Spaces*. Pure and Applied Mathematics. Academic Press, New York, 1975.

[2] T. Apel. *Anisotropic finite elements: Local estimates and applications*. Habilitation, TU Chemnitz, 1999.

[3] T. Apel and S. Nicaise. The finite element method with anisotropic mesh grading for elliptic problems in domains with corners and edges. *Mathematical Methods in the Applied Sciences*, 21:519–549, 1998.

[4] T. Apel, A. Sändig, and J. Whiteman. Graded mesh refinement and error estimates for finite element solutions of elliptic boundary value problems in non-smooth domains. *Mathematical Methods in the Applied Sciences*, 19:63–85, 1996.

[5] Schankula Architekten. Vier- und achtgeschossige Wohn- und Bürogebäude in Massivholzbauweise. Standort Bad Aibling, Bauherr B&O Wohnungswirtschaft GmbH, schalltechnische Begleitung ift Rosenheim, 2011.

[6] I. Babuška. Finite element method for domains with corners. *Computing (Arch. Elektron. Rechnen)*, 6:264–273, 1970.

[7] I. Babuška and M.B. Rosenzweig. A finite element scheme for domains with corners. *Numerische Mathematik*, 20:1–21, 1973.

[8] I. Babuška, B.Q. Guo, and J.E. Osborn. Regularity and numerical solution of eigenvalue problems with piecewise analytic data. *SIAM Journal on Numerical Analysis*, 26:1534–1560, 1989.

[9] I. Babuška and J.E. Osborn. Finite element-Galerkin approximation of the eigenvalues and eigenvectors of selfadjoint problems. *Mathematics of Computation*, 52:275–297, 1989.

[10] I. Babuška and J.E. Osborn. Eigenvalue problems. In *Handbook of Numerical Analysis*, volume 2, pages 641–787. North Holland, Amsterdam, 1991.

[11] I. Babuška and M. Rosenzweig. A finite element scheme for domains with corners. *Numerische Mathematik*, 20:1–21, 1972.

[12] H.T. Banks and N. Lybeck. Modeling methodology for elastomer dynamics. *Systems & Control: Foundations & Applications*, 22:37–50, 1997.

[13] D.Z. Bare, J. Orlik, and G. Panasenko. Asymptotic dimension reduction of a Robin-type elasticity boundary value problem in thin beams. *Applicable Analysis*, 93:1217–1238, 2014.

[14] K.-J. Bathe and J. Dong. Component mode synthesis with subspace iterations for controlled accuracy of frequency and mode shape solutions. *Computers and Structures*, 139:28–32, 2014.

[15] L. Beirão Da Veiga, A. Buffa, G. Sangalli, and R. Vásquez. Mathematical analysis of variational isogeometric methods. *Acta Numerica*, 23:157–287, 2014.

[16] F. Ben Belgacem. The mortar finite element method with Lagrange multipliers. *Numerische Mathematik*, 84:173–197, 1999.

[17] F. Ben Belgacem and Y. Maday. The mortar finite element method for three dimensional finite elements. *ESAIM: Mathematical Modelling and Numerical Analysis*, 31:289–302, 1997.

[18] F. Ben Belgacem, P. Seshaiyer, and M. Suri. Optimal convergence rates of hp mortar finite element methods for second-order elliptic problems. *ESAIM:Mathematical Modelling and Numerical Analysis*, 34:591–608, 2000.

[19] C. Bernardi, Y. Maday, and A.T. Patera. A new non conforming approach to domain decomposition: The mortar element method. In *Collège de France Seminar*, pages 13–51. Pitman, Paris, 1994.

[20] P. Binev, A. Cohen, W. Dahmen, R. DeVore, G. Petrova, and P. Wojtaszczyk. Convergence rates for greedy algorithms in reduced basis methods. *SIAM Journal of Mathematical Analysis*, 43:1457–1472, 2011.

[21] H. Blum and M. Dobrowolski. On finite element methods for elliptic equations on domains with corners. *Computing*, 28:53–63, 1982.

[22] H. Blum and R. Rannacher. Extrapolation techniques for reducing the pollution effect of reentrant corners in the finite element method. *Numerische Mathematik*, 52:539–564, 1988.

[23] D. Boffi. Finite element approximation of eigenvalue problems. *Acta numerica*, 19:1–120, 2010.

[24] A. Boström, P. Bövik, and P. Olsson. A comparison of exact first order and spring boundary conditions for scattering by thin layers. *Journal of Nondestructive Evaluation*, 11:175–184, 1992.

[25] F. Bourquin. Component mode synthesis and eigenvalues of second order operators: Discretization and algorithm. *RAIRO Modélisation Mathématique et Analyse Numérique*, 26:385–423, 1992.

[26] F. Bourquin and F. d'Hennezel. Intrinsic component mode synthesis and plate vibrations. *Computers and Structures*, 44:315–324, 1992.

[27] F. Bourquin and F. d'Hennezel. Numerical study of an intrinsic component mode synthesis method. *Computer Methods in Applied Mechanics and Engineering*, 97:49–76, 1992.

[28] F. Bourquin and R. Namar. Decoupling and modal synthesis of vibrating continuous systems. In *Ninth International Conference on Domain Decomposition Methods*, pages 290–302, 1998.

[29] D. Braess. *Finite elements: Theory, fast solvers, and applications in solid mechanics*. Cambridge University Press, New York, 3rd edition, 2007.

[30] S. Brenner and R. Scott. *The mathematical theory of finite element methods*, volume 15 of *Texts in Applied Mathematics*. Springer, 3rd edition, 2008.

[31] E. Brivadis, A. Buffa, B. Wohlmuth, and L. Wunderlich. Isogeometric mortar methods. *Computer Methods in Applied Mechanics and Engineering*, 284:292–319, 2015.

[32] A. Buffa, Y. Maday, A.T. Patera, C. Prud'homme, and G. Turinici. *A priori* convergence of the greedy algorithm for the parametrized reduced basis method. *ESAIM: Mathematical Modelling and Numerical Analysis*, 46:595–603, 2012.

[33] A. Buffa, I. Perugia, and T. Warburton. The mortar-discontinuous Galerkin method for the 2D Maxwell eigenproblem. *Journal of Scientific Computing*, 40:86–114, 2009.

[34] E. Cancès, V. Ehrlacher, and T Lelièvre. Greedy algorithms for high-dimensional eigenvalue problems. *Constructive Approximation*, 40:387–423, 2014.

[35] F. Casadei, E. Gabellini, G. Fotia, F. Maggio, and A. Quarteroni. A mortar spectral/finite element method for complex 2D and 3D elastodynamic problems. *Computer Methods in Applied Mechanics and Engineering*, 191(45):5119–5148, 2002.

[36] A. Castellani, G. Kajon, P. Panzeri, and P. Pezzoli. Elastomeric materials used for vibration isolation of railway lines. *Journal of Engineering Mechanics*, 124:614–621, 1998.

[37] P. Ciarlet. *The finite element method for elliptic problems*, volume 40 of *Classics in Applied Mathematics*. SIAM, Philadelphia, 2002.

[38] J.A. Cottrell, T.J.R. Hughes, and Y. Bazilevs. *Isogeometric analysis. Towards integration of CAD and FEA.* Wiley, Chichester, 2009.

[39] R.R. Craig Jr. *Structural dynamics - an introduction to computer methods.* John Wiley & Sons, New York, 1981.

[40] R.R. Craig Jr. A review of time domain and frequency domain component mode synthesis methods. In *Proceedings of the 85th joint ASCE/ASME mechanics conference*, volume 67, pages 49–76, 1985.

[41] R.R. Craig Jr. and M.C.C. Bampton. Coupling of substructures for dynamic analysis. *AIAA Journal*, 6:1313–1321, 1986.

[42] W. Dahmen, C. Plesken, and G. Welper. Double greedy algorithms: Reduced basis methods for transport dominated problems. *ESAIM: Mathematical Modelling and Numerical Analysis*, 48:623–663, 2014.

[43] M. Dauge. Benchmark computations for Maxwell equations. http://perso.univ-rennes1.fr/monique.dauge/benchmax.html., 2003.

[44] C. De Falco, A. Reali, and R. Vásquez. Geopdes: A research tool for isogeometric analysis of pdes. *Advances in Engineering Software*, 42:1020–1034, 2011.

[45] D. de Klerk, D.J. Rixen, and Voormeeren S.N. General framework for dynamic substructuring: history, review, and classification of techniques. *AIAA Journal*, 46:1169–1181, 2008.

[46] P. Destuynder. Remarks on dynamic substructuring. *European Journal of Mechanics - A/Solids*, 8:201–218, 1989.

[47] R. DeVore, G. Petrova, and P. Wojtaszczyk. Greedy algorithms for reduced bases in Banach spaces. *Constructive Approximation*, 37:455–466, 2013.

[48] M. Dittmann, M. Franke, İ. Temizer, and C. Hesch. Isogeometric analysis and thermomechanical mortar contact problems. *Computer Methods in Applied Mechanics and Engineering*, 274:192–212, 2014.

[49] W. Dornisch, G. Vitucci, and S. Klinkel. The weak substitution method and application of the mortar method for patch coupling in NURBS-based isogeometric analysis. *International Journal for Numerical Methods in Engineering*, 103:205–234, 2015.

[50] M. Drohmann, B. Haasdonk, S. Kaulmann, and M. Ohlberger. A software framework for reduced basis methods using DUNE-RB and RBmatlab. In *Advances in DUNE: Proceedings of the DUNE User Meeting, Held in October 6th–8th 2010 in Stuttgart, Germany*, pages 77–88, Berlin Heidelberg, 2012. Springer.

[51] M. Drohmann, B. Haasdonk, and M. Ohlberger. Adaptive reduced basis methods for nonlinear convection-diffusion equations. *Finite Volumes for Complex Applications VI Problems & Perspectives*, 4:369–377, 2011.

[52] J.L. Eftang and A.T. Patera. A port-reduced static condensation reduced basis element method for large component-synthesized structures: Approximation and *a posteriori* error estimation. *Advanced Modeling and Simulation in Engineering Sciences*, 1, 2013.

[53] H. Egger, U. Rüde, and B. Wohlmuth. Energy-corrected finite element methods for corner singularities. *SIAM Journal on Numerical Analysis*, 52:171–193, 2014.

[54] H. Elman and Q. Liao. Reduced basis collocation methods for partial differential equations with random coefficients. *SIAM/ASA Journal on Uncertainty Quantification*, 1:192–217, 2013.

[55] L.C. Evans. *Partial differential equations*. American Mathematical Society, 1998.

[56] U. Schanda Fakultät für Angewandte Natur-und Geisteswissenschaften Hochschule Rosenheim. Schlussbericht zu dem IGF-Vorhaben: Vibroakustik im Planungsprozess für Holzbauten - Modellierung, numerische Simulation,

Validierung - Teilantrag 3: Parameterentwicklung und SEA-Modellierung, 2015.

[57] B. Flemisch, M. Kaltenbacher, and B. Wohlmuth. Elasto-acoustic and acoustic-acoustic coupling on non-matching grids. *International Journal for Numerical Methods in Engineering*, 67(13):1791–1810, 2006.

[58] B. Flemisch and B. Wohlmuth. Nonconforming methods for nonlinear elasticity problems. In *Domain Decomposition Methods in Science and Engineering XVI*, Lecture Notes in Computational Science and Engineering, pages 65–76. Springer, Berlin, 2007.

[59] N. H. Fletcher and T.D. Rossing. *The physics of musical instruments*. Springer, New York, 2nd edition, 1998.

[60] I. Fumagalli, A. Manzoni, N. Parolini, and M. Verani. Reduced basis approximation and *a posteriori* error estimates for parametrized elliptic eigenvalue problems. *ESAIM: Mathematical Modelling and Numerical Analysis*, 2016.

[61] M.J. Gander, C. Japhet, Y. Maday, and F. Nataf. *A new cement to glue nonconforming grids with Robin interface conditions : The finite element case*, pages 259–266. 15th International Conference on Domain Decomposition Methods. Springer, Berlin Heidelberg, 2004.

[62] J.-C. Garcia-Betancur, A. Goni-Moreno, T. Horger, M. Schott, M. Sharan, J. Eikmeier, B. Wohlmuth, A. Zernecke, K. Ohlsen, C. Kuttler, and D. Lopez. Cell-fate decision defines acute and chronic infection cell lineages in *Staphylococcus aureus*. *In preparation*, 2016.

[63] A.-L. Gerner and K. Veroy. Certified reduced basis methods for parametrized saddle point problems. *SIAM Journal on Scientific Computing*, 34:2812–2836, 2012.

[64] D. Gilbarg and N.S. Trudinger. *Elliptic partial differential equations of second order*, volume 224 of *Grundlagen der mathematischen Wissenschaften*. Springer, 1977.

[65] S. Glas and K. Urban. On non-coercive variational inequalities. *SIAM Journal on Numerical Analysis*, 52:2250–2271, 2013.

[66] M.A. Grepl and A.T. Patera. *A posteriori* error bounds for reduced-basis approximations of parametrized parabolic partial differential equations. *ESAIM: Mathematical Modelling and Numerical Analysis*, 39:157–181, 2005.

[67] P. Grisvard. *Elliptic problems in nonsmooth domains*. Pitman Advanced Publishing, 1985.

[68] B. Haasdonk and M. Ohlberger. Reduced basis method for finite volume approximations of parametrized linear evolution equations. *ESAIM: Mathematical Modelling and Numerical Analysis*, 42:277–302, 2008.

[69] B. Haasdonk, J. Salomon, and B. Wohlmuth. A reduced basis method for parametrized variational inequalities. *SIAM Journal of Mathematical Analysis*, 50:2656–2676, 2012.

[70] P. Hauret and M. Ortiz. BV estimates for mortar methods in linear elasticity. *Computer Methods in Applied Mechanics and Engineering*, 195:4783–4793, 2006.

[71] P. Hauret and P. Tallec. A discontinuous stabilized mortar method for general 3D elastic problems. *Computer Methods in Applied Mechanics and Engineering*, 196(49-52):4881–4900, 2007.

[72] P. Hauret and P. Tallec. Two-scale Dirichlet-Neumann preconditioners for elastic problems with boundary refinements. *Computer Methods in Applied Mechanics and Engineering*, 196(8):1574–1588, 2007.

[73] C. Hesch and P. Betsch. Isogeometric analysis and domain decomposition methods. *Computer Methods in Applied Mechanics and Engineering*, 213–216:104–112, 2012.

[74] T. Horger, M. Huber, U. Rüde, C. Waluga, and B. Wohlmuth. Energy-corrected finite element methods for scalar elliptic problems. *ENUMATH 2013 proceedings*, 103:19–36, 2014.

[75] T. Horger, S. Kollmannsberger, F. Frischmann, E. Rank, and B. Wohlmuth. A new mortar formulation for modeling elastomer bedded structures with modal-analysis in 3D. *Advanced Modeling and Simulation in Engineering Sciences*, 1, 2014.

[76] T. Horger, C. Kuttler, B. Wohlmuth, and A. Zhigun. Analysis of a bacterial model with nutrient-dependent degenerate diffusion. *Mathematical Methods in the Applied Sciences*, 38:3851–3865, 2015.

[77] T. Horger, M. Melenk, and B. Wohlmuth. On optimal L2- and surface flux convergence in FEM. *Computing and Visualization in Science*, 16:231–246, 2015.

[78] T. Horger, A. Oelker, C. Kuttler, and J. Pérez-Velázquez. Mathematical modeling of tumor-induced angiogenesis using porous medium diffusion. *International Journal of Biomathematics and Biostatistics*, 2:145–165, 2013.

[79] T. Horger, P. Pustejovska, and B. Wohlmuth. Higher order energy-corrected finite element methods. *Submitted*, 2016.

[80] T. Horger, B. Wohlmuth, and T. Dickopf. Simultaneous reduced basis approximation of parameterized elliptic eigenvalue problems. *ESAIM: Mathematical Modelling and Numerical Analysis*, 2016.

[81] T. Horger, B. Wohlmuth, and L. Wunderlich. Reduced basis isogeometric mortar approximations for eigenvalue problems in vibroacoustics. *Accepted for publication in MoRePaS 2015*, 2016.

[82] T.J.R. Hughes, J.A. Cottrell, and Y. Bazilevs. Isogeometric analysis: CAD, finite elements, NURBS, exact geometry and mesh refinement. *Computer Methods in Applied Mechanics and Engineering*, 194:4135–4195, 2005.

[83] T.J.R. Hughes, J.A. Evans, and A. Reali. Finite element and NURBS approximations of eigenvalue, boundary-value, and initial-value problems. *Computer Methods in Applied Mechanics and Engineering*, 272:290–320, 2014.

[84] W.C. Hurty. Dynamic analysis of structural systems using component modes. *AIAA Journal*, 3:678–685, 1965.

[85] D.B.P. Huynh, D.J. Knezevic, and A.T. Patera. A static condensation reduced basis element method: Approximation and *a posteriori* error estimation. *ESAIM: Mathematical Modelling and Numerical Analysis*, 47:213–251, 2013.

[86] D.B.P. Huynh, G. Rozza, S. Sen, and A.T. Patera. A successive constraint linear optimization method for lower bounds of parametric coercivity and inf-sup stability constants. *Comptes Rendus Académie des Sciences - Series I - Mathematics*, 345:473–478, 2007.

[87] L. Iapichino, A. Quarteroni, G. Rozza, and S. Volkwein. Reduced basis method for the Stokes equations in decomposable domains using greedy optimization. *ECMI 2014 proceedings*, pages 1–7, 2014.

[88] L. Jézéquel. *Synthèse modale: théorie et extensions.* PhD thesis, Université Claude Bernard, Lyon, 1985.

[89] K.L. Johnson. *Contact Mechanics*. Cambridge University Press, Cambridge, 1985.

[90] M. Kahlbacher and S. Volkwein. Galerkin proper orthogonal decomposition methods for parameter dependent elliptic systems. *Discussiones Mathematicae: Differential Inclusions, Control and Optimization*, 27:95–117, 2007.

[91] S. Kaufmann, T. Horger, A. Oelker, S. Beck, M. Schulze, K. Nikolaou, D. Ketelsen, and M. Horger. Volume perfusion computed tomography (VPCT)-based evaluation of response to TACE using two different sized drug eluting beads in patients with nonresectable hepatocellular carcinoma: Impact on tumor and liver parenchymal vascularisation. *European Journal of Radiology*, 84:2548–2554, 2015.

[92] S. Kaufmann, T. Horger, A. Oelker, C. Kloth, K. Nikolaou, M. Schulze, and M. Horger. Characterization of hepatocellular carcinoma (HCC) lesions using a novel CT-based volume perfusion (VPCT) technique. *European Journal of Radiology*, 84:1029–1035, 2015.

[93] S. Kaufmann, M. Schulze, T. Horger, A. Oelker, K. Nikolaou, and M. Horger. Reproducibility of VPCT parameters in the normal pancreas: Comparison of two different kinetic calculation models. *Academic Radiology*, 22:1099–1105, 2015.

[94] B.N. Khoromskij and J.M. Melenk. Boundary concentrated finite element methods. *SIAM Journal on Numerical Analysis*, 41:1–36, 2003.

[95] T. Klöppel, A. Popp, U. Küttler, and W. Wall. Fluid-structure interaction for non-conforming interfaces based on a dual mortar formulation. *Computer Methods in Applied Mechanics and Engineering*, 200(45-46):3111–3126, 2011.

[96] V. Kondratiev. Boundary value problems for elliptic equations in domains with conical or angular points. *Transactions of the Moscow Mathematical Society*, 16:227–313, 1967.

[97] A. Kufner. *Weighted Sobolev spaces*. Wiley, New York, 1985.

[98] B.P. Lamichhane and B. Wohlmuth. Mortar finite elements with dual Lagrange multipliers: Some application. *Lecture Notes in Computational Science and Engineering*, 40:319–326, 2005.

[99] R.B. Lehoucq, D.C. Sorensen, and C. Yang. ARPACK users guide: Solution of large-scale eigenvalue problems by implicitely restarted Arnoldi methods. *SIAM*, 1998.

[100] J. Li, J.M. Melenk, B. Wohlmuth, and J. Zou. Optimal *a priori* estimates for higher order finite elements for elliptic interface problems. *Applied Numerical Mathematics*, 60:19–37, 2010.

[101] X. Liu and S. Oishi. Verified eigenvalue evaluation for the Laplacian over polygonal domains of arbitrary shape. *SIAM Journal on Numerical Analysis*, 51:1634–1654, 2013.

[102] A.E. Lovgren, Y. Maday, and E.M. Ronquist. A reduced basis element method for the steady Stokes problem. *ESAIM: Mathematical Modelling and Numerical Analysis*, 40:529–552, 2006.

[103] R. Mac Neal. A hybrid method of component mode synthesis. *Computers and Structures*, 1:581–601, 1971.

[104] L. Machiels, Y. Maday, I.B. Oliveira, A.T. Patera, and D.V. Rovas. Output bounds for reduced-basis approximations of symmetric positive definite eigenvalue problems. *Comptes Rendus Académie des Sciences - Series I - Mathematics*, 331:153–158, 2000.

[105] Y. Maday, A.T. Patera, and J. Peraire. A general formulation for *a posteriori* bounds for output functionals of partial differential equations; application to the eigenvalue problem. *Comptes Rendus Académie des Sciences - Series I - Mathematics*, 328:823–828, 1999.

[106] Y. Maday, A.T. Patera, and G. Turinici. Global *a priori* convergence theory for reduced basis approximations of single-parameter symmetric coercive elliptic partial differential equations. *Comptes Rendus Académie des Sciences - Series I - Mathematics*, 335:289–294, 2002.

[107] Y. Maday, A.T. Patera, and G. Turinici. *A priori* convergence theory for reduced-basis approximations of single-parametric elliptic partial differential equations. *Journal of Scientific Computing*, 17:437–446, 2002.

[108] The Mathworks, Inc., Natick, Massachusetts. *MATLAB version 8.5.0.197613 (R2015a)*, 2015.

[109] V.G. Maz´ja and B.A. Plamenevskii. The coefficients in the asymptotic expansion of the solutions of elliptic boundary value problems to near conical points. *Proceedings of the USSR Academy of Sciences*, 219:286–289, 1974.

[110] J.M. Melenk. *hp finite element methods for singular perturbations*, volume 1796 of *Lecture Notes in Mathematics*. Springer, 2002.

[111] J.M. Melenk, D. Praetorius, and B. Wohlmuth. Simultaneous quasi-optimal convergence rates in FEM-BEM coupling. *Mathematical Methods in the Applied Sciences*, 2014.

[112] J.M. Melenk, H. Rezaijafari, and B. Wohlmuth. Quasi-optimal *a priori* estimates for fluxes in mixed finite element methods and applications to the Stokes-Darcy coupling. *IMA Journal of Applied Mathematics*, 34:1–27, 2014.

[113] J.M. Melenk and B. Wohlmuth. Quasi-optimal approximation of surface based Lagrange multipliers in finite element methods. *SIAM Journal on Numerical Analysis*, 50:2064–2087, 2012.

[114] H. Morand and R. Ohayon. Substructure variational analysis of the vibrations of coupled fluid-structure systems. Finite element results. *International Journal for Numerical Methods in Engineering*, 14:201–218, 1979.

[115] C.B. Morrey. *Multiple integrals in the calculus of variations*. Springer, 1966.

[116] F. Negri, A. Manzoni, and G. Rozza. Reduced basis approximation of parametrized optimal flow control problems for the Stokes equations. *Computers & Mathematics with Applications*, 69:319–336, 2015.

[117] A.K. Noor and J.M. Peters. Reduced basis technique for nonlinear analysis of structures. *AIAA Journal*, 18:455–462, 1980.

[118] T.C. Nwofor. Finite element modeling of brick-mortar interface stresses. *International Journal of Civil & Environmental Engineering*, 12:48–67, 2012.

[119] C. Papadimitriou and D.-C. Papadioti. Component mode synthesis techniques for finite element model updating. *Computers and Structures*, 126:15–28, 2013.

[120] M. Pastor, M. Binda, and T. Harcarik. Modal assurance criterion. *Procedia Engineering*, 48:543–548, 2012.

[121] A.T. Patera and G. Rozza. Reduced basis approximation and *a posteriori* error estimation for parametrized partial differential equations. Version 1.0, Copyright MIT 2006–2007, to appear in (tentative rubric) MIT Pappalardo Graduate Monographs in Mechanical Engineering.

[122] G.S.H. Pau. Reduced-basis method for band structure calculations. *Physical Review E*, 76, 2007.

[123] G.S.H. Pau. *Reduced basis method for quantum models of crystalline solids.* PhD thesis, MIT, 2007.

[124] G.S.H. Pau. Reduced basis method for simulation of nanodevices. *Physical Review B*, 78, 2008.

[125] M. Peszynska. Mortar adaptivity in mixed methods for flow in porous media. *International Journal of Numerical Analysis and Modeling*, 2:241–282, 2005.

[126] M. Peszynska, M. Wheeler, and I. Yotov. Mortar upscaling for multiphase flow in porous media. *Computational Geosciences*, 6(1):73–100, 2002.

[127] M.A. Puso. A 3D mortar method for solid mechanics. *International Journal for Numerical Methods in Engineering*, 59:315–336, 2004.

[128] A. Quarteroni. *Numerical models for differential problems*, volume 8 of *Modeling, Simulation and Applications.* Springer, Milan, 2nd edition, 2014.

[129] A. Quarteroni, A. Manzoni, and F. Negri. *Reduced basis methods for partial differential equations. An introduction.* Springer International Publishing, 1 edition, 2015.

[130] A. Rabold. *Anwendung der Finite Element Methode auf die Trittschallberechnung.* Dissertation, Chair for Computation in Engineering, Fakultät für Bauingenieur- und Vermessungswesen, Technische Universität München, 2010.

[131] A. Rabold. Schalltechnische Lösungen für Massivholzelemente in der Geschossbauweise. In *Tagungsband 4. Europäischer Kongress für energieeffizientes Bauen mit Holz*, 2011.

[132] A. Rabold, A. Düster, J. Hessinger, and E. Rank. Optimization of lightweight floors in the low frequency range with a FEM based prediction model. In *Conference proceedings DAGA*, 2009.

[133] A. Rabold, A. Düster, and E. Rank. FEM based prediction model for the impact sound level of floors. In *Conference proceedings EURONOISE*, 2008.

[134] O. Rand and V. Rovenski. *Analytical methods in anisotropic elasticity: With symbolic computational tools*. Birkhäuser, Boston, 2007.

[135] E. Rank, A. Düster, V. Nübel, K. Preusch, and O.T. Bruhns. High order finite elements for shells. *Computer Methods in Applied Mechanics and Engineering*, 194:2494–2512, 2005.

[136] T. Ranz. *Ein feuchte- und temperaturabhängiger anisotroper Werkstoff: Holz*. Beiträge zur Materialtheorie. Universität der Bundeswehr München, 2007.

[137] P.A. Raviart and J.M. Thomas. *Introduction à l'analyse numérique des équations aux dérivées partielles*. Masson, Paris, 1983.

[138] A. Rössle. Corner singularities and regularity of weak solutions for the two-dimensional Lamé equations on domains with angular corners. *Journal of Elasticity*, 60:57–75, 2000.

[139] D.V. Rovas, L. Machiels, and Y. Maday. Reduced basis output bound methods for parabolic problems. *IMA Journal of Numerical Analysis*, 26:423–445, 2006.

[140] G. Rozza, D.B.P. Huynh, and A. Manzoni. Reduced basis approximation and *a posteriori* error estimation for Stokes flows in parametrized geometries: Roles of the inf-sup stability constants. *Numerische Mathematik*, 125:115–152, 2013.

[141] G. Rozza, D.B.P. Huynh, and A.T. Patera. Reduced basis approximation and *a posteriori* error estimation for affinely parametrized elliptic coercive partial differential equations. application to transport and continuum mechanics. *Archives of Computational Methods in Engineering*, 15:229–275, 2008.

[142] G. Rozza and K. Veroy. On the stability of the reduced basis method for Stokes equations in parametrized domains. *Computer Methods in Applied Mechanics and Engineering*, 196:1244–1260, 2007.

[143] T. Rüberg and M. Schanz. Coupling finite and boundary element methods for static and dynamic elastic problems with non-conforming interfaces. *Computer Methods in Applied Mechanics and Engineering*, 198:449–458, 2008.

[144] U. Rüde. Local corrections for eliminating the pollution effect of reentrant corners. In *Proceedings of the Fourth Copper Mountain Conference on Multigrid Methods*, pages 365–382, Philadelphia, 1989. SIAM.

[145] U. Rüde, C. Waluga, and B. Wohlmuth. Nested Newton strategies for energy-corrected finite element methods. *SIAM Journal on Scientific Computing*, 36:1359–1383, 2014.

[146] U. Rüde and C. Zenger. On the treatment of singularities in the multigrid method. In *Multigrid methods, II (Cologne, 1985)*, volume 1228 of *Lecture Notes in Mathematics*, pages 261–271. Springer, Berlin, 1986.

[147] M.H. Sadd. *Elasticity theory, applications, and numerics.* Elsevier, 1st edition, 2009.

[148] A. H. Schatz and L. B. Wahlbin. Maximum norm estimates in the finite element method on plane polygonal domains. II. Refinements. *Mathematics of Computation*, 33:465–492, 1979.

[149] M. Schramm, F. Dolezal, A. Rabold, and U. Schanda. Stoßstellen im Holzbau Planung, Prognose und Ausführung. In *Tagungsband DAGA*, 2010.

[150] L.R. Scott and S. Zhang. Finite element interpolation of nonsmooth functions satisfying boundary conditions. *Mathematics of Computation*, 54:483–493, 1990.

[151] A. Seitz, P. Farah, J. Kremheller, B. Wohlmuth, W.A. Wall, and A. Popp. Isogeometric dual mortar methods for computational contact mechanics. *Computer Methods in Applied Mechanics and Engineering*, 301:259–280, 2016.

[152] P. Seshaiyer and M. Suri. Uniform hp convergence results for the mortar finite element method. *Mathematics of Computation*, 69:521–546, 1999.

[153] S. Sitzmann, K. Willner, and B.I. Wohlmuth. A dual Lagrange method for contact problems with regularized contact conditions. *International Journal for Numerical Methods in Engineering*, 99:221–238, 2014.

[154] K. Smetana and A.T. Patera. Optimal local approximation spaces for component-based static condensation procedures. *Submitted*, 2016.

[155] G. Strang and G. Fix. *An Analysis of the Finite Element Method.* Wellesley-Cambridge Press, Wellesley, 2nd edition, 2008.

[156] R. Syha, L. Grünwald, T. Horger, D. Spira, D. Ketelsen, W. Vogel, C.D. Claussen, and M. Horger. Assessment of the nature of residual masses at end of treatment in lymphoma patients using volume perfusion computed tomography. *European Radiology*, 24:770–779, 2014.

[157] B.A. Szabó and I. Babuška. *Finite element analysis*. John Wiley & Sons, Hoboken, New Jersey, 1991.

[158] B.A. Szabó, A. Düster, and E. Rank. The p-version of the finite element method. In *Encyclopedia of Computational Mechanics*, volume 1, chapter 5, pages 119–139. John Wiley & Sons, Hoboken, New Jersey, 2004.

[159] L. Tartar. *An introduction to Sobolev spaces and interpolation spaces*, volume 3 of *Lecture Notes of the Unione Matematica Italiana*. Springer, Berlin, 2007.

[160] D.-M. Tran. Hybrid methods of component mode synthesis using attachment modes or residual attachment modes. In *Proceedings of the 2nd ESA International Workshop on Modal representation of flexible structures by continuum methods*, page Noordwijk. ESTEC, 1992.

[161] D.-M. Tran. Méthode de sous-structuration pour l'analyse de sensibilité et la réactualisation des modes propres des structures localement perturbées. *Revue Européenne des Éléments Finis*, 5:75–99, 1996.

[162] D.-M. Tran. Méthodes de synthèse modale mixtes. *Revue Européenne des Eléments Finis*, 1996.

[163] H. Triebel. *Interpolation theory, function spaces, differential operators*. Johann Ambrosius Barth, Heidelberg, 2nd edition, 1995.

[164] S. Triebenbacher, M. Kaltenbacher, B. Wohlmuth, and B. Flemisch. Applications of the mortar finite element method in vibroacoustics and flow induced noise computations. *Acta Acustica united with Acustica*, 96:536–553, 2010.

[165] K. Urban and A.T. Patera. An improved error bound for reduced basis approximation of linear parabolic problems. *Mathematics of Computation*, 83:1599–1615, 2014.

[166] K. Urban, S. Volkwein, and O. Zeeb. Greedy sampling using nonlinear optimization. *Reduced Order Methods for Modeling and Computational Reductions*, 9:137–157, 2014.

[167] K. Urban and B. Wieland. Affine decompositions of parametric stochastic processes for application within reduced basis methods. In *7th Vienna International Conference on Mathematical Modelling*, MATHMOD 2012, Vienna, 2012.

[168] R. Valid. Une méthode de calcul des structures au flambage par sous-structuration et synthèse modale. *Comptes Rendus de l'Académie des Sciences - Series II*, 294:299–302, 1982.

[169] S. Vallaghé, D.B.P. Huynh, D.J. Knezevic, T. Loi Nguyen, and A.T. Patera. Component-based reduced basis for parametrized symmetric eigenproblems. *Advanced Modeling and Simulation in Engineering Sciences*, 2, 2015.

[170] K. Veroy. *Reduced-basis methods applied to problems in elasticity: Analysis and applications.* PhD thesis, MIT, 2003.

[171] L. Wahlbin. Local behavior in finite element methods. In *Handbook of numerical Analysis. Volume II: Finite element methods (Part 1)*, pages 353–522. North Holland, 1991.

[172] L. Wahlbin. *Superconvergence in Galerkin finite element methods*, volume 1605 of *Lecture Notes in Mathematics.* Springer, 1995.

[173] C. Waluga and B. Wohlmuth. Quasi-optimal *a priori* interface error bounds and *a posteriori* estimates for the interior penalty method. *SIAM Journal on Numerical Analysis*, 51:3259–3279, 2013.

[174] L. Wang, S. Hou, and L. Shi. A numerical method for solving 3D elasticity equations with sharp-edged interfaces. *International Journal of Partial Differential Equations*, 2013, 2013.

[175] Z. Wassouf. *The mortar method for the finite element method of high order.* PhD thesis, Technische Universität München, 2010.

[176] B.I. Wohlmuth. *Discretization methods and iterative solvers based on domain decomposition.*, volume 17 of *Lecture Notes in Computational Science and Engineering.* Springer, Berlin New York, 2001.

[177] B.I. Wohlmuth, A. Popp, M.W. Gee, and W.A. Wall. An abstract framework for *a priori* estimates for contact problems in 3D with quadratic finite elements. *Computational Mechanics*, 49:735–747, 2012.

[178] J. Woodhouse. On the bridge hill of the violin. *Acta Acustica united with Acustica*, 91:155–165, 2005.

[179] H. Xie, Z. Li, and Z. Qiao. A finite element method for elasticity interface problems with locally modified triangulations. *International Journal of Numerical Analysis and Modeling*, 8:189–200, 2013.

[180] M. Yano. A minimum-residual mixed reduced basis method: Exact residual certification and simultaneous finite-element reduced-basis refinement. *ESAIM: Mathematical Modelling and Numerical Analysis*, 50, 2016.

[181] L. Zanon and K. Veroy-Grepl. The reduced basis method for an elastic buckling problem. *Proceedings in Applied Mathematics and Mechanics*, 13:439–440, 2013.

[182] C. Zenger and H. Gietl. Improved difference schemes for the Dirichlet problem of Poisson's equation in the neighbourhood of corners. *Numerische Mathematik*, 30:315–332, 1978.

[183] O.C. Zienkiewicz and R.L. Taylor. *The finite element method: Solid mechanics*, volume 2. Butterworth-Heinemann, 5th edition, 2000.